Emission of Multiple Messengers from Gamma-Ray Bursts

DISSERTATION

zur Erlangung des akademischen Grades
doctor rerum naturalium
(Dr. rer. nat.)
im Fach: Physik
Spezialisierung: Theoretische Physik

eingereicht an der
Mathematisch-Naturwissenschaftlichen Fakultät
der Humboldt-Universität zu Berlin

von

M.Sc. Annika Lena Rudolph

Präsident der Humboldt-Universität zu Berlin:
Prof. Dr. Peter A. Frensch (komm.)

Dekan der Mathematisch-Naturwissenschaftlichen Fakultät:
Prof. Dr. Elmar Kulke

Gutachter: 1. PD Dr. Walter Winter
2. Prof. Dr. David Berge
3. Prof. Dr. Robert Mochkovitch

Tag der mündlichen Prüfung: 20.05.2022

Selbständigkeitserklärung

Ich erkläre, dass ich die Dissertation selbständig und nur unter Verwendung der von mir gemäß § 7 Abs. 3 der Promotionsordnung der Mathematisch-Naturwissenschaftlichen Fakultät, veröffentlicht im Amtlichen Mitteilungsblatt der Humboldt-Universität zu Berlin Nr. 42/2018 am 11.07.2018, angegebenen Hilfsmittel angefertigt habe.

Abstract

Gamma-Ray Bursts (GRBs) are among the most energetic transients in the Universe and candidate sources of Ultra-High-Energy Cosmic Rays (UHECRs). A clear confirmation from UHECR measurements is however challenging, as the directional information of cosmic rays is partially lost due to deflection by (inter-)galactic magnetic fields. Alternatively, in a multi-messenger approach, the presence of UHECRs in an astrophysical object is indicated by neutrino or photon signatures produced in nuclear interactions. The absence of these signatures in turn imposes a limit on the nuclear interaction efficiency. This allows to indirectly set an upper limit on the amount of cosmic rays in a source: For instance, the lack of detected High-Energy (HE) neutrinos that could be associated with known GRBs challenges the most simple UHECR-GRB scenarios that predict a high neutrino flux.

This dissertation examines the prompt phase of GRBs as potential source of UHECRs, HE neutrinos and Very-High-Energy (VHE) photons by means of numerical radiation modelling. For this purpose we adapt the lepto-hadronic code AM3 to model particle spectra in the dense, high B-field environments realised in GRBs. AM3 is further validated by comparison to results obtained by other leading research groups.

Our simulations are carried out in the framework of the internal shock scenario. In this model, the GRB jet is discretized as a series of plasma layers ('shells') of varying velocities. Particle acceleration and emission take place in shocks induced as shells of different velocities collide with each other. In multi-zone internal shock models collisions between shells occur over a range of radii, allowing to account for different emission regions along the jet. We demonstrate that for such a model the population of GRBs can still describe UHECR data without violating neutrino limits for a wide range of initial Lorentz factor configurations of the outflow that reflect in the gamma-ray light curves. We discuss the implications of an increasingly pure UHECR composition at the highest energies and the amount of energy transferred to non-thermal baryons (quantified as baryonic loading) necessary to power the observed UHECR flux.

Neutrino limits may alternatively be met in low-luminosity objects, where the neutrino production efficiency is typically low. We present leptonic radiation models of the sub-class of low-luminosity GRBs in the internal shock model. In this context we evaluate how the amount of energy transferred to the magnetic field impacts a leptonic VHE inverse Compton component potentially observable by Imaging Air Cherenkov Telescopes (IACTs) and determine maximal energies of different cosmic-ray nuclei.

The baryonic loading may further be constrained from hadronic signatures in the photon spectra. We explore this approach in lepto-hadronic models of high-luminosity bursts. Our results illustrate the effect of the secondary particle cascade on multi-wavelength spectra as well as the impact of intermediate muon and pion cooling on neutrino peak energies. We further critically review the conditions necessary to reproduce typical GRB spectra within our model. Finally, the applicability of these findings to observed events is demonstrated at the example of GRBs detected by the *Fermi*-LAT.

Kurzzusammenfassung

Gammastrahlenblitze (Gamma-Ray Bursts, GRBs) gehören zu den energiereichsten transienten Ereignissen im Universum und werden als mögliche Quellen von ultra-hochenergetischen kosmischen Strahlen (Ultra-High-Energy Cosmic Rays, UHECRs) gehandelt. Eine eindeutige Bestätigung durch UHECR-Messungen ist jedoch schwierig, da die Richtungsinformation der kosmischen Strahlen während ihrer Ausbreitung aufgrund von Ablenkung durch Magnetfelder teilweise verloren geht. In einem alternativen multi-messenger Ansatz wird die Anwesenheit von kosmischen Strahlen in einem astrophysikalischen Objekt durch Neutrino- oder Photon-Signaturen angezeigt. Auf der anderen Seite kann die Abwesenheit dieser Signaturen die Effizienz von nuklearen Wechselwirkungen begrenzen. Damit kann indirekt eine Aussage über die Obergrenze an kosmischen Strahlen in einer Quelle getroffen werden: So werden die einfachsten UHECR-GRB-Szenarien durch den Mangel an gemessenen hoch-energetischen (High-Energy, HE) Neutrinos, die mit bekannten GRBs assoziert werden konnten, ausgeschlossen.

Diese Dissertation untersucht Gammastrahlenblitze mithilfe von Strahlungsmodellierungen als mögliche Quellen von UHECRs, HE Neutrinos und sehr hochenergetischer (Very-High-Energy, VHE) Photonen. Hierfür wird der lepto-hadronische Code AM3 angepasst, um Teilchenspektren in dichten Umgebungen mit starken Magnetfeldern (wie in GRBs) simulieren zu können. Zusätzlich validieren wir AM3 durch Abgleich mit Ergebnissen anderer führender Arbeitsgruppen.

Unsere Simulationen werden im Rahmen des Internal-Schock-Szenarios ausgeführt. In diesem Modell wird der GRB-Jet als Reihe von Plasma-Schichten ('Schalen') diskretisiert. Teilchenbeschleunigung und -emission finden in Schocks statt, die induziert werden, wenn Schalen verschiedener Geschwindigkeiten miteinander kollidieren. In Multi-Zonen-Modellen ereignen sich diese Kollisionen über verschiedene Radien, wodurch verschiedene Emissionszonen entlang des Jets erfasst werden können. Wir zeigen, dass für ein solches Multi-Zonen-Modell die Quellklasse von GRBs nach wie vor UHECR-Daten beschreiben kann, ohne Neutrinolimits zu verletzen. Dies gilt für eine große Vielfalt von initialen Lorentz-Faktor-Konfigurationen des Jets, die sich in den Gammastrahlen-Lichtkurven spiegeln. Wir diskutieren weiterhin die Implikationen einer zunehmend reinen UHECR-Zusammensetzung bei den höchsten Energien und die Energiemenge, die an nicht-thermische Baryonen übertragen werden muss (quantifiziert als baryonische Ladung), damit der UHECR-Fluss gespeist werden kann.

Alternativ können die Neutrinolimits in Objekten niedriger Leuchtkraft, in denen die Neutrinoproduktionseffizienz gering ist, eingehalten werden. Wir präsentieren leptonische Strahlungsmodellierungen für die Unterklasse von GRBs niedriger Leuchktraft im Internal-Schock-Modell. In diesem Zusammenhang evaluieren wir, wie die an Magnetfelder abgegebene Energiemenge eine leptonische inverse-Compton VHE Komponente beeinflusst (die mit Imaging Air Cherenkov Telescopes beobachtet werden könnte) und bestimmen die maximalen Energien verschiedener Atomkerne der kosmischen Strahlung.

Die baryonische Ladung kann alternativ mithilfe hadronischer Signaturen in Photonspektren eingeschränkt werden. Wir erforschen diesen Ansatz in lepto-hadronischen Modellen für GRBs mit hoher Leuchtkraft. Unsere Resultate illustrieren sowohl den Effekt der induzierten sekundären Teilchenkaskade auf Spektren in allen Wellenlängen als auch die Auswirkung des Abkühlens von Zwischenprodukten wie Myonen und Pionen auf Neutrinospektren. Wir diskutieren kritisch, welche Bedingungen erfüllt sein müssen, damit typische GRB-Spektren reproduziert werden können. Schließlich demonstrieren wir anhand von GRBs, die mit dem *Fermi*-LAT-Teleskop detektiert wurden, dass unsere Ergebnisse auf beobachtete Ereignisse anwendbar sind.

Acknowledgements

I want to dedicate this work to my grandmother Elsbeth – I so wish she would still be here and I could share the finishing of this thesis with her.

I also want to thank everyone who supported me during this time, I could never have made it without my mentors, colleagues, friends and family.

During my work leading to this thesis, I was supported by the European Research Council (ERC) under the European Union's Horizon 2020 research and innovation program (Grant No. 646623). I further was a scholarship holder of the Foundation of German Economy (Stiftung der deutschen Wirtschaft, SDW) and received support from the International Helmholtz-Weizmann Research School for Multimessenger Astronomy, largely funded through the Initiative and Networking Fund of the Helmholtz Association.

List of publications

The following articles were published in connection with this dissertation.

Peer-reviewed publications:

* Annika Rudolph, Jonas Heinze, Anatoli Fedynitch, and Walter Winter. "Impact of the Collision Model on the Multi-messenger Emission from Gamma-Ray Burst Internal Shocks". In: *Astrophys. J.* 893 (2020). arXiv: 1907.10633 [astro-ph.HE]
* Jonas Heinze, Daniel Biehl, Anatoli Fedynitch, Denise Boncioli, Annika Rudolph, and Walter Winter. "Systematic parameter space study for the UHECR origin from GRBs in models with multiple internal shocks". In: *Mon. Not. Roy. Astron. Soc.* 498.4 (2020). arXiv: 2006.14301 [astro-ph.HE]
* Annika Rudolph, Željka Bošnjak, Andrea Palladino, Iftach Sadeh, and Walter Winter. "Multi-wavelength radiation models for low-luminosity GRBs and the implications for UHECRs". In: *Mon. Not. Roy. Astron. Soc.* 511.4 (2022). arXiv: 2107.04612 [astro-ph.HE] *

In addition, three articles are currently being prepared for publication.

* Matteo Cerruti, Michael Kreter, Maria Petropoulou, Annika Rudolph, Foteini Oikonomou, and others. "The Hadronic Code Comparison Project"
  Published in the proceedings of the International Cosmic Ray Conference (ICRC) 2021:
  Matteo Cerruti et al. "The Blazar Hadronic Code Comparison Project". In: *PoS* ICRC2021 (2021). arXiv: 2107.06377 [astro-ph.HE]
* Annika Rudolph, Maria Petropoulou, Željka Bošnjak, and Walter Winter. "Full lepto-hadronic treatment of GRBs in the internal shock scenario and application to Fermi-LAT detected events"
* Leonel Morejon, Xavier Rodrigues, Annika Rudolph, Shan Gao and Walter Winter. "Revisiting possible signatures of heavy nuclei in Centaurus A" †

* This project was accepted for publication between submission and publication of the thesis
† This project is listed here for completeness only, the findings are not part of this thesis.

List of abbreviations

AGN	active galactic nucleus
CC	charged current
CMB	cosmic microwave background
CR	cosmic ray
DIS	deep inelastic scattering
DOM	digital optical module
EBL	extragalactic background light
GRB	gamma-ray burst
GW	gravitational wave
GZK	Greisen-Zatsepin-Kuz'min
HCCP	hadronic code comparison project
HE	high-energy
HESE	high-energy starting event
IACT	imaging air cherenkov telescope
IGM	intergalactic medium
LE	low-energy
LL-GRB	low-luminosity gamma-ray burst
NC	neutral current
PIC	particle-in-cell
PMT	photo-multiplier tube
RMHD	relativistic magneto-hydro-dynamics
SED	spectral energy distribution
SSC	synchrotron-self-Compton
SN	supernova
SNR	supernova remnant
TDE	tidal disruption event
TGM	through-going muon track
UHE	ultra-high-energy
UHECR	ultra-high-energy cosmic ray
VHE	very-high-energy

Contents

Abstract **v**

Acknowledgements **ix**

List of publications **xi**

List of abbreviations **xiii**

Contents **xv**

1 Introduction **1**

2 Multi-messenger astronomy **5**
2.1 Our Universe in multiple messengers 5
2.2 Potential UHECR sources 16
2.3 Status of multi-messenger astronomy 20

3 Radiation processes in high-energy astrophysics and comparison of approaches **23**
3.1 Basic concepts 23
3.2 Leptonic processes 27
3.3 Hadronic processes 31
3.4 Special scenarios 37

4 Gamma-ray bursts **41**
4.1 A historical introduction 41
4.2 The complete picture 42
4.3 Prompt phase energy dissipation mechanism 45
4.4 Prompt phase radiation models 47
4.5 GRBs as UHECR and HE neutrino sources 52

5 GRB internal shock models in a multi-messenger context **55**
5.1 Two internal-shock formalisms 55
5.2 Modified collision dynamics and impact on multi-messenger predictions 61
5.3 UHECR fit for different GRB engine realisations 64

6 Low-luminosity GRBs as potential sources of VHE photons and UHECRs **69**
6.1 The population of LL-GRBs and selection of representative examples 69
6.2 LL-GRB models 71
6.3 Methods and parameter choices 73

6.4 VHE gamma-ray predictions from a leptonic radiation modelling 76
6.5 Maximal energies of cosmic-ray nuclei 81

7 Lepto-hadronic GRB models and application to *Fermi*-LAT detected events 85
7.1 Methods 85
7.2 Educative example: Leptonic models 88
7.3 Educative example: Lepto-hadronic models 93
7.4 Secondary pion/muon cooling and relevance for neutrino spectra 101
7.5 The sample of LAT-detected bursts and reference events 104
7.6 Simulated results for the *Fermi*-LAT inspired prototypes 107

8 Conclusion and Outlook 111

Bibliography 117

A Details on AM3 145
A.1 Changes to the original code 147

B Additional material on multi-collision internal shock models 149
B.1 The discretisation time in the Daigne and Mochkovitch model 149
B.2 Probability of two-shell post-collision states 150
B.3 Radiation regimes in LL-GRBs 153
B.4 Additional parameter tables for the radiation modelling 154

1 Introduction

The oldest document proving the human fascination with the stars of the night sky is probably the Nebra Sky Disk, dated 3700 - 4100 b.C. (see picture on the right). For the longest time, astronomical observations were conducted solely by bare eye. The exploration of the sky beyond the visible spectrum and through other particle species became possible only during the last century, marking the beginning of *multi-messenger astronomy*.

Figure 1.1: The Nebra Sky Disk. Image Credit: *Juraj Lipták/State Office for Heritage Management and Archaeology Saxony-Anhalt*

The first additional messenger discovered more than 100 years ago were *cosmic rays*, charged particles reaching earth from space [1]. The discovery was an unexpected one, as Victor Hess was originally investigating the radioactivity of the earth. It proved to be fruitful though and paved the way to an entirely new field of study with profound implications both for astrophysics as well as particle physics (such as the later discovery of the muon [2] and pion [3] particles).
The advances in observational cosmic-ray physics in the following decades were complemented by breakthroughs in other astronomical disciplines: First, radio- to gamma-ray telescopes made 25 orders of magnitude of the electro-magnetic spectrum accessible [4, 5]. Second, already shortly after their theoretical introduction, the history of neutrinos became closely linked to astrophysics. For example, the fact that neutrinos carry a non-zero mass was first deduced from solar neutrino experiments [6]. In contrast to these early discoveries, neutrinos of cosmological origin were detected only a few years ago [7]. The most recent breakthrough was the long-awaited detection of gravitational waves, which opened an entirely new window to the universe to us [8].
The numerous advances in observational techniques achieved over the last centuries lay the base for modern technologies. Ground-based detector arrays like the Pierre Auger Observatory [9] and the Telescope Array [10] now provide precision measurements of cosmic rays up to extreme energies. Even more novel instruments, like the kilometer-scale IceCube observatory in the South Pole [11], allow us to detect some of the high-energy neutrinos that are emitted through cosmic-ray interactions in the cosmos. These instruments are helping us achieve the long-sought goal of unveiling the sources of the cosmic rays and the astrophysical processes behind their production.
Nonetheless, the sources of high-energy cosmic rays and neutrinos still are one of the big mysteries of modern astronomy. And although some questions still remain to be answered experimentally, there also is a gap that has to be bridged by theorists.

One possible way of constraining sources of high-energy particles on a theoretical level is by simple analytical estimates. For example, in

[1]: Hess (1912), "Über Beobachtungen der durchdringenden Strahlung bei sieben Freiballonfahrten"
[2]: Neddermeyer et al. (1937), "Note on the Nature of Cosmic Ray Particles"
[3]: Lattes et al. (1947), "Processes involving charged mesons"

[4]: Jansky (1933), "Radio Waves from Outside the Solar System"
[5]: Kraushaar et al. (1962), "Search for Primary Cosmic Gamma Rays with the Satellite Explorer XI"
[6]: Bahcall et al. (1976), "Solar Neutrinos - a Scientific Puzzle"
[7]: Aartsen et al. (2013), "Evidence for High-Energy Extraterrestrial Neutrinos at the IceCube Detector"
[8]: Abbott et al. (2016), "Observation of Gravitational Waves from a Binary Black Hole Merger"
[9]: Aab et al. (2015), "The Pierre Auger Cosmic Ray Observatory"
[10]: Fukushima (2003), "Telescope array project for extremely high energy cosmic rays"
[11]: Aartsen et al. (2017), "The IceCube Neutrino Observatory: Instrumentation and Online Systems"

order to be accelerated by a source, a particle should be confined by the source magnetic field [12]. From this requirement alone many objects can be ruled out as potential origin of Ultra-High-Energy Cosmic Rays (UHECRs) with energies above 10^{18} eV. Among the remaining source candidates are the centers of active galaxies (Active Galactic Nuclei, AGN), winds in starburst galaxies and Gamma-Ray Bursts (GRBs, that are the focus of this thesis).

[12]: Hillas (1984), "The Origin of Ultrahigh-Energy Cosmic Rays"

GRBs are short, energetic outbursts in X-rays to gamma-rays that release the energetic equivalent to a supernova over the course of a few seconds. They emerge after the merger of two compact objects or the cataclysmic death of a supermassive star where in either case a relativistic jet is launched. In principle, GRBs could provide the energy budget to power the UHECR flux and the magnetic field to confine high-energy particles [13].

[13]: Waxman (1995), "Cosmological gamma-ray bursts and the highest energy cosmic rays"

Naively one may expect that the GRB-UHECR connection could simply be confirmed by spatial and temporal association of a measured cosmic ray with a detected GRB. In reality, a clear association from cosmic-ray measurements is challenging, as cosmic-ray directions are blurred by magnetic fields during propagation. An alternative approach considers secondary particles such as neutrinos and photons produced in nuclear interactions with in-source photon fields. Those neutral particles are not magnetically deflected on their way to earth and may serve as evidence for the presence of cosmic rays in an astrophysical object. Indeed, an accompanying astrophysical neutrino flux from GRBs due to in-source cosmic-ray interactions was predicted *e.g.* in [14]. However, as of now no detected High-Energy (HE) neutrino could be associated with a known GRB [15, 16]. This puts rather strong limits on the efficiency of nuclear interactions in GRBs and rules out the most simple GRB-UHECR scenarios.

[14]: Waxman et al. (1997), "High-energy neutrinos from cosmological gamma-ray burst fireballs"

[15]: Aartsen et al. (2016), "An All-Sky Search for Three Flavors of Neutrinos from Gamma-Ray Bursts with the IceCube Neutrino Observatory"

[16]: Aartsen et al. (2017), "Extending the search for muon neutrinos coincident with gamma-ray bursts in IceCube data"

Still, certain parts of the parameter space remain unconstrained (*e.g.* [17]). This establishes the necessity of refined models to obtain better constraints on the actual role of GRBs as UHECR sources. Such models can include spatially resolved emission zones (as in [18]) and/or a self-consistent treatment of cosmic-ray, photon and neutrino spectra. The latter opens the additional possibility of limiting the cosmic-ray interaction efficiency by examining the impact on photon observables.

[17]: Biehl et al. (2018), "Cosmic-Ray and Neutrino Emission from Gamma-Ray Bursts with a Nuclear Cascade"

[18]: Bustamante et al. (2017), "Multi-messenger light curves from gamma-ray bursts in the internal shock model"

Following this idea, this thesis will explore GRBs as potential sources of UHECRs, HE neutrinos and HE radiation by means of state-of-the-art numerical radiation modelling. Our modelling will be carried out in the framework of the internal shock scenario for the prompt phase of the event. In this phenomenological model, the relativistic outflow of a GRB is approximated as a series of discrete layers ('shells') of varying velocities. Particle acceleration and emission occur in collisionless shocks induced as shells of different velocities collide. Multi-zone internal shock scenarios allow to account for different emission regions along the jet and

to simulate complex patterns in source observables like the photon light curves (that represents the photon flux as a function of time). Within this approach we will investigate which processes can lead to a HE gamma-ray component, whether observed photon spectra are compatible with cosmic-ray interactions in the jet and under which conditions GRBs can account for UHECR measurements while obeying other multi-messenger constraints.

This thesis is structured as follows: We commence with an introduction to the field of multi-messenger astronomy in Chapter 2. An overview of photons, neutrinos, cosmic rays and gravitational waves as astrophysical messengers will be followed by an in-depth discussion of the properties and detection of particles of the highest energies. We further review potential sources and the current status of multi-messenger astronomy.
Following this, Chapter 3 recapitulates the radiation processes at play in environments relevant for high-energy astrophysics. Leptonic and hadronic processes are introduced making use of scenarios of the Hadronic Code Comparison Project (HCCP). The HCCP is a recent initiative that I am part of, which aims to compare the numerical methods used in cosmic-ray simulations by today's leading research groups. The results are also compared to analytical estimates.
Chapter 4 introduces GRBs as high-energy sources with a special focus on the prompt phase of the event. The framework of the internal shock model will be introduced (in two different formalisms) in Chapter 5. The chapter also reviews the impact of modified collision dynamics on multi-messenger predictions and presents a fit to the UHECR energy spectrum and composition as measured by the Pierre Auger Observatory. The fit will be performed by doing a systematic scan over initial Lorentz factor distributions of the jet which reflect in the observed light curve. This will allow to connect the light curve structure with the abundance of different nuclear species at the base of the jet.
In Chapter 6, we turn to Low-Luminosity GRBs (LL-GRBs) as potential sources of Very-High-Energy (VHE) gamma-rays and UHECRs. We present time-resolved simulations of LL-GRBs within the internal shock model at the example of three prototypes representing different GRBs of the population. From our leptonic radiation modelling we deduce the maximal energies attainable for different cosmic-ray nuclei and discuss whether LL-GRBs are viable UHECR source candidates.
Finally, in Chapter 7 we assess lepto-hadronic radiation models of standard high-luminosity GRBs. At a simple, academic GRB dubbed 'educative example' we first review the impact of modelling choices and parameter sets in a leptonic scenario. The same educative example is employed to investigate neutrino and electro-magnetic signatures of proton interactions in lepto-hadronic scenarios. In this context we further study the impact of secondary pion and muon cooling on neutrino spectra. From our educative example we turn to GRBs detected in HE

gamma-rays by the *Fermi*-LAT. Simulating GRBs with properties similar to two bursts of this sample, we evaluate whether the behaviour found for the educative example is reproduced in prototypes closer to real events. We close with our conclusions and outlook in Chapter 8. The main text is complemented by a description of the radiation code that I co-developed and applied in the GRB simulations in Appendix A. We further provide additional material for the multi-collision internal shock model in Appendix B.

Multi-messenger astronomy 2

2.1 Our Universe in multiple messengers 5
2.2 Potential UHECR sources . 16
2.3 Status of multi-messenger astronomy 20

Astrophysical objects can emit diverse particle species: Electromagnetic radiation of different frequencies, cosmic rays, neutrinos and gravitational waves. While each of these messengers carries unique information, probably most enticing is the combination of all observational possibilities. The comparatively new field following this approach is called multi-messenger astronomy and will be introduced in this chapter.

In Section 2.1 we will give an overview of the different cosmic messengers: Their properties, how we measure them and what the combined observation of them can tell us about the universe. The focus of this part will be on particles of the highest energies. We will further discuss potential sources of high-energy particles in Section 2.2 and review recent advances in multi-messenger astronomy in Section 2.3.

2.1 Our Universe in multiple messengers

As of today, we experience our Universe through *photons*, *cosmic rays*, *neutrinos* and *gravitational waves*. Before turning to particles of the highest energies, which due to their special importance for this thesis will be covered in more detail, we give a brief general introduction to each of the four messengers:

* **Photons**
  Until today, photons of different wavelengths remain the main source of information in astronomy and astrophysics. Overall, observed spectra of astrophysical sources are classified as *thermal* or *nonthermal*. Thermal (or black-body) spectra, as for example the emission from stars like our Sun, are generated by the motion of hot particles. Their spectral energy density u_ν (per unit frequency ν) can be calculated with Planck's Law:

$$u_\nu = \frac{4\pi}{c} \cdot \frac{2h\nu^3}{c^2} \cdot (e^{\frac{h\nu}{k_B T}} - 1)^{-1}\,, \tag{2.1}$$

  where h is the Planck constant, c the speed of light, k_B the Boltzmann constant and T the temperature of the black body.
  Non-thermal spectra, which will be the focus of this thesis, often have energy densities that can be described by power laws. They are typically produced by distributions of accelerated particles. Additional sources of radiation are *e.g.* the Cosmic Microwave Background (CMB, created by the decoupling of matter and radiation

during the cooling of the universe in its early phase) or emission lines from excited nuclei.

As photons are uncharged particles they are not deflected by magnetic fields as they propagate through space. However they interact with other particles on their way to earth: Namely, the photon background fields (for example the CMB) limit the mean free path of high-energy photons.

Indeed, photons with energies above a few TeV can only travel as far as a few kpc, which we illustrate with the mean free path of photons as a function of energy in Figure 2.1. At these highest energies photons are thus no adequate carriers of information about far-away objects.

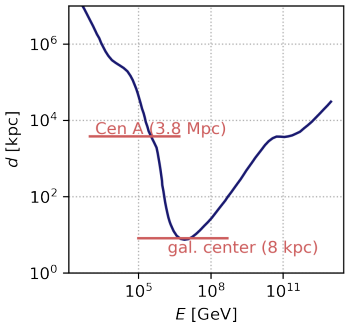

Figure 2.1: Gamma-ray horizon: Mean free path d at which the optical depth equals $1/e$ as a function of photons observed energy E, reproduced with data from [19].

The detection technology strongly depends on the photon energy: As the atmosphere is transparent to the radio and optical spectrum, those photons can be observed with ground-based telescopes. In contrast, other wavelengths like X-ray, gamma-ray and Ultra-Violet (UV) are detected with instruments aboard satellites. At the highest energies the low flux demands large detector volumes. Additionally, high-energy photons may not deposit their energy entirely in the small volume of space-based detectors. Consequently, large ground-based observatories detect air showers initiated by photon interactions with the atmosphere.

[1]: Hess (1912), "Über Beobachtungen der durchdringenden Strahlung bei sieben Freiballonfahrten"

* **Cosmic Rays**

Charged nuclei with extraterrestrial origin called *cosmic rays* were first discovered by Victor Hess during his balloon flights in 1912 [1]. The overall cosmic-ray composition is dominated by protons (86%). Helium and heavier nuclei only account for 11% and 1%, respectively. The remaining 2% are electrons and a small fraction of anti-protons and positrons. The exact composition varies with observed energy E and is, as we will see, an important variable to constrain potential sources.

The flux of cosmic rays follows a power-law approximately $\propto E^{-2.7}$ which is evidence for a non-thermal particle population. The steep decay of observed flux with energy is illustrated in Table 2.1, where we list the cosmic-ray fluxes at 10^{11}, 10^{15} and 10^{19} eV .

Table 2.1: Observed cosmic-ray fluxes F at different energies

E [eV]	F [(cm^2 s sr GeV)$^{-1}$]
10^{11}	$5.2 \cdot 10^{-2}$
10^{15}	$1.8 \cdot 10^{-12}$
10^{19}	$1.3 \cdot 10^{-24}$

The flux dependence on energy has observational implications: While at the lower energies, direct detection with small space-based instruments is feasible, at the highest energies only indirect detection of hadronic air showers initiated by interactions of cosmic rays with the atmosphere is possible.

Due to their charge, cosmic rays are deflected by intergalactic and galactic magnetic fields on their way to earth; in addition they also interact with the photon background fields. As a result, the arrival directions of cosmic rays can only limitedly be used to identify their origin.

* **Neutrinos**

  In the context of beta decays Wolfgang Pauli proposed the existence of neutral, weakly-interacting particles [20]. The corresponding theory was built up by Encrico Fermi, who named them "neutrinos" [21] – however, they were not discovered until the mid 1950s.
  Their importance for astrophysics was demonstrated around 30 years later when neutrinos from supernova 1987A were detected [22, 23]. Later solar and atmospheric neutrinos played an important role in discovering neutrino oscillations and hence the finding that neutrinos have a non-zero rest-mass. They are produced in environments containing hadrons, which means that they can be unique identifiers of acceleration sites of cosmic rays.
  Neutrinos participate only in the weak interaction and in gravity, however their rest masses are so low that the latter can mostly be neglected. As a result, they can travel large distances without interacting or being deflected – on the other hand detection is extremely challenging. For astrophysical neutrinos this is nowadays mostly realised through large Cherenkov detectors either in water or ice. Those catch the radiation emitted by secondaries produced in interactions of neutrinos in the medium.

[20]: Pauli (1930), "Dear radioactive ladies and gentlemen"

[21]: Fermi (1934), "An attempt of a theory of beta radiation. 1."

[22]: Bionta et al. (1987), "Observation of a Neutrino Burst in Coincidence with Supernova SN 1987a in the Large Magellanic Cloud"

[23]: Hirata et al. (1987), "Observation of a Neutrino Burst from the Supernova SN 1987a"

* **Gravitational waves**

  Any body moving with a non-vanishing quadrupole moment creates distortions in space-time that travel as gravitational waves. As an observer is encountered by these waves he will again experience space-time distortions. The gravitational wave amplitude and frequency depend on the properties of the generating object or system. Overall, the length scales and sensitivities of current instruments limit the potential sources we may discover. Due to the relative weakness of the gravitational force we can only observe gravitational waves produced by very massive objects.
  The first indirect detection was on the occasion of the orbital decay of a binary pulsar [24] which led to the Nobel Prize in 1993. The direct detection finally had its breakthrough with the observation of the merger of two black holes by the Laser Interferometer Gravitational-Wave Observatory (LIGO) in 2015 [8]. The Michelson interferometers of current observatories like LIGO are sensitive in a frequency range that corresponds to the merger of compact objects like neutron stars or black holes. The proposed Laser Interferometer Space Antenna (LISA) [25] would be an interferometer in space with 2.5 million km arm length (in comparison to LIGO's 4 km). Among other science objectives it would extend the observable mass range for mergers and the list of accessible sources.

[24]: Hulse et al. (1975), "Discovery of a pulsar in a binary system"

[8]: Abbott et al. (2016), "Observation of Gravitational Waves from a Binary Black Hole Merger"

[25]: Amaro-Seoane et al. (2017), "Laser Interferometer Space Antenna"

In *multi-messenger astronomy*, different particle species are combined in order to gain insights about astrophysical sources and our Universe but also about particle physics. There is a special connection between gamma-

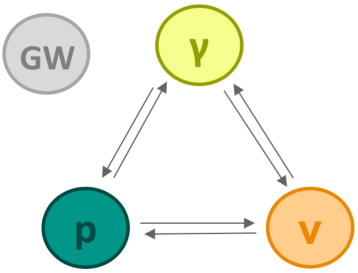

rays, cosmic rays and neutrinos which comes from the production of energetic neutrinos and photons through photo-pion production. It may be illustrated by the $\Delta^+(1232)$ resonance produced in the interaction of a proton p and a photon γ:

$$p + \gamma \rightarrow \Delta^+ \rightarrow \begin{cases} p + \pi^0 \text{ , 2/3 of all cases} \\ n + \pi^+ \text{ , 1/3 of all cases} \end{cases} . \tag{2.2}$$

For a detailed review of photo-hadronic interactions we point to Chapter 3. The produced pions in Eq. 2.2 are unstable and decay into two photons (in the case of the π^0) or neutrinos and leptons (in the case of the π^+). While photons may be produced in a variety of processes, neutrinos thus allow to pinpoint photo-hadronic interactions as unique identifiers. In this sense, photons, cosmic rays and neutrinos together reveal microscopic properties of the emitting plasma like the composition and the particle acceleration mechanism. On the other hand, gravitational waves contain information about macroscopic object properties such as the mass and (angular) momentum. They are however not within the focus of this thesis and will thus not be discussed in more detail.

With the objective of detecting different messengers from the same source, observatories coordinate their searches. In the most simple form, this is carried out by real-time alerts for 'promising' events measured with high spatial accuracy. GCN/TAN alerts are widely used, additionally observatories have their own specified work flows (*e.g.* for high-energy neutrinos see [26]). On top of providing access to this simple alert system, the Astrophysical Multimessenger Observatory Network (AMON) [27] aims at identifying sources that are sub-threshold for single observatories but will exceed the threshold significance if different signals are combined.

https://gcn.gsfc.nasa.gov/

[26]: Aartsen et al. (2017), "The IceCube Realtime Alert System"

[27]: Smith et al. (2013), "The Astrophysical Multimessenger Observatory Network (AMON)"

After giving this brief overview and introduction we will now discuss the most energetic particles (cosmic rays, neutrinos and photons) in more detail.

(Ultra-)High-Energy Cosmic Rays

In Figure 2.2 we show the spectral flux of high-energy cosmic rays $F(E)$ multiplied by $E^{2.6}$ for better visibility of the spectral features at which the spectral slope changes.
The first steepening at the *knee* and *2nd knee* (10^{15} - 10^{16} eV) is usually linked to the transition from galactic to extragalactic sources. It may either be due to the energetic limitations of galactic accelerators such as supernovae or due to particles escaping the Galactic plane as they can no longer be confined by the Galactic magnetic field [29]. The spectrum becomes harder at the *ankle* ($\sim 10^{18.5}$ eV) until finally it is strongly

[29]: Horandel (2007), "Cosmic rays from the knee to the second knee: 10^{14} to 10^{18}-eV"

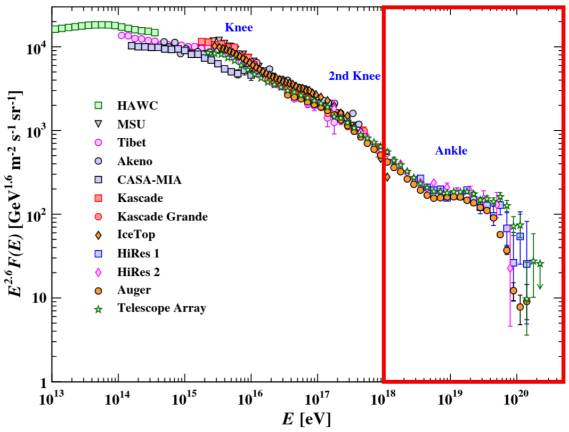

Figure 2.2: High-energy cosmic-ray spectrum as a function of observed energy E, with data from different observatories. The UHECR region above 10^{18} eV is marked with a red box. Figure from [28]

suppressed at $\sim 5 \cdot 10^{19}$ eV. This cut-off was first theoretically predicted by Greisen [30], Zatsepin and Kuz'min [31]. Within their picture, the so-called GZK cutoff arises because the mean free path of protons is limited by interactions with background photon fields such as the CMB (see Eq. 2.2). As those photon fields peak at low energies, the interaction threshold can only be surpassed by particles of the highest energies. For heavier nuclei the dominating interaction is photo-disintegration instead of photo-pion production (as described by Eq. 2.2 for protons). The resulting expected maximal energy is however around the same energy [32].

[30]: Greisen (1966), "End to the cosmic ray spectrum?"

[31]: Zatsepin et al. (1966), "Upper limit of the spectrum of cosmic rays"

[32]: Puget et al. (1976), "Photonuclear Interactions of Ultrahigh-Energy Cosmic Rays and their Astrophysical Consequences"

For high-energy cosmic rays above 10^{15} eV the low particle fluxes demand large ground-based facilities for detection. These detect not the primary cosmic rays but the extensive air showers that are created by the interaction of primary cosmic rays in the atmosphere: If a nucleus interacts with atmospheric molecules, a cascade of secondary particles is initiated. This shower, illustrated in Figure 2.3, contains three main components that differ in horizontal spread. The innermost core is hadronic, surrounded by a muon and finally an $e^{\pm}/\gamma$ component. As the cascade develops, the shower spreads horizontally until the energies of secondary particles are too small for further interactions. Overall, the shower front remains intact throughout the shower evolution since the particles move with velocities close to the speed of light. In consequence, the difference in arrival time between particles at the shower front can be used to determine the incident direction of the primary cosmic ray.

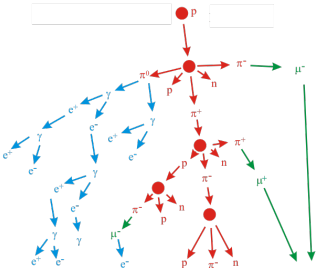

Figure 2.3: Illustration of a cosmic-ray initiated air shower, with the hadronic (red), muon (green) and $e^{\pm}/\gamma$ (blue) components. Figure adjusted from [33].

A range of detection techniques is employed by different observatories. For the purpose of illustration we introduce a few, ordered by increasing primary cosmic-ray energy that can be observed.

The High-Altitude Water Cherenkov Gamma-Ray Observatory (HAWC) [34] in Mexico at 4100 m altitude is sensitive to cosmic rays and photons between 10^{11} eV and 10^{14} eV. As suggested by the name, it detects the Cherenkov radiation from air-shower particles as they pass through the tanks filled with purified water. Distinction between primary photons/

[34]: Abeysekara et al. (2017), "The 2HWC HAWC Observatory Gamma Ray Catalog"

cosmic rays is possible by the lateral particle distribution.

The KArlsruhe Shower Core and Array DEtector (KASCADE, later upgraded to KASCADE-Grande [35, 36]) is a scintillator array designed to measure the $e^{\pm}$/photon and muon shower components for cosmic-ray energies between 10^{14} eV and 10^{17} eV. This technique enabled the first precision measurements of the knee for different element groups.

[35]: Antoni et al. (2003), "The Cosmic ray experiment KASCADE"

[36]: Apel et al. (2010), "The KASCADE-Grande experiment"

Between 1997 and 2006, High Resolution Fly's Eye (HiRes) [37] detected the blue fluorescence light that is created as atmospheric nitrogen molecules excited by air shower particles return to their ground state. The instrument was sensitive to primary cosmic rays above $\sim 10^{17}$ eV. Although limited to observation in moonless nights (which translates to 10% duty cycle), HiRes established the cut-off of the cosmic-ray spectrum around $\sim 10^{20}$ eV [38].

[37]: Abu-Zayyad et al. (2000), "The prototype high-resolution Fly's Eye cosmic ray detector"

[38]: Abbasi et al. (2008), "First observation of the Greisen-Zatsepin-Kuz'min suppression"

Today, both the Pierre Auger Observatory (PAO, in Argentina) [9] and the Telescope Array Project (TA, in the US) [10] are hybrid detectors which combine large ground arrays (water Cherenkov tanks in the case of PAO and scintillators in the case of TA) with fluorescence detectors. At PAO 1600 water tanks of the *Surface Detector* (SD) cover an area of 3000 km^2. In addition, 4 stations with 6 telescopes each overlook the field, constituting the *Fluorescence Detector* (FD). With a smaller area of only 762 km^2 (filled by 507 SDs and three FDs), TA reaches roughly 1/10 of the PAO statistics. Both observatories are currently being upgraded: AugerPrime adds scintillators to the SD stations and upgrades the instruments within the tanks [39], complemented by an upgrade of the radio antenna network [40]. With TAx4, TA is extending its area to approximately 3000 km^2, though still slightly smaller than PAO [41] . While the SDs which measure the muon and electron components of the shower at ground level have almost 100% duty cycle, the FDs observe again only $\sim$ 10% of the time. Nevertheless, the FD measurements are an important complement to the SD results, since 'hybrid' events (detected by both SD and FD) enable energy calibration. Additionally, FD measurements allow to reconstruct the shower development within the atmosphere.

[9]: Aab et al. (2015), "The Pierre Auger Cosmic Ray Observatory"

[10]: Fukushima (2003), "Telescope array project for extremely high energy cosmic rays"

[39]: Aab et al. (2016), "The Pierre Auger Observatory Upgrade - Preliminary Design Report"

[40]: Pont (2021), "A Large Radio Detector at the Pierre Auger Observatory - Measuring the Properties of Cosmic Rays up to the Highest Energies"

[41]: Kido (2018), "The TAx4 experiment"

Indeed, the vertical position where the shower achieves its maximal lateral spread (called X_{max}) is an important measurement variable that allows to draw conclusions on the mass of the primary cosmic ray. On average, the interaction probability with atmospheric molecules increases with mass. Hence, protons traverse longer paths in the atmosphere before their first interaction than heavier nuclei and consequently have larger X_{max}. Thus at a given observed energy E the mean X_{max} (denoted $\langle X_{\mathrm{max}} \rangle$) can give insights about the mean mass of primary cosmic rays at this energy. To determine the purity of the composition at a given energy another measurement variable is used: the spread of X_{max} (denoted $\sigma(X_{\mathrm{max}})$). Generally, lighter elements have larger fluctuations in their first point of interactions, thus larger $\sigma(X_{\mathrm{max}})$. Also, a mixed composition (composed of equal parts of iron and protons, for example) results in a large spread of X_{max} measurements. On the other hand, if the flux is

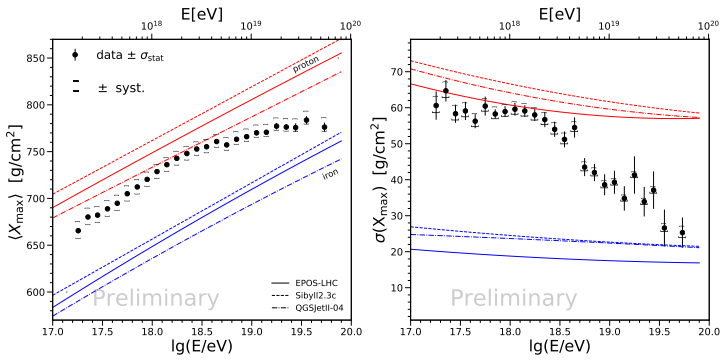

Figure 2.4: $\langle X_{\mathrm{max}} \rangle$ and $\sigma(X_{\mathrm{max}})$ as a function of observed energy, measured by the Pierre Auger Observatory. Figure from [42]

dominated by a single element or mass group, the X_{max} measurements will cluster around the same point without much spread.

Overall, the composition of UHECR is an object of debate. While TA favours a light (helium and proton) composition [43], the findings of PAO suggest a heavy composition (up to iron) at the highest energies. This is illustrated with the current $\langle X_{\mathrm{max}} \rangle$ and $\sigma(X_{\mathrm{max}})$ as observed by PAO in Figure 2.4 from [42]. While around 10^{18} eV the PAO results are compatible with a proton dominated composition, the measurements demand a heavier composition at the highest energies. We point out that interpretation of $\langle X_{\mathrm{max}} \rangle$ and $\sigma(X_{\mathrm{max}})$ measurements relies on shower simulations which are informed by hadronic interaction models. These however impose one of the major uncertainties, as can be inferred from the spread between theoretical predictions (for the EPOS-LHC, SYBILL2.3c and QGSJETII-04 interaction model) in Figure 2.4.

A prime way of pinpointing UHECR sources would be through spatial correlations of arrival directions with specific objects or object classes. For low *rigidity* (particle energy E divided by charge number Z) the initial direction is strongly blurred because of deflections due to magnetic fields. On the other hand, at the highest rigidities only small deflections of less than ten degrees are expected. Indeed, both TA and PAO report arrival-direction anisotropies in the northern and southern sky respectively. PAO observes a large-scale dipole for $E_{\mathrm{UHECR}} > 8 \cdot 10^{18}$ eV centered 125° from the Galactic center, which provides evidence for an extragalactic origin at these energies [44]. The strongest deviation from isotropy at intermediate scales was found for $E_{\mathrm{UHECR}} > 5.4 \cdot 10^{18}$ eV in the direction of the radio galaxy Centaurus A [45]. A more recent study has found 4 σ evidence for correlation of intermediate scale anisotropy with starburst galaxies and 2.7 σ for gamma-ray bright Active Galactic Nuclei (AGN) [46]. Although constraining the list of potential UHECR sources these anisotropy measurements alone cannot reveal the origin of UHECR.

[43]: Hanlon (2021), "Telescope Array 10 Year Composition"

[42]: Castellina (2021), "Highlights from the Pierre Auger Observatory"

[44]: Aab et al. (2017), "Observation of a Large-scale Anisotropy in the Arrival Directions of Cosmic Rays above 8×10^{18} eV"

[45]: Aab et al. (2015), "Searches for Anisotropies in the Arrival Directions of the Highest Energy Cosmic Rays Detected by the Pierre Auger Observatory"

[46]: Aab et al. (2018), "An Indication of anisotropy in arrival directions of ultra-high-energy cosmic rays through comparison to the flux pattern of extragalactic gamma-ray sources"

High-Energy Neutrinos

High-energy neutrinos above ~ 10 GeV are a smoking gun signature of hadronic interactions in astrophysical environments, see Eq. 2.2. They are thus recognised as a key messenger to identify cosmic-ray sources.

The requirement of km-scale detectors for sufficient high detection rates despite the low interaction probability of neutrinos was formulated early on [47]. It is supported by the upper *Waxman-Bahcall bound* on the neutrino flux [48] which assumes that neutrinos and cosmic rays are produced in the same sources and predicts an upper flux limit of $E_\nu^2 \Phi_\nu < 2 \cdot 10^8$ GeV cm^{-2} s^{-1} sr^{-1} for neutrinos between 10^{14} eV to 10^{16} eV. The widely used detection technique is based on catching the Cherenkov light that is emitted as energetic particles (created in weak neutrino interactions in the medium) propagate through water or ice. The largest observatory today is the IceCube Neutrino Observatory [11] at the South Pole. Other detectors to be mentioned are Astronomy with a Neutrino Telescope and Abyss environmental RESearch project (ANTARES) [49] by the Mediterranean Coast in Toulon, France and BAIKAL-GVD [50] at lake Baikal in Russia (still under construction). Also in the building phase is KM3Net [51] with two detection sites in the Mediterranean Sea.

[47]: Gaisser et al. (1995), "Particle astrophysics with high-energy neutrinos"
[48]: Waxman et al. (1999), "High-energy neutrinos from astrophysical sources: An Upper bound"
[11]: Aartsen et al. (2017), "The IceCube Neutrino Observatory: Instrumentation and Online Systems"
[49]: Ageron et al. (2011), "ANTARES: the first undersea neutrino telescope"
[50]: Avrorin et al. (2018), "Baikal-GVD: status and prospects"
[51]: Adrian-Martinez et al. (2016), "Letter of intent for KM3NeT 2.0"

We will from here on restrict ourselves to discussing the IceCube detector and related results, as it is the instrument with the highest (current) sensitivity. Its predecessor and proof-of-concept was the Antarctic Muon And Neutrino Detector Array (AMANDA) [52], operating from the mid-90s until 2006. In December 2010, after five years of construction, IceCube was completed to its full size of 1 km^3 of instrumented ice. To ensure good optical properties of the ice, the detector system lies 1450 m below the ground. The hexagonal setup is filled by 86 strings (125 m apart and of 1 km length), which carry 60 Digital Optical Modules (DOMs) each. The DOMs are the heart of the detector: A glass pressure sphere containing the PhotoMultiplier Tube (PMT) and the electronics that finally convert the Cherenkov light into a measurable current. The setup is supplemented by a surface array, IceTop, to detect cosmic rays [53] and a denser in-fill array called DeepCore [54] to extend the observable neutrino energy range to lower energies. The proposed next generation system, IceCube Gen2 [55] aims at increasing the number of detected events by a factor 10 by means of enlarging the detector volume to 7.9 km^3.

[52]: Halzen et al. (1999), "The AMANDA neutrino telescope"
[53]: Abbasi et al. (2013), "IceTop: The surface component of IceCube"
[54]: Abbasi et al. (2012), "The Design and Performance of IceCube DeepCore"
[55]: Aartsen et al. (2021), "IceCube-Gen2: the window to the extreme Universe"

The energetic secondaries detected by IceCube are created in Deep Inelastic Scatterings (DIS) of neutrinos with nuclei in the ice: In Charged Current (CC) interactions, a charged lepton (of the same flavour as the incoming neutrino) is created through a $W^\pm$-Boson exchange with the nucleus. This is in contrast to Neutral Current (NC) interactions through a Z^0-Boson exchange where the nucleus remains intact. Electron neutrinos can additionally scatter on the electrons in the ice. Due to its small cross

section, this process is mostly negligible. An exception is the *Glashow resonance*, where the energy of the incoming $\bar{\nu}_e$ is such that the center of mass energy equals the mass of the W^--Boson ($E_{\bar{\nu}_e} = m_W^2/2m_e \sim 6.3\,\text{PeV}$). A particle cascade corresponding to this process was observed recently [56].

[56]: Aartsen et al. (2021), "Detection of a particle shower at the Glashow resonance with IceCube"

Depending on the process (NC or CC) and the flavour of the created lepton (e, μ or τ), the signal in the detector varies: Due to their larger mass muons traverse large paths before decaying or interacting and produce a *muon-track* of Cherenkov radiation in the ice. Those track events are characterised by their good angular resolution. On the other hand, electrons interact on very short lengthscales, initiating a cascade of secondary particles that appear as a *cascade* Cherenkov signal. A similar signal is expected from NC reactions where part of the neutrino energy is transferred to the nucleus. As the events usually are fully contained in the detector, the energy resolution is high. Tau neutrinos create a *double-bang* signal: The first cascade is produced with the initial CC-interaction, the second one as the tau decays into a lighter lepton. Due to the short lifetime of the tau, both signals can potentially be captured by the detector. However, the two cascades are only distinguishable for the highest-energy taus, otherwise the signal may resemble a simple cascade. The first clear identification of tau neutrinos through a double-bang signature was announced in 2020 [57].

[57]: Abbasi et al. (2020), "Measurement of Astrophysical Tau Neutrinos in IceCube's High-Energy Starting Events"

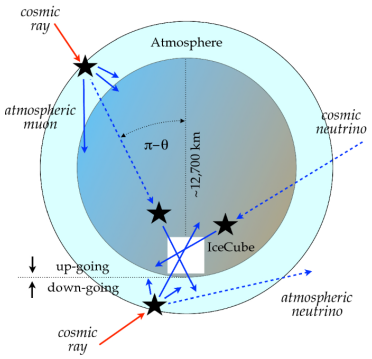

Figure 2.5: Illustration of the IceCube veto system and event classification. Figure from [58]

For neutrino energies below $\sim$ 300 TeV a main challenge for detection is the high background rate from atmospheric muons and neutrinos which are created in cosmic-ray air showers. To filter out these backgrounds, three different techniques are employed: *(i)* The *Through-Going Muon track (TGM)* sample selects up-going track-like events (for illustration see Figure 2.5). This implies that the the earth is used as a shield against atmospheric muons. Atmospheric and astrophysical neutrinos may be discriminated by energy: While the first follow a power-law $\propto E^{-3.7}$, the latter are expected to have a harder energy spectrum close to the parent cosmic-ray spectrum of $\sim E^{-2}$. *(ii)* For *High-Energy Starting Events (HESE)* the neutrino interaction takes place inside the detector, thus excluding the contribution of muons from atmospheric showers. This is ensured by using the outer region of the detector as a veto system. The sample in principle contains cascade and track-like events, however tracks are usually not fully contained within the detector. *(iii)* A third method is to consider only electron and tau neutrino induced showers. Since atmospheric neutrinos are predominantly of muon flavour, these *cascade* events are less contaminated by atmospheric contributions.

Table 2.2: IceCube power-law spectral fits to the different samples: High-Energy Starting Events (HESE) [59], Through-Going Muon tracks (TGM) [60], cascade [61] and preliminary results of a combined TGM and cascade fit [62]

Sample	γ_{astro}
HESE	$2.87^{+0.20}_{-0.19}$
TGM	$2.37^{-0.09}_{+0.09}$
Cascade	2.53 ± 0.07
TGM + Cascade	2.37

The discovery of an astrophysical neutrino flux by IceCube was announced in 2013, using a HESE sample of 3.5 years [7]. In lack of unambiguous distinct spectral features, the data is usually fit by a single power-law of index γ_{astro}. We report the most recent results for the differ-

[7]: Aartsen et al. (2013), "Evidence for High-Energy Extraterrestrial Neutrinos at the IceCube Detector"

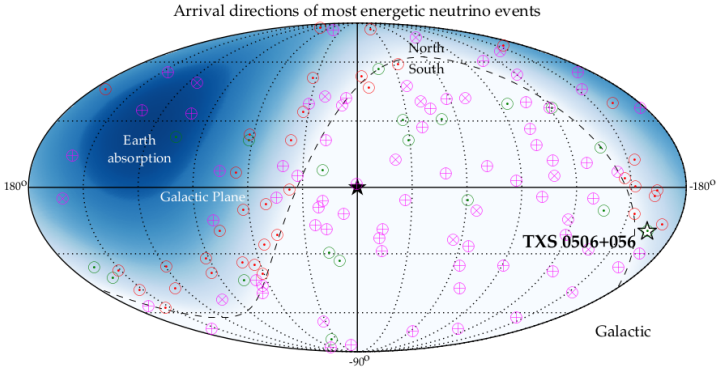

Figure 2.6: Arrival directions of the most energetic neutrinos detected by IceCube in galactic coordinates. The earth's equatorial plane is marked as a dashed line, in the (dark) blue region the earth's absorption hinders neutrinos of the highest energies from reaching the detector. Red circles mark the TGM sample(⊙), purple ones the HESE tracks (⊗) and HESE cascades (⊕). For the green circles (⊙), public multi-messenger alerts were sent out. The star indicates the location of the blazar TXS0506+056. Figure from [63]

ent samples (HESE [59], TGM [60], cascade [61] and preliminary results for a combined fit of through-going and cascade [62]) in Table 2.2.

As neutrinos are not deflected during propagation, their sources could potentially be revealed by spatial correlations with known objects. Figure 2.6 shows the arrival directions of the most energetic IceCube neutrinos, in galactic coordinates with the equatorial plane as x-axis. The dashed line is the projection of the equatorial plane, in the (dark) blue regions IceCube becomes increasingly blind to neutrinos above ~ 100 TeV due to the earth's absorption. Symbols mark the different samples: Red circles for through-going muon tracks from the northern hemisphere (⊙), purple ones for the HESE tracks (⊗) and cascades (⊕). The green circles (⊙) highlight events sent out as public alerts for multi-messenger searches. Finally, the location of the neutrino source candidate blazar TXS 0506+056 is indicated with a star. Overall, the arrival directions of high-energy neutrinos are consistent with isotropy.

Correlation searches between arrival directions of high-energy neutrinos and catalogues of high-energy photon sources such as blazars [64, 65], gamma-ray bursts [15, 16] or starburst galaxies [66] find their contributions to be subdominant at most. More general limits for minute-scale transients are provided in [67]. It is mostly the contribution of less luminous sources such as non-blazar active galactic nuclei that are less constrained [68]. Another possible solution are multi-component fits with contributions by different source classes [69, 70]. The few events where a potential electromagnetic counterpart of IceCube neutrinos could be identified will be introduced in Section 2.3.

[59]: Abbasi et al. (2021), "The IceCube high-energy starting event sample: Description and flux characterization with 7.5 years of data"

[60]: Abbasi et al. (2021), "Improved Characterization of the Astrophysical Muon-Neutrino Flux with 9.5 Years of IceCube Data"

[61]: Aartsen et al. (2020), "Characteristics of the diffuse astrophysical electron and tau neutrino flux with six years of IceCube high energy cascade data"

[62]: Abbasi et al. (2021), "A Combined Fit of the Diffuse Neutrino Spectrum using IceCube Muon Tracks and Cascades"

[64]: Aartsen et al. (2017), "The contribution of Fermi-2LAC blazars to the diffuse TeV-PeV neutrino flux"

[65]: Smith et al. (2021), "Revisiting AGN as the source of IceCube's diffuse neutrino flux"

[15]: Aartsen et al. (2016), "An All-Sky Search for Three Flavors of Neutrinos from Gamma-Ray Bursts with the IceCube Neutrino Observatory"

[16]: Aartsen et al. (2017), "Extending the search for muon neutrinos coincident with gamma-ray bursts in IceCube data"

[66]: Bechtol et al. (2017), "Evidence against star-forming galaxies as the dominant source of IceCube neutrinos"

[67]: Aartsen et al. (2019), "Constraints on minute-scale transient astrophysical neutrino sources"

[68]: Palladino et al. (2019), "Interpretation of the diffuse astrophysical neutrino flux in terms of the blazar sequence"

[69]: Palladino et al. (2018), "A multi-component model for observed astrophysical neutrinos"

[70]: Bartos et al. (2021), "The IceCube Pie Chart: Relative Source Contributions to the Cosmic Neutrino Flux"

(Very-)High-Energy Photons

The identification of high-energy photon sources is essential for multi-messenger studies. However, similar to cosmic rays, the astrophysical photon flux decays steeply with energy. As a result, satellite based instruments are feasible until up to a few GeV only. The first instrument to establish gamma-ray astronomy in space was NASAs SAS-2, a satellite equipped with a spark-chamber and operating for a short period between November 1972 and June 1973 [71]. Nowadays, the instrument with the highest sensitivity is the Large Area Telescope (LAT) onboard the *Fermi* satellite [72], detecting photons between 20 MeV and 300 GeV. With a large field of view covering roughly 20% of the sky it can survey the complete sky in approximately 3 hours. It works in analogy to high-energy physics instruments on earth through the principle of pair conversion: As an incoming gamma-ray interacts within the detector, an electron-positron pair is created. For reconstruction of the parent γ direction, the lepton trajectories are tracked with silicon strips. Finally, the primary photon energy is determined with a calorimeter.

[71]: Fichtel et al. (1975), "High-energy gamma-ray results from the second Small Astronomy Satellite."

[72]: Atwood et al. (2009), "The Large Area Telescope on the Fermi Gamma-ray Space Telescope Mission"

At even higher energies, the low fluxes again demand large-area terrestrial observatories. Similar to UHECR, VHE photons interact with atmospheric molecules, initiating a cascade of secondary particles. In contrast to hadronic showers, leptonic ones contain an electromagnetic component only. As a result, they may observationally be distinguished by their smaller horizontal shower spread. The Cherenkov radiation of shower particles moving faster than the speed of light in air is detected by Imaging Air Cherenkov Telescopes (IACTs). Their large concave mirror planes (of ~ 10 m diameter) focus the light on a centrally mounted camera, as illustrated in Figure 2.7.

The first of its kind was WHIPPLE on Mount Hopkins in Arizona, constructed in 1968. Nowadays, IACTs usually consist of a handful of telescopes, which enables better reconstruction of the primary photon direction and increases the effective area. Currently operating are the WHIPPLE successor VERITAS [73], the High Energy Stereoskopic System (H.E.S.S.) in Namibia [74] and MAGIC on the Canary island of La Palma [75]. The next-generation instrument will be the Cherenkov Telescope Array (CTA) [76], composed of a mix of Large, Medium and Small Size Telescopes (LST, MST and SST) and with one observation site on the southern, one on the northern hemisphere. Overall, it will consist of over 100 telescopes.

At higher energies even arrays of IACTs cannot cover sufficient area to compensate the low flux. Here, large water-Cherenkov tank arrays like HAWC (introduced as UHECR observatory earlier) or LHAASO [77] are employed.

[73]: Holder et al. (2006), "The first VERITAS telescope"

[74]: Aharonian et al. (2006), "Observations of the Crab Nebula with H.E.S.S"

[75]: Aleksić et al. (2016), "The major upgrade of the MAGIC telescopes, Part II: A performance study using observations of the Crab Nebula"

[76]: Actis et al. (2011), "Design concepts for the Cherenkov Telescope Array CTA: An advanced facility for ground-based high-energy gamma-ray astronomy"

[77]: Cao (2010), "A future project at Tibet: The large high altitude air shower observatory (LHAASO)"

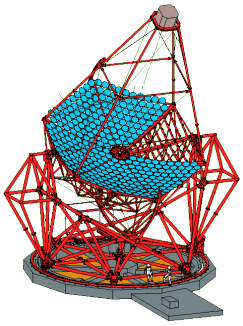

Figure 2.7: A schematic view of a H.E.S.S. telescope, Figure from [a]

[a] http://wwwiexp.desy.de/groups/astroparticle/de/archive/hess/pages/hes_overview.html

The list of objects detected in HE gamma-rays is extensive. They are collected in *catalogues* like the LAT point source catalogue [78], or even

[78]: Abdollahi et al. (2020), "*Fermi* Large Area Telescope Fourth Source Catalog"

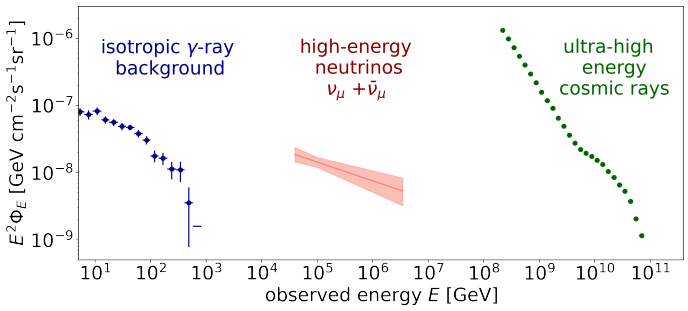

Figure 2.8: Energy flux of the isotropic gamma-ray background (as measured by *Fermi*, data from [80]), high-energy neutrinos (IceCube data per flavour from the through-going muon track sample [81]) and UHECR (as measured by the Pierre Auger Observatory, data from [42]).

source class specific catalogues dedicated only to GRBs or AGN detected also in other wavelengths. In the same sense, for example H.E.S.S. published a catalogue of VHE gamma-ray sources in the galactic plane [79] and has a catalogue of detected sources available on their website.

[79]: Abdalla et al. (2018), "The H.E.S.S. Galactic plane survey"

On the common sources

While UHECRs, HE neutrinos and (V)HE photons individually prove acceleration of particles to the highest energies within their sources, it is not guaranteed that they originate from the same astrophysical objects. An intriguing argument for their common origin is that of comparable energy budget, illustrated in Figure 2.8: The differential energy flux of the isotropic gamma-ray background (measured by *Fermi*), IceCube astrophysical neutrinos and UHECRs is surprisingly equal. Indeed, for gamma-ray transparent sources there is a direct connection between VHE photons and neutrinos, as they are produced by the same interaction (Eq. 2.2). Contrary to neutrinos, VHE photons loose their energy in interactions with background photon fields. Eventually, they will reach earth with energies only above 10 GeV and contribute to the *Fermi*-LAT background shown in Figure 2.8. An equal discussion can be made for UHECRs, for more details we point to [82].

[82]: Ahlers et al. (2018), "Opening a New Window onto the Universe with IceCube"

2.2 Potential UHECR sources

In addition to targeted multi-messenger correlation searches, the list of potential UHECR sources can be constrained by analytical estimates. The most simple energetical requirement (dubbed *Hillas criterion*) was proposed by Hillas in 1984 [12]: In order to be accelerated, particles need to be confined within the acceleration region. In other words, the particle Larmor radius R_L should not exceed the size of the region R. In the most general form the Hillas criterion for the maximal cosmic-ray energy E_max achievable within the outflow reads

$$E_\mathrm{max} = qBR\,, \tag{2.3}$$

[12]: Hillas (1984), "The Origin of Ultrahigh-Energy Cosmic Rays"

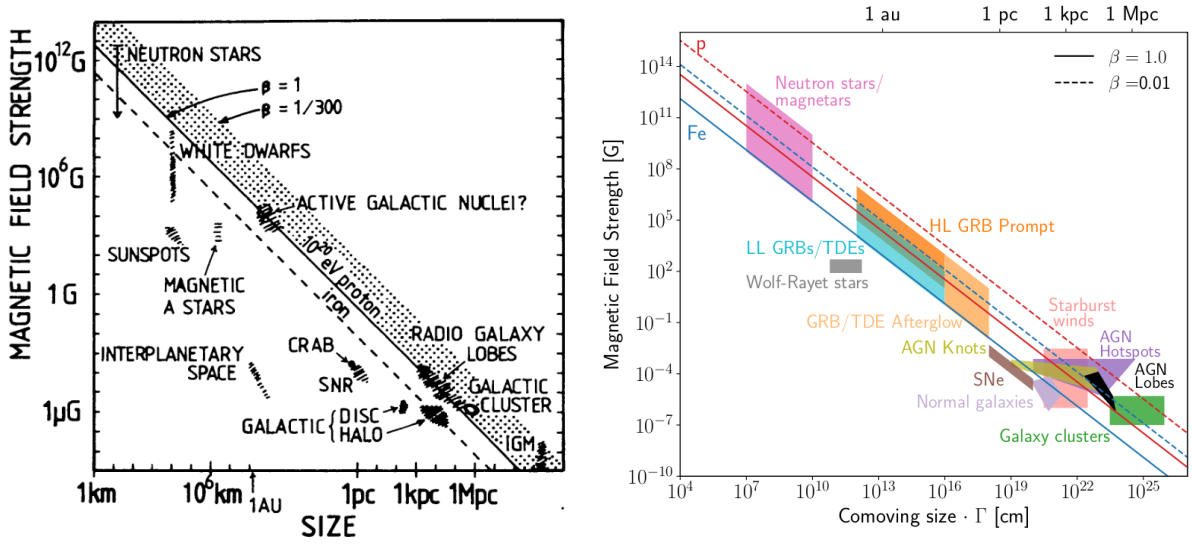

Original Hillas Plot (1984) Updated Hillas Plot (2019)

Figure 2.9: Left side: Original Hillas plot (from [12]) showing the parameter space of magnetic field and size, with expected parameter space regions of different source candidates. On the dashed (solid) line, Eq. 2.4 is satisfied for a 10^{20} eV proton (iron) nucleus for a shock of velocity $\beta = 1$. The dotted lines mark the results for the same 10^{20} eV proton, however with decreasing shock velocity β.
Right side: Updated version of the Hillas plot (from [83]). The characteristic radial size R is written as the product of the comoving size with the Lorentz factor of the emitting material, Γ. Note that the magnetic field is in the comoving frame of the source. On the dashed (solid) lines, cosmic rays of 10^{20} eV can be confined at a shock of $\beta = 0.01$ ($\beta = 1$), the colours mark the results for different nuclei (blue for iron, red for protons).

where the Larmor Radius was calculated as $R_{\mathrm{L}} = \frac{E}{qB}$ for a particle of energy E and charge q in a magnetic field B. In the more specific case of acceleration at a shock front of velocity βc, the formula is modified to

$$E_{\mathrm{max}} = \beta q B R \,. \tag{2.4}$$

The B-R parameter space occupied by different source classes is displayed in the Hillas Plot in Figure 2.9. The left side shows the original version, whereas the right side shows an updated version produced 35 years later [83]. The lines mark where Eq. 2.4 is satisfied for a proton/iron nucleus of the indicated energy. Thus, a potential accelerator needs to be to the upper right of the line in order to confine the aforementioned particles. Comparing the two plots we observe that some source classes such as SuperNova Remnants (SNR)/SuperNovae (SNe) are excluded in both. For others like Active Galactic Nuclei (AGN), the parameter space has been updated and again others like Tidal Disruption Events (TDEs) were not yet discovered at the time of Hillas.

[83]: Alves Batista et al. (2019), "Open Questions in Cosmic-Ray Research at Ultrahigh Energies"

In the following, we will biefly introduce the most promising candidates from Figure 2.9, see also the review and list of references in [83].

* **Pulsars**
  Fastly spinning, strongly magnetised neutron stars called pulsars are long-standing UHECR source candidates whose large magnetic fields may enable cosmic-ray acceleration to the highest energies.

Originating from the death of massive stars and often ocurring in regions with enhanced star formation, their surrounding material may be rich in heavy elements. This is compatible with the heavy composition claimed by the Pierre Auger Observatory.

* **Active Galactic Nuclei (AGN)**
  Supermassive black holes at the center of galaxies that are the source of luminous, broad-band radiation are called active galactic nuclei. The black hole in the center is encircled by an accretion disk which in around 10% of cases powers a pc-scale relativistic jet. The system may additionally be surrounded by a dust torus and/or molecular clouds above the disk. The observed properties depend on the orientation of the AGN jet/system with respect to the line of sight and are classified according to the AGN unification scheme [84]. Of special importance for high-energy astrophysics are *blazars*, which are radio-loud AGN where the jet is pointed towards earth. They can be sub-divided into Flat Spectrum Radio Quasars (FSRQs, with broad atomic emission lines) and BL-Lacertae objects (BL-Lacs, without prominent line features). Proposed particle acceleration sites are *knots* (small-scale blobs along the jet observed in X-rays), *lobes* (kpc-scale, un-collimated extension of the jet) and *hotspots* (in the termination region with the external medium). For illustration see the radio-image of Cygnus A in Figure 2.10.

[84]: Urry et al. (1995), "Unified schemes for radio-loud active galactic nuclei"

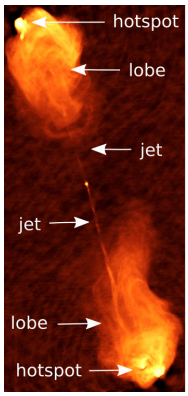

Figure 2.10: Radio image of Cygnus A with possible particle acceleration sites. *Original image from NRAO/AUI.*

* **Gamma-Ray Bursts (GRBs)**
  Gamma-ray bursts are flashes of gamma-rays with durations ranging from a few ms to 100 s and an energy release comparable to supernovae. Their prompt emission is believed to originate from high Lorentz factor jets that are formed at the creation of a compact object (neutron star or black hole) after the merger of two compact objects or the violent death of a super-massive star. In addition to the prompt phase, cosmic-ray acceleration may also take place as the jet interacts with the circumburst medium, creating the longer lasting *afterglow*. While multi-messenger constraints put rather stringent limits on the UHECR content of standard high-luminosity GRBs, low-luminosity GRBs have recently been discussed as a distinct source class that may account for the observed UHECR flux. They are however less well understood, due to the low number of detected events (as of now, only about 20).
* **Starburst Galaxies**
  Starburst galaxies exhibit an enhanced star-formation rate compared to normal galaxies like the Milky Way. Consequently, they contain a comparatively large amount of hot gas which may be accelerated in their large, magnetised winds. They reside in the lower right part of the R-B parameter space and there is some controversy if they indeed fulfil the necessary conditions to accelerate UHECR, see for example [85].

[85]: Romero et al. (2018), "Particle acceleration in the superwinds of starburst galaxies"

* **Tidal Disruption Events (TDEs)**
  A star with circular orbit close to a black hole may be torn apart by the tidal forces due to the strong gravitation of the central black hole. As parts of the stellar material are accreted to the black hole, they emit bright thermal emission that can be observed for weeks to months. In a few percent of the cases, a jet is additionally launched [86]. The phenomenology of these jetted events may be understood in a unified model depending on the viewing angle (similar to AGNs) [87]. UHECR acceleration may be possible in jetted TDEs. However, due to the low number of detected events (70 events as of July 2021 [88]) it remains unclear whether the population of TDEs can indeed power the UHECR flux.

[86]: Gezari (2021), "Tidal Disruption Events"

[87]: Dai et al. (2018), "A unified model for tidal disruption events"

[88]: Stein (2021), "Tidal Disruption Events and High-energy Neutrinos"

Fermi acceleration

The Hillas criterion of confinement is a necessary but not sufficient condition. To find out if particle acceleration to the highest energies will indeed occur, detailed models of acceleration are required. Focussing again on simple analytical arguments, we will here only discuss the principle of *Fermi acceleration*. Relying on collisionless plasmas where accelerated particles do not loose energy in interactions with other particles, this acceleration mechanism is widely believed to be the leading particle acceleration mechanism. Overall, it describes the scattering of particles at shock fronts (*1st order Fermi acceleration*) and between magnetised gas clouds (*2nd order Fermi acceleration*) in collisionless plasmas:

* **Diffusive shock acceleration (1st order Fermi)**
  Shock waves passing through plasmas are frequent phenomena occurring in numerous astrophysical environments like supernova remnants, termination shocks or GRBs. Overall, they convert the upstream (unshocked) ram pressure into thermal/internal energy of the downstream (shocked) compressed plasma. In proximity to the shock, magnetic field turbulences are expected. The diffusive acceleration of particles at shock fronts is illustrated in Figure 2.11: A particle from the upstream region crosses the shock boundary to the downstream and then (through multiple scatterings due to magnetic turbulences) enters back to the upstream. If the shock moves at velocity $u = \beta c$, the energy gain per shock crossing is proportional to β (hence the term *1st order* Fermi acceleration).
  For a particle distribution undergoing multiple scatterings and escaping the shock region at a fixed probability, eventually a power-law distribution will form :

$$\frac{\mathrm{d}N(E)}{\mathrm{d}E} \propto E^{-p} \,, \tag{2.5}$$

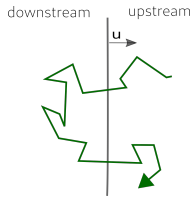

Figure 2.11: Schematic representation of 1st order Fermi acceleration.

with the spectral index $p \sim 2$.

* **Stochastic acceleration (2nd order Fermi)**
  The original idea of Fermi [89] referred to particles scattering between randomly moving 'magnetic mirros', for example gas clouds in the InterGalactic Medium (IGM). On average the energy gain for head-on collisions is larger than the loss for tail-on ones, so over many scatterings the particle energy will be increased. If the clouds move at mean speed $\langle v \rangle = \beta c$, the energy gain is proportional to β^2 (thus *2nd order* Fermi acceleration).

[89]: Fermi (1949), "On the Origin of the Cosmic Radiation"

A thorough overview (including alternative mechanisms like magnetic reconnection) can be found in [90]. The theoretical concepts are verified by current (Relativistic-)Magneto-HydroDynamic (RMHD), Particle-in-Cell (PIC) or combined simulations. For comprehensive recent reviews on this lively field we point to [91–93]. Overall, simulation results reveal that acceleration on shocks indeed does occur, however may be inhibited *e.g.* in relativistic shocks. With increasing computational possibilities, substantial advances in this field are to be expected within the next decade. As of now, important limitations remain. For example, due to the computationally expensive setups, it is not possible to cover the full range of scales between the scale on which acceleration occurs up to the astrophysical scales of jets. Additionally, parameter space regions like mildly relativistic shocks are only recently being explored.

[90]: Matthews et al. (2020), "Particle acceleration in astrophysical jets"

[91]: Pohl et al. (2020), "PIC Simulation Methods for Cosmic Radiation and Plasma Instabilities"
[92]: Marcowith et al. (2020), "Multi-scale simulations of particle acceleration in astrophysical systems"
[93]: Nishikawa et al. (2021), "PIC methods in astrophysics: Simulations of relativistic jets and kinetic physics in astrophysical systems"

2.3 Status of multi-messenger astronomy

Finally, we review the current status of multi-messenger astronomy and the recent highlights of the field. As of now, no detection combining **all** three direct, uncharged messengers (gravitational waves, neutrinos and photons) has been made. We will cover three multi-messenger aspects: The joint photon and gravitational detection of GW 170817 / GRB 170817A that was the first breakthrough, the statistical associations of the blazar TXS 0506+056 and TDE AT2019dsg with IceCube neutrinos and some recent advances in multi-wavelength observations. We point out that this compilation does not claim to be complete and focuses on events relevant also for the following chapters.

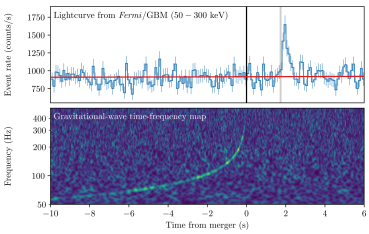

Figure 2.12: Top: *Fermi* GBM light curve (50 keV) of GRB 170817A. Bottom: Time-frequency map of the gravitational wave event. Figure adapted from [94]

The photon - gravitational wave connection: GW 170817/GRB 170814A

Shortly after Advanced *Virgo* joined the 2nd observation run of Advanced *Ligo* on August 1st 2017, the first gravitational wave signal of the merger of two neutron stars was observed on August 17th. An automatic comparison to Gamma-ray Burst Monitor (GBM, onboard the *Fermi* satellite) notices

within the GCN revealed a short GRB (GRB 170817A) in temporal and spatial proximity [94]. Although the theory of short GRBs emerging from the merger of two compact objects is long-standing and supported by wealthy indirect evidence, this was the first time the nature of short GRBs could directly be confirmed. After the initial detections, an extensive multi-wavelength campaign was triggered and revealed a kilo/macronova on top of the GRB afterglow [95, 96].

In Figure 2.12 we show the GRB light curve (detected by the GBM) between 50 an 300 keV and the time-frequency map of the gravitational wave event. The black vertical time marks the time of merger, the grey vertical line the onset of the GRB. A range of answers to the natural question of *What happened in the 1.7 s between merger and GRB?* have been given. The delay may for example be related to the low luminosity of the GRB when compared to the sample of observed GRBs. This low luminosity may be explained either by an intrinsically weak jet or by a normal jet observed off-axis [97]. Indeed, long-term multi-wavelength coverage seem to support a structured jet observed off-axis [98]. Alternative theories include *e.g.* the time it took to successfully launch a jet and the jet propagation time to the emission radius.

Additionally, the kilonova associated emission uncovered the synthesis of elements heavier than iron (like gold and platinum) through neutron capture (*r -process*) [99, 100]. This is another puzzle piece in the search for the origin of heavy elements in our Universe which are not produced in the life cycle of stars.

[94]: Abbott et al. (2017), "Gravitational Waves and Gamma-rays from a Binary Neutron Star Merger: GW170817 and GRB 170817A"

[95]: Arcavi et al. (2017), "Optical emission from a kilonova following a gravitational-wave-detected neutron-star merger"

[96]: Abbott et al. (2017), "Multi-messenger Observations of a Binary Neutron Star Merger"

[97]: Granot et al. (2017), "Lessons from the Short GRB 170817A: The First Gravitational-wave Detection of a Binary Neutron Star Merger"

[98]: Troja et al. (2019), "A year in the life of GW 170817: the rise and fall of a structured jet from a binary neutron star merger"

[99]: Pian et al. (2017), "Spectroscopic identification of r-process nucleosynthesis in a double neutron star merger"

[100]: Tanvir et al. (2017), "The Emergence of a Lanthanide-Rich Kilonova Following the Merger of Two Neutron Stars"

The photon - neutrino connection : TXS 0506+056 and TDE AT2019dsg

The first association of an IceCube high-energy neutrino with a known gamma-ray source was on 9th of September 2017 with the bright BL-Lac blazar TXS 0506+056. This source is generally characterised by strong temporal variations of gamma-ray flux. Interestingly, during the time of 2017 neutrino emission the blazar was in a flaring state of enhanced flux [101]. A re-analysis of archival data revealed a flare in 2015 of 13 ± 5 neutrinos from the same source, though during a quiescent gamma-ray state [102]. While the 2017 event is comparatively easy to accommodate in lepto-hadronic emission models of blazars, the 2015 flare remains challenging [103, 104]. Despite this single neutrino association, the contribution of blazars to the IceCube diffuse flux still remains very limited ($\lesssim 11\%$ in [70]).

The second event that could statistically be associated with an IceCube neutrino was the tidal disruption event AT2019dsg [105]. As a result, TDEs are hotly discussed UHECR source candidates and may contribute non-negligibly to the observed neutrino flux. However, the number of observed TDEs is still rather small (order of 100) and it is not clear if

[101]: Aartsen et al. (2018), "Multimessenger observations of a flaring blazar coincident with high-energy neutrino IceCube-170922A"

[102]: Aartsen et al. (2018), "Neutrino emission from the direction of the blazar TXS 0506+056 prior to the IceCube-170922A alert"

[103]: Rodrigues et al. (2019), "Lepto-hadronic Blazar Models Applied to the 2014–2015 Flare of TXS 0506+056"

[104]: Petropoulou et al. (2020), "Multi-Epoch Modeling of TXS 0506+056 and Implications for Long-Term High-Energy Neutrino Emission"

[70]: Bartos et al. (2021), "The IceCube Pie Chart: Relative Source Contributions to the Cosmic Neutrino Flux"

[105]: Stein et al. (2021), "A tidal disruption event coincident with a high-energy neutrino"

the IceCube TDE is representative for the population. This issue is to be tackled by current and future survey instruments such as the Zwicky Transient Facility (ZTF) [106], Vera Rubin Observatory (former LSST) [107] and Ultraviolet Transient Astronomy Satellite (ULTRASAT) [108] which will significantly increase the number of detected TDEs.

[106]: Graham et al. (2019), "The Zwicky Transient Facility: Science Objectives"
[107]: Ivezić et al. (2019), "LSST: from Science Drivers to Reference Design and Anticipated Data Products"
[108]: Sagiv et al. (2014), "Science with a wide-field UV transient explorer"

Recent highlights in multi-wavelength astronomy

As detailed before, (very-)high-energy photons from astrophysical objects guide the search for cosmic-ray sources. There is, for example, the attempt to identify *Pevatrons* (sources of PeV particles and cosmic rays below the knee) within our Galaxy with IACTs. A prominent potential source is the H.E.S.S. Pevatron in the galactic center region [109] but also other observatories like HAWC or Tibet-ASγ have announced Pevatron candidates [110, 111].

In the same sense extragalactic TeV photon sources may reveal the origin of UHECRs. Indeed, the UHECR source candidate Centaurus A has been observed at TeV gamma-ray energies [112]. Recently the H.E.S.S. collaboration was able to provide the first spatially resolved analysis of this source which proved an extended VHE emission site consisting of the inner core region and the kpc-scale jet [113]. This is a valuable information for UHECR acceleration and emission models as it constrains the size and properties of UHECR production regions. Recently, also LHAASO has announced the observation of TeV gamma-ray sources (*e.g.* [114, 115]).

Another breakthrough was the observation of VHE photons from GRB afterglows first by the H.E.S.S. and later by the MAGIC collaborations in GRBs 180720B, 190114C, 190829A, 201015A and 201216C [116–121]. The exact mechanism producing the gamma-rays remains a topic of debate: While the modelling seems to favour a two component model for the MAGIC GRB 190114C, a single component one may explain the H.E.S.S. GRB 180720B. Alternative scenarios also involve hadronic signatures that may produce the VHE emission [122].

[109]: Abramowski et al. (2016), "Acceleration of petaelectronvolt protons in the Galactic Centre"
[110]: Albert et al. (2020), "HAWC J2227+610 and its association with G106.3+2.7, a new potential Galactic PeVatron"
[111]: Amenomori et al. (2021), "Potential PeVatron supernova remnant G106.3+2.7 seen in the highest-energy gamma rays"
[112]: Aharonian et al. (2009), "Discovery of very high energy gamma-ray emission from Centaurus A with H.E.S.S"
[113]: Abdalla et al. (2020), "Resolving acceleration to very high energies along the jet of Centaurus A"
[114]: Cao et al. (2021), "Discovery of the Ultra-high energy gamma-ray source LHAASO J2108+5157"
[115]: Cao et al. (2021), "Discovery of a New Gamma-Ray Source, LHAASO J0341+5258, with Emission up to 200 TeV"
[116]: Abdalla et al. (2019), "A very-high-energy component deep in the γ-ray burst afterglow"
[117]: Acciari et al. (2019), "Observation of inverse Compton emission from a long γ-ray burst"
[118]: Acciari et al. (2019), "Teraelectronvolt emission from the γ-ray burst GRB 190114C"
[119]: Abdalla et al. (2021), "Revealing x-ray and gamma ray temporal and spectral similarities in the GRB 190829A afterglow"
[120]: Suda et al. (2021), "Observation of a relatively low luminosity long duration GRB 201015A by the MAGIC telescopes"
[121]: Fukami et al. (2021), "Very-high-energy gamma-ray emission from GRB 201216C detected by MAGIC"
[122]: Sahu et al. (2020), "Origin of sub-TeV afterglow emission from gamma-ray bursts GRB 190114C and GRB 180720B"

Radiation processes in high-energy astrophysics and comparison of approaches

3

3.1 Basic concepts 23
3.2 Leptonic processes 27
3.3 Hadronic processes 31
3.4 Special scenarios 37

Numerical modelling is a powerful tool in astrophysics connecting observations to source models. In a complete picture these source models include both the macroscopic properties as well as the microphysical processes. While the macroscopic parameters strongly depend on the source class or individual object, particle interactions are more universal. Hence, before turning to specific objects, this chapter will review the basic radiation processes that are at play in high-energy astrophysics.

After introducing some basic concepts in Section 3.1, we will give a summary of the basic leptonic and hadronic processes that shape the observed multi-wavelength spectra in Section 3.2 and Section 3.3. This will however not include a full derivation of the cross sections and formulas and thus may be viewed as a more qualitative summary. Finally, in Section 3.4 we introduce special scenarios including non-linear feedback loops.

We illustrate the different processes with results obtained in the Hadronic Code Comparison Project (HCCP) [123]. This initiative compares different numerical codes currently available in high-energy astrophysics with the aim of estimating the uncertainties due to numerical approaches. I participated in this project on behalf of the development team of the AM3 code [124] (for details on the code see Appendix A). Furthermore, the results will be compared with analytical estimates that I derived from the literature.

We note that this section does not claim to be comprehensive as we limit ourselves to non-thermal sources and certain processes will be neglected due of their low impact on the observed spectra. Among those are electron-positron pair annihilation, neutron decay and photon-Compton down-scattering.

[123]: Cerruti et al. (2021), "The Blazar Hadronic Code Comparison Project"

[124]: Gao et al. (2017), "On the direct correlation between gamma-rays and PeV neutrinos from blazars"

3.1 Basic concepts

Numerical models solve the coupled differential equations of different particle species. This section introduces the general form of these equations and provides insights to some basic concepts as well as terms that will be used later on.

General form of equations

In a homogeneous, isotropic plasma we can write the Partial Differential Equation (PDE) for a particle density $n_i = \frac{\partial^2 N}{\partial E \partial V}$ of species i as

$$\partial_t n_i(E,t) = Q_i(E,t) - \alpha_i(E,t)n_i(E,t) \\ - \tau_{i,\mathrm{esc}}(E,t)n_i(E,t) - \partial_E(\dot{E}_i(E.t)n_i(E,t))\,, \quad (3.1)$$

where we have used the notation $\partial_X = \partial/\partial X$. In this equation, $Q_i(E,t)$ is the *injection term* which is composed of both external and interaction-induced injection (particles being created as secondaries, in decays, etc.). We further identify $\alpha_i(E,t)$ as the *sink term* (*e.g.* particles disappearing as they interact) and $\tau_{i,\mathrm{esc}}(E,t)$ as the *escape rate* due to the finite size of the system which is usually simply given by the light crossing time of the region (of size R, $\tau_{i,\mathrm{esc}}(E,t) = \frac{1}{R/c}$). Finally, $\dot{E} = dE/dt$ is the continuous loss term accounting for *cooling*.
We point out that the PDEs of different particle species are coupled through the interaction-induced injection terms and the corresponding sink terms. This creates a system of coupled PDEs.

Steady-state solutions
For $\partial_t n_i(E,t) = 0$ the particle distribution is in a steady state. In this case we may find some approximate behaviors that will help understanding more complex scenarios later:

1. In the case of a mono-energetic energy injection term $Q_i(E,t) = Q_0\delta(E - E_0)$ and neglecting escape and sink terms the solution for $n_i(E)$ takes the form of

$$n_i \propto \begin{cases} 1/\dot{E} & , E < E_0 \\ 0 & , E > E_0 \end{cases}. \quad (3.2)$$

   This means that if the cooling scales as $\dot{E} \propto E^{\gamma_{\mathrm{cool}}}$ the particle distribution is $n_i(E) \propto E^{-\gamma_{\mathrm{cool}}}$.
2. For continuous power-law injection ($Q_i(E,t) = Q_0 E^{-p}$), again with $\dot{E} \propto E^{\gamma_{\mathrm{cool}}}$ and omitting all other processes we easily find that

$$n_i \propto E^{-p-\gamma_{\mathrm{cool}}+1}\,. \quad (3.3)$$

Although these scenarios are simplified ones, they may help us to develop an intuition for the final particle spectra in dependence of the injection and loss terms.

The steady state equilibrium may be reached relatively fast if energy losses and radiation processes act on timescales much smaller than dynamical time of the system. However, there are also scenarios in which the radiation processes operate on timescales comparable to the

dynamical timescale of the system; hence we do not expect a steady-state system in objects with fast time variability such as GRBs.

Characteristic timescales
For each energy loss process in Eq. (3.1), we can define the cooling timescale over which particles loose their energy as

$$t_{\mathrm{cool}} = \left(\frac{\dot{E}}{E}\right)^{-1} , \tag{3.4}$$

with the corresponding *cooling rate* t_{cool}^{-1}. Cooling rates may depend on energy and are a characteristic measure for particle interactions. The dominant energy loss mechanism can be found by comparing the cooling times/rates of different processes. Furthermore it is possible to calculate the maximal particle energy by balancing the total loss rate (adding up all cooling rates) with the acceleration rate. From here on we will assume the acceleration timescale for a particle of charge number Z in a magnetic field B (with Larmor radius R_{L}) as

$$t_{\mathrm{acc}} = \frac{1}{\eta}\frac{R_{\mathrm{L}}}{c} = \frac{1}{\eta}\frac{E}{cBZe} . \tag{3.5}$$

Here, we additionally introduced the acceleration efficiency η which will be equal to one for our models if not noted otherwise.

Shape of accelerated particle distribution
Non-thermal accelerated particle distributions are often of power-law shape (see *e.g.* Fermi acceleration in Section 2.2). The injection term in Eq. 3.1 is then characterised by a power law (of index $-p$) above a minimum energy E_{min} with exponential cutoff at a maximum energy E_{max}:

$$\frac{\mathrm{d}N}{\mathrm{d}E} \propto \begin{cases} 0 & , E < E_{\mathrm{min}} \\ E^{-p} \cdot e^{-E/E_{\mathrm{max}}} & , \text{else} \end{cases} . \tag{3.6}$$

For relativistic particles it can equally be described in terms of Lorentz factor $\gamma = E/m$, where m is the particle mass.

The Hadronic Code Comparison Project

The association of an IceCube neutrino to the blazar TXS 0506+056 triggered a community-wide effort to model the same source and provide theoretical interpretations for the observation. With this, the question of compatibility of the predictions given by different numerical schemes

and codes naturally arose. The HCCP is an initiative to compare several codes currently available for numerical modelling of high-energy astrophysical phenomena. The aim of the project is to quantify the uncertainties introduced by different numerical approaches. Participating in the comparison are two steady-state codes (*B13* [125] and *Le-Ha Paris* [126], which calculate only the steady-state solution of the system) and two time-dependent codes (*AM3* [124] and *ATHEνA* [127–130], which follow the evolution of particle densities dynamically). The results are complemented by analytical estimates of neutrino fluxes.

[125]: Boettcher et al. (2013), "Leptonic and Hadronic Modeling of Fermi-Detected Blazars"
[126]: Cerruti et al. (2015), "A hadronic origin for ultra-high-frequency-peaked BL Lac objects"
[124]: Gao et al. (2017), "On the direct correlation between gamma-rays and PeV neutrinos from blazars"
[127]: Mastichiadis et al. (1995), "Self-consistent particle acceleration in active galactic nuclei"
[128]: Mastichiadis et al. (2005), "Spectral and temporal signatures of ultrarelativistic protons in compact sources. 1. Effects of Bethe-Heitler pair production"
[129]: Dimitrakoudis et al. (2012), "The time-dependent one-zone hadronic model - First principles"
[130]: Petropoulou et al. (2014), "Implications of a PeV neutrino spectral cutoff in GRB models"

Inspired by TXS 0506+056, the assumed source type for the comparison was a 'knot' in an AGN jet. In a simplified scenario this region is modelled as a spherical emission region (characterised by a comoving radius R' with corresponding volume $V' = \frac{4}{3}\pi R'^3$), a Doppler factor δ and a magnetic field B'. The distance to earth is specified by the redshift z.

The implementation of specific particle interactions was tested comparing cooling rates and/or the injection rates of created secondaries. To quantify the impact on observational predictions we compared the Spectral Energy Distribution (SED) νF_ν. In the following we will limit ourselves to sharing the different results for the observable quantities (νF_ν and slope of F_ν).

List of symbols

We briefly summarise the main parameters/quantities relevant for the HCCP with corresponding symbols. The introduced notations/conventions will also be used in the other parts of this thesis.

Table 3.1: List of symbols and notation conventions for the HCCP and presentation of radiation models.
We point out that particle Lorentz factors γ, although not primed, are always reported in the **comoving frame**. For all other quantities (frequencies, energies, magnetic fields etc.), we will indicate the comoving quantities as primed ones.

	Symbol	Quantity
source properties	z	redshift
	Γ	Lorentz factor
	δ	Doppler factor
	R	size of region
	V	volume of region
	B	magnetic field
particle distributions	E	particle/ photon energy
	γ	particle Lorentz factor $\gamma = E'/m$
	p	slope of particle distribution $n(\gamma) = \frac{\mathrm{d}n}{\mathrm{d}\gamma} \propto \gamma^{-p}$
	ν	photon frequency $\nu = E_\gamma/h$
	ϵ	dimensionless photon energy $\epsilon = E_\gamma/m_e c^2$
observed quantities	F_ν	Differential energy Flux $F_\nu = \frac{\nu \mathrm{d}N}{\mathrm{d}\nu \mathrm{d}A \mathrm{d}t}$
	α	slope of $F_\nu \propto \nu^\alpha$
	νF_ν	Spectral Energy Distribution (SED) $\nu F_\nu = \frac{\nu^2 \mathrm{d}N}{\mathrm{d}\nu \mathrm{d}A \mathrm{d}t}$
	$'$ (primed)	comoving quantities

3.2 Leptonic processes

This section introduces the most relevant processes for **leptons** in photon fields: Synchrotron radiation due to motion in magnetic fields, (inverse) Compton scattering processes between photons and electrons, as well as the concept of Synchrotron Self-Compton spectra and photon-photon pair annihilation. We will not derive the full cross-sections and spectra (for this we point to comprehensive works like [131–133]), but only recapitulate the main formulas and illustrate the processes using results of the HCCP.

[131]: Longair (1992), *High-energy astrophysics. Vol. 1: Particles, photons and their detection*
[132]: Dermer et al. (2009), *High energy radiation from black holes: Gamma rays, cosmic rays and neutrinos*
[133]: Ghisellini (2013), *Radiative Processes in High Energy Astrophysics*

Synchrotron radiation and inverse Compton scattering

Synchrotron radiation

If a charged particle is accelerated radially in a magnetic field due to the Lorentz force, it emits *synchrotron radiation*.
Of course, synchrotron emission is emitted by **all** charged particles in magnetic fields. The energy loss of a particle of Lorentz factor γ_i (energy E_i), charge number Z_i and mass m_i in a magnetic field B is given by

$$-\frac{\mathrm{d}E_i}{\mathrm{d}t} = \frac{\sigma_\mathrm{T}}{6\pi c} Z_i^4 \left(\frac{m_e}{m_i}\right)^4 E_i^2 \propto E_i^2/m_i^4. \tag{3.7}$$

Hence light particles radiate more and cool faster by synchrotron radiation. In the following we will discuss the synchrotron emission of electrons as lightest particles and most efficient synchrotron emitters (recall, *e.g.* that $m_p/m_e \simeq 1.8 \cdot 10^3$).

The spectrum F'_ν emitted by a single electron of Lorentz factor γ_e in a magnetic field of strength B' peaks at a frequency $\nu'_\mathrm{sy} \simeq 0.29\nu'_c$, where the *critical frequency* $\nu'_c = \gamma_e^2 \frac{3}{2} \sin\theta\, \nu'_L$ can be calculated with the Larmor frequency $\nu'_L = \frac{eB'}{2\pi m_e c}$. The angle θ is the *pitch angle* between the electron velocity $\vec{v}'$ and the magnetic field $\vec{B}'$. Below the peak, the spectrum is well approximated by a power-law of index 1/3, above by an exponential decay (proportional to $e^{-\nu'/\nu'_c}$). While this formulas still invoke the pitch angle, we will now move to pitch-angle averaged models and simply approximate $\nu'_\mathrm{sy} \simeq \gamma_e^2 \nu'_L$.

This simple shape emitted by a single electron can lead us to the F'_ν spectrum from by a power-law distribution of electrons of index $-p$ between $\gamma_{e,\mathrm{min}}$ and $\gamma_{e,\mathrm{max}}$. In principle, this photon spectrum is the superposition of the synchrotron spectra of all emitting electrons. Integrating over the emission of all electrons between $\gamma_{e,\mathrm{min}}$ and $\gamma_{e,\mathrm{max}}$ one finds that the resulting photon spectrum is a power law of index $\alpha = -\frac{p-1}{2}$ between $\nu'_\mathrm{min} = \gamma_{e,\mathrm{min}}^2 \nu'_L$ and $\nu'_\mathrm{max} = \gamma_{e,\mathrm{max}}^2 \nu'_L$. In this region, the electron and synchrotron slopes are thus directly related. Above ν'_max the photon spectrum follows the emission of the electrons at $\gamma_{e,\mathrm{max}}$ and $F'_\nu \propto e^{-\nu'/\nu'_\mathrm{max}}$.

In steady state an electron distribution $\propto \gamma_e^{-2}$ forms below $\gamma_{e,\mathrm{min}}$ (since the cooling rate $\dot{E}' \propto E'^2$, see Eq. (3.2)). This tail produces synchrotron radiation of slope $\alpha = -(2-1)/2 = -1/2$.

To predict the characteristic synchrotron energy ϵ'_{sy} for a power-law distribution of electrons, two basic considerations can be of help: *(1)* Since the emitted synchrotron power scales with γ_e^2, the synchrotron spectrum will be dominated by electrons at $\gamma'_{e,\mathrm{min}}$ if the electron slope $p > 2$ and by electrons at $\gamma_{e,\mathrm{max}}$ if the electron slope $p < 2$. *(2)* The photon energy ϵ' corresponding to a electron Lorentz factor γ_e is approximately given by $\epsilon' \simeq \gamma_e^2 B'/B_{\mathrm{crit}}$ with $B_{\mathrm{crit}} \simeq 4.4 \cdot 10^{13}$G. Overall, the spectral peak will thus be at

$$\epsilon'_{\mathrm{sy}} \simeq B'/B_{\mathrm{crit}} \begin{cases} \gamma_{e,\mathrm{max}}^2 \,, & p < 2 \\ \gamma_{e,\mathrm{min}}^2 \,, & p > 2 \,. \end{cases} \tag{3.8}$$

The counter-effect to synchrotron radiation is *synchrotron absorption*: In a magnetic field, electrons can re-absorb photons. This leads to a depletion in the photon spectrum and a corresponding additional break at ν'_a. For a power-law distribution of electrons above $\gamma_{e,\mathrm{min}}$ (which emit synchrotron radiation of frequency ν'_{min}), the spectrum below ν'_a scales as $\nu'^{\frac{5}{2}}$ (ν'^2) if $\nu'_a < \nu'_{\mathrm{min}}$ ($\nu'_a > \nu'_{\mathrm{min}}$). In more complex systems, the real self-absorption slope and frequency can only be obtained by integrating over the photon and electron distributions.

Inverse Compton scattering

The scattering process between free charged particles and photons is called *Compton scattering*. Again, all charged particles in principle can take part in this process. Similar to synchrotron radiation the loss rate scales with $1/m^4$, which means that the process is strongly suppressed for all particles heavier than electrons. In the following we will only discuss the results for electrons.

In the classical Compton scattering an incoming photon transfers a part of its energy to an electron at rest. However, astrophysical plasmas contain highly relativistic electrons. Those may transfer parts of their energy to the photon if their energy is greater than the energy of the incoming photon. This process is called *inverse Compton scattering*. It may occur either in the *Thomson regime* (if the photon energy in the electron rest frame is much smaller than the electron rest mass energy, $\gamma_e h\nu' \ll m_e c^2$) or in the *Klein-Nishina regime* (if $\gamma_e h\nu' \gtrsim m_e c^2$).

In the Thomson regime the electron recoil can be neglected. The energies of outgoing particles can be derived in a simple way treating the process as a particle-particle scattering in the electron rest frame. In principle also this process depends on the angle between two initial particles, but we will again only consider angle-averaged results. In this case, the final photon energy ϵ'_f (in the approximation of $\gamma_e \gg 1$) is given by

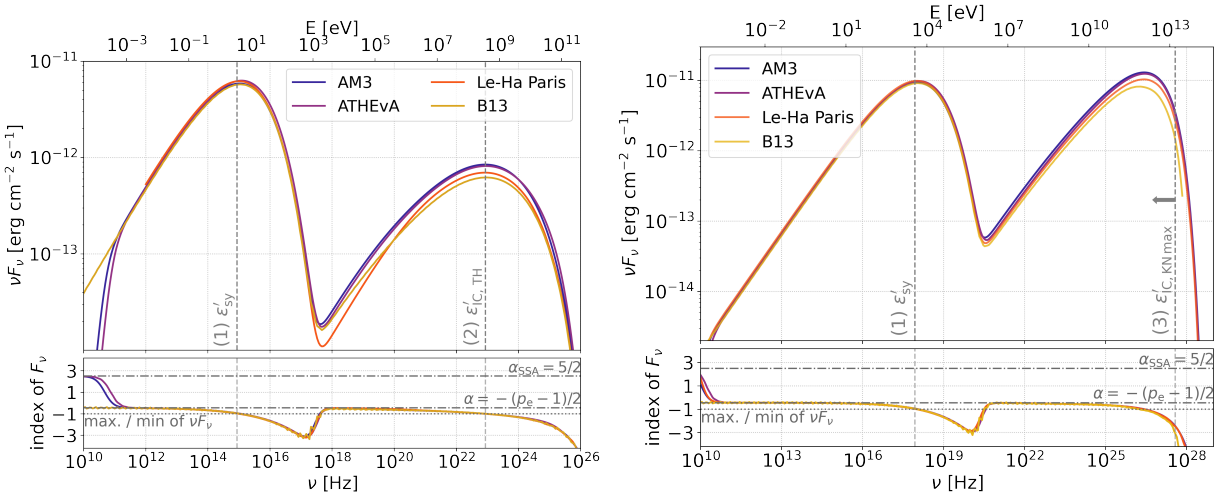

SSC (Thomson regime) SSC (Klein-Nishina regime)

Figure 3.1: Synchrotron-Self Compton spectrum in the Thomson regime (left) and in the Klein-Nishina regime (right), for input parameters see Table 3.2. The upper panels show the spectral energy distribution νF_ν as a function of observed photon frequency ν, the lower panels the corresponding spectral indices of F_ν. Results of different codes of the HCCP are marked with different colours. We indicate analytical estimates for the following characteristic energies ϵ': *(1)* The synchrotron peak energy $\epsilon'_{\rm syn} = \gamma^2_{e,\rm max}\, B'/B_{\rm crit}$, *(2)* the Thomson inverse Compton energy $\epsilon'_{\rm IC,\,TH} = \gamma^4_{e,\rm max}\, B'/B_{\rm crit}$ and *(3)* the Klein-Nishina inverse Compton maximal energy $\epsilon'_{\rm IC,\,KN\,max} = \gamma_{e,\rm max}$, see text for details. They are converted into observed quantities with $\nu = \epsilon'\, m_e c^2\, \delta/h(1+z)$.
For the spectral index we indicate the slope expected for synchrotron self absorption ($\alpha_{\rm SSA}$) and for synchrotron and self-Compton radiation of a particle distribution of slope $p_{\rm e}$ ($\alpha = -(p_{\rm e}-1)/2$). On the dotted line νF_ν is minimal/maximal.

$\epsilon'_f \sim \gamma_e^2 \epsilon'_i$ (where ϵ_i is the initial photon dimensionless energy). Similar to synchrotron cooling, the electron cooling scales as $\dot{E}' \propto E'^2$.
In the Klein-Nishina regime quantum effects and the electron recoil have to be taken into account. Again without deriving the exact formulas we just report that the overall result is a suppression of the cross section and that the scaling of the electron cooling in pure Klein-Nishina regime is $\dot{E}' = \text{cst}$. For an electron distribution extending over a wide range of energies the cooling timescale will smoothly transition between $\dot{E} \propto E'^2$ at low energies (Thomson regime) to $\dot{E}' = \text{cst}$ at high energies (Klein-Nishina regime). Energy conservation implies that the maximal photon energy after the scattering is limited by $\epsilon'_f \lesssim \gamma_e$.

Synchrotron Self-Compton

Observed spectra of many astrophysical sources are well-described by so-called Synchrotron Self-Compton (SSC) spectra. These are a natural product of accelerated particles in a magnetic field: First, relativistic particles generate a synchrotron spectrum which then serves as a target photon field for inverse Compton scatterings with the same electron population. The result is the typical double-hump νF_ν spectrum in which the first peak is generated by synchrotron radiation, the second one by inverse Compton radiation.
To illustrate these SSC scenarios Figure 3.1 shows show the predicted steady-state SED νF_ν (upper panel) and the corresponding spectral indices of F_ν (lower panel) for an AGN in the Thomson and Klein-

Nishina regime. We account for injection, synchrotron radiation, inverse Compton radiation and escape (with $t'_{\rm esc} = R'/c$ for all particles). All particle cooling mechanisms except escape are neglected. The inverse Compton scatterings occur in the Thomson (left plot) and in Klein-Nishina regime (right plot), see Table 3.2 for the corresponding input parameters. Injected particles follow a power law with exponential cut-off (defined in Eq. 3.6) between $\gamma_{\rm min}$ and $\gamma_{\rm max}$. Their injection rate $Q'_\gamma = {\rm d}N/{\rm d}\gamma {\rm d}t' {\rm d}V' \propto \gamma^{-p_{\rm inj}}$ is normalised to the injected power $P'_{\rm inj}$ via

$$P'_{\rm inj} = V' \int_{\gamma_{\rm min}}^{\gamma_{\rm max}} \gamma m c^2 Q'_\gamma {\rm d}\gamma \,. \tag{3.9}$$

Table 3.2: Input parameters for the SSC-scenarios

Regime	TH	KN
z	0.01	
δ	30	
R' [cm]	10^{15}	
B' [G]	0.01	0.1
$\gamma_{e,\rm min}$	1	1
$\gamma_{e,\rm max}$	10^4	10^8
$p_{e,\rm inj}$	1.9	1.9
$P'_{e,\rm inj}$ [erg/s]	$1.56 \cdot 10^{40}$	$3.03 \cdot 10^{40}$

The curves show the predictions of the different HCCP codes. With maximal deviations of around 30 % (and even less at the peaks), the overall agreement for the SED in the upper panel is very good. We point out that B13 sets the escape rate to $\frac{3}{4}R'/c$, which we corrected for in the Figure. Further, both LeHa-Paris and B13 apply a geometrical averaging factor of $\frac{3}{4}$ to the synchrotron spectrum (when calculating the target photon spectrum for inverse Compton scatterings). This reduces the flux in their inverse-Compton component, as can be inferred from the Figure. In addition to the numerical results we indicate analytical estimates for the synchrotron and inverse Compton peaks:

(1) Since all cooling effects except escape are neglected, the electron slope remains $-p_e = -p_{e,\rm inj} = -1.9$. From Eq. 3.8 we thus calculate the characteristic synchrotron energy with the maximum electron Lorentz factor as $\epsilon'_{\rm syn} = \gamma^2_{e,\rm max} \frac{B'}{B_{\rm crit}}$.

(2) If inverse Compton scatterings occur in the Thomson regime, photon energies are increased by a factor $\gamma^2_{e,\rm max}$. Thus $\epsilon'_{\rm IC,\,TH} = \gamma^4_{e,\rm max} \frac{B'}{B_{\rm crit}}$.

(3) In the Klein-Nishina regime the maximal energy of inverse Compton photons is given by $\epsilon'_{\rm IC,\,KN\,max} = \gamma_{e,\rm max}$.

As these are derived in the comoving frame, they are here cited as primed quantities. The vertical lines in Figure 3.1 correspond to these ϵ' Doppler-boosted and redshifted into observed energies. Overall, we find that these are acceptable estimates of the peak positions/the upper limit. The lower panel shows the spectral slopes of F_ν, including theoretical predictions for the asymptotic behavior. At the lowest energies, the Synchrotron Self-Absorption (SSA) slope is reached for ATHEνA and AM3 which include the effect in their calculations. The spectral slope of the synchrotron spectrum is predicted as $\alpha = -(p_e - 1)/2 = -(p_{e,\rm inj} - 1)/2 = -0.45$. This spectral slope reproduced by all codes and also (approximately) conserved below the inverse Compton peaks.

Photon-photon pair annihilation

In dense, non-thermal plasmas two energetic photons of frequency ν_1' and ν_2' might annihilate into a $e^{\pm}$ pair if the invariant rest frame energy $s = h^2\nu_1'\nu_2'(1-\cos\theta)$ is larger than the rest mass energy of the two leptons:

$$h^2\nu_1'\nu_2'(1-\cos\theta) > 2(m_e c^2)^2\,. \tag{3.10}$$

Again, θ is the angle between the colliding photons. The cross section (illustrated in Figure 3.2) rises sharply at the threshold. It reaches it maxiumum at $\approx 4m_e^2c^4$ before decaying steeply.
As a consequence, most interactions occur close to the threshold (in the interaction frame). This allows for a simple estimate of the typical energy carried by leptons created by interactions of photons of a given energy: A photon of dimensionless energy $\epsilon_1' = h\,\nu_1'/(m_e c^2)$ will interact predominantly with photons of dimensionless energy $\epsilon_2' = \frac{1}{\epsilon_1'}$. Assuming the two leptons receive equal parts of the total energy in the plasma frame $E_{\rm tot} = (\epsilon_1' + \frac{1}{\epsilon_1'})m_e c^2 \simeq h\,\nu_1'$ implies that each lepton carries the energy $\frac{h\,\nu_1'}{2}$.

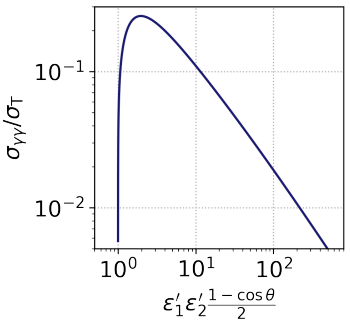

Figure 3.2: Photo-photon cross section (normalised to the Thomson cross-section, $\sigma_{\rm T}$) as a function of $\epsilon_1'\epsilon_2'\frac{1-\cos\theta}{2}$ with $\epsilon' = h\nu'/(m_e c^2)$, calculated following [133]

To illustrate the importance of photon-photon pair annihilation for (very-)high-energy gamma-ray astrophysics, we calculate the threshold energy of photons that will interact with the CMB and an X-ray source, with characteristic photon energies of $6.6\cdot10^{-4}$ eV and 1 keV respectively: For the CMB, photons above $3.9\cdot10^{14}$ eV can participate in photon-photon pair annihilation, for the X-ray source the threshold photon energy is only $2.6\cdot10^{8}$ eV.

3.3 Hadronic processes

After capturing leptonic processes we will now introduce the interactions of non-thermal hadrons in astrophysical photon fields. Of course, as any other charged particle, hadrons also synchrotron radiate and participate in (inverse) Compton scatterings. As detailed above, these interactions are mostly subdominant due to the larger mass of nuclei compared to electrons; additionally they can be described within the same framework as for electrons. We will further neglect nucleon-nucleon collisions, since they are subdominant in dense photon fields where *photo-pion* and *photo-pair production* are the most relevant processes. For nuclei heavier than protons we additionally have to account for *photo-disintegration*.

In principle, photo-pion and photo-pair production are similar for protons and heavier nuclei. The main difference is the relative importance of the two processes: While for protons, photo-pion production is the

dominating loss process above its interaction threshold, photo-pair production gains importance for heavier nuclei. We will not discuss photo-disintegration of nuclei in this section.

Again we give a brief introduction of the processes, following [132, 134]. For useful approximations we point to [127].

[132]: Dermer et al. (2009), *High energy radiation from black holes: Gamma rays, cosmic rays and neutrinos*
[134]: Kelner et al. (2008), "Energy spectra of gamma-rays, electrons and neutrinos produced at interactions of relativistic protons with low energy radiation"
[127]: Mastichiadis et al. (1995), "Self-consistent particle acceleration in active galactic nuclei"

Photo-pion production

If a nucleus N interacting with a gamma-ray γ of energy E'_γ produces a pion π, this is called *photo-pion production*. The produced pion can be a neutral π^0, where the nucleus' charge does not change, or a charged $\pi^\pm$, where the nucleus charge is changed by one. For the sake of simplicity, we continue discussing the process at the example of cosmic-ray protons (characterised by their Lorentz factor γ_p).

The reaction may be realised through different channels. They are visualised in Figure 3.3 as function of photon energy in the proton rest frame $\epsilon_r = \gamma_p \cdot E'_\gamma$ and will shortly be summarised:

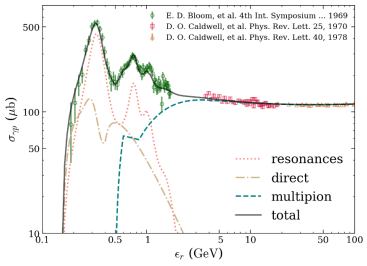

Figure 3.3: Photo-pion cross section as a function of photon energy in the proton rest frame, ϵ_r. Figure taken from [135]

(a) The most simple production channel is *direct production* of the outgoing particles. Due to Isospin, all channels except $p\gamma \to n\pi^+$ are strongly suppressed. Direct production dominates between the π^+ production threshold of ~ 0.15 GeV and ~ 0.25 GeV and then contributes 30 % of the total cross section up to 1 GeV.

(b) *Resonance production* of $\Delta^+(1232)$ is the overall leading contribution to the cross section peaking at $\epsilon_r \simeq 0.32$ GeV. Following Eq. 2.2, outgoing π^0 and π^+ are produced in a ratio of 2:1. The smaller peaks at higher energies in Figure 3.3 correspond to the subdominant contribution of heavier resonances.

(c) *Multi-pion* production defines the high-energy tail of the cross section at $\epsilon_r \gtrsim 1$ GeV.

The produced pions are unstable and decay through the following interactions:

$$\pi^0 \to 2\gamma\,, \tag{3.11}$$

$$\pi^+ \to \mu^+ + \nu_\mu \to e^+ + \nu_e + \bar{\nu}_\mu + \nu_\mu\,, \tag{3.12}$$

$$\pi^- \to \mu^- + \bar{\nu}_\mu \to e^- + \bar{\nu}_e + \nu_\mu + \bar{\nu}_\mu\,. \tag{3.13}$$

We estimate the energies of the outgoing particles (γ, e and ν) with two simple steps: *(1)* We assume the cross-section to be a δ-Function at $\epsilon_r \sim 320$ MeV (the peak of the Δ^+ resonance). If the target photon field has a characteristic energy $E'_{\gamma,\mathrm{target}}$ this allows to calculate the Lorentz factor of the proton participating in the interaction. *(2)* The inelasticity

of this process is 0.2, which means that the proton looses 20 % of its energy. We assume the pions to decay instantaneously and the energy to be distributed equally among the outgoing particles. Consequently the two photons receive 10 % of the initial $E'_p = m_p \gamma_p$ in the π^0 decay and each of the four outgoing particles receives 5 % of E'_p in the π^+ decay. The outgoing particle energies thus are

$$E_{\text{secondaries},\pi^0} \simeq \frac{30\,\text{GeV}}{E'_{\gamma,\text{target}\,[\text{GeV}]}}\,, \tag{3.14}$$

$$E_{\text{secondaries},\pi^+} \simeq \frac{15\,\text{GeV}}{E'_{\gamma,\text{target}\,[\text{GeV}]}}\,. \tag{3.15}$$

We point out that this formula relies on the assumption that protons of all energies are available. If instead the interaction is dominated by particles with Lorentz factor γ'_p, the energies of outgoing particles can be calculated easily with

$$E_{\text{secondaries},\pi^0} \simeq 93.8 \cdot \gamma_p\,\text{MeV}\,, \tag{3.16}$$

$$E_{\text{secondaries},\pi^+} \simeq 46.9 \cdot \gamma_p\,\text{MeV}\,. \tag{3.17}$$

Photo-pair production (Bethe-Heitler)

Below the threshold of photo-pion production, the main interaction channel between photons and protons is *photo-pair production* (Bethe-Heitler pair production in the rest frame of the proton): An incident photon produces a $e^\pm$ pair in the Coulomb field of the nucleus. For this the photon energy in the nucleus' rest frame must exceed twice the electron rest mass. The threshold condition thus reads

$$\gamma_p h\nu' > 2 m_e c^2\,. \tag{3.18}$$

In [127] it has been argued that under the assumptions that the interactions occur predominantly around the interaction threshold, the leptons will have approximately the same Lorentz factor as the initial proton. In a more realistic picture the final lepton distributions have a bell shape with a rather broad peak around $\gamma_e \sim \gamma_p$ [134].

This broad shape as well as the relative importance of photo-pair and photo-pion production are illustrated in Figure 3.4. The Figure shows the $e^\pm$ distributions from proton interactions with the 2.7 K CMB obtained by [134]. In their calculations intermediate particles in Eq. 3.13 decay instantaneously and without any energy losses. This assumption is justified if magnetic fields are comparatively low. In objects with high

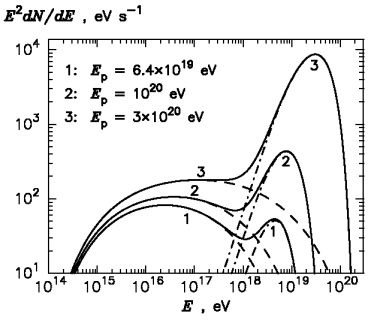

Figure 3.4: Distribution of secondary leptons from photo-pair (dashed) and photo-pion (dash-dotted) productions, for interactions of mono-energetic protons (with energies indicated in the plot) with the CMB. Figure from [134]

Table 3.3: Mean energies of photo-pion and photo-pair produced leptons from interactions of monoenergetic protons with the CMB. They are obtained as $\langle E_{e^\pm,\text{BH}}\rangle = \frac{E_p}{m_p} \cdot m_e$ and $\langle E_{e^+,\pi}\rangle = 0.05 \cdot E_p$.

E_p [eV]	$\langle E_{e^\pm,\text{BH}}\rangle$ [eV]	$\langle E_{e^+,\pi}\rangle$ [eV]
$6.4 \cdot 10^{19}$	$3.5 \cdot 10^{16}$	$3.2 \cdot 10^{18}$
10^{20}	$5.4 \cdot 10^{16}$	$5 \cdot 10^{18}$
$3 \cdot 10^{20}$	$1.6 \cdot 10^{17}$	$1.5 \cdot 10^{19}$

magnetic fields such as GRBs, synchrotron losses of intermediate particles should not be neglected.

Figure 3.4 displays the lepton distributions for three different proton energies (listed in Table 3.3). We compare the results with analytical estimates: As detailed above, the Bethe-Heitler pairs form a broad peak around $\langle E_{e^\pm,\mathrm{BH}} \rangle = \frac{E_p}{m_p} \cdot m_e$. The $\langle E_{e^\pm,\mathrm{BH}} \rangle$ values for the three proton energies are listed in Table 3.3 and agree reasonably well with the center of the broad bell-shape distribution in Figure 3.4. To calculate the characteristic energy of electrons from photo-pion production we follow Eq. 3.17 and find $\langle E_{e^+,\pi} \rangle = 0.05 \cdot E_p$. Again, the values obtained with these simplified approach listed in Table 3.3 are roughly consistent with the position of the peak.

The relative heights of the photo-pair and photo-pion produced lepton distributions reflect the relative importance of the two processes. For $E_p = 6.4 \cdot 10^{19}$ eV, the threshold for photo-pion production is only just surpassed and the process is subdominant compared to photo-pair production. With increasing proton energy photo-pion production becomes more efficient and for $E_p = 10^{20}$ eV is the dominating production mechanism of leptons.

A complete lepto-hadronic scenario

We illustrate the impact of hadronic processes on the SED in a full lepto-hadronic AGN model (for the input parameters see Table 3.4).

The escape time is set as $t'_{\mathrm{esc}} = R'/c$ for all particles and photon-photon annihilation is neglected. The injected particles follow a power law with exponential cut-off (Eq. 3.6) and are normalised through Eq. 3.9. Only three codes provided results for this scenario (AM3, ATHEνA and Le-Ha Paris), their predictions are shown in Figure 3.5. This time, we corrected for the geometrical averaging factor of $\frac{3}{4}$ that is used in the Paris code. The left plot of the Figure shows the photon SED νF_ν (upper panel) and the spectral slope of F_ν (lower panel). We complement this by the all-flavour neutrino SED on the right plot, including the analytical prediction from the HCCP.

All three codes predict similar spectral slopes for the photon SED: At the lowest energies, they approach the synchrotron self-absorption slope α_{SSA}. Further, both below the first and the second peak a slope of $-\frac{p_{\mathrm{inj}}-1}{2}$ is reported for all codes. The SEDs differ at most 30 % around the first two peaks generated by primary synchrotron radiation (which is in agreement with the findings for the SSC scenarios). We observe larger deviations in the high-energy part of the spectrum and in the neutrino SED. Both of these are generated by secondaries created in hadronic interactions.

At this point an explanation of the different implementations of hadronic processes may be due.

Table 3.4: Input parameters for the hadronic scenario

z	0.01	
δ	30	
R' [cm]	10^{15}	
B' [G]	10	
	e^-	p^+
γ_{min}	1	1
γ_{max}	10^3	10^8
p_{inj}	1.9	1.9
P'_{inj} [erg/s]	$1.6 \cdot 10^{37}$	$1.6 \cdot 10^{43}$

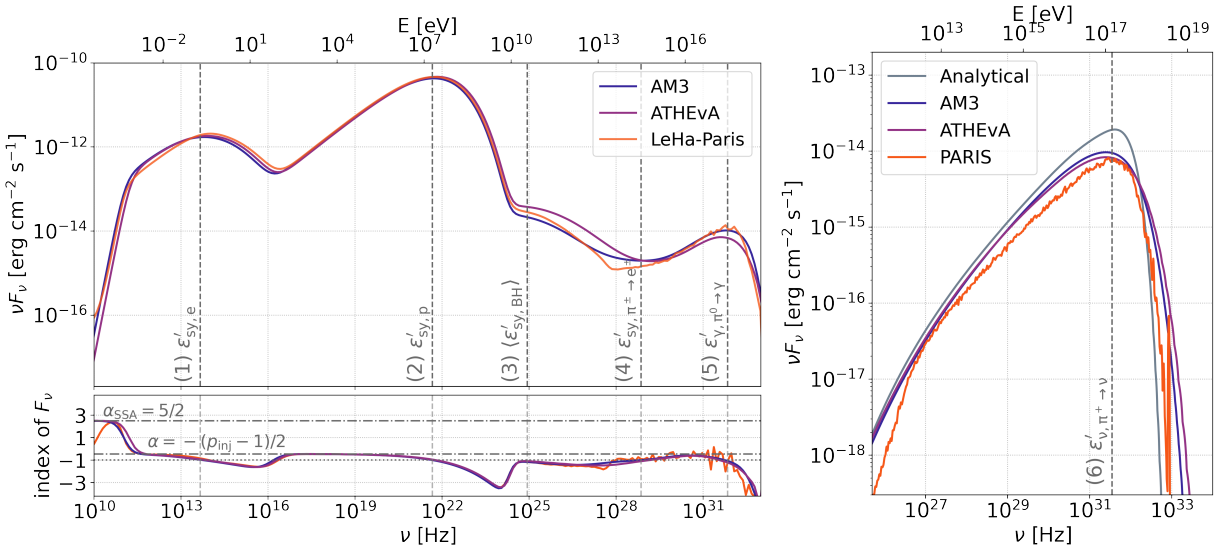

Photon spectrum

Neutrino spectrum

Figure 3.5: Left: Photon SED νF_ν and corresponding spectral indices of F_ν as a function of observed photon frequency ν for the lepto-hadronic scenario (input parameters in Table 3.4). Different colours mark the predictions of the HCCP codes available for this scenario.
We indicate analytical estimates for the following characteristic energies ϵ': *(1)* Primary electron synchrotron peak $\epsilon'_{sy} = \gamma^2_{e,c} B'/B_{crit}$, *(2)* primary proton synchrotron peak $\epsilon'_{sy,p} = \gamma^2_{p,max}\, m_e/m_p\, B'/B_{crit}$, *(3)* photo-pair synchrotron peak $\langle\epsilon'_{sy,BH}\rangle = \gamma^2_{p,max} B'/B_{crit}$, *(4)* synchrotron peak from e^+ from π^+ decays $\epsilon'_{sy,\pi^\pm\to e^\pm} = (0.05\,\gamma_{p,max}\, m_p/m_e)^2 B'/B_{crit}$, *(5)* peak from γs from π^0 decays $\epsilon'_{\gamma,\pi^0\to\gamma} = 0.1\,\gamma_{p,max}\, m_p/m_e$, see text for details.
For the spectral index we indicate the slope expected for synchrotron self absorption (α_{SSA}) and for synchrotron radiation of a particle distribution of slope p_{inj} ($\alpha = -(p_{inj} - 1)/2$).
Right: All-flavour neutrino SED as a function of frequency ν for the three codes and the analytical estimate from the HCCP. We additionally indicate the characteristic energy of the secondary neutrinos as *(6)* $\epsilon'_{\nu,\pi^+\to\nu} = 0.05\,\gamma_{p,max}\, m_p/m_e$.
All comoving energies are converted into observed quantities with $\nu = \epsilon'\, m_e c^2\, \delta/h(1+z)$.

The broad peak around $9 \cdot 10^{24}$ Hz is generated by synchrotron radiation from photo-pair produced leptons. Its normalisation and shape (which differ largely for the three codes) are thus defined by the implementation of photo-pair production in the numerical schemes. While AM3 and Le-Ha Paris follow [134] for this, ATHEνA uses tabulated results from [136]. ATHEνA predicts roughly 80 % higher luminosity in this regime than the other two codes. We find an overproduction of lepton pairs also in other scenarios, however less pronounced. It is hence unclear whether this is a feature originating from the specific implementation. The VHE peak at $\sim 7 \cdot 10^{31}$ Hz is generated from the decay of π^0 and hence depends on the implementation of photo-pion production. All three codes rely on the SOPHIA event generator [137], a Monte-Carlo code for photo-hadronic interactions. ATHEνA uses tabulated SOPHIA results. AM3 follows [138] who also provide tabulated SOPHIA results, however optimised for fast computations of power-law spectra. In contrast to this, Le-Ha Paris explicitly runs SOPHIA for every single SED calculation - which is also the reason why their SED is so spiky. For this process we report better agreement with deviations below ~50%. The lower photon production rate from π^0 of ATHEνA compared to the other codes could systematically be reproduced in examples with fixed external radiation

[136]: Protheroe et al. (1996), "Propagation of ultrahigh-energy protons over cosmological distances and implications for topological defect models"

[137]: Mucke et al. (2000), "SOPHIA: Monte Carlo simulations of photo-hadronic processes in astrophysics"

[138]: Hummer et al. (2010), "Simplified models for photohadronic interactions in cosmic accelerators"

fields. It may thus be an imprint of the different implementations.
Finally, the spectrum at intermediate energies around $7 \cdot 10^{28}$ Hz and the neutrinos are generated from charged pion decays. Those are implemented through the same procedures as the neutral pions discussed above. Here, Le-Ha Paris clearly predicts a lower energy flux. We also validated this by comparing the injection rate of lepton pairs that is 30% to 40% lower in comparison to the other codes. We point out that this could not be reproduced in simulations with fixed, external radiation fields. It may be related to differences in the electron synchrotron flux, which serves as a target for the photo-hadronic interactions, but the exact origin so far remains undetermined. In agreement with this, Le-Ha Paris also predicts a 40% lower all-flavour neutrino flux than the other two codes. On the other hand, the analytical estimates from the HCCP exceed the numerical results by a factor of 2.
Overall we find that the deviations in the hadronic parts of the photon SED are below 80% and for the neutrino SED below 50%. The predictions agree reasonably well around the prominent peaks and the largest differences are found in the photo-pair dominated regime. We stress that for this scenario photon-photon annihilation (both in the source and due to extragalactic background fields) is neglected. If accounted for, this process would suppress the high-energy spectrum such that only the neutrinos could serve as probes of hadronic interactions.

In addition to the HCCP results we provide simple analytical estimates for the position of the following prominent SED features: *(1)* The primary electron synchrotron peak, *(2)* the primary proton synchrotron peak, *(3)* the mean synchrotron energy of photo-pair leptons, *(4)* the characteristic synchrotron energy of leptons from π^+ decays, *(5)* the energy of photons from π^0 decays and *(6)* the energy of neutrinos from π^+ decays.
(1) For the characteristic synchrotron energy of primary electrons, we need to estimate the Lorentz factor of electrons that contribute most. Due to the high(er) magnetic field in the current scenario, synchrotron cooling effects cannot be neglected: The critical Lorentz factor $\gamma_{e,\mathrm{c}} = \frac{6\pi m_e c^2}{\sigma_T B'^2 t'_{\mathrm{esc}}}$ is defined as the electron Lorentz factor above which synchrotron cooling dominates above escape. This means that a cooling break forms from $p_e = 1.9$ (below to $\gamma_{e,\mathrm{c}}$, the spectral index does not change) to $p_e = 2.9$ (synchrotron cooling reduces the spectral index by one). The synchrotron peak will thus be dominated by electrons around $\gamma_{e,c}$ and be located at $\epsilon'_{\mathrm{sy}} = \gamma^2_{e,\mathrm{c}} \frac{B'}{B_{\mathrm{crit}}}$.
(2) The second peak in this scenario is produced by proton synchrotron radiation. Its characteristic energy can be calculated as $\epsilon'_{\mathrm{sy,p}} = \gamma^2_{p,\mathrm{max}} \frac{m_e}{m_p} \frac{B'}{B_{\mathrm{crit}}}$.
(3) Bethe-Heitler pair production is dominated by protons at $\gamma_{p,\mathrm{max}}$, thus $\langle \gamma'_{\mathrm{e,BH}} \rangle = \gamma_{p,\mathrm{max}}$ and $\langle \epsilon'_{\mathrm{sy,BH}} \rangle = \gamma^2_{p,\mathrm{max}} B'/B_{\mathrm{crit}}$.
(4) Photons are most abundant around the synchrotron self-absorption frequency of $\nu_{\mathrm{SSA}} \sim 10^{11}$ Hz (read off from plot). This corresponds to a comoving energy of $\epsilon_{\mathrm{SSA}} \simeq 2.6 \cdot 10^{-11}$ and would thus would require

protons of Lorentz factor of $\gamma_p \sim 10^{13}$ to reach the $\epsilon_r = 320\,\mathrm{MeV}$ where the cross section for photo-pion production is maximal. This is orders of magnitude higher than $\gamma_{p,\mathrm{max}}$ and photo-pion production is thus dominated by protons at $\gamma_{p,\mathrm{max}}$. Secondary leptons from π^+ decays receive 5 % of the proton energy will hence have a Lorentz factor of $\frac{1}{20}\,\gamma_p\,\frac{m_p}{m_e}$ and produce synchrotron radiation of energy $\epsilon'_{\mathrm{sy},\pi^\pm\to\mathrm{e}^\pm} = \left(\frac{1}{20}\,\gamma_{p,\mathrm{max}}\,\frac{m_p}{m_e}\right)^2 \frac{B'}{B_\mathrm{crit}}$.
(5) If the photons produced by π^0 decays receive 10 % of the proton energy their frequency is equal to $\epsilon'_{\gamma,\pi^0\to\gamma} = \frac{1}{10}\,\gamma_{p,\mathrm{max}}\,\frac{m_p}{m_e}$.
(6) Additionally we can estimate the peak of the neutrino spectrum as $\epsilon'_{\nu,\pi^+\to\nu} = \frac{1}{20}\,\gamma_{p,\mathrm{max}}\,\frac{m_p}{m_e}$.
Overall, this simple estimates agree reasonably well with the numerical results. Of course they do not provide insights on the relative importance of the different processes and/or the exact shape of the photon spectrum – They may still prove useful when estimating the importance of these processes on spectra in specific energy regimes.

3.4 Special scenarios

Within the HCCP non-linear feedback processes like the inverse Compton catastrophe and hadronic feedback loops could only be captured by the time-dependent AM3 and ATHEνA codes. Those scenarios are realised in very specific regions of the parameter space and thus of limited relevance for the most common source models. However, as they represent somewhat extreme scenarios, they can prove that even in extreme conditions the numerical approaches yield the same results.

Inverse Compton Catastrophe (ICC)

The term 'inverse Compton catastrophe' [139] refers to scenarios in which the luminosity in the inverse Compton component is dramatically increased and even may outshine the synchrotron emission. It can be realised if the energy density in photons exceeds the energy density of the magnetic field such that inverse Compton cooling becomes the dominating energy-loss process for electrons.

[139]: Longair (2011), *High Energy Astrophysics*

Closely related is the concept of multiple inverse Compton generations: The first generation inverse Compton photons are generated by electrons up-scattering the synchrotron photons. From there on, the $i+1$th generation is generated by inverse Compton up-scattering the ith generation. The leptons participating in the up-scattering are always the same primary electron population. Over multiple generations, energy may be transferred efficiently from lower energies to the high-energy regime, until it is finally limited by Klein-Nishina suppression around the maximal energy of electrons.

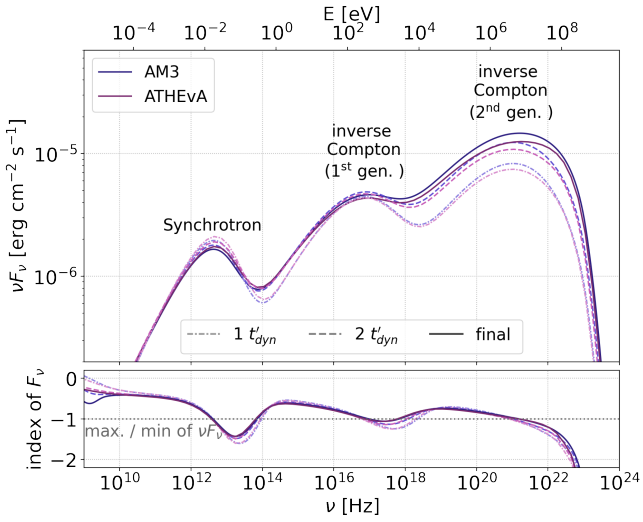

Figure 3.6: SED νF_ν and corresponding spectral slope of F_ν for the inverse Compton catastrophe. We show the results for the steady state ('final') and after one and two dynamical timescales $t'_{\rm dyn} = R'/c$.

The ICC was first proposed to explain the (observed) upper limit in brightness temperatures of radio sources (early on *e.g.* [140], more recently [141]). In a broader source context it was explored in [142].

The scenario can be realised for a high-density mono-energetic electron distribution. For numerical reasons this is mimicked by $\gamma_{e,\rm min} = 10^{1.9}$ and $\gamma_{e,\rm max} = 10^{2.1}$ in the HCCP (see Table 3.5 for the full list of input parameters). The escape time was again set to $t'_{\rm esc} = R'/c$. Overall, the setup approximately corresponds to the highest density scenario in Figure 6 of [142].

The simulated photon spectra are shown in Figure 3.6. The particle distributions are evolved until $t' = 10\, t'_{\rm dyn} = 10\, R'/c$ where the system is in steady state. To illustrate the temporal evolution we additionally show the spectra at $t' = t'_{\rm dyn}$ and $t' = 2\, t'_{\rm dyn}$. As indicated in the Figure, the first peak is generated by synchrotron radiation. The second and third peak are identified as 1st and 2nd generation inverse Compton peaks. The evolution of the SED in Figure 3.6 illustrates how the luminosity in the synchrotron peak is reduced as photons are Compton up-scattered to higher energies as the system evolves from $1\, t'_{\rm dyn}$ to the steady state.

We find that the ATHEνA and AM3 results differ only little. The largest deviations of ~ 10 % are observed at the 2nd generation inverse Compton peak.

[140]: Readhead (1994), "Equipartition brightness temperature and the inverse Compton catastrophe"

[141]: Tsang et al. (2007), "The inverse Compton catastrophe and high brightness temperature radio sources"

[142]: Petropoulou et al. (2015), "Spectral signatures of compact sources in the inverse Compton catastrophe limit"

Table 3.5: Input parameters for the inverse Compton catastrophe

z	0.01
δ	10
R' [cm]	10^{16}
B' [G]	10
$\gamma_{e,\rm min}$	$10^{1.9}$
$\gamma_{e,\rm max}$	$10^{2.1}$
$p_{e,\rm inj}$	2
$P'_{e,\rm inj}$ [erg/s]	$4.6 \cdot 10^{45}$

Pair-Production Synchrotron (PPS) loop

The idea of a runaway process initiating an abrupt, dramatic increase of photon densities due to secondaries from hadronic interactions was first introduced in the 90s (*e.g.* [143] for AGN X-ray flares). They were later dubbed 'hadronic supercriticalities' and have since then been studied anaytically and numerically in a range of contexts (among other [144]).

[143]: Kirk et al. (1992), "X-ray flares from runaway pair production in active galactic nuclei"

[144]: Petropoulou et al. (2014), "Hadronic supercriticality as a trigger for γ-ray burst emission"

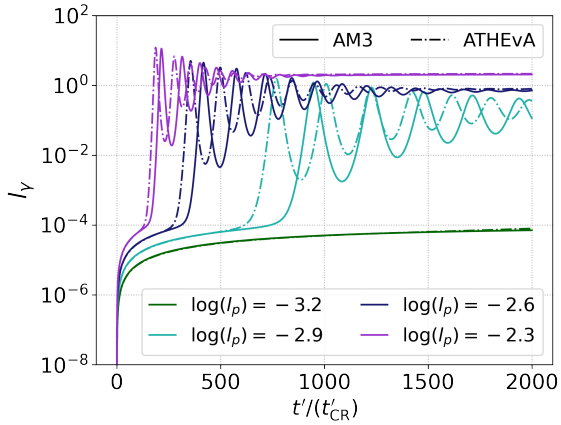

Figure 3.7: Photo-Pair Synchrotron (PPS) compactness l_γ as a function of simulation time t' (divided by the cosmic-ray escape time t'_{CR}) for different proton injection compactness(l_p, marked by different colours) for AM3 and ATHEνA (solid and dashed lines respectively).

A broad examination of the parameter space in which they can occur complemented by an educative review was published recently in [145].

[145]: Mastichiadis et al. (2020), "A roadmap to hadronic supercriticalities: a comprehensive study of the parameter space for high-energy astrophysical sources"

The phenomenon can be realised in a pure hadronic scenario: First the primary protons build up a target photon field for photo-hadronic interactions by proton synchrotron radiation. Then, if the proton densities exceed a critical value, the system enters a *supercritical regime* in which photo-hadronic interactions are strongly enhanced. As a result, secondary leptons are generated at large rates. Their synchrotron radiation further builds up the target photon fields, again increasing the rate of photo-hadronic interactions. This runaway process leads to an exponential increase of the photon densities and an efficient energy transfer from protons to photons.
The supercriticality can be realised both via photo-pair and photo-pion production. In the case of photo-pion production the photon densities are enhanced by synchrotron radiation of secondary lepton pairs from $\pi^\pm$. Additional contributions come from gamma-rays produced in π^0 decays and the secondary lepton cascades generated as these gamma-rays photon-photon annihilate. In photo-pair scenarios the radiation densities rise through synchrotron radiation of the produced lepton pairs.

So far, systems in supercritical regime were only explored with ATHEνA. To confirm that they are not a non-physical result of numerical instabilities, we examined a Photo-Pair Synchrotron (PPS) loop in the HCCP. The corresponding parameters are summarised in Table 3.6. To reach high enough proton densities, the escape time is increased to $t'_{CR} = 1000\, R'/c$ for protons. This way they are practically trapped, while all other particles escape over $t'_{esc} = R'/c$. All processes except photo-pair production, synchrotron radiation and escape are neglected.

Table 3.6: Input parameters for the Photo-Pair Synchrotron (PPS) loop

R' [cm]	10^{15}
B' [G]	31.6
$\gamma_{p,\mathrm{min}}$	$10^{0.1}$
$\gamma_{p,\mathrm{max}}$	10^5
$p_{p,\mathrm{inj}}$	2
$P'_{p,\mathrm{inj}}$ [erg/s]	$5.4 \cdot 10^{44}$
	$1.1 \cdot 10^{45}$
	$2.1 \cdot 10^{45}$
	$4.3 \cdot 10^{45}$

For the following we will measure the density of photons and primary protons by their *compactness*. For the primary protons and the energy density of photons $u'_{\epsilon'}$, ($\epsilon' = E'/(m_e c^2)$) with this dimensionless quantity

is defined as

$$l_{\mathrm{p}} = \frac{\sigma_{\mathrm{T}} P'_{\mathrm{inj}}}{4\pi R' m_p c^3} \,, \tag{3.19}$$

$$l_{\gamma} = \frac{\sigma_{\mathrm{T}} R'}{3} u'_{\epsilon'} = \frac{\sigma_{\mathrm{T}} R'}{3} \int \left(\epsilon' \frac{\mathrm{d}N}{\mathrm{d}\epsilon' \mathrm{d}V'} \right) \mathrm{d}\epsilon' \,. \tag{3.20}$$

We explore four different proton injection luminosities (expressed as proton injection compactnesses). The resulting comoving photon compactness as a function of simulation time t' divided by cosmic-ray escape time t'_{CR} are shown in Figure 3.7. For the lowest proton injection compactness, the system never enters the supercritical regime. For the other three values of l_{p} the PPS loop is initiated: As the system surpasses the critical point, the photon density increases exponentially until the photons abruptly cool the protons. From this, the system enters an oscillating state (with decreasing amplitude and periodicity). After a number of cycles a steady state is reached - with a photon compactness almost four orders of magnitude higher than without the PPS loop.
The onset, amplitude and periodicity depend on the particle compactnesses in the source. Overall, for high compactness the onset is earlier, the amplitude larger and the periodicity smaller. Consequently, the steady state is reached earlier.
This trend (as well as the general phenomenon) is reproduced both by ATHEνA and AM3. Also the values of l_{γ} at the peaks and the change of photon compactness as a function of time ($\mathrm{d}l_{\gamma}/\mathrm{d}t$) are similar. Differences remain in the onset time of the PPS loop and the period length.
Overall, these results confirm that the PPS loop is not a numerical artefact. As it is realised in an extreme parameter regime, small differences of the numerical solver and in the implementation of photo-pair production (that manifested already in our earlier tests) impact the onset and periodicity of the loop. The absolute photon densities however are on a similar level.

Gamma-ray bursts 4

Gamma-ray bursts (GRBs) are among the most energetic events observed in our universe and fancied as high-energy particle sources. A wide range of scientific questions is posed by these luminous transients (recall, for example, their connection to gravitational wave astrophysics) – we will however focus on the initial bright gamma-ray flash called the *prompt phase*.

After the general introduction to radiation processes in Chapter 3, this chapter lays the base to radiation modelling of GRBs (and more particular, their prompt phase) as specific objects by introducing their main properties. For this purpose we first give a brief historical introduction in Section 4.1 which is followed by an overview of the stages a GRB is going through in Section 4.2. Turning to the prompt phase of the event, we discuss possible energy dissipation mechanisms and radiation models in Section 4.3 and Section 4.4. We close this chapter by reviewing GRBs as potential sources of UHECRs and HE neutrinos in Section 4.5.

4.1 A historical introduction . . 41
4.2 The complete picture 42
4.3 Prompt phase energy dissipation mechanism 45
4.4 Prompt phase radiation models 47
4.5 GRBs as UHECR and HE neutrino sources 52

4.1 A historical introduction

The United States VELA satellites were launched in the early 1960s to monitor Russian activities in space (or, more particularly their obedience to the Nuclear Test Ban Treaty). Though they did not uncover any nuclear weapon test, they unveiled a new astrophysical phenomenon called *gamma-ray bursts*. The discovery was only made public a few years later, after the detection of a dozen events which reassured scientists that the signals were indeed of astrophysical origin [147]. A huge research interest in those mysterious events arose.

[147]: Klebesadel et al. (1973), "Observations of Gamma-Ray Bursts of Cosmic Origin"

Few basic conclusions could soon be drawn: To reconcile the extreme observed luminosities with realistic source energy budgets, the emission was proposed to originate from a collimated jet. Furthermore, in order not to be opaque to its own radiation, this jet had to move at relativistic velocities and Lorentz factors of $\Gamma \sim 100$.

Nevertheless, the initial years were characterised by sparse data that had little potential in limiting the wealth of theories. A new era began with the launch of the Compton Gamma-Ray Observatory (CGRO) in 1991 with the Burst Alert and Transient Source Experiment (BATSE) on board. Over the course of its lifetime, BATSE detected about 2700 GRBs, finally enabling the study of a larger event sample. This led to important milestones: First, the division in the two populations of short and long GRBs with durations below and above 2s respectively [146]. The bi-modal distribution of durations that lay the base for this is shown in

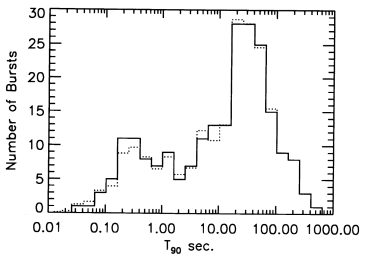

Figure 4.1: Histogram of durations (T_{90}) of BATSE detected Gamma-Ray Bursts. Figure from [146]

[146]: Kouveliotou et al. (1993), "Identification of two classes of gamma-ray bursts"

Figure 4.1. Second, the universal empirical 'Band'-function was developed to describe the spectra [148]. Third, it was now possible to fully appreciate the wealth of different light curves of this population and better resolve their time variability. Finally, the isotropic distribution of events further supported an extra-galactic origin [149]. With the first detection of a multi-wavelength GRB afterglow in 1997 [150] and the first determination of a GRB redshift soon after, the cosmological origin could be settled without any doubts.
Today, the most important observatories are the *Swift* and *Fermi* missions. *Swift* is equipped with optical to X-ray instruments, and its Burst Alert Telescope (BAT) in the hard X-ray band between 15 and 50 keV detects 100 GRBs per year [151]. *Fermi* on the other hand aims at higher photon energies: The Gamma-Ray Burst Monitor (GBM, sensitive between 8 keV and 40 MeV) records 250 GRBs yearly [152]. Only a few (about 8 per year) are also seen by the Large Area Telescope (LAT) that covers an even higher energy range of 20 MeV to 300 GeV [72].

Even though scientists can now access a wealth of data, GRBs remain mysterious events. For example, it is yet unclear which radiation processes generate the early, bright emission during the prompt phase and what the underlying energy dissipation mechanism is. Interestingly it is most often the few bursts with wealthy and precise data that have the largest potential in constraining models.
Due to the large amounts of energies they release, GRBs have also long been discussed as potential UHECR sources (early on *e.g.* in [13]). However, this paradigm is challenged by the absence of high-energy neutrinos that could be associated with known GRBs [15, 16]. Additional constraints come from the energy budget required to power the UHECR flux and the high amount of energy that consequently needs to be transferred to non-thermal baryons.

It can be expected that advances in (R)MHD jet modelling and Particle-In-Cell (PIC) simulations of particle acceleration can provide useful insights that may help to constrain the mechanisms at play in the next years. For example, the energy dissipation mechanism could be constrained by jet launching simulations that give insights on the amount of energy carried by magnetic fields.

4.2 The complete picture

The canonical GRB picture can be divided in three main stages: *(1)* The *pre-burst phase*: From the death of the GRB precursor (either a supermassive star or a compact binary system) a new compact object is formed. This freshly born central engine launches an energetic astrophysical jet that accelerates to relativistic velocities. *(2)* This jet generates a short and intense photon flash in X-rays and gamma-rays, the *prompt phase*.

[148]: Band et al. (1993), "BATSE observations of gamma-ray burst spectra. 1. Spectral diversity."

[149]: Meegan et al. (1992), "Spatial distribution of gamma-ray bursts observed by BATSE"

[150]: Costa et al. (1997), "Discovery of an X-ray afterglow associated with the gamma-ray burst of 28 February 1997"

[151]: Barthelmy et al. (2005), "The Burst Alert Telescope (BAT) on the Swift MIDEX mission"

[152]: Meegan et al. (2009), "The Fermi Gamma-Ray Burst Monitor"

[72]: Atwood et al. (2009), "The Large Area Telescope on the Fermi Gamma-ray Space Telescope Mission"

[13]: Waxman (1995), "Cosmological gamma-ray bursts and the highest energy cosmic rays"

[15]: Aartsen et al. (2016), "An All-Sky Search for Three Flavors of Neutrinos from Gamma-Ray Bursts with the IceCube Neutrino Observatory"

[16]: Aartsen et al. (2017), "Extending the search for muon neutrinos coincident with gamma-ray bursts in IceCube data"

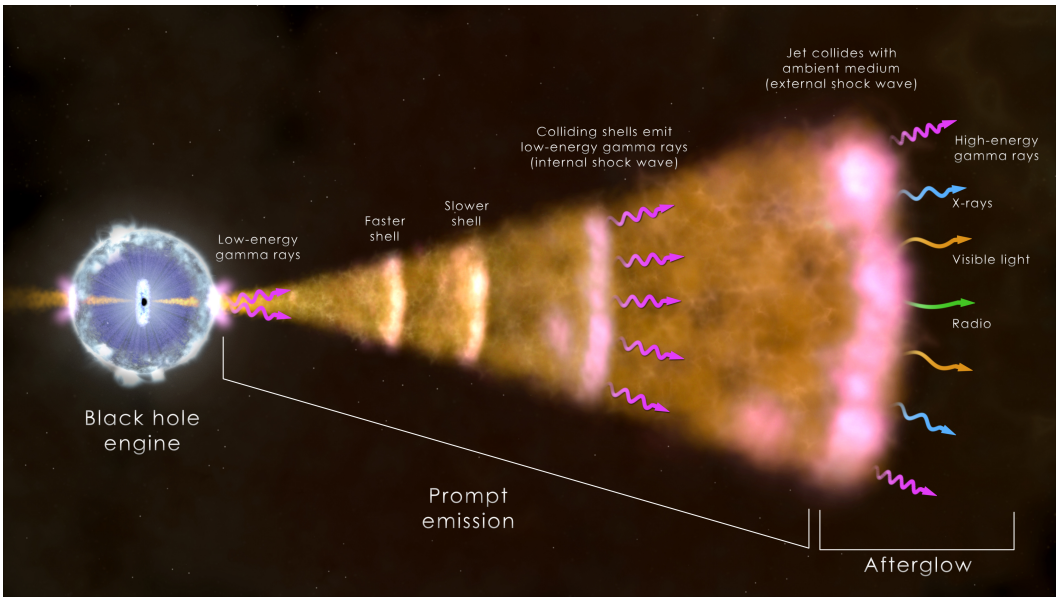

Figure 4.2: Schematic view of the prompt and afterglow phase of a GRB in the internal shock model with the central black hole engine towards the left. The relativistic jet (propagating towards the right) is initially opaque to its own radiation, due to the high density of the plasma. As the jet expands, the density drops and it becomes optically thin at the so-called *photosphere*. At this point the first photon signal in form of low-energy gamma-rays is expected. In the internal shock model, the bulk of the prompt emission is then generated as faster parts of the ejecta (called *shells*) catch up with slower ones and internal shock waves form. Finally, the afterglow arises from the interaction of the jet with the ambient medium. Note that the length scales on this schematic picture are not representative.
Image credit: *NASA's Goddard space flight center*

(3) As the jet starts to decelerate due to its interaction with the ambient medium, a multi-wavelength signal sets in. This *afterglow* fades over the duration of days to weeks or even months. Phase *(2)* and *(3)* of this time line of events are visualised in Figure 4.2 in the fireball internal shock model. The fireball model [153] captures the processes after the jet launching: The hot plasma released by the central engine at an initial radius R_* and with Lorentz factor Γ_0 is optically thick and dominated by radiation. As it expands under the radiation pressure, the energy of lepton pairs and photons is transferred to the baryons contained in the outflow. Finally, at the saturation radius $R_{\rm sat}$, baryons and leptons carry equal amounts of energy and the acceleration stops. From this point on, the jet is called 'matter dominated'. During its further expansion the optical depth decreases until it is equal to one at the photospheric radius $R_{\rm PH}$. Above this radius, the prompt phase emission starts. Finally, at the deceleration radius $R_{\rm dec}$ the Lorentz factor starts to decrease and the afterglow sets in. The evolution of Lorentz factor with radius and the characteristic radii are depicted in Figure 4.3. The theoretical picture may of course differ in case of a Poynting flux dominated jet.

[153]: Rees et al. (1992), "Relativistic fireballs - energy conversion and time - scales"

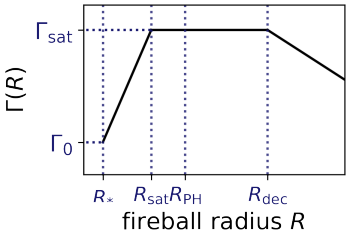

Figure 4.3: Sketch of the evolution of the fireball Lorentz factor with radius.

In the following, we briefly introduce the main characteristics of the three phases complemented by an overview of the corresponding theories.

***(1)* The pre-burst phase**

GRB progenitors differ by sub-class: Long GRBs originate from the cataclysmic death of supermassive stars. Evidence for this comes from associated supernova observations and their high occurrence rate in

star-forming regions. In short GRBs the central engine is formed after the merger of two compact objects (neutron stars or black holes). After a long period of indirect hints, this was unambiguously confirmed by the association of a short GRB to the *Ligo/Virgo* detection of a neutron star merger in 2017 [94].

The subsequent jet launching is a complex question on its own. Magnetic fields are usually assumed to play an essential role, as already highlighted in early analytical works like [154, 155]. Over the last decades numerical RMHD simulations have contributed to a better understanding. Overall, they confirm that jet launching occurs in the vicinity of compact objects through magnetohydrodynamic effects and accretion (see reviews [156, 157]). We point out that most simulations are performed for AGN-like systems, whereas (long) GRBs require the special setup of jet launching in an ambient medium, as *e.g.* in [158].

Even if during the launch the jet is Poynting flux dominated, mechanisms like impulsive acceleration may convert the magnetic energy of the outflow such that in the end the jet is matter dominated, *e.g.* [159, 160].

(2) The prompt phase

The prompt phase is usually characterised by a *light curve* and a *spectrum*. The light curve of detected photons is highly irregular with temporal fluctuations that go down to the ms-scale. Single pulses can often be described by a Fast-Rise-Exponential-Decay (FRED) profile. The duration of the prompt phase is mostly measured as T_{90}, the time interval during which 90% of the total energy is detected. Overall, a large variety of light curves is observed in the population (illustrated by two BATSE light curves in Figure 4.4).

In contrast to this, the non-thermal νF_ν spectra are surprisingly similar and mostly have peak energies $E_{\rm peak} = h\nu_{\rm peak}$ in the keV to MeV range. Their photon spectrum $N(E) \propto F_\nu/\nu$ can be fitted well by the phenomenological *Band-function* [148], a smoothly broken power law:

$$N(E) = A \begin{cases} \left(\frac{E}{100\,\mathrm{keV}}\right)^{\alpha} e^{-E/E_0}\,, & \text{if } E \lesssim (\alpha-\beta)E_0 \\ \left(\frac{(\alpha-\beta)E_0}{100\,\mathrm{keV}}\right)^{\alpha-\beta} \left(\frac{E}{100\,\mathrm{keV}}\right)^{\beta} e^{\beta-\alpha}\,, & \text{if } E > (\alpha-\beta)E_0 \end{cases} . \tag{4.1}$$

The break energy $E_{\rm b}$ is related to the peak energy through $E_{\rm peak} = (2+\alpha)E_{\rm b}$. Typical values for the indices are $\alpha \sim -1.0$ and $\beta \sim -2.2$ [161]. This means that GRB peaks are narrower than the spectra of other sources like AGNs [162, 163].

In lack of the exact jet opening angle, the total energy output of the prompt phase is usually reported in the *isotropic equivalent gamma-ray energy* $E_{\gamma,\rm iso}$. It is defined as the total energy released in the energy range of 1 keV to 10000 keV in the source frame (redshift-corrected).

A range of possibilities that have been proposed for the jet energy

[94]: Abbott et al. (2017), "Gravitational Waves and Gamma-rays from a Binary Neutron Star Merger: GW170817 and GRB 170817A"

[154]: Blandford et al. (1977), "Electromagnetic extractions of energy from Kerr black holes"

[155]: Blandford et al. (1982), "Hydromagnetic flows from accretion discs and the production of radio jets"

[156]: Hawley et al. (2015), "Disks and Jets - Gravity, Rotation and Magnetic Fields"

[157]: Komissarov et al. (2021), "Numerical simulations of jets"

[158]: Bromberg et al. (2016), "Relativistic MHD simulations of core-collapse GRB jets: 3D instabilities and magnetic dissipation"

[159]: Granot et al. (2011), "Impulsive Acceleration of Strongly Magnetized Relativistic Flows"

[160]: Granot (2012), "The effects of subshells in highly magnetized relativistic flows"

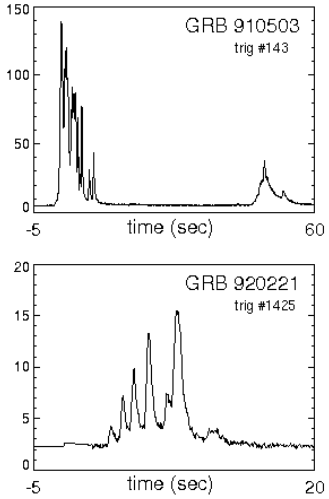

Figure 4.4: Two exemplary BATSE light curves, from [a]

[a] https://gammaray.nsstc.nasa.gov/batse/grb/lightcurve/index.html

[161]: Poolakkil et al. (2021), "The Fermi-GBM Gamma-Ray Burst Spectral Catalog: 10 yr of Data"

[162]: Axelsson et al. (2015), "The width of gamma-ray burst spectra"

[163]: Yu et al. (2015), "The sharpness of gamma-ray burst prompt emission spectra"

dissipation will be introduced in Section 4.3, followed by the radiation processes that could create the prompt spectra in Section 4.4.

***(3)* The Afterglow**

Once the jet has swept up a mass comparable to its own, it decelerates. This is the onset of the afterglow. It is usually well explained by a blast-wave scenario in which an external shock propagates through the ambient medium. In principle, the afterglow light curve is just a power-law decaying with time. In some bursts, X-ray flares or plateaus manifest, mostly during the early afterglow.

It is also during the afterglow that an observer will for the first time actually experience the effect of the jet opening angle θ_e. During the prompt phase, the emission is relativistically beamed in a cone of angle $\frac{1}{\Gamma}$ that is smaller than the jet opening angle θ_e. For any observer it is thus impossible to distinguish between jetted or isotropic emission. As the jet decelerates, the relativistic beaming angle becomes wider. Finally, when $\frac{1}{\Gamma} = \theta_e$, the emission from the complete jet can be observed. This point introduces a monochromatic *jet break* in the afterglow light curve. This feature (that allows to determine the jet opening angle and thus the true GRB energy) is observed for some but not all GRBs; see *e.g.* [164] who find a jet break in 55 out of 99 GRBs.

[164]: Wang et al. (2018), "Gamma-ray burst jet breaks revisited"

4.3 Prompt phase energy dissipation mechanism

A major riddle in GRB theories is that of energy dissipation, *i.e.* how the jet energy is transferred to plasma particles.

A broad range of theories is discussed in the literature. We here limit ourselves to the internal shock model, magnetic energy dissipation and neutron collisions while referring to reviews as [165] for more alternatives. We conclude by reviewing some recent results of 3D (M)HD jet simulations for context.

[165]: Zhang (2018), *The Physics of Gamma-Ray Bursts*

The internal shock scenario

The internal shock model was proposed in the 1990s [166–168]. It relies on a central engine emitting an unsteady outflow of variable velocity. As faster parts of the ejecta catch up with slower ones, shock waves form. These shocks convert kinetic energy of the outflow into plasma internal energy. Through turbulent magnetic fields around the shock front, particles can be accelerated *e.g.* by the Fermi mechanism. However, particle acceleration at mildly relativistic shocks is still poorly understood, and the regime is only recently been explored in Particle-In-Cell simulations (*e.g.* [169]).

In a simplified description, the outflow is often approximated as a series of plasma shells of finite width. Each light curve pulse/spike can then be attributed to an interaction between two of such shells. This way the variety of observed light curves and their short time variability can easily be explained.

[166]: Rees et al. (1994), "Unsteady outflow models for cosmological gamma-ray bursts"

[167]: Kobayashi et al. (1997), "Can internal shocks produce the variability in GRBs?"

[168]: Daigne et al. (1998), "Gamma-ray bursts from internal shocks in a relativistic wind: temporal and spectral properties"

[169]: Crumley et al. (2019), "Kinetic simulations of mildly relativistic shocks – I. Particle acceleration in high Mach number shocks"

The main criticism of the internal shock model is that of low energy conversion efficiency: In a typical setup, only about 10% of the fireball kinetic energy are dissipated. This means that the fireball is still very energetic when it produces the afterglow – which means that a bright afterglow signal incompatible with observations is expected.
The model will be introduced in more detail in Chapter 5.

Magnetic energy dissipation

The part of the jet energy stored in magnetic fields can be measured by the *magnetisation* σ. For a plasma of magnetic field B, mass density ρ and the Lorentz factor Γ it is defined as the ratio between Poynting flux and matter flux:

$$\sigma = \frac{F_\mathrm{B}}{F_\mathrm{matter}} = \frac{B^2}{4\pi\Gamma\rho c^2} = \frac{B'^2}{4\pi\rho' c^2}\,, \tag{4.2}$$

where primed quantities again refer to the comoving frame of the plasma. If the magnetisation is high ($\sigma \gtrsim 1$), magnetic fields carry the bulk of jet energy. In this case, magnetic energy dissipation through magnetic reconnection or current-driven instabilities may be significant. A range of models invoking magnetic reconnection have been proposed (among others [170, 171]. The exact mechanism of particle acceleration in those models is poorly understood. A combined magnetic reconnection and internal shock scenario that naturally explains the short time variability was presented in the ICMART model [172]. Here, subsequent collisions of magnetised plasma shells distort the plasma until magnetic reconnection is enabled at large distances from the central engine.

[170]: Giannios et al. (2005), "Poynting - flux powered GRB outflows: Spectral predictions"
[171]: McKinney et al. (2012), "A Reconnection Switch to Trigger Gamma-Ray Burst Jet Dissipation"
[172]: Zhang et al. (2011), "The Internal-Collision-Induced Magnetic Reconnection and Turbulence (ICMART) Model of Gamma-Ray Bursts"

Neutron collisions

Various progenitor scenarios predict a neutron-rich outflow. Although initially in equilibrium through inelastic collisions, protons and neutrons decouple at a certain distance to the central engine. If this happens during the fireball acceleration phase (thus before reaching the coasting phase of final Γ), protons and neutrons end up travelling at different speeds because neutrons are no longer accelerated with the plasma. This difference in velocity enables proton-neutron collisions in which pions are produced. The leptons generated through pion decays have typical Lorentz factors of $\gamma_e \sim 300$.
As the cross-section for proton-neutron collisions is smaller than the Thomson cross-section, the decoupling radius of protons and neutrons is below the photosphere.

Results from (M)HD simulations

A series of 3D simulations of intermittent and continuous jets with no/low magnetisation propagating through a stellar envelope have been performed in [173–176]. From jet interaction with this surrounding material, a cocoon of shocked stellar and jet material forms around the jet edges. In all scenarios, a photospheric model was assumed for the prompt phase (for more details on this mechanism see Section 4.4).

[173]: Gottlieb et al. (2019), "High efficiency photospheric emission entailed by formation of a collimation shock in gamma-ray bursts"
[174]: Gottlieb et al. (2020), "The structure of weakly magnetized γ-ray burst jets"
[175]: Gottlieb et al. (2020), "Intermittent hydrodynamic jets in collapsars do not produce GRBs"
[176]: Gottlieb et al. (2021), "Intermittent mildly magnetized jets as the source of GRBs"

Table 4.1: Overview table (M)HD simulations of GRB jets, reproduced from [176]. Findings in contradiction with observations are marked red. For each setup, we list the source of baryon mixing (head-like or at the Jet-Cocoon-Interface boundary), the source of temporal variability (due to turbulences in the mixing regions or from an intermittent engine), the variability timescale, the efficiency of converting the jet energy into radiation and if dissipative processes are available that could broaden the thermal spectrum such that it is compatible with observations.

Jet type Reference	Continuous HD [173]	Continuous MHD [174]	Intermittent HD [175]	Intermittent MHD [176]
Mixing source (head/boundary)	both (boundary dominates)	stable	head	head
Variability source (mixing/engine)	mixing	none	both	engine
Variability timescales	$\sim$ ms	none	set by engine & mixing	set by engine
Efficiency	high	high	$\lesssim 1\%$	high
Spectrum broadening by shocks	unlikely	no	no	possible

They find that a substantial mixing of jet and cocoon material increases the baryonic loading in the boundary of the Jet-Cocoon-Interface (JCI). The turbulent structures responsible for this mixing may produce efficient temporally variable signatures in hydrodynamic jets [173]. For intermittent hydrodynamic jets, the mixing is strongly enhanced through additional mixing regions at the head of each 'active' period. This type of mixing will be called 'head'-like in the following. In their view, the resulting heavy baryon loading likely inhibits any photospheric gamma-ray production mechanism [175]. We point out that this limitation may be overcome by hadronic contributions to the photon emission – although the details of a possible baryon acceleration close to the photosphere are unclear. Overall, mixing with the cocoon is suppressed for mildly magnetised jets but can occur at the heads of active periods for intermittent jets [176]. For continuous, magnetised jets there is thus no source of short-time variability [174].

As mentioned above, photospheric emission was considered as source of the prompt gamma-ray signal. In order to reproduce observed spectra, some additional energy dissipation process that can broaden the spectra such that they deviate from pure thermal ones is necessary. One possibility are shocks which were only found for intermittent, magnetised jets. [176]

The basic findings are summarised in Table 4.1, where we mark features in conflict with observations red. Overall, intermittent, mildly magnetised jets are the ones that have least trouble in explaining the prompt emission.

For highly magnetised jets, [158] find that small-scale internal kink instabilities could dissipate half of the magnetic energy into heat.

[158]: Bromberg et al. (2016), "Relativistic MHD simulations of core-collapse GRB jets: 3D instabilities and magnetic dissipation"

4.4 Prompt phase radiation models

After the plasma particles are heated and/or accelerated due to the energy dissipation process, they generate the prompt emission.

Overall, the radiation processes may operate either in *optically thin* or in *optically thick* regime, depending on whether the optical depth to Thomson scatterings $\tau_{\mathrm{TH}} = \sigma_{\mathrm{T}} n_e l$ (with the number density of electrons n_e and the path length l) is below or above unity. Following [177], in GRBs the τ_{TH} experienced by photons at a distance R propagating until infinity is given by

[177]: Beloborodov et al. (2017), "Photospheric Emission of Gamma-Ray Bursts"

$$\tau_{\mathrm{TH}} = \frac{Z_{\pm} \dot{M}_p \sigma_{\mathrm{T}}}{4\pi R \Gamma^2 m_p c} , \tag{4.3}$$

where Γ the Lorentz factor of the outflow, $\dot{M}_p$ the proton mass outflow rate and $Z_{\pm}$ the number of electrons and positrons per proton.

Optically thin regime

In the optically thin regime, populations of accelerated non-thermal particles participate in the interactions introduced in the last chapter.

We first consider a primary population of electrons characterised by a minimum Lorentz factor $\gamma_{e,\mathrm{min}}$ and power-law slope $-p_e$. Motivated by GRB observed spectra, we assume $p_e > 2$.
For simplicity, we only account for synchrotron and adiabatic cooling due to the expansion of the plasma (with corresponding cooling timescale $t'_{\mathrm{ex}} = \frac{R}{\Gamma c}$). At the *critical Lorentz factor* $\gamma_{e,\mathrm{c}}$, the synchrotron and adiabatic cooling timescales of electrons are equal:

$$\gamma_{e,\mathrm{c}} \equiv \frac{6\pi m_e c}{\sigma_t B'^2 t'_{\mathrm{ex}}} . \tag{4.4}$$

In the following, we denote the characteristic synchrotron frequencies in the observers frame of electrons with Lorentz factors $\gamma_{e,\mathrm{min}}$ ($\gamma_{e,\mathrm{c}}$) as ν_{m} (ν_{c}). Additionally, ν_a is the synchrotron self-absorption frequency and will in the following assume that $\nu_a < \min(\nu_c, \nu_m)$. In this case, the synchrotron-self-absorption spectrum scales as ν^2 [178].
We will describe the spectra as a series of power-laws representing different regimes. Note that in reality the reported slopes are only reached at a certain distance from the break frequencies, as the breaks are smooth. Two regimes were identified in [179] which we connect to the findings of Chapter 3:

[178]: Piran (2004), "The physics of gamma-ray bursts"

[179]: Sari et al. (1998), "Spectra and light curves of gamma-ray burst afterglows"

Fast cooling regime: $\gamma_{e,\mathrm{c}} < \gamma_{e,\mathrm{min}}$
At the lowest energies, synchrotron self-absorption results in a spectrum proportional to ν^2. Between the synchrotron absorption break at ν_a and ν_c the spectrum in this range is just the sum of all synchrotron tails of electrons and thus a power-law $\propto \nu^{1/3}$. Between $\gamma_{e,\mathrm{c}}$ and $\gamma_{e,\mathrm{min}}$, an

electron distribution of slope $-p_e = -2$ is formed (as synchrotron cooling scales as γ^2, see Eq. 3.2). This distribution produces a photon spectrum of $\alpha = -(2-1)/2 = -1/2$. Above $\gamma_{e,\min}$, the initial electron distribution is modified from spectral slope $-p_e$ to $-p_e + 1$ due to synchrotron cooling (see Eq. 3.3). The corresponding photon spectrum has spectral slope $\alpha = -(p_e + 1 - 1)/2 = -p_e/2$.
Overall, the spectrum is thus approximated by

$$\frac{F_\nu}{F_{\nu,\max}} = \begin{cases} (\frac{\nu_a}{\nu_c})^{1/3}(\frac{\nu}{\nu_a})^2 & , \nu < \nu_a \\ (\frac{\nu}{\nu_c})^{1/3} & , \nu_a < \nu < \nu_c \\ (\frac{\nu}{\nu_c})^{-1/2} & , \nu_c < \nu < \nu_m \\ (\frac{\nu_m}{\nu_c})^{-1/2}(\frac{\nu}{\nu_m})^{-p/2} & , \nu_m < \nu \end{cases} . \tag{4.5}$$

This F_ν spectrum is illustrated in Figure 4.5 (with the corresponding SED νF_ν in the upper panel), assuming an injected electron distribution of slope $-p_e = -2.5$.
In this regime, all primary electrons efficiently cool via synchrotron cooling. The spectrum F_ν peaks at ν_c, whereas the peak of the SED (that is the peak of νF_ν) is at ν_m.

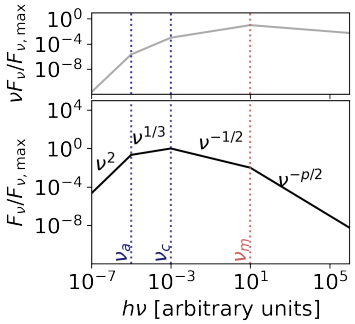

Figure 4.5: Spectrum F_ν (lower panel) and νF_ν (upper panel) for the synchrotron spectrum of a fast-cooling electron distribution with initial power-law index $-p_e = -2.5$.

Slow cooling regime: $\gamma_{e,c} > \gamma_{e,\min}$
Again, at the lowest energies the spectrum is defined by synchrotron self-absorption and the synchrotron tail of all electrons. Between $\gamma_{e,\min}$ and $\gamma_{e,c}$, electrons cool predominantly via adiabatic cooling which leaves the power-law index of electrons unchanged. The synchrotron spectrum thus has slope $\alpha = -(p_e - 1)/2$. Above $\gamma_{e,c}$, synchrotron cooling is more efficient than adiabatic cooling and the electron power-law index is increased by one. The synchrotron spectral index is then again given by $\alpha = -p_e/2$.
The approximate spectrum thus reads

$$\frac{F_\nu}{F_{\nu,\max}} = \begin{cases} (\frac{\nu_a}{\nu_m})^{1/3}(\frac{\nu}{\nu_a})^2 & , \nu < \nu_a \\ (\frac{\nu}{\nu_m})^{1/3} & , \nu_a < \nu < \nu_m \\ (\frac{\nu}{\nu_m})^{-(p-1)/2} & , \nu_m < \nu < \nu_c \\ (\frac{\nu_c}{\nu_m})^{-(p-1)/2}(\frac{\nu}{\nu_c})^{-p/2} & , \nu_c < \nu \end{cases} . \tag{4.6}$$

We illustrate this F_ν spectrum in Figure 4.6 (with the corresponding SED νF_ν in the upper panel), assuming an injected electron distribution of slope $-p_e = -2.5$.
In this regime, only primary electrons above $\gamma_{e,c}$ efficiently cool via synchrotron cooling. Hence, while the flux F_ν peaks at ν_m, the peak of νF_ν is at ν_c.

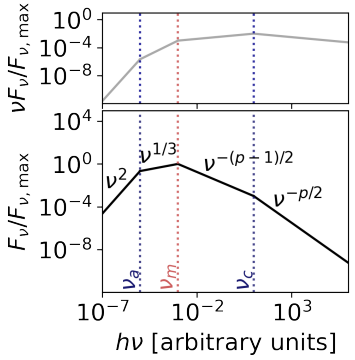

Figure 4.6: Spectrum F_ν (lower panel) and νF_ν (upper panel) for the synchrotron spectrum of a slow-cooling electron distribution with initial power-law index $-p = -2.5$.

Open issues

The long-standing criticism on a synchrotron origin of the observed spectra mostly revolves around the photon index α (of the power-law index of the photon spectrum F_ν/ν) below ν_m: With pure synchrotron it is only possible to achieve $\alpha = -3/2$ or $\alpha = 2/3$. This was pointed out to be in conflict with observations already early on (*e.g.* [180, 181]. Also current GRB catalogues find values of α that differ from pure synchrotron predictions [161, 182]). On the other hand, [183] argue that it is indeed possible to fit the large majority of burst with synchrotron spectra.
Further, for the slow-cooling regime, the radiative efficiency (defined as $f_{\rm rad} = u_\gamma/u_e$, energy density of photons divided by the energy density of injected non-thermal electrons) is low. This is especially problematic for models like the internal shock scenario which suffer from a low dissipation efficiency. The problem may be alleviated by the *marginally fast cooling regime* [184], where $\gamma_{e,\rm min} \simeq \gamma_{e,c}$. Here, low-energy spectral slopes of $-1 < \alpha < -2/3$ can be realised despite a moderate radiative efficiency. This scenario is supported by [185] who found a small ratio of the spectral peak energy and the cooling break frequency when fitting the sample of prompt GRB spectra observed down to ~ 0.5 keV energies by two low-energy power laws. It has further been explored in [186], with a focus on optical fluxes.

An additional criticism arises from the position of the synchrotron peak which in the observers frame is proportional to $\Gamma B' \gamma^2_{e,\rm min}$. First, with B', Γ and $\gamma_{e,\rm min}$ varying between different GRBs, a large variety of peak energies can be realised. This is in contradiction to the observed narrow distribution of $E_{\rm peak}$. Second, if in simple internal shock models all electrons are assumed to be accelerated, $\gamma_{e,\rm min}$ is relatively low. This results in low $E_{\rm peak}$ incompatible with observations. A possible solution is to set the number fraction of accelerated electrons low, such that high $\gamma_{e,\rm min}$ and high peak energies can be realised. Overall, fine-tuning of parameters is thus required to reproduce the observed $E_{\rm peak}$.

Beyond synchrotron radiation

For a full calculation of the spectra, additional processes should be accounted for:

1. *Thermal radiation* of particles that are not accelerated to high-energy power laws may contribute at lower energies.
2. *Inverse Compton radiation* introduces a second component at high energies. Additionally, the spectral shape below the peak may be affected by inverse Compton scatterings in Klein-Nishina regime resulting in harder low energy spectral slopes [184, 187, 188]: If electrons below the peak cool predominantly through Compton scatterings in Klein-Nishina regime, their cooling rate will not scale as γ_e^2. This reflects in the electron spectral slope and, consequently, in the synchrotron power-law index of these electrons.

[180]: Preece et al. (2002), "On the Consistency of Gamma-Ray Burst Spectral Indices with the Synchrotron Shock Model"
[181]: Ghisellini et al. (2000), "Constraints on the emission mechanisms of gamma-ray bursts"
[161]: Poolakkil et al. (2021), "The Fermi-GBM Gamma-Ray Burst Spectral Catalog: 10 yr of Data"
[182]: Lien et al. (2016), "The Third Swift Burst Alert Telescope Gamma-Ray Burst Catalog"
[183]: Burgess et al. (2019), "Gamma-ray bursts as cool synchrotron sources"
[184]: Daigne et al. (2011), "Reconciling observed GRB prompt spectra with synchrotron radiation ?"
[185]: Oganesyan et al. (2017), "Detection of Low-energy Breaks in Gamma-Ray Burst Prompt Emission Spectra"
[186]: Oganesyan et al. (2019), "Prompt optical emission as a signature of synchrotron radiation in gamma-ray bursts"

[184]: Daigne et al. (2011), "Reconciling observed GRB prompt spectra with synchrotron radiation ?"
[187]: Nakar et al. (2009), "Klein-Nishina effects on Synchrotron and Synchrotron self-Compton spectrum"
[188]: Duran et al. (2012), "Inverse Compton cooling in Klein-Nishina regime and GRB prompt spectrum"

3. *$\gamma\gamma$-annihilation* is possible for high photon densities. The secondary lepton pairs are expected to contribute via synchrotron radiation at low energies (and therefore may reshape the spectrum below the synchrotron peak) and inverse Compton radiation (at intermediate energies) [189, 190].

[189]: Asano et al. (2007), "Prompt GeV-TeV Emission of Gamma-Ray Bursts Due to High-Energy Protons, Muons and Electron-Positron Pairs"
[190]: Asano et al. (2011), "Spectral-Temporal Simulations of Internal Dissipation Models of Gamma-Ray Bursts"

Hadronic models

Three categories of hadronic scenarios complement the leptonic ones: *(1)* Leptonic models where hadrons are co-accelerated, *(2)* proton synchrotron models and *(3)* hadronic supercriticality models.
In *(1)*, the bulk of the radiation is still explained by leptonic processes. As a result, the hadronic emission is required to not outshine the emission of primary leptons. This can put constraints on the energy transferred to non-thermal baryons (see [191] and Chapter 7). Contrary to this, the full spectrum is dominated by protons in *(2)* where the peak is generated by proton synchrotron radiation [192]. Recently, [193] have shown that marginally fast cooling proton scenario is likely to be in tension with optical constraints unless the outflow has very high Lorentz factors ($\Gamma \gtrsim 1000$). Finally, in *(3)* a hadronic feedback loop in the supercritical regime (see Section 3.4) enhances the photon luminosities. This was proposed as a potential mechanism powering GRB emission in [144]. Corresponding light curves were recently explored in [194].

[191]: Asano et al. (2009), "Prompt High-Energy Emission from Proton-Dominated Gamma-Ray Bursts"
[192]: Ghisellini et al. (2020), "Proton–synchrotron as the radiation mechanism of the prompt emission of gamma-ray bursts?"
[193]: Florou et al. (2021), "A marginally fast-cooling proton–synchrotron model for prompt GRBs"
[144]: Petropoulou et al. (2014), "Hadronic supercriticality as a trigger for γ-ray burst emission"
[194]: Florou et al. (2021), "An expanding hadronic supercritical model for γ-ray burst emission"

Optically thick regime

In *photospheric models*, the observed spectrum originates from the point where the plasma becomes optically thin. In the most simple scenarios, this radiation is purely thermal. Although thermal components should accompany the non-thermal ones [195], they cannot reproduce Band-like spectra. Thus, dissipative processes below or at the photosphere are required to broaden the spectra. A range of mechanisms have been proposed (for a complete list see [165, 177] and references therein):
Internal shocks just below the photosphere could heat electrons contained in the plasma (either directly or through hadronic cascades [196]). *Magnetic dissipation* through reconnection is possible for a striped-wind-like magnetic field configuration as expected for magnetars. The exact formalism and corresponding photon spectrum has been presented *e.g.* in [197, 198]. As outlined above, *neutron collisions* naturally occur below the photosphere if the outflow is neutron-rich. The secondary lepton pairs of those collisions may produce a spectrum compatible with GRB observations [199, 200]. Finally, *collimation shocks* are induced as the jet breaks out of the stellar material, heating the material and contributing to an efficient photosphere [201, 202].
All these mechanisms may heat the plasma and accelerate plasma particles. For the latter, it is important to keep in mind that shocks operating in optically thick regime are radiation mediated, and particle acceleration

[195]: Pe'er et al. (2017), "Photospheric Emission in Gamma-Ray Bursts"
[165]: Zhang (2018), *The Physics of Gamma-Ray Bursts*
[177]: Beloborodov et al. (2017), "Photospheric Emission of Gamma-Ray Bursts"
[196]: Murase et al. (2012), "The Role of Stochastic Acceleration in the Prompt Emission of Gamma-Ray Bursts: Application to Hadronic Injection"
[197]: Drenkhahn et al. (2002), "Efficient acceleration and radiation in Poynting flux powered GRB outflows"
[198]: Giannios et al. (2007), "Spectral and timing properties of a dissipative GRB photosphere"
[199]: Beloborodov (2010), "Collisional mechanism for GRB emission"
[200]: Vurm et al. (2011), "Gamma-ray bursts from magnetized collisionally-heated jets"
[201]: Lazzati et al. (2009), "Very high efficiency photospheric emission in long duration gamma-ray bursts"
[202]: Lazzati et al. (2013), "Photospheric emission as the dominant radiation mechanism in long-duration gamma-ray bursts"

may thus differ from the classical Fermi picture [177]. Nevertheless, the spectrum may be broadened through bulk Comptonisation of photons or energetic secondary leptons created in hadronic interactions. Additional broadening may come from geometrical effects [203, 204].

Overall, dissipative photosphere models usually explain well the narrow distribution of peak energies as they have less free parameters. Also, they can account for the hard spectra (with large α below the peak) of some GRBs. This was recently shown in a direct fit in [205].
On the other hand, very soft α are hard to explain. Finally, also these models only work in a certain region of the parameter space and thus require some fine-tuning of jet parameters.

[203]: Pe'er (2008), "Temporal Evolution Of Thermal Emission From Relativistically Expanding Plasma"
[204]: Lundman et al. (2013), "A theory of photospheric emission from collimated outflows"
[205]: Samuelsson et al. (2021), "An efficient method for fitting radiation-mediated shocks to gamma-ray burst data: The Kompaneets RMS approximation"

Discussion

The validity of a model is often evaluated through its compatibility with either Band-function or cut-off power-law fits reported in GRB catalogues. However, those fits are purely empirical and cannot capture more complex spectral shapes. Indeed, models that invoke a thermal component or a second break energy below the peak have been proposed to better explain data (among others [206, 207]). Moreover, the spectral slopes of the fits are very sensitive to the functional fitting range (and the position of E_{peak} in the latter) which is informed by the sensitivity of the experiments.
For those reasons, several authors have instead argued that a direct comparison of forward-folded model and data is required. Indeed, if this is performed, the 'physical' models often explain data better than anticipated [183].

[206]: Ryde (2005), "Is thermal emission in gamma-ray bursts ubiquitous?"
[207]: Toffano et al. (2021), "The slope of the low energy spectrum of Gamma-Ray Burst prompt emission"

[183]: Burgess et al. (2019), "Gamma-ray bursts as cool synchrotron sources"

Additionally, it might just be the case that 'one size fits all' does not work for GRBs and depending on the properties of the individual event, different mechanisms are at work. This has been explored *e.g.* in [208], who find five clusters of GRBs in the GBM sample, out of which they suggest three to be dominated by photospheric emission and two by synchrotron radiation.

[208]: Acuner et al. (2018), "Clustering of gamma-ray burst types in the Fermi-GBM catalogue: indications of photosphere and synchrotron emissions during the prompt phase"

4.5 GRBs as UHECR and HE neutrino sources

The possibility of UHECR originating from GRBs was first explored in [13], who argued that GRB internal shocks may fulfil the Hillas criterium as well as provide the energy budget to power the UHECR flux. Equally focussing on cosmic rays of the highest energies, this idea was further explored in publications such as [17, 209–211]. A dedicated fit to the UHECR spectrum and composition was presented in [212], who also

[13]: Waxman (1995), "Cosmological gamma-ray bursts and the highest energy cosmic rays"
[17]: Biehl et al. (2018), "Cosmic-Ray and Neutrino Emission from Gamma-Ray Bursts with a Nuclear Cascade"
[209]: Wang et al. (2008), "On the Origin and Survival of UHE Cosmic-Ray Nuclei in GRBs and Hypernovae"
[210]: Murase et al. (2008), "High-energy cosmic-ray nuclei from high- and low-luminosity gamma-ray bursts and implications for multi-messenger astronomy"
[211]: Metzger et al. (2011), "Heavy Nuclei Synthesized in Gamma-Ray Burst Outflows as the Source of UHECRs"
[212]: Globus et al. (2015), "UHECR acceleration at GRB internal shocks"

compared to multi-messenger constraints such as the *Fermi*-LAT diffusive gamma-ray background and IceCube neutrino limits.

Indeed, it was pointed out early that baryon-loaded GRB jets naturally imply the production of secondary neutrinos [14]. However, as of now there has been no association of an IceCube detected HE neutrino with a known GRB. The resulting neutrino limits strongly constrain the baryonic loading in the most simple models [15, 16]. [17] reported that an UHECR fit from GRBs may still be viable in the parameter-space region of low luminosities or large radii where the neutrino production efficiency is low. This regime could be realised for the sub-class of low-luminosity GRBs (see Chapter 6) or in magnetic reconnection scenarios. Further, [18] showed that multi-zone models decouple the production regions of different messengers along the jet: While (HE) neutrinos originate from close to the source, UHECR are produced at intermediate and gamma-rays at large radii. Indeed, they find that multi-zone models generally predict lower neutrino fluxes and may still allow for a large amounts of energy transferred to non-thermal baryons.

[14]: Waxman et al. (1997), "High-energy neutrinos from cosmological gamma-ray burst fireballs"

[15]: Aartsen et al. (2016), "An All-Sky Search for Three Flavors of Neutrinos from Gamma-Ray Bursts with the IceCube Neutrino Observatory"

[16]: Aartsen et al. (2017), "Extending the search for muon neutrinos coincident with gamma-ray bursts in IceCube data"

[18]: Bustamante et al. (2017), "Multi-messenger light curves from gamma-ray bursts in the internal shock model"

Further constraints may come from the photon spectra: For example [191, 213] conclude that for high baryonic loadings the photon spectra may be distorted by the secondary particle cascade initiated from hadronic interactions. We point out that their models assume a single radiation zone representative for the complete burst and point to Chapter 7 for a more in-depth discussion.

[191]: Asano et al. (2009), "Prompt High-Energy Emission from Proton-Dominated Gamma-Ray Bursts"

[213]: Petropoulou (2014), "The role of hadronic cascades in GRB models of efficient neutrino production"

Overall, GRBs are thus not unambiguously ruled out as UHECR sources; the multi-messenger constraints are however fairly strong.

GRB internal shock models in a multi-messenger context

5

5.1 Two internal-shock formalisms 55
5.2 Modified collision dynamics and impact on multi-messenger predictions 61
5.3 UHECR fit for different GRB engine realisations . . 64

Due to the large amounts of energy they release, GRBs are among the oldest UHECR source candidates. However, the absence of IceCube high-energy neutrinos that could be associated with detected GRBs challenges the most simple UHECR-GRB scenarios. In this chapter, we introduce multi-zone internal shock models that may help to reconcile GRBs as UHECR sources with current neutrino limits.

For this we first discuss two different formalisms that were both developed in the mid 90s in Section 5.1. The section further connects these descriptions to our radiation modelling procedure. In Section 5.2 we introduce alternative collision models and their impact on multi-messenger predictions, based on [214]. During my master thesis, I implemented modified collision dynamics in our fireball code. This was extended during my PhD by examining a sample of 100 (random) initial Lorentz factor distributions of the outflow. Further, we verified the feasibility of modified collision dynamics through shock-tube simulations with the (RM)HD code Pluto, where I implemented a simple energy dissipation mechanism. Finally, in Section 5.3 we review the results of our fit to the UHECR spectrum and composition performed in a systematic scan over different initial jet Lorentz factor distributions ('engine realisations'), presented in [215]. Here, I contributed to the model development and analysis of the results.

[214]: Rudolph et al. (2020), "Impact of the Collision Model on the Multi-messenger Emission from Gamma-Ray Burst Internal Shocks"

[215]: Heinze et al. (2020), "Systematic parameter space study for the UHECR origin from GRBs in models with multiple internal shocks"

5.1 Two internal-shock formalisms

The idea of an unsteady outflow in which interactions of fast and slow parts release energy through collisionless shocks was introduced in [166]. The exact formalism describing the outflow as a succession of discrete 'shells' (or 'layers') was described around at the same time by [167, 168]. Although in principle following the same idea, subtle differences between the two models remain. Here we will introduce the main ideas and formulas and explain how they lead to a full fireball evolution and can be used to calculate the corresponding radiation.

[166]: Rees et al. (1994), "Unsteady outflow models for cosmological gamma-ray bursts"

[167]: Kobayashi et al. (1997), "Can internal shocks produce the variability in GRBs?"

[168]: Daigne et al. (1998), "Gamma-ray bursts from internal shocks in a relativistic wind: temporal and spectral properties"

The Kobayashi, Piran and Sari model

In [167], an engine with active ('up') and inactive ('down') times (of duration $t_{\rm up}$ and $t_{\rm down}$, respectively) emits a series of discrete plasma shells. The initial shells thus have widths $\Delta = ct_{\rm up}$ and are separated by distances $d = ct_{\rm down}$ (all in the source frame). Their initial Lorentz

[167]: Kobayashi et al. (1997), "Can internal shocks produce the variability in GRBs?"

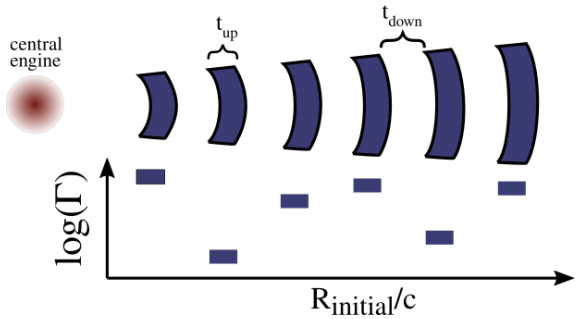

Figure 5.1: Setup of the internal shock model as proposed by [167]: The jet is approximated as a series of plasma shells (released during engine 'up' times t_{up} and separated by engine 'down' times t_{down}). For the initial setup (here represented as function of initial Radius R_{initial} divided by c) shell Lorentz factors are often assumed to be distributed randomly in log-space.

factors Γ are often assumed to follow a random distribution in log or normal space. Such an initial setup is illustrated in Figure 5.1.
Throughout the evolution of the system, shells are characterised by their width Δ, mass m and Lorentz factor Γ. At a distance R from the central engine, the comoving shell volume is given by $V' = 4\pi R^2 \Delta \cdot \Gamma$ (where primed quantities again refer to the comoving frame). The initial setup is often chosen such that all shells share the same mass, energy or mass density.

As the shells propagate, fast shells catch up with slower ones. A collision between a fast (subscript f) and a slow (s) shell at a radius R_{C} creates a new merged (m) shell that continues in the fireball.
(a) The merged shell
From momentum and mass conservation the merged shell mass and Lorentz factor are calculated as

$$m_m = m_f + m_s \,, \tag{5.1}$$

$$\Gamma_m = \sqrt{\frac{m_f \Gamma_f + m_s \Gamma_s}{m_f/\Gamma_f + m_s/\Gamma_s}} \,. \tag{5.2}$$

(b) During the collision
From energy conservation we can calculate the internal energy produced in the collision process as

$$E_{\mathrm{int}} = m_f \Gamma_f + m_s \Gamma_s - m_m \Gamma_m \,. \tag{5.3}$$

During the encounter, a forward and a reverse shock (FS and RS) develop that propagate through the slow and fast shell respectively. Their shock speeds can be calculated as

$$\Gamma_{\mathrm{FS(RS)}} \simeq \Gamma_m \sqrt{\frac{\Gamma_{s(f)} + 2\Gamma_m}{2\Gamma_{s(f)} + \Gamma_m}} \,. \tag{5.4}$$

With the corresponding velocities $\beta_{\mathrm{FS(RS)}} \simeq \sqrt{1 - \Gamma_{\mathrm{FS(RS)}}^{-2}}$ one can calculate the merged shell width after the compression of the two shells due to the

hydrodynamic shocks:

$$\Delta_m = \Delta_s \frac{\beta_{\rm FS} - \beta_m}{\beta_{\rm FS} - \beta_s} + \Delta_f \frac{\beta_m - \beta_{\rm RS}}{\beta_f - \beta_{\rm RS}} \,. \tag{5.5}$$

This allows also to calculate the (comoving) density of the shocked shell as

$$\rho'_m = \frac{m_m}{4\pi R_{\rm C} \Delta_m \Gamma_m} \,. \tag{5.6}$$

Additionally, the shock crossing times are given by

$$t_{\rm RS} = \frac{\Delta_f}{c(\beta_f - \beta_{\rm RS})} \,, \tag{5.7}$$

$$t_{\rm FS} = \frac{\Delta_s}{c(\beta_s - \beta_{\rm FS})} \,. \tag{5.8}$$

At both shock fronts particles are accelerated and radiate. Particle emission occurs over the shock crossing time of the forward shock:

$$\delta t_{\rm em} = t_{\rm FS} \,. \tag{5.9}$$

Two timescales govern the plasma evolution: The escape time for free streaming particles $t'_{\rm esc}$ and the adiabatic cooling timescale due to the expansion of the system $t'_{\rm ad}$. They are given by

$$t'_{\rm esc} = \frac{\Gamma \Delta_m}{c} \,, \tag{5.10}$$

$$t'_{\rm ad} = \frac{R_{\rm C}}{c\Gamma} \,. \tag{5.11}$$

The Daigne and Mochkovitch model

In contrast to this discrete shell model, [168] assume a steady outflow ('wind') that is discretised as a series of layers. Each layer (from here on also called 'shell') has the width $\Delta = c\,{\rm d}\tau$, where ${\rm d}\tau$ is the discretisation time of the engine active time $t_{\rm eng}$ (for illustration see Figure 5.2). The initial Lorentz factors are usually assumed to follow a smooth distribution connecting fast and slow parts of the outflow. The model aims at capturing the evolution of plasma properties (such as mass and energy density and Lorentz factor) as shock waves pass through the outflow and was validated in hydrodynamic simulations in [216].

[168]: Daigne et al. (1998), "Gamma-ray bursts from internal shocks in a relativistic wind: temporal and spectral properties"

[216]: Daigne et al. (2000), "Gamma-ray bursts from internal shocks in a relativistic wind: an hydrodynamical study"

(a) The merged shell

Again, a merged shell is formed in a collision between a fast and a slow shell. The merged shell Lorentz factor and mass are described by the same Equations 5.1 and 5.2.

(b) During the collision

For calculating the plasma properties during the collision it is assumed

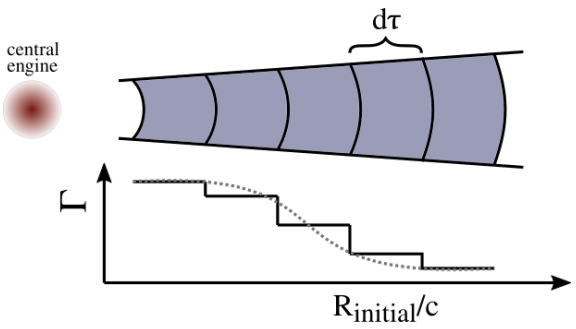

Figure 5.2: Setup of the internal shock model as proposed by [168]: A steady wind of varying Lorentz factor is discretised as a series of shells emitted during time intervals $\mathrm{d}\tau$. We again display the initial Lorentz factor distribution as function of initial radius R_{initial} divided by c.

that most of the energy is released as the less massive of the two shells sweeps up a mass comparable to its own. Then the Lorentz factor of the plasma Γ_r and the internal energy E_{int} simplify to

$$\Gamma_r = \sqrt{\Gamma_s \Gamma_f}\,, \tag{5.12}$$

$$E_{\mathrm{int}} = m(\Gamma_s + \Gamma_f - 2\Gamma_r)\,,\ m = \min(m_s, m_f)\,. \tag{5.13}$$

The total mass of the shocked plasma is thus

$$M = 2m\,,\ m = \min(m_s, m_f)\,. \tag{5.14}$$

Assuming that all internal energy is dissipated, it is conventional to further define the comoving dissipated energy per unit mass as

$$\epsilon'_{\mathrm{diss}} = \frac{E'_{\mathrm{int}}}{M} \simeq \frac{(\sqrt{\kappa}-1)^2}{2\sqrt{\kappa}} c^2\,, \tag{5.15}$$

where $\kappa = \Gamma_f/\Gamma_s$. The comoving plasma density is often re-expressed as a function of wind luminosity L_{wind} ejected by the central engine

$$\rho' = \frac{M}{V'} \simeq \frac{L_{\mathrm{wind}}}{4\pi R_{\mathrm{C}}^2 \Gamma_r^2 c^3}\,, \tag{5.16}$$

where it was assumed that the comoving volume is given by $V' = 4\pi R_{\mathrm{C}}^2 \Gamma_r \mathrm{d}\tau c$ and $M = \frac{E}{\Gamma c^2} \simeq \frac{L_{\mathrm{wind}}\mathrm{d}\tau}{\Gamma_r c^2}$. The statements above are valid for a discretisation scheme in which the contrast of Lorentz factors and masses between neighbouring shells is small. In Appendix B.1 we show that the results are independent of the discretisation $\mathrm{d}\tau$ as long as the number of initial shells is large enough to adequately capture the evolution of plasma parameters. In this model, the shell width is an artificial parameter resulting from the discretisation and hence does not represent a physical timescale. Instead, the characteristic timescale of the system is identified as the shell expansion time

$$t'_{\mathrm{ex}} = \frac{R_{\mathrm{C}}}{\Gamma_r c}\,. \tag{5.17}$$

This timescale can also be identified as potential escape time for free

	Kobayashi, Piran and Sari		Daigne and Mochkovitch	
Collision parameter	Symbol	Equation	Symbol	Equation
Mass m_C	m_m	Eq. 5.1	M	Eq. 5.14
Lorentz factor Γ_C	Γ_m	Eq. 5.2	Γ_r	Eq. 5.12
Mass density ρ'	ρ'_m	Eq. 5.6	ρ'	Eq. 5.16
Dissipated energy $E_{\rm diss}$	$E_{\rm int}$	Eq. 5.3	$E_{\rm int}$	Eq. 5.13
Free-streaming timescale $t'_{\rm esc}$	$t'_{\rm esc}$	Eq. 5.10	$t'_{\rm ex}$	Eq. 5.17
Adiabatic cooling time $t'_{\rm ad}$	$t'_{\rm ad}$	Eq. 5.11	$t'_{\rm ex}$	Eq. 5.17

Table 5.1: Conversion Table for collision properties for the Kobayashi, Piran and Sari [167]/ Daigne and Mochkovitch [168] models. The plasma during a collision is characterised by its mass m_C, Lorentz factor Γ_C and mass density ρ' and may be heated by the dissipated energy $E_{\rm diss}$. The evolution of the plasma is further governed by the free-streaming timescale $t'_{\rm esc}$ (that is also the dynamic timescale of the system $t'_{\rm dyn}$) and the adiabatic cooling time $t'_{\rm ad}$.

streaming particles.

The complete fireball evolution and application to radiation modeling

In both models, the evolution of a system of shells is fully determined from the configuration of initial shells. In the end, the fireball is represented as a set of collisions and the overall fireball emission is obtained by adding the contributions of all single collisions.
A collision occurring at time t_C in the source frame is characterised by its radius R_C, Lorentz factor Γ_C, dissipated energy $E_{\rm diss}$, mass m_C and mass density ρ'. Two characteristic timescales govern the system: The escape time for free-streaming particles ($t'_{\rm esc}$, that we also identify as the dynamic time of the system $t'_{\rm dyn}$) and the adiabatic cooling time ($t'_{\rm ad}$). Table 5.1 summarises how these quantities can be obtained in the two models introduced above; we will from here on use unified symbols while referring to the Table for conversion from single models. For a source located at redshift z the, a collision occurring at t_C, R_C starts to be observed at

$$T_{\rm obs} = (1+z)(t_C - \frac{R_C}{c})\,. \tag{5.18}$$

For single-collision radiation calculations it is useful to define the comoving energy density of the shocked plasma as

$$u'_{\rm E',diss} \equiv \frac{\rho' E'_{\rm diss}}{m_C}\,. \tag{5.19}$$

Conditions in the shocked plasma

In ignorance of the complicated reality of (mildly) relativistic shocks, the physical conditions in the shocked plasma are often described by the *microphysics parameters*:

- ϵ the fraction of energy transferred to different particle species and the magnetic field B.
  For a comoving volume V', the magnetic field can be calculated from ϵ_B as
  $$B' = \sqrt{8\pi\epsilon_B u'_{\rm E',diss}}\,. \tag{5.20}$$

With the fraction of energy going into non-thermal cosmic rays (ϵ_{CR}) and electrons (ϵ_e) it is often convenient to define the *baryonic loading* as

$$f_p = \epsilon_{CR}/\epsilon_e \,. \tag{5.21}$$

ζ the number fraction of accelerated particles (per particle species).

p the power-law slope of the accelerated particle distributions (per particle species).

Non-thermal particle distributions

From the conditions in the shocked plasma, the characteristics of non-thermal (power-law) particle distributions can be calculated. They are characterised by the maximal/minimal particle Lorentz factors ($\gamma_{i,\mathrm{min}}$ and $\gamma_{i,\mathrm{max}}$) and power-law slope ($-p_i$) and the time over which energetic particles are injected, t'_{inject}.

For each particle species i, the number fraction of accelerated particles and the minimum Lorentz factor are related through

$$\gamma_{i,\mathrm{min}} = \frac{p_i - 2}{p_i - 1}\frac{\epsilon_i}{\zeta_i}\frac{m_p}{m_i}\frac{u'_{E',\mathrm{diss}}}{\rho' c^2} \,, \tag{5.22}$$

which is obtained by setting the total particle density $n_{i,\mathrm{acc}}$ (integrated over γ_i) equal to $\zeta_i \frac{\rho'}{m_p}$. To change the minimum Lorentz factor of a distribution, one can thus either adjust $\gamma_{i,\mathrm{min}}$ directly, or indirectly set it through the fraction of accelerated particles ζ_i. If particles are injected over a timescale t'_{inject}, we calculate the normalisation $n_{i,0}$ of the injection term $Q_i = \frac{\mathrm{d}n_i}{\mathrm{d}t'\mathrm{d}\gamma_i} = n_0 \gamma_i^{-p_i} e^{-\gamma_i/\gamma_{i,\mathrm{max}}}$ from the energy density as

$$\epsilon_i u'_{\mathrm{E}',\mathrm{diss}} = m_i c^2 \int_{\hat{t}=0}^{\hat{t}=t'_{\mathrm{inject}}} \int_{\gamma_{\mathrm{i,min}}}^{\gamma_{\mathrm{i,max}}} \mathrm{d}\gamma_i \mathrm{d}\hat{t} \left(n_{i,0} \cdot \gamma_i^{-p_i+1} \right) \,. \tag{5.23}$$

From the injection terms, the time evolution/the steady state of particle spectra can be obtained by solving the coupled differential equations of all particle species (taking into account all loss processes), see Section 3.1. We point out that for charged particles confined by magnetic fields, additional assumptions on the escape mechanism are typically required to calculate emitted spectra.

Adiabatic cooling

In addition to the radiation processes introduced in Chapter 3, charged particles in GRBs suffer from *adiabatic cooling* due to the expansion of the plasma. The corresponding loss term $\dot{E}'$ is given by

$$\dot{E}' = -\frac{E'}{t'_{\mathrm{ad}}} \,. \tag{5.24}$$

As this cooling process scales with E'^{-1}, it leaves the particle power-law index unchanged (see Section 3.1).

5.2 Modified collision dynamics and impact on multi-messenger predictions

A long-standing criticism on the internal shock model is that of low energy dissipation efficiency *i.e.* that only a low fraction of the fireball kinetic energy is converted into radiation. Indeed, already [167] point out that efficiencies of ~ 25 % require a random Lorentz factor distribution between $\Gamma_{\rm min} = 20$ and $\Gamma_{\rm max} = 1000$. A possible solution was presented with the *ultra-efficient shock scenario* [217] that is a modification of the Sari, Piran and Kobayashi model introduced above. In the proposed scenario shells bounce off each other instead of merging when they collide (for illustration see Figure 5.3).

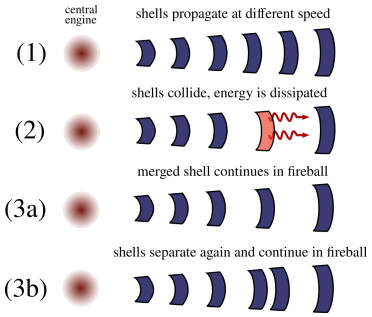

Figure 5.3: Sketch of the collision process in the standard internal shock model (3a) and ultra-efficient shock scenario (3b).

[217]: Kobayashi et al. (2001), "Ultra efficient internal shocks"

During the collision process the merged shell is described by the same formulas as above (Eq. 5.1 to Eq. 5.9), with the only modification that the dissipated energy is reduced by a factor $\eta_{\rm diss}$ ($E_{\rm diss} = \eta_{\rm diss} E_{\rm int}$). The remaining internal energy is reconverted into kinetic energy of the plasma such that the post-collision (marked with a $*$) Lorentz factors in the center-of-mass frame are given by

$$\Gamma'^{*}_{f} = (M^2 + m^{*2}_{f} - m^{*2}_{s})/2m^{*}_{f}M\,, \tag{5.25}$$

$$\Gamma'^{*}_{s} = (M^2 + m^{*2}_{s} - m^{*2}_{f})/2m^{*}_{s}M\,, \tag{5.26}$$

with $M = (m_f\Gamma_f + m_s\Gamma - \eta_{\rm diss}E_{\rm int}/c)$ and the post-collision masses $m^{*}_{f} = (1-\delta)m_f$ and $m^{*}_{s} = m_s + \delta m_f$. In the source frame, the Lorentz factors after the collision are given by

$$\Gamma^{*}_{f} = \Gamma_m\Gamma'^{*}_{f} - \sqrt{(\Gamma'^{*2}_{f} - 1)(\Gamma^2_m - 1)}\,, \tag{5.27}$$

$$\Gamma^{*}_{s} = \Gamma_m\Gamma'^{*}_{s} + \sqrt{(\Gamma'^{*2}_{s} - 1)(\Gamma^2_m - 1)}\,. \tag{5.28}$$

After being compressed by the shock during the collision, the shells are assumed to recover their pre-collision widths.

Impact on fireball evolution

We study the impact on the fireball evolution for this collision model, summarising our findings of [214]. The initial shells are set out with Lorentz factors Γ_k following a random log-normal distribution defined by

[214]: Rudolph et al. (2020), "Impact of the Collision Model on the Multi-messenger Emission from Gamma-Ray Burst Internal Shocks"

$$\ln\left(\frac{\Gamma_k - 1}{\Gamma_0 - 1}\right) = A \cdot x\,, \tag{5.29}$$

where x follows a Gaussian distribution $P(x)dx = \exp(-x^2)/\sqrt{2\pi}dx$, and $\Gamma_0 = 500$ and $A = 1.0$. Initially, all shells share the same mass and same width and are separated by a distance equal to their width. The system

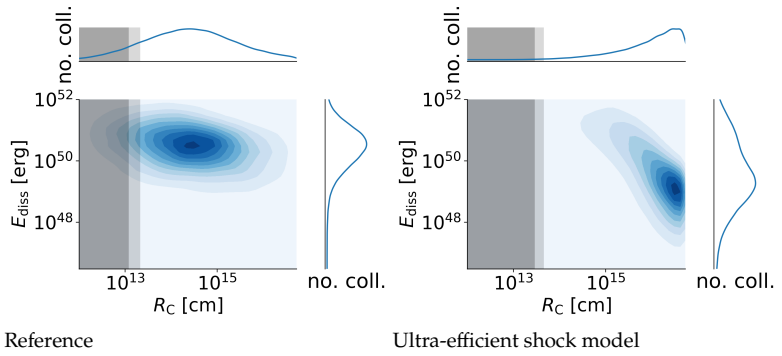

Figure 5.4: Density map showing the distribution of collisions as a function of collision radius $R_{\rm C}$ and dissipated energy $E_{\rm diss}$ for *(left)* the standard internal shock model and *(right)* the ultra-efficient shock model, obtained from 100 realisations of the initial Lorentz factor distribution. Figures adapted from [214]

of shells is set out above a minimum radius $R_{\rm min} = 10^8$ cm and occupies a total space of $20c$s.

All scenarios are normalised such that they release the same isotropic gamma-ray energy in the optically thin regime and produce light curves of the same duration T_{90} (time interval in which 90% of the energy is observed) and time variability ($t_v = \frac{T_{90}}{N_{\rm coll}}$, where $N_{\rm coll}$ is the total number of collisions). The corresponding number and widths of initial shells and average initial fireball kinetic energy (for 100 realisations) for the standard (dubbed 'reference') and ultra-efficient shock scenario are summarised in Table 5.2. The Table further lists the average number of collisions and overall dissipation efficiency of the system ($\varepsilon_{\rm diss} \equiv E_{\rm diss,tot}/E_{\rm kin,initial}$).
Figure 5.4 displays a density map of the distribution of collisions in the parameter space of dissipated energy per collision $E_{\rm diss}$ and collision radius $R_{\rm C}$ for 100 random realisations of the initial Lorentz factor distribution (Eq. 5.29). In the dark (light) shaded regions, all (some) collisions are in the optically thick regime, defined as the region where the optical depth to Thomson scatterings $\tau_T \gtrsim 1$. In the ultra-efficient shock scenario, the system thermalises as shells repeatedly bounce off each other. Therefore, each shell undergoes more collisions than in the standard scenario and the same number of total collisions can be realised with less initial shells (see Table 5.2). Late collisions (occurring at large radii) are between shells that already have collided several times and whose Lorentz factors converge to the same value. The colliding shells hence have little difference in Γ, which leads to comparatively small amounts of energies being released. In Figure 5.4 this is represented by the bulk of collisions moving to the lower right corner of the plot.
The main promise of the ultra-efficient shock scenario is that of increased efficiency. Indeed, although per collision only 50 % of the internal energy are dissipated ($\eta_{\rm diss} = 0.5$), the system reaches the same overall efficiency as the reference scenario. However, as also pointed out by [218], a two-shell post-collision state is only realised for very specific pre-collision shell parameters. We verify this by performing shock-tube simulations of two-shell encounters with Pluto [219], scanning over a parameter range of pre-collision masses and Lorentz factor ratios. Due to the expected impact of energy dissipation on shock evolution, we include a simple

Table 5.2: For the reference ('Ref') and ultra-efficient shock model ('Ultra-eff.'): Input parameters (single collision dissipation efficiency $\eta_{\rm diss}$, number of initial shells $N_{\rm shells}^{\rm initial}$ and initial width and separation $\Delta_{\rm shells}^{\rm initial}$) as well as the mean number initial fireball kinetic energy ($E_{\rm kin,initial}$), the mean number of collisions ($N_{\rm coll}$) and the mean fireball dissipation efficiency ($\varepsilon_{\rm diss} \equiv E_{\rm diss,tot}/E_{\rm kin,initial}$) for 100 random engine realisations.

	Ref.	Ultra-eff.
$\eta_{\rm diss}$	1.0	0.5
$N_{\rm shells}^{\rm initial}$	1000	125
$\Delta_{\rm shells}^{\rm initial}$	$0.01c$ s	$0.08c$ s
$\frac{E_{\rm kin,initial}}{10^{54}{\rm erg}}$	1.75±0.07	1.76±0.22
$N_{\rm coll}$	970.1±3.3	1107±220
$\varepsilon_{\rm diss}$ [%]	35.8±1.4	36.0±4.3

[218]: Kino et al. (2004), "Hydrodynamical effects in internal shock of relativistic outflows"

[219]: Mignone et al. (2007), "PLUTO: A Numerical Code for Computational Astrophysics"

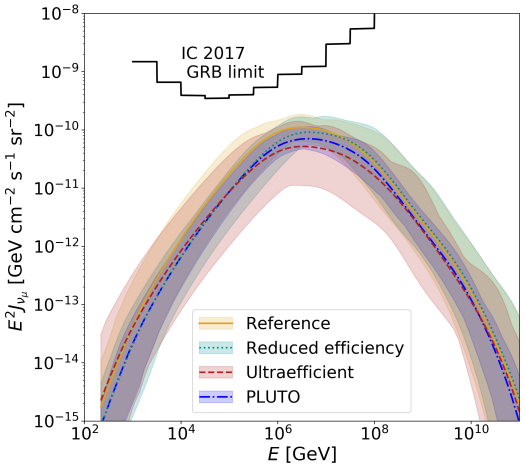

Figure 5.5: Neutrino fluxes for 100 realisations of different collision dynamics (10 in realisations for the Pluto model). The all-sky quasi-diffuse $\nu_\mu + \bar{\nu}_\mu$ flux J_{ν_μ} is calculated from the neutrino fluence F_{ν_μ} from one GRB through $J_{\nu_\mu} = F_{\nu_\mu} \dot{N} (4\pi)^{-1}$ (assuming a rate of $\dot{N} = 667$ GRBs per year located at $z = 2$). Shaded areas show the range of fluxes obtained, curves the corresponding average. For comparison, we show the GRB stacking limit from [220].
Figure from [214]

energy dissipation scheme in Pluto. We find that a two-shell final states is less probable if energy dissipation is accounted for; for details see Appendix B.2.

Impact on neutrino predictions

From these findings we proceed to evaluate how the difference in fireball evolution reflects in multi-messenger predictions. For this, we evaluate four collision models: *(1)* The *reference* scenario of Sari, Piran and Kobayashi, *(2)* the *reduced efficiency* scenario that follows the same description, but with $\eta_{\rm diss} = 0.5$, *(3)* the *ultra-efficient shock* scenario with $\eta_{\rm diss} = 0.5$ and finally *(4)* the *PLUTO* model where each two-shell encounter is simulated in Pluto, also with $\eta_{\rm diss} = 0.5$ (full description in Appendix B.2). These findings were also presented in [214].

Again, we compute 100 realisations of random initial Lorentz factors (10 for the Pluto model due to computational limitations) and assume 1000 initial shells for models 1,2,4 and 125 initial shells for model 3. Similar to before, each realisation is normalised to the same gamma-ray output.

For the radiation calculations we assume $\epsilon_e = \epsilon_B = 1/12$ and $\epsilon_p = 5/6$ for all collisions. We further pre-define a photon spectrum $\mathrm{d}N'_\gamma/\mathrm{d}E'_\gamma$ resembling observations, *i.e.* with spectral slopes $\alpha = -1$ and $\beta = -2$ below and above the peak located at comoving energy $E'_{\rm peak} = 1$ keV. With this target photon field we evolve the system until steady state with the Neucosma code [17] that includes photo-pair and photo-pion production, synchrotron and adiabatic losses. The injected proton distribution is set to a power-law with exponential cut-off (Eq. 3.6 with $-p = -2$). For the calculation of the maximal proton energy $E'_{p,\rm max}$ NeuCosmA balances all hadronic loss processes with the acceleration timescale $t'_{\rm acc} = E'/(cB'e)$ (Eq. 3.5). Finally, to retrieve the emitted particle spectra we assume that neutrinos and neutrons are free streaming while protons can only escape from the boundaries [221]. The emitted particle spectra of the full burst are given by the superposition of all single-collision contributions.

The all-sky quasi diffuse neutrino fluxes for the four models are shown in Figure 5.5, where bands show the maximum/minimum fluxes of the

[17]: Biehl et al. (2018), "Cosmic-Ray and Neutrino Emission from Gamma-Ray Bursts with a Nuclear Cascade"

[221]: Baerwald et al. (2013), "UHECR escape mechanisms for protons and neutrons from GRBs, and the cosmic ray-neutrino connection"

100 engine realisations and lines the obtained average.
We point out that several assumptions impact the overall normalisation of the diffuse flux: First, the baryonic loading of $f_p = \epsilon_p/\epsilon_e = 10$ is an ad-hoc choice. Although in consistency with other UHECR-GRB studies, this baryonic loading would not suffice to power the UHECR flux. As the flux of emitted neutrinos scales with the baryonic loading, a higher f_p compatible with the observed flux of UHECR would increase the neutrino flux. Second, to convert the neutrino fluence of one GRB to a quasi-diffuse flux, we assume a rate of $\dot{N} = 667$ GRBs per year located at $z = 2$. This is in consistency with the stacking analysis (and hence with the shown IceCube limits from [220]), but of course also a somewhat arbitrary choice that directly reflects in the normalisation. Finally, also the gamma-ray observables that were chosen for the normalisation were selected somewhat ad-hoc.
While the exact values should thus be taken cautiously, we can more robustly say that the collision model (within our assumptions of comparable gamma-ray observables) has little impact on the predicted neutrino flux: The ultra-efficient shock model, which has the lowest neutrino fluxes, is just a factor of 2 below the reference model that predicts the highest neutrino fluxes.

[220]: Aartsen et al. (2017), "Extending the search for muon neutrinos coincident with gamma-ray bursts in IceCube data"

5.3 UHECR fit for different GRB engine realisations

An enticing characteristic of the internal shock model is that it can easily explain a variety of light curves by linking them to the initial Lorentz factor distribution (that, in turn, reflects the engine activity).
While it was shown in [212] that GRBs in principle may still describe UHECRs, the study only explored a smooth initial Lorentz factor distribution that did not account for any short-time light-curve variability. Aiming at a larger phase space we performed a systematic parameter scan over initial Lorentz factor distributions ('engine realisations') while fitting to UHECR data in [215]. In the following we introduce selected findings of this study.

[212]: Globus et al. (2015), "UHECR acceleration at GRB internal shocks"

[215]: Heinze et al. (2020), "Systematic parameter space study for the UHECR origin from GRBs in models with multiple internal shocks"

We modify two assumptions of the Kobayashi, Sari and Piran model: *(1)* The Lorentz factor of the plasma during the collision is chosen as $\Gamma_m = \Gamma_r$ (Eq. 5.12, as in the Daigne and Mochkovitch model) and *(2)* after the initial compression during the collision, the merged shell continues in the fireball with width $\Delta_m = \Delta_f = \Delta_s$.

Exploring different engine realisations
To characterise different engine realisations we decompose the initial Lorentz factor distribution into two components:

1. *Ramp-up*
   A smooth Lorentz factor distribution between a maximum and minimum Lorentz factor ($\Gamma_{\max}$ and $\Gamma_{\min}$). For the kth shell of a total of N_{shells} emitted by the central engine, the Lorentz factor is given by

$$\Gamma_{0,k} = \begin{cases} \frac{\Gamma_{\max}-\Gamma_{\min}}{2} - \frac{\Gamma_{\max}-\Gamma_{\min}}{2}\cos\left(\frac{k\pi}{0.4N_{\text{shells}}}\right) & \text{, if } k \leq 0.4N_{\text{shells}} \\ \Gamma_{\max} & \text{, if } k > 0.4N_{\text{shells}} \end{cases} . \tag{5.30}$$

2. *Stochasticity*
   Random fluctuations defined by Eq. 5.29 are added on top of this deterministic distribution, characterised by their spread A_Γ.

Overall, our initial Lorentz factor distribution is thus characterised by three parameters: $\Gamma_{\max}$, $\Gamma_{\min}$ and A_Γ. In all models we assume 1000 initial shells set out with a minimum radius $R_{\min} = 10^8$ cm and initial shell widths $\Delta = c \cdot 0.002$ s and separations $d = c \cdot 0.002$ s.
In the upper panel Figure 5.6 we introduce three realisations of initial shell distributions, ordered by increasing stochasticity from 'SR-0S' (**S**trong **R**amp-up -**0** **S**tochasticity) through 'WR-MS' (**W**eak **R**amp-up -**M**edium **S**tochasticity) to 'WR-HS' (**W**eak **R**amp-up -**H**igh **S**tochasticity).

In the middle panel of Figure 5.6 we illustrate how the Lorentz factor distributions reflect in the predicted light curve. As before, the pre-set photon spectrum is a broken power law of indices $\alpha = -1.0$, $\beta = -2.0$ and $E'_{\text{peak}} = 1$ keV. The fireball kinetic energy is normalised to a total gamma-ray output of $E_{\gamma,\text{tot}} = 10^{53}$ erg (counting both sub- and super-photospheric collisions). For each collision the time-dependent photon flux is calculated following [18, 167] who describe the temporal behaviour as a 'Fast-Rise-Exponential-Decay' profile, in agreement with observations. Comparing the initial Lorenz factor distribution with the light curve, one can see that the stochasticity and ramp-up intensity of the engine realisation are mirrored in the light-curve shape.
As a next step, we perform a fit to the UHECR energy spectrum and $\langle X_{\max} \rangle$ as observed by the Pierre Auger Observatory for each engine realisation. The free fit parameters are the baryonic loading ($f_p = \epsilon_{CR}/\epsilon_e$) and the injection luminosities of different isotope groups at the base of the jet, defined as

$$I_A \equiv \frac{\int_{1\,\text{GeV}}^{\infty} \frac{dN'}{dE'_{\text{CR}}} E'_{\text{CR}} dE'_{\text{CR}}}{\sum_A \int_{1\,\text{GeV}}^{\infty} \frac{dN'}{dE'_{\text{CR}}} E'_{\text{CR}} dE'_{\text{CR}}} \tag{5.31}$$

per element group A. The injected isotope groups are Hydrogen (H), Helium (He), Nitrogen (Ni), Silicon (Si) and Iron (Fe).

[18]: Bustamante et al. (2017), "Multi-messenger light curves from gamma-ray bursts in the internal shock model"
[167]: Kobayashi et al. (1997), "Can internal shocks produce the variability in GRBs?"

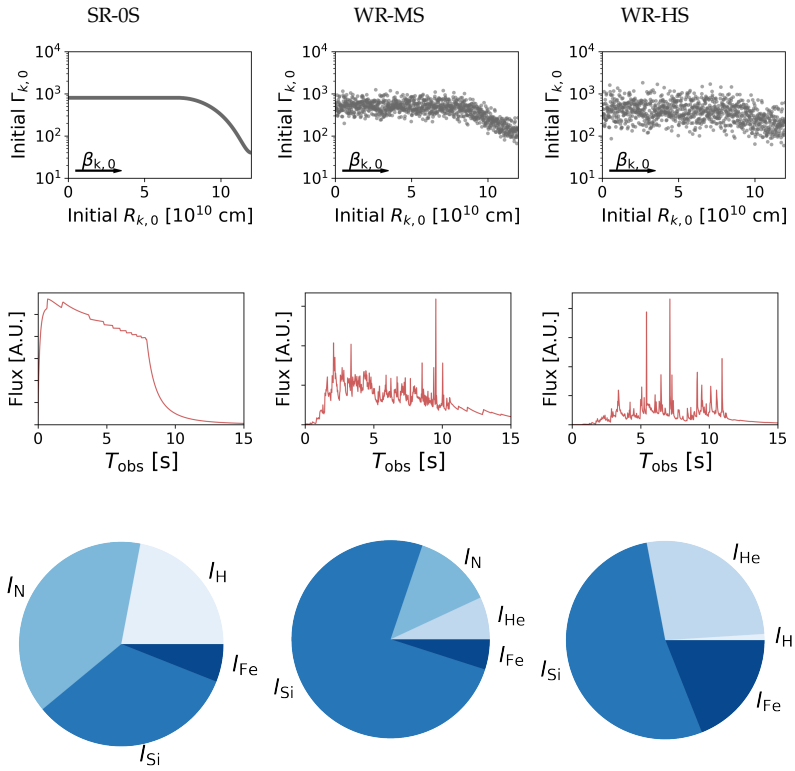

Figure 5.6: Exploring different engine realisations.
Top panel: Initial (input) Lorentz factor distribution as a function of initial radius.
Middle panel: Corresponding light curve from super-photospheric collisions (for a representative redshift $z = 2$).
Bottom panel: Fraction of different element groups injected at the jet base determined by the fit to the UHECR energy spectrum and $\langle X_{max} \rangle$ as observed by the Pierre Auger Observatory for the respective engine setup.
Figures adapted from [215]

We first compute the source spectra for each engine realisation. For efficient computation we perform the simulations separate by isotope and superimpose them after the fit. This has no impact on our results as nucleon-nucleon interactions are inefficient compared to photo-nuclear ones (and not accounted for) and the nuclear feedback on photon spectra is neglected. Again, the injected cosmic rays follow a power law with exponential cut-off (Eq. 3.6 with $p- = -2$, $E'_{min} = 1$ GeV and E'_{max} determined by balancing acceleration and losses). The comoving spectra are computed with NeuCosmA and extracted after one dynamical timescale $t'_{dyn} = t'_{esc}$. A bell-shape escape rate for cosmic rays is assumed that effectively acts as a high-pass filter. As our method cannot represent sub-photospheric collisions, they are excluded from the calculations. As a second step, those source spectra are propagated using the PriNCe code [222] adopting the cosmological GRB distribution derived by [223]. Finally the fit is performed with the Minuit fitting framework [224].
The fit-determined injection luminosities at the base of the jet for the three example cases are shown in the lower panel of Figure 5.6. A high level of engine stochasticity induces collisions close to the central engine. As the shell volume scales with R_C^{-2}, these collisions have high plasma densities. This enables efficient hadronic interactions and nuclear disintegration. Thus, for larger stochasticity, the injected composition is usually heavier and light isotopes are generated by photo-disintegration. On the other hand, the survival rate of heavy nuclei is high in models with low stochasticity. These two tendencies reflect in the low I_H for the two stochastic engines and the low I_{Si} and I_{Fe} for SR-0S in Figure 5.6.

[222]: Heinze et al. (2019), "A new view on Auger data and cosmogenic neutrinos in light of different nuclear disintegration and air-shower models"
[223]: Wanderman et al. (2010), "The luminosity function and the rate of Swift's Gamma Ray Bursts"
[224]: James et al. (1975), "Minuit: A System for Function Minimization and Analysis of the Parameter Errors and Correlations"

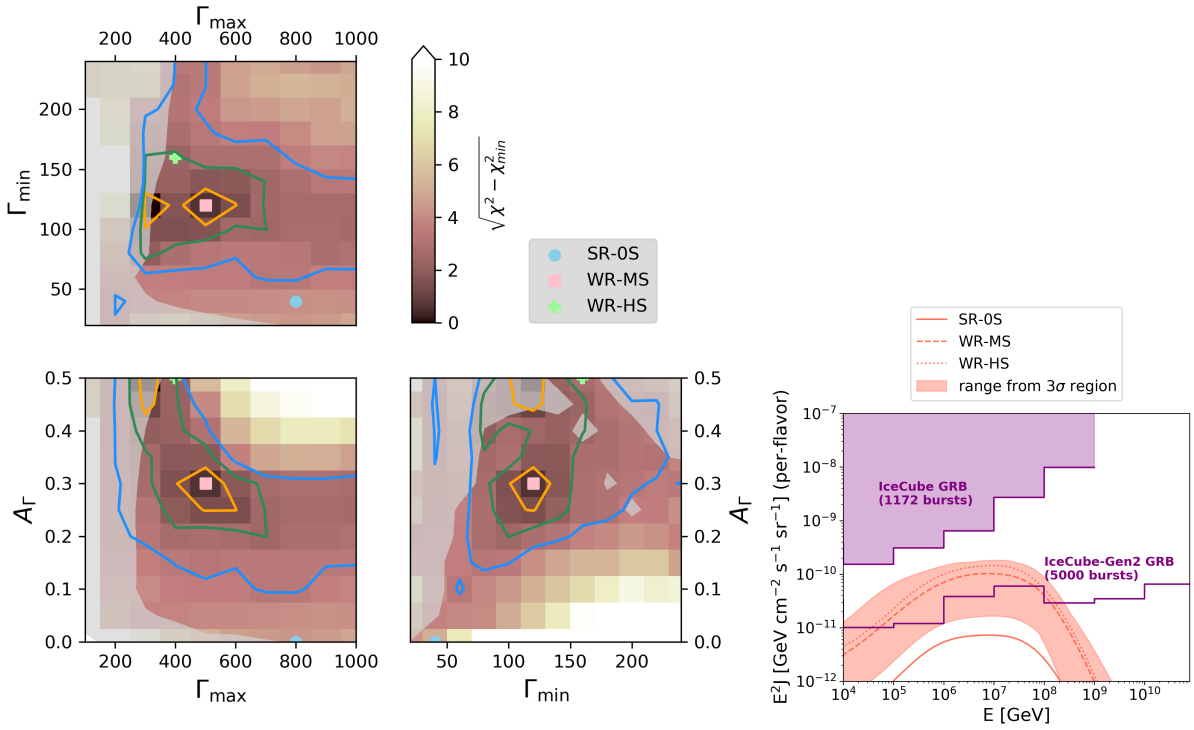

Figure 5.7: Left: Parameter scan result for engines characterised by $\Gamma_{\rm min}$, $\Gamma_{\rm max}$ and A_Γ for the fit to the UHECR energy spectrum and $\langle X_{\rm max}\rangle$ as observed by the Pierre Auger Observatory. The orange, green and blue lines correspond to the 1, 2 and 3σ regions (for 1 d.o.f. in a Gaussian likelihood). For each two-dimensional plot, $\Delta\chi^2$ is minimised over the third parameter. The grey shaded areas is excluded from our results because >60 % of the energy is dissipated in the optically thick regime. We further indicate the positions of the examples from Figure 5.6.
Right: Corresponding post-dicted single-flavour neutrino fluxes. The shaded region shows the range from the 3σ region, the lines indicate the neutrino fluxes of the examples introduced before. For comparison we show the current IceCube GRB stacking limit [220] and the predicted IceCube Gen2 limit (for 5000 bursts) [225].
Figures adapted from [215]

Parameter scan result an post-dicted neutrino fluxes

Finally, we move to the full parameter scan over $\Gamma_{\rm min}$, $\Gamma_{\rm max}$ and A_Γ, shown in the left plot of Figure 5.7. For each engine realisation we follow the procedure described earlier and calculated the baryonic loading and composition that provide the best fit to the UHECR energy spectrum and $\langle X_{\rm max}\rangle$. In principle we find a very broad parameter-space region where the observables can be described well. Indeed, both stochastic examples introduced before lie within the 3σ region. Overall, engines with medium stochasticity and a bulk Lorentz factor of ~ 350 such as WR-MS are preferred. The required baryonic loading $f_p = \epsilon_{\rm CR}/\epsilon_e$ is of the order 50 -100 ($f_p = 60$ for WR-MS which roughly corresponds to the best fit of our parameter scan).

If $\sigma(X_{\rm max})$ were included in the fit, the preferred region would move to engines with low stochasticity. The reasoning behind this is as follows: The $\sigma(X_{\rm max})$ measurements of the Pierre Auger Observatory indicate that the increasingly heavy composition at the highest energies is realised through a smooth transition between neighbouring mass groups, without much overlapping contributions of different mass spectra. This is difficult to reproduce with stochastic engines where the contributing

collisions (with spectra extending to different E'_{max}) are distributed more randomly. In contrast, the smooth succession of collisions with little nuclear disintegration in low stochasticity engines is better suited to explain $\sigma(X_{\mathrm{max}})$ measurements.

We compare to the typical variability of GRB light curves: Variability studies of the GRB prompt phase have mostly focused on the Minimum Variability Timescale (MVT) [226–228] instead of the average intensity of the variability with respect to broader light curve peaks. [228] report a broad distribution of MVT with respect to the observed T_{90} (see their Figure 7), which suggests that smooth light curves without stochasticity are not representative for the population. In this sense, the $\sigma(X_{\mathrm{max}})$ measurements as currently reported by the Pierre Auger Observatory may strongly constrain the contribution of GRBs to the UHECR flux.

[226]: MacLachlan et al. (2013), "Minimum Variability Time Scales of Long and Short GRBs"
[227]: Bhat (2013), "Variability Time Scales of Long and Short GRBs"
[228]: Golkhou et al. (2014), "Uncovering the Intrinsic Variability of Gamma-ray Bursts"

The right plot of Figure 5.7 shows the corresponding post-dicted single-flavour source neutrino fluxes. The bands represent the fluxes from the 3σ region of the fit, we further indicate the neutrino fluxes of the three examples. Here, stochastic engines with a high level of nuclear interactions naturally produce higher neutrino fluxes. In this sense, the light-curve stochasticity is an indicator for the neutrino production efficiency. All scenarios in the 3σ region are below current IceCube limits [220], but in reach of the predicted IceCube Gen2 limit [225].

[220]: Aartsen et al. (2017), "Extending the search for muon neutrinos coincident with gamma-ray bursts in IceCube data"
[225]: Aartsen et al. (2020), "IceCube-Gen2: The Window to the Extreme Universe"

Overall, our results indicate that GRBs can not generally be ruled out as UHECR sources. However, a number of issues remain: First, our fit requires $f_p \sim 50 - 100$. It is unclear if these high f_p would be compatible with observed photon spectra in the sense that hadronic contributions should not distort the spectra. Studying these effects however requires detailed radiation models as *e.g.* in [191], see also Chapter 7. Second, it is difficult to reconcile $\sigma(X_{\mathrm{max}})$ measurements with stochastic engines. We point out that similar effects are expected for a superposition of sources with different ejection spectra instead of assuming a redshift distribution of identical GRBs. Finally, we require initial engine kinetic energies of $10^{55} - 10^{56}$ erg per GRB. This is a rather extreme energetic requirement and may not be realised in a typical long GRB. We point out that this is a general issue for UHECR fits: In order to power UHECRs, a local emissivity of $\sim 10^{44}$ erg Mpc^{-3} yr^{-1} is necessary. For a local GRB rate of approximately 1 Gpc^{-3} yr^{-1} this means that roughly $4 \cdot 10^{53}$ erg per GRB have to be emitted in UHECRs [229]. With standard assumptions like the injection spectrum extending down to 1 GeV, a high engine kinetic energy is thus unavoidable. For GRBs, it is unclear if these kinetic energies would be compatible with the afterglow energy budget: If a the fireball is still very energetic when producing the afterglow, a signal brighter than the typical detected afterglow may be produced. On the other hand, analysis like [230, 231] and recent VHE observations (*e.g.* [116, 232]) indicate that afterglow energy budgets may be higher than previously thought.

[191]: Asano et al. (2009), "Prompt High-Energy Emission from Proton-Dominated Gamma-Ray Bursts"

[229]: Baerwald et al. (2015), "Are gamma-ray bursts the sources of ultra-high energy cosmic rays?"
[230]: Fan et al. (2006), "Grb efficiency and possible physical processes shaping the early afterglow"
[231]: Beniamini et al. (2015), "Energies of GRB blast waves and prompt efficiencies as implied by modelling of X-ray and GeV afterglows"
[116]: Abdalla et al. (2019), "A very-high-energy component deep in the γ-ray burst afterglow"
[232]: Acciari et al. (2019), "Observation of inverse Compton emission from a long γ-ray burst"

Low-luminosity GRBs as potential sources of VHE photons and UHECRs

6

6.1 The population of LL-GRBs and selection of representative examples 69

6.2 LL-GRB models 71

6.3 Methods and parameter choices 73

6.4 VHE gamma-ray predictions from a leptonic radiation modelling 76

6.5 Maximal energies of cosmic-ray nuclei 81

The strong neutrino constraints that limit the baryonic loading of (conventional) high-luminosity GRBs have led to increased interest in Low-luminosity GRBs (LL-GRBs) with $L_{\rm iso} \lesssim 10^{49}$ erg/s. Although less than 20 events of this sub-class have been detected, they are explored as potential sources of UHECRs and HE neutrinos in a number of recent publications.

In this chapter we present time-dependent radiation models of LL-GRBs within the internal shock model. In this context, we study LL-GRBs as potential sources of VHE gamma-ray emission and UHE cosmic rays. For overview we first introduce the population of LL-GRBs (and our selection of three representative examples) in Section 6.1 and review the current state of models in Section 6.2. Our modelling procedure and parameter choices are described in Section 6.3. Finally, we show the results of our leptonic radiation modelling in Section 6.4 and calculate the maximal energies of cosmic-ray nuclei in Section 6.5.
The chapter closely follows and summarises the findings of [233]. For this project I adapted AM3 such that it can treat leptonic GRB models (for a summary of code adaptations see Appendix A). I further coupled the code to the fireball simulation code described previously and implemented a framework for time-dependent predictions that takes into account the curvature of the emitting surface. In collaboration with Daniel Biehl we self-consistently determined the maximal energies of different nuclei with NeuCosmA using the results of the radiation and fireball modelling as input.

[233]: Rudolph et al. (2022), "Multi-wavelength radiation models for low-luminosity GRBs and the implications for UHECRs"

The applied procedure and parameter choices in this chapter rely on optically thin synchrotron models that have been shown to reproduce the observed properties of high-luminosity GRBs in [184, 234, 235]– In this sense we do not explore the impact of modelling choices derived in those papers but rather explore whether the framework is equally applicable to low-luminosity GRBs.

[184]: Daigne et al. (2011), "Reconciling observed GRB prompt spectra with synchrotron radiation ?"
[234]: Bosnjak et al. (2009), "Prompt high-energy emission from gamma-ray bursts in the internal shock model"
[235]: Bošnjak et al. (2014), "Spectral evolution in gamma-ray bursts: predictions of the internal shock model and comparison to observations"

6.1 The population of LL-GRBs and selection of representative examples

Due to their low fluences only a handful of LL-GRBs have been detected so far. Additional challenges arise in the classification since follow-up observations are equally difficult. Restricting ourselves to events with a strong supernova association (that strengthens the GRB interpretation)

Table 6.1: LL-GRBs with associated supernovae. We list the isotropic equivalent emitted energy $E_{\gamma,\mathrm{iso}}$, the observed duration T_{90}, the redshift z, and the reported peak energy E_{peak}. We further derive $L_{\gamma,\mathrm{iso}} \equiv E_{\gamma,\mathrm{iso}}(1+z)/T_{90}$. The GRBs which will serve as references for our prototypes are marked bold, and the prototype names are listed in the last column. Table adapted from [233].

GRB	$E_{\gamma,\mathrm{iso}}$ [erg]	$L_{\gamma,\mathrm{iso}}$ [erg/s]	E_{peak} [keV]	T_{90} [s]	z	SN	Reference	Prototype
980425	$\mathbf{1.6 \cdot 10^{48}}$	$\mathbf{4.6 \cdot 10^{46}}$	**122**	**34.9**	**0.0085**	**1998bw**	[242, 243]	**GRB-SP**
031203	$1.2 \cdot 10^{49}$	$3.6 \cdot 10^{47}$	291	37	0.105	2003lw	[242, 243]	
060218	$4.3 \cdot 10^{49}$	$2.1 \cdot 10^{46}$	4.7	2100	0.0335	2006aj	[243, 244]	
100316D	$\mathbf{3.9 \cdot 10^{49}}$	$\mathbf{3.2 \cdot 10^{46}}$	**30**	**1300**	**0.0591**	**2010bh**	[237, 245]	**GRB-UL**
120121B	$1.4 \cdot 10^{48}$	$7.7 \cdot 10^{46}$	92	18.4	0.017	2012ba	[246]	
120422A	$4.5 \cdot 10^{49}$	$1.1 \cdot 10^{49}$	53	5.4	0.283	2012bz	[247]	
120714B	$\mathbf{5.9 \cdot 10^{50}}$	$\mathbf{5.2 \cdot 10^{48}}$	**101**	**159**	**0.3984**	**2012eb**	[248]	**GRB-HL**
130702A	$6.6 \cdot 10^{50}$	$1.3 \cdot 10^{49}$	15	59	0.145	2013dx	[249, 250]	
161219B	$8.5 \cdot 10^{49}$	$1.4 \cdot 10^{49}$	106	7	0.1475	2016jca	[251]	
171205A	$2.2 \cdot 10^{49}$	$1.2 \cdot 10^{47}$	125	190	0.0368	2017iuk	[252]	
190829A	$1.9 \cdot 10^{50}$	$1.7 \cdot 10^{49}$	11	11	0.0785	2019oyw	[119, 253]	
201015A	$1.1 \cdot 10^{50}$	$1.6 \cdot 49^{50}$	10	10	0.426	AT2020wyy	[120]	

we list the entire sample that to our knowledge was identified as LL-GRB in Table 6.1.

A few properties distinguish the population from high-luminosity GRBs: First, in comparison to high-luminosity events, LL-GRBs occur at a higher local rate of $\rho_0 \sim 200\,\mathrm{Gpc}^{-3}\,\mathrm{yr}^{-1}$. Second, the estimated Lorentz factors of the order of $\Gamma \lesssim 50$ are relatively low; the same is true for the reported peak energies $E_{\mathrm{peak}} \lesssim 100$ keV [236, 237]. In addition, some LL-GRBs have characteristics that deviate from known correlations: For example, GRB 980425 and GRB 031203 are outliers to the E_{iso} - E_{peak} correlation (established in [238]). Also, some LL-GRBs have unusually long durations of the order of 10^3 s [239–241].

[236]: Ghirlanda et al. (2018), "Bulk Lorentz factors of Gamma-Ray Bursts"

[237]: Cano et al. (2017), "The Observer's Guide to the Gamma-Ray Burst Supernova Connection"

[238]: Amati et al. (2002), "Intrinsic spectra and energetics of BeppoSAX gamma-ray bursts with known redshifts"

[239]: Liang et al. (2007), "Low Luminosity Gamma-Ray Bursts as a Unique Population: Luminosity Function, Local Rate, and Beaming Factor"

[240]: Virgili et al. (2009), "Low-Luminosity Gamma-Ray Bursts as a Distinct GRB Population:A Monte Carlo Analysis"

[241]: Sun et al. (2015), "Extragalactic High-energy Transients: Event Rate Densities and Luminosity Functions"

Reference GRBs and prototypes

We select three events as benchmark scenarios that represent different sub-classes of LL-GRBs: GRB 980425, GRB 100316D and GRB 120714B. Those GRBs will guide our simulations in the sense that our prototypes will have (approximately) the same $E_{\gamma,\mathrm{iso}}$, T_{90}, E_{peak} and light curve structure. We explicitly do not aim at exactly reproducing the events. Below, we summarise the main characteristics for the three events and connect them to our prototypes.

Our first prototype *GRB-SinglePeak (GRB-SP)* is based on GRB 980425, which has a smooth single peaked light curve of $T_{90} \simeq 35$ s and a relatively high time-integrated peak energy of $E_{\mathrm{peak}} = 122 \pm 17$ keV (from a fit of 'Comptonisation' photon model to BATSE LAD data [243]). For comparison, [254] perform a Band-function fit to BeppoSAX GRBM data and find $E_{\mathrm{peak}} = 68 \pm 40$ keV and a spectral index below the peak of $\alpha = -0.78 \pm 0.27$. The event was explored in an internal-shock context in [255].

For our second prototype, *GRB-UltraLong (GRB-UL)*, we use the observed properties of GRB 100316D which is one of the two ultra-long GRBs in our table. Most studies instead use GRB 060218 as a proxy for the

[243]: Kaneko et al. (2006), "Prompt and Afterglow Emission Properties of Gamma-Ray Bursts with Spectroscopically Identified Supernovae"

[254]: Frontera et al. (2000), "Prompt and delayed emission properties of gamma-ray bursts observed with BeppoSAX"

[255]: Daigne et al. (2007), "The low-luminosity tail of the GRB distribution: The case of GRB 980425"

population of ultra-long LL-GRBs. However, for GRB 060218 the black-body component comprises 13 % of the prompt spectrum. In contrast, GRB 100316D has a sub-dominant black-body component contributing only 3 % to the the X-Ray flux (0.3 - 10 keV, [245]). In our view, this makes it a more suitable candidate for the internal shock model than GRB 060218. The non-thermal radiation origin is further supported by its higher peak energy of ≈ 30 keV. The light curve (of overall duration $T_{90} \simeq 1300$ s) comprises multiple peaks with maximal photon fluxes decreasing with time. The spectral index below the peak (for a cut-off power-law fit) is found to be $\alpha \approx -1.4$ [245], which is comparable to the one for GRB 060218 ([243] find $\alpha = -1.44 \pm 0.006$). For this GRB, optical constraints are available: *Swift*-UVOT reported non-detection in the u-band for three different time-intervals (of exposure times 35 s, 194 s and 36 s with mid-times 324 s, 440 s and 634 s after the BAT trigger) [245]. In [256] Figure 4, these are translated into time-averaged limits between $1.9 \cdot 10^{-13}$ erg/cm^2/s and $6.3 \cdot 10^{-13}$ erg/cm^2/s, where absorption in our own and the host galaxy are accounted for.

Finally, our third prototype *GRB-HighLuminosity (GRB-HL)* will approximately reproduce the observed characteristics of GRB 120714B. This GRB has one of the highest luminosities of the sample, which strengthens the case for an engine-driven scenario [257]. The *Swift*-BAT power-law fit finds a peak energy of 101 keV and a photon index of $\alpha = -1.52 \pm 0.17$ [258]. The light curve is simple and single-peaked, with T_{90}=159 s. With a redshift of $z = 0.3964$ it is also among the most distant events of the sample and will enable us to study the impact of EBL absorption on VHE spectra.

[245]: Starling et al. (2011), "Discovery of the nearby long, soft GRB 100316D with an associated supernova"

[256]: Fan et al. (2011), "XRF 100316D/SN 2010bh: clue to the diverse origin of nearby supernova-associated GRBs"

[257]: Zhang et al. (2012), "GRB 120422A: A Low-luminosity Gamma-ray Burst Driven by Central Engine"

[258]: Cummings et al. (2012), "GCN Circ. 13481"

6.2 LL-GRB models

It is still unclear whether LL-GRBs can be accommodated within the same theoretical framework as high-luminosity events. Three main scenarios are being discussed: *Off-axis scenarios* attribute the low luminosity to usual GRBs observed at large viewing angles [259, 260]. We point out that this model predicts very bright afterglow possibly in conflict with observations [255]. *Weak jet models* also use the same framework as for standard GRBs, but impose mildly relativistic jets and mildly energetic outflows [255] [257, 261, 262]. Finally, in the *shock-breakout model* ([263–266], introduced below in more detail) the jet is choked and dissipates its energy in the progenitor environment. The prompt emission is produced as the jet-induced shock breaks out of the surrounding material.

[259]: Pescalli et al. (2015), "Luminosity function and jet structure of Gamma-Ray Burst"

[260]: Aloy et al. (2018), "On the existence of a luminosity threshold of GRB jets in massive stars"

[255]: Daigne et al. (2007), "The low-luminosity tail of the GRB distribution: The case of GRB 980425"

[257]: Zhang et al. (2012), "GRB 120422A: A Low-luminosity Gamma-ray Burst Driven by Central Engine"

[261]: Ghisellini et al. (2007), "Did we observe the supernova shock breakout in GRB 060218?"

[262]: Irwin et al. (2016), "Jet or Shock Breakout? The Low-Luminosity GRB 060218"

[263]: Waxman et al. (2007), "GRB060218: A Relativistic Supernova Shock Breakout"

[264]: Bromberg et al. (2011), "Are Low-luminosity Gamma-Ray Bursts Generated by Relativistic Jets?"

[265]: Nakar et al. (2012), "Relativistic shock breakouts - a variety of gamma-ray flares: from low luminosity gamma-ray bursts to type Ia supernovae"

[266]: Nakar (2015), "A unified picture for low-luminosity and long gamma-ray bursts based on the extended progenitor of llgrb 060218/SN 2006aj"

The shock-breakout scenario

The low kinetic energy connected to the low luminosity may imply a jet too weak to break out of the surrounding material: It cannot fully penetrate the envelope and is choked. From its head, a mildly relativistic

shock propagates through the medium and finally breaks out at a radius $R_{\rm ext} \sim 10^{14}$ cm. The breakout emission has been proposed as origin of the LL-GRB radiation. The breakout is almost spherical and creates a signal whose properties are fully determined by the breakout radius $R_{\rm ext}$. This allows to relate the (observed) breakout time $T_{\rm SB}$ to the released energy (that defines $E_{\gamma,\rm iso}$) and the temperature (that defines the observed $E_{\rm peak}$) [265]:

$$T_{\rm SB} = 20 \cdot (1+z)^{\frac{9+\sqrt{3}}{4}-1} \left(\frac{E_{\gamma,\rm iso}}{10^{46}\,\rm erg}\right)^{\frac{1}{2}} \left(\frac{E_{\rm peak}}{50\,\rm keV}\right)^{-\frac{9+\sqrt{3}}{4}} \rm s\,, \qquad (6.1)$$

where we included the conversion of observed quantities into the source frame through the redshift z.

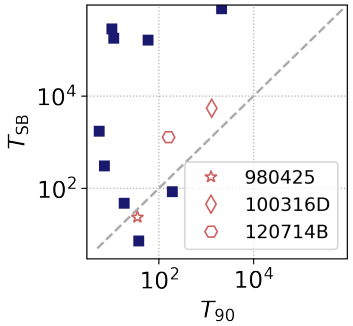

Figure 6.1: Shock breakout duration $T_{\rm SB}$ (from Eq. 6.1) vs. reported T_{90} for the sample for LL-GRBs from Table 6.1. We indicate the three representative examples identified in Section 6.1. On the dashed line $T_{\rm SB} = T_{90}$.

In Figure 6.1 we show the calculated $T_{\rm SB}$ vs. the reported T_{90} for the sample of LL-GRBs listed in Table 6.1. The dashed line indicates where $T_{\rm SB} = T_{90}$. Some GRBs are very close to this line, for others $T_{\rm SB}$ is orders of magnitude higher than T_{90}. From this we conclude that the shock-breakout scenario may explain only a sub-set of LL-GRBs. From our sample of reference GRBs (indicated by red symbols) T_{90} and $T_{\rm SB}$ differ most for GRB 120714B. The validity of the shock-breakout scenario can further be tested by comparing the jet breakout time $t_{\rm jet,BO}$ to the engine active time (that is approximately given by $t_{\rm eng} = T_{90}/(1+z)$): If $t_{\rm jet,BO} > t_{\rm eng}$, the jet likely does not fully penetrate the progenitor environment and a shock-breakout scenario seems plausible. We point out that the estimates on $t_{\rm jet,BO}$ depend on the mass of the surrounding material that is usually not well constrained.

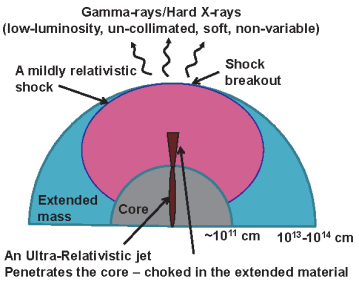

Figure 6.2: Sketch of the shock-breakout scenario where the surrounding material consists of a dense core and a less dense extended mass. Figure adapted from [266].

A unified picture for GRBs was proposed in [266]. In this model (illustrated in Figure 6.2), the surrounding material is composed of a dense core and a less dense extended mass. For LL-GRBs, the jet does leave the core but is then choked in the extended mass. For high-luminosity GRBs jets fully penetrate all surrounding material in absence of an extended mass.

An interesting example potentially connecting the different scenarios is GRB 190829A which is among the few events observed at late times during the afterglow phase by H.E.S.S. at very-high (> 100 GeV) energies. The double-peaked light curve with a quiescent phase in between has been proposed to be a combination of a shock breakout and a collimated emission episode [253]. In this sense, both the breakout and the jetted emission may be realised in the same GRB, depending on the properties of a particular progenitor.

[253]: Chand et al. (2020), "Shock-breakout and central engine activities in H.E.S.S. detected GRB 190829A"

		GRB 980425	GRB 100316D	GRB 120714B
observed properties	$E_{\gamma,\mathrm{iso}}$ [erg]	$1.6 \cdot 10^{48}$	$3.9 \cdot 10^{49}$	$5.9 \cdot 10^{50}$
	T_{90} [s]	35	1300	159
	E_{peak} [keV]	122	30	101
	z	0.0085	0.059	0.3984
		GRB-SP	GRB-UL	GRB-HL
fireball parameters	$\Gamma^{\mathrm{initial}}_{\mathrm{min}}$, $\Gamma^{\mathrm{initial}}_{\mathrm{max}}$	10, 40	10, 40	20, 80
	L_{wind} [erg/s]	$2.5 \cdot 10^{48}$	$5.8 \cdot 10^{48}$	$3 \cdot 10^{50}$
	$N^{\mathrm{initial}}_{\mathrm{shells}}$	1000	1000	1000
	t_{eng} [s]	40	1000	130

Table 6.2: Observed properties for the reference GRBs (isotropic equivalent emitted gamma-ray energy $E_{\gamma,\mathrm{iso}}$, redshift z, observed duration T_{90} and reported peak energy E_{peak}), as well as input parameters to our model used to reproduce alike events GRB-SP, GRB-UL and GRB-HL (maximum and minimum of the initial Lorentz factor distribution $\Gamma^{\mathrm{initial}}_{\mathrm{max}}$, $\Gamma^{\mathrm{initial}}_{\mathrm{min}}$), wind luminosity L_{wind}, engine active time t_{eng} and the number of initial shells $N^{\mathrm{initial}}_{\mathrm{shells}}$).

6.3 Methods and parameter choices

Following [255] we assume that LL-GRBs can be explained within the same internal shock model as HL-GRBs but with mildly relativistic jets and mildly energetic outflows and apply the Daigne and Mochkovitch internal shock model introduced in Section 5.1 [168].

We thus characterise the outflow by the wind luminosity L_{wind}, the engine active time t_{eng}, the number of initial plasma shells $N^{\mathrm{initial}}_{\mathrm{shells}}$ (that define the discretisation as $\mathrm{d}\tau = t_{\mathrm{eng}}/N^{\mathrm{initial}}_{\mathrm{shells}}$) and the initial Lorentz factor distribution. The latter is chosen such that the light curve structure of the three reference events is reproduced (single peaked for GRB-SP and GRB-HL and multi-peaked with decreasing maximal flux for GRB-UL). We summarise the observational characteristics and wind parameters for the three prototypes in Table 6.2 and the initial Lorentz factor distributions in Figure 6.3. The fireball evolution of plasma parameters as a function of collision radius is illustrated for GRB-SP in Figure 6.4.

[255]: Daigne et al. (2007), "The low-luminosity tail of the GRB distribution: The case of GRB 980425"

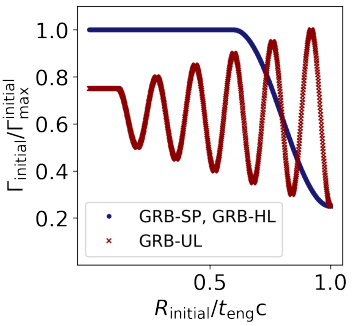

Figure 6.3: Initial Lorentz factor distributions for the three LL-GRB prototypes.

Microphysics parameters and injected electron spectrum

For all bursts and realisations we assume $\epsilon_e = 1/3$ (as suggested for relativistic shocks [267]) and set the power-law slope of injected electrons $-p_e = -2.5$ (that reproduces the typical GRB high-energy photon index of $\beta = -2.25$). In the following, we will adjust the microphysics parameters ζ_e (the number fraction of accelerated electrons) and ϵ_B such that a given, observed peak energy E_{peak} is reproduced. [234] give the observed synchrotron peak energy of a single collision between two plasma shells for a GRB at redshift z as

[267]: Spitkovsky (2008), "Particle acceleration in relativistic collisionless shocks: Fermi process at last?"

[234]: Bosnjak et al. (2009), "Prompt high-energy emission from gamma-ray bursts in the internal shock model"

$$E_{\mathrm{syn}} \simeq 17\ \mathrm{eV} \frac{1}{1+z} \left(\frac{\Gamma_{\mathrm{C}}}{10}\right) \left(\frac{B'}{100\,\mathrm{G}}\right) \left(\frac{\gamma_{e,\mathrm{min}}}{1000}\right)^2 . \tag{6.2}$$

The minimum Lorentz factor can be re-expressed in terms of microphysics parameters (see Eq. 5.22 in the last chapter). As in [235], we assume that the fraction of accelerated electrons is proportional to the dissipated

[235]: Bošnjak et al. (2014), "Spectral evolution in gamma-ray bursts: predictions of the internal shock model and comparison to observations"

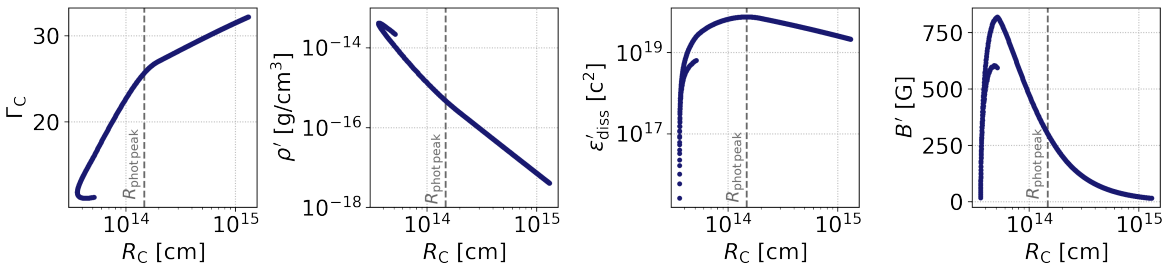

Figure 6.4: Evolution of plasma properties with collision radius R_C for GRB-SP: The Lorentz factor Γ_C, the comoving mass density ρ', the dissipated energy per unit mass ϵ'_{diss} and the magnetic field B' (for $f_B = 3 \cdot 10^{-1}$). We further indicate the radius where ϵ'_{diss} is maximal as $R_{phot\,peak}$.

energy per unit mass ϵ'_{diss} ($\zeta_e = \zeta_{e,0}\epsilon'_{diss}/c^2$). This allows to re-write $\gamma_{e,min}$ (that remains constant throughout the fireball evolution) as

$$\gamma_{e,\mathrm{min}} = \frac{p_e - 1}{p_e - 1} \frac{\epsilon_e}{\zeta_{e,0}} \frac{m_p}{m_e} \,. \tag{6.3}$$

We combine Eq. 6.2 and Eq. 6.3 to create a relation between E_{syn}, ϵ_B and $\zeta_{e,0}$:

$$\zeta_{e,0} = \left[8.5 \cdot 10^{-10} \frac{p_e - 1}{p_e - 1} \frac{m_p}{m_e} \sqrt{u'_{\mathrm{E}',\mathrm{diss}}} \frac{\epsilon_e \Gamma_C}{(1+z)} \right]^{\frac{1}{2}} \cdot E_{\mathrm{syn}}^{-\frac{1}{2}} \epsilon_B^{\frac{1}{4}} \,, \tag{6.4}$$

where we have calculated the comoving magnetic field following Eq. 5.20. For a fixed fireball evolution (that sets $\sqrt{u_{\mathrm{E}',\mathrm{diss}}}$ and Γ_C) and pre-defined ϵ_e and p_e, this Equation thus describes how the synchrotron peak (in a single collision) is controlled by $\zeta_{e,0}$ and ϵ_B. For our radiation modelling we set $\zeta_{e,0}$ and ϵ_B such that for the collision where ϵ'_{diss} is maximal (with corresponding $\Gamma_C|_{\epsilon'_{diss,max}}$ and $u'_{\mathrm{E}',\mathrm{diss}}|_{\epsilon'_{diss,max}}$) the predicted peak energy matches the one of the reference event, $E_{syn} = E_{peak}$ in Eq. 6.4. Releasing the highest amount of energy, this collision can be expected to dominate the observed photon spectrum; we label the corresponding collision radius as $R_{phot,peak}$ (see Figure 6.4). The pairs of $\zeta_{e,0}$ and $f_B = \epsilon_B/\epsilon_e$ used for our radiation models are listed in Table B.2.

Radiation modelling and conversion to observed quantities

From the fireball evolution and microphysics parameters we calculate the comoving spectra of each collision with AM3 [124]. The code (introduced in Chapter 3 and Appendix A) includes all relevant leptonic processes such as synchrotron, synchrotron self-absorption, inverse Compton scatterings (in the Klein-Nishina and the Thomson regime), $\gamma\gamma$-annihilation and adiabatic cooling of charged particles. Secondary particles (*e.g.* lepton pairs from $\gamma\gamma$-annihilation) are treated the same way as primary electrons.

For the injected particle distribution we follow [234] and assume that particles are accelerated on timescales much smaller than the dynamical time of the system. This corresponds to a δ-injection in time in Eq. 5.23,

[234]: Bosnjak et al. (2009), "Prompt high-energy emission from gamma-ray bursts in the internal shock model"

which leads to the normalisation of the injected, initial electron density distribution $n(\gamma_e) = \frac{\mathrm{d}n}{\mathrm{d}\gamma_e} = n_{e,0}\gamma^{-p_e}$ at $t' = 0$ through

$$\epsilon_e u'_{\mathrm{E'},\mathrm{diss}} = \int_{\gamma_{e,\min}}^{\gamma_{e,\max}} d\gamma_e n(\gamma_e, t' = 0)\gamma_e m_e c^2 \,. \tag{6.5}$$

The maximal electron Lorentz factor $\gamma_{e,\max}$ is determined balancing adiabatic and synchrotron loss rates with the acceleration rate.
From this initial state we evolve the system until $t' = t'_{\mathrm{dyn}} = t'_{\mathrm{ex}}$. As this corresponds to the adiabatic cooling time, all initial electrons have cooled. The final, emitted spectrum $u'_{E',\mathrm{emitted}}$ is then given by

$$u'_{E',\mathrm{emitted}} = u'_{E'}(t'_{\mathrm{dyn}}) \,. \tag{6.6}$$

Within this approach we expect (roughly) same results as if an escape term with $t'_{\mathrm{esc}} = t'_{\mathrm{dyn}}$ were included. However, a full treatment of photon escape (integrating over all escaped photons) would capture the temporal evolution of the spectrum, which is not the case here.

The full fireball emission is obtained by adding the contributions of all single collisions. For the calculation of time-dependent quantities (light curves and time-resolved spectra), we take into account the curvature of the emitting surface following [268]. We define θ as the angle between the emitting material and the z-axis that is pointing towards the observer, see illustration on the side. For a cylindrical coordinate system with $\mu = \cos\theta$, photons emitted at a radius R and time t are observed at a time $T = (1+z)(t - \frac{R\mu}{c})$ and their comoving energy is converted as $E' = E\Gamma(1-\beta\mu)/(1+z) \equiv E\Lambda/(1+z)$. Then, the differential flux $F_E(T)$ is given by

$$F_E(T) = \frac{1}{2D^2}\int_{-1}^{1}\mathrm{d}\mu\int_0^\infty \mathrm{d}R\, R^2 \frac{P'(E', R, \frac{T}{1+z} + \frac{R\mu}{c})}{(1+z)^2\Lambda^2} \,, \tag{6.7}$$

where $P'_{E'}$ can be calculated as $P'_{E'} = j_{E'}/4\pi$ from the comoving differential emissivity $j_{E'}$. In [132] the emissivity of a thin shell is defined as

$$j_{E'} = \frac{cu'_{E'}}{\Delta'} \,, \tag{6.8}$$

where $\Delta' = V'_{\mathrm{C}}/4\pi R'^2_{\mathrm{C}}$ is the comoving shell width.

We follow a simplified approach where the emission from the thin shell is approximated to be released from a single surface at R_{C}. For calculations that invoke only a single radiation zone this over-simplification would severely impact the observed profile. In our case of ~1000 collisions, the emission profile is dominated by the fireball evolution and our simplified approach will not impact the predictions significantly.
For a given collision (with radius R_{C}, emission time t_{C}, Lorentz factor Γ_{C} and width Δ'_{C}) we thus calculate the photon flux per second ($F(T)$, in photons/s/cm^{-2} in a observational energy interval $E_{\min}$, $E_{\max}$) and

[268]: Granot et al. (1999), "Images and spectra from the interior of a relativistic fireball"

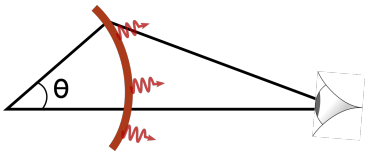

[132]: Dermer et al. (2009), *High energy radiation from black holes: Gamma rays, cosmic rays and neutrinos*

the energy flux ($EF(T)$, in energy/s/cm^{-2} and integrated over the full energy range) as

$$F(T) = \frac{1}{2D^2} \int_{\Lambda(1+z)E_{\min}}^{\Lambda(1+z)E_{\max}} \mathrm{d}E' \, \frac{R_C c}{(1+z)\Lambda^2} \frac{u'_{E',\mathrm{emitted}} \Delta'_C}{E'} \,, \tag{6.9}$$

$$EF(T) = \frac{1}{2D^2} \int \mathrm{d}E' \, \frac{R_C c}{(1+z)\Lambda^2} u'_{E',\mathrm{emitted}} \Delta'_C \,, \tag{6.10}$$

where $\Lambda = \Gamma_C \left[1 - \frac{c\beta_C}{R_C} \left(t_C - \frac{T}{1+z}\right)\right]$. The time-integrated differential fluence $\mathcal{F}_E$ between two observed times T_1 and T_2 is given by

$$\mathcal{F}_E = \frac{1}{2D^2} \int_{T_1}^{T_2} \mathrm{d}\hat{T} \, \frac{c R_C \Delta'_C}{(1+z)} \frac{u'_{E',\mathrm{emitted}}(\Lambda(\hat{T})E)}{\Lambda^2(\hat{T})} \,, \tag{6.11}$$

where $\Lambda(\hat{T}) = \Gamma_C \left[1 - \frac{c\beta_C}{R_C} \left(t_C - \frac{\hat{T}}{1+z}\right)\right]$ varies as a function of observed time $\hat{T}$.

For spectra integrated over the full duration of the burst we apply a simplified procedure: The (differential) observed Fluence $\mathcal{F}_E$ of a single collision is simply given by

$$E\mathcal{F}_E = u'_{E',\mathrm{emitted}} V'_C \frac{\Gamma_C E'}{4\pi(1+z)D^2} \,, \tag{6.12}$$

with the comoving distance D and comoving volume V'_C .

Finally, we calculate the absorption due to interactions with the Extragalactic Background Light (EBL) with the open-source GAMMAPY-package [269, 270], selecting the model of [271].

[269]: Deil et al. (2018), "Gammapy - A prototype for the CTA science tools"
[270]: Nigro et al. (2019), "Towards open and reproducible multi-instrument analysis in gamma-ray astronomy"
[271]: Dominguez et al. (2011), "Extragalactic Background Light Inferred from AEGIS Galaxy SED-type Fractions"

6.4 VHE gamma-ray predictions from a leptonic radiation modelling

The small impact of EBL absorption due to their low redshifts makes LL-GRBs potential targets for IACTs like H.E.S.S., MAGIC or the upcoming CTA observatory. Since in our model the sub-MeV peak is generated by synchrotron radiation, inverse Compton scatterings are a natural contender for VHE emission. For SSC scenarios in the Thomson regime, the ratio of luminosities of the inverse Compton and synchrotron components is labelled 'Thomson-Y parameter':

$$Y_{\mathrm{TH}} = \frac{L_{\mathrm{IC,\,TH}}}{L_{\mathrm{syn}}} \,. \tag{6.13}$$

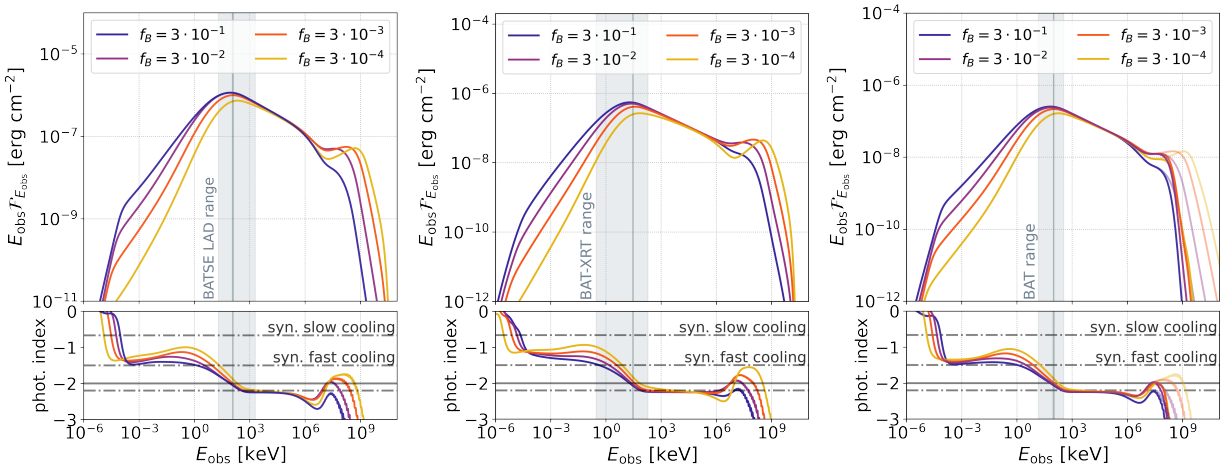

GRB-SP GRB-UL GRB-HL

Figure 6.5: Simulated spectra for the three prototypes, exploring $f_B \in \{3 \cdot 10^{-1}, 3 \cdot 10^{-2}, 3 \cdot 10^{-3}, 3 \cdot 10^{-4}\}$.
Upper panels: Simulated spectra $E_{\rm obs}\mathcal{F}_{E_{\rm obs}}$ for different values of f_B. The vertical lines mark the reported peak energies $E_{\rm peak}$ for the corresponding reference event, the shaded regions indicate the energy range of the observing instrument. For GRB-HL, we show the results without EBL absorption as thin lines.
Lower panels: Photon index (defined as spectral index of $\mathcal{F}_{E_{\rm obs}}/E_{\rm obs}$). We indicate the synchrotron predictions for the slow- and fast-cooling regime ($-2/3$ and -1.5) and the synchrotron spectral slope of a primary distribution $-p_e = -2.5$ that has cooled to $-p_{e,\rm cool} = -3.5$ (-2.25). The solid line corresponds to a photon index of -2, where $E_{\rm obs}\mathcal{F}_{E_{\rm obs}}$ is maximal/minimal.

In the internal shock model, this parameter is simply given by $Y_{\rm TH} = \frac{p-2}{p-1}\frac{\epsilon_e}{\epsilon_B} \propto (f_B)^{-1}$ [184]. Although the inverse Compton efficiency deviates from $Y_{\rm TH}$ in the Klein-Nishina regime, this simple relation emphasises the importance of the microphysics parameters for a potential VHE component induced by inverse Compton scatterings.

[184]: Daigne et al. (2011), "Reconciling observed GRB prompt spectra with synchrotron radiation ?"

Motivated by this, we vary f_B in order to examine under which conditions inverse Compton radiation generates a VHE component potentially observable by IACTs and will explore $f_B \in \{3{\cdot}10^{-1}, 3{\cdot}10^{-2}, 3{\cdot}10^{-3}, 3{\cdot}10^{-4}\}$ (corresponding to $\epsilon_B \in \{10^{-1}, 10^{-2}, 10^{-3}, 10^{-4}\}$ for our choice of $\epsilon_e = 1/3$). From the definition of the comoving magnetic field (Eq. 5.20) we see that large (small) f_B correspond to large (small) magnetic field strengths. As outlined in Section 6.3, for each choice of f_B we adjust $\zeta_{e,0}$ (that is a proxy for the constant minimal Lorentz factor of electrons $\gamma_{e,\rm min}$) such that the observed peak energy of the reference event is approximately reproduced.

We show the simulated time-integrated spectra $E_{\rm obs}\mathcal{F}_{E_{\rm obs}}$ for the three prototype GRBs in Figure 6.5. The energy range of the X-ray instruments that provided the initial detection of the reference events are marked as grey bands, the vertical lines mark the reported peak energies of Table 6.1. Our model is constructed such that synchrotron emission of primary electrons generates the sub-MeV peak, and the fireball wind luminosities are chosen to reproduce the fluence of the reference events. This naturally implies that the spectra around the sub-MeV peak are largely independent of f_B. The exception are the results obtained for $f_B = 3 \cdot 10^{-4}$, where the fluences at the synchrotron peak are much lower than for the other

choices of f_B and may be in disagreement with the observed fluences of the reference events. In principle the fluences in this case could be enhanced by imposing a higher wind luminosity, however at the cost of a reduced comparability to the other results due to changed dynamical properties of the outflow. However, as we show in Appendix B.3, for $f_B = 3 \cdot 10^{-4}$ the physical conditions in the shocked plasma correspond to the slow cooling regime for the majority of collisions of the fireball evolution. This implies that throughout most of the jet evolution, the energy transferred to non-thermal electrons is not converted efficiently into radiation. As this further aggravates the efficiency problem of the internal shock model, we suggest that $f_B = 3 \cdot 10^{-4}$ is not a realistic parameter assumption for our LL-GRB prototypes. We will show the corresponding results in the following only for completeness.

First and foremost, we report a systematic dependence of the VHE fluences on f_B (low f_B lead to high VHE fluences and vice versa). This behaviour is common to all prototypes. We identify two additional probes of f_B:

* *Low-energy fluence*: A systematic dependence of Low-Energy (LE) fluences (in optical/UV regime) on f_B complements the behaviour in the VHE regime: For low f_B we find low LE and high VHE fluences, for high f_B vice versa. The depletion in the LE regime is attributed to two effects: First, low peak-energy spectra generated in late collisions that are in the (marginally) fast-cooling regime, and second the effect of IC scatterings occurring in Klein-Nishina regime for low f_B (see Appendix B.3 and [184]). Beyond the absolute fluence, also the ratio of fluences in the optical and UV band ($\mathcal{F}_{\text{optical}}/\mathcal{F}_{\text{UV}}$) changes for the different magnetic field strengths and could be employed to discriminate between scenarios, as illustrated for GRB-SP in Table 6.3.

  This will however require LL-GRBs to be within the sensitivity range of instruments. For context we compare the optical flux (calculated as the fluence divided by a duration of 1300s) of GRB-UL to *Swift*-UVOT u-band limits reported for GRB 100316D. Out of our scenarios, only $f_B = 3 \cdot 10^{-4}$ is not in tension with the most stringent limit of $1.9 \cdot 10^{-13}$ erg/cm^2/s. For the least stringent *Swift*-UVOT limit both $f_B = 3 \cdot 10^{-3}$ and $f_B = 3 \cdot 10^{-4}$ are not ruled out. We point out that limits were obtained for observation intervals with exposure times much shorter than the burst duration. They should thus be taken cautiously for the scenario of a temporally variable source (as GRB-UL). Further, the limits were obtained assuming a certain absorption in the host galaxy and our own Galaxy. Especially the former is often not well determined from measurements. Nonetheless, these results illustrate how the LE regime could be a useful diagnostic of f_B independent of VHE

Table 6.3: Ratio of optical fluence $\mathcal{F}_{\text{optical}}$ (560 - 730 nm, the r band of ZTF) and UV fluence $\mathcal{F}_{\text{UV}}$ (220-280 nm, the energy range of ULTRASAT) for GRB-SP for different choices of f_B.

f_B	$\mathcal{F}_{\text{optical}}/\mathcal{F}_{\text{UV}}$
$3 \cdot 10^{-1}$	1.24
$3 \cdot 10^{-2}$	1.11
$3 \cdot 10^{-3}$	1.04
$3 \cdot 10^{-4}$	0.93

emission that is subject to EBL absorption. It may constrain the magnetic field strength and can potentially help with the rejection of models and parameter sets (as recently also shown in [186, 272]).

* *Low-energy photon index α:* The lower panels of Figure 6.5 show the spectral index of $\mathcal{F}_{E_{\rm obs}}/E_{\rm obs}$ (called the photon index). In Section 4.4, the photon index below the peak was predicted as $-2/3$ (in the slow-cooling regime)/ $-3/2$ (in the fast-cooling regime). For our prototypes, the photon indexes below the peak reach the fast-cooling prediction for high f_B. Similar to [184] we find that inverse Compton scatterings in the Klein-Nishina regime can result in values of α up to -1 for low f_B, where the photon index systematically increases with lower f_B. This systematic dependence on f_B is common to all prototypes. From this we conclude that in our framework the photon index below the peak may be used as a second complementary probe of f_B. We point out that the spectral slope changes as a function of energy, which means that the fit energy range will have a large impact on the fit result – an effect which should be taken into account when comparing these predictions to data.

[186]: Oganesyan et al. (2019), "Prompt optical emission as a signature of synchrotron radiation in gamma-ray bursts"
[272]: Samuelsson et al. (2020), "Constraining Low-luminosity Gamma-Ray Bursts as Ultra-high-energy Cosmic Ray Sources Using GRB 060218 as a Proxy"

[184]: Daigne et al. (2011), "Reconciling observed GRB prompt spectra with synchrotron radiation ?"

From our sample GRB-HL is the only event that is affected noticeably by EBL absorption. For this prototype we show the spectra without EBL absorption as transparent lines. We infer from the Figure that for its redshift of $z = 0.39$ emission above ~ 0.1 TeV is attenuated and this prototype could not be observed by IACTs. An in-depth investigation of the maximal redshift at which this prototype may be observed by IACTs will be presented below.

Light curves

From Eq. 6.9 we calculate the light curves for our three prototypes in different energy bands, displayed in Figure 6.6. All simulations reproduce the light curve structure of the reference event. The results for the soft gamma-ray and HE regime are mostly independent of f_B (except for $f_B = 3{\cdot}10^{-4}$, for reasons outlined above). In agreement with Figure 6.5 low f_B generate the highest photon fluxes in the (V)HE regimes. Despite the absolute normalisation, we predict a delayed onset of the VHE emission that increases with decreasing f_B.

It may be explained the following way: The early signal in a single-peaked light curve is related to collisions close to the source. These are subject to strong internal $\gamma\gamma$-absorption, which suppresses the high-energy component [18, 273]. This suppression could potentially be slowed by continuous up-scatterings of photons which contribute to a high-energy component. For this, however, relativistic electrons need to be present in the region. As we don't consider a steady injection term but instead follow a cooling electron distribution, this may be realised if electron cooling timescales are long. This is the case for low f_B scenarios, where the synchrotron cooling timescale is long; it is in fact the dominating

[18]: Bustamante et al. (2017), "Multi-messenger light curves from gamma-ray bursts in the internal shock model"
[273]: Hascoet et al. (2012), "Do Fermi-LAT observations imply very large Lorentz factors in GRB outflows ?"

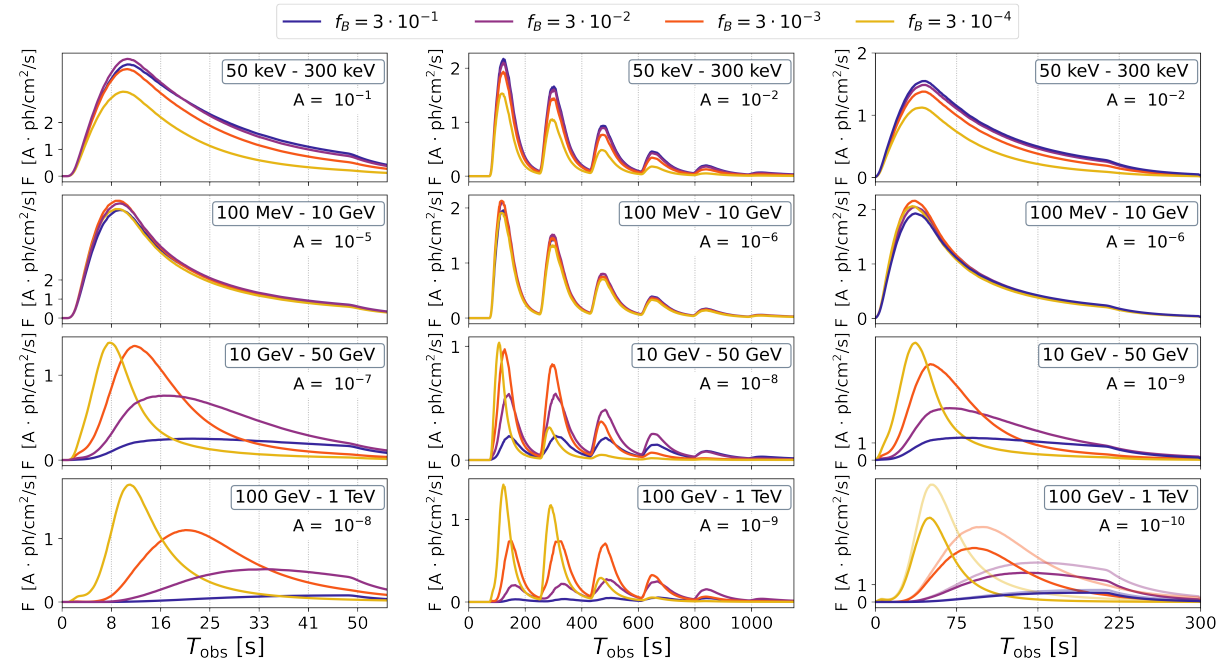

Figure 6.6: Simulated light curves for the three prototypes, exploring $f_B \in \{3 \cdot 10^{-1}, 3 \cdot 10^{-2}, 3 \cdot 10^{-3}, 3 \cdot 10^{-4}\}$. We show the results for different energy bands: 50 - 300 keV (corresponding to a typical soft gamma-ray instrument like *Fermi*-GBM), 100 MeV - 20 GeV (corresponding to a typical gamma-ray instrument like *Fermi*-LAT), 10 GeV - 50 GeV and 100 GeV-1 TeV (somewhat similar to the CTA Large-Sized Telescope, LST and Medium-Sized Telescope, MST).

cooling timescale for high-energy electrons for low f_B scenarios. Another way of preventing an early suppression of the high-energy flux due to $\gamma\gamma$-absorption may be a continuous injection of accelerated particles (ensuring the continuous presence of relativistic electrons in an emission region). The latter could be fuelled by either a slow enough acceleration process or by the injection of relativistic electrons from (neighbouring) collisions and plasma layers. To summarise, for weak magnetic fields an early and strong HE-peak (> 10 GeV) is predicted, it will become wider and peak later in time with increasing f_B. This larger peak width for high f_B might be connected to the high(er) efficiency in late collisions further away from the source for strong magnetic fields.

Redshift study

We study the impact of EBL absorption by placing the same source prototype (GRB-HL) at different redshifts. The corresponding time-integrated spectra are shown in Figure 6.7. Note that the observed duration scales with $(1 + z)$ (see Eq. 5.18); for the smallest redshift of $z = 0.01$ we calculate a duration of ~ 150 s.

The Figure further presents the differential sensitivity of CTA assuming an observation interval of 150s. The latter is defined as the minimum fluence that can be detected with $> 5\sigma$ significance for a given energy range. To derive the sensitivity for the Northern site of CTA we use CTOOLS [274]. We use instrument response functions optimised for short (30 minutes) observations at zenith angles of 20°. The position of the

[274]: Knödlseder et al. (2016), "GammaLib and ctools: A software framework for the analysis of astronomical gamma-ray data"

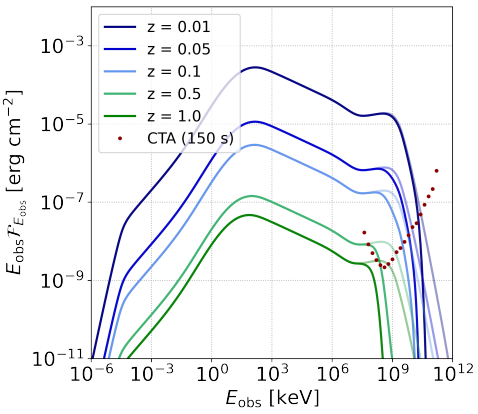

Figure 6.7: Simulated spectra placing the same source prototype (GRB-HL with $f_B = 3 \cdot 10^{-3}$) at different redshifts. The solid lines include EBL absorption, the thin lines are without. We additionally indicate the 150 ms time-integrated sensitivity of CTA.

putative source is displaced by 0.5° from the centre of the field of view of the instrument.

From the Figure we can inter that the observable emission above 1 TeV is strongly attenuated for redshifts of $z > 0.5$. In this sense, the detection of a VHE component requires events to be located at $z < 0.5$. This requirement may be fulfilled for a comparatively large rate number of LL-GRBs which have a high local rate compared to high-luminosity events [239].

6.5 Maximal energies of cosmic-ray nuclei

An increased interest in LL-GRBs has recently risen within a multi-messenger context due to the strong constraints on the amount of non-thermal baryons in conventional long GRBs from neutrino limits. These constraints may be alleviated in the parameter-space region of low luminosities or large emission radii, which typically yield a low neutrino production efficiency [17]. In the context of ultra-long LL-GRBs it is further unclear if neutrino limits are applicable to events with durations longer than 100s (where atmospheric background reduction is difficult, see [67]). With this in mind, LL-GRBs have been proposed as potential sources of UHECRs and/or HE neutrinos in [210, 275–279].

On the other hand [272, 280] argue that cosmic-ray nuclei cannot reach the high energies demanded by UHECR fits in LL-GRBs. We point out a few limitations of their approach: First, the modelling is simplified in the sense that they consider a single radiation zone representative for the complete bust. However past studies such as [18] find that different particle species (UHCERs, neutrinos, gamma-rays) originate from different emission sites along the jet. Second, [272] do not reproduce the observed spectrum of GRB 060218 although using it as a proxy for the population. Third, this GRB is one of the ultra-long GRBs of the sample and it remains questionable whether it can be representative of the complete population. Finally, the limits are obtained under the assumption that LL-GRBs power the UHECR flux, while fixing the fraction of energy that escapes

[239]: Liang et al. (2007), "Low Luminosity Gamma-Ray Bursts as a Unique Population: Luminosity Function, Local Rate, and Beaming Factor"

[17]: Biehl et al. (2018), "Cosmic-Ray and Neutrino Emission from Gamma-Ray Bursts with a Nuclear Cascade"

[67]: Aartsen et al. (2019), "Constraints on minute-scale transient astrophysical neutrino sources"

[210]: Murase et al. (2008), "High-energy cosmic-ray nuclei from high- and low-luminosity gamma-ray bursts and implications for multi-messenger astronomy"

[275]: Murase et al. (2006), "High Energy Neutrinos and Cosmic-Rays from Low-Luminosity Gamma-Ray Bursts?"

[276]: Liu et al. (2011), "Nearby low-luminosity GRBs as the sources of ultra-high energy cosmic rays revisited"

[277]: Senno et al. (2016), "Choked Jets and Low-Luminosity Gamma-Ray Bursts as Hidden Neutrino Sources"

[278]: Zhang et al. (2018), "Low-luminosity gamma-ray bursts as the sources of ultrahigh-energy cosmic ray nuclei"

[279]: Boncioli et al. (2019), "On the common origin of cosmic rays across the ankle and diffuse neutrinos at the highest energies from low-luminosity Gamma-Ray Bursts"

[272]: Samuelsson et al. (2020), "Constraining Low-luminosity Gamma-Ray Bursts as Ultra-high-energy Cosmic Ray Sources Using GRB 060218 as a Proxy"

[280]: Samuelsson et al. (2019), "The Limited Contribution of Low- and High-Luminosity Gamma-Ray Bursts to Ultra-High Energy Cosmic Rays"

[18]: Bustamante et al. (2017), "Multi-messenger light curves from gamma-ray bursts in the internal shock model"

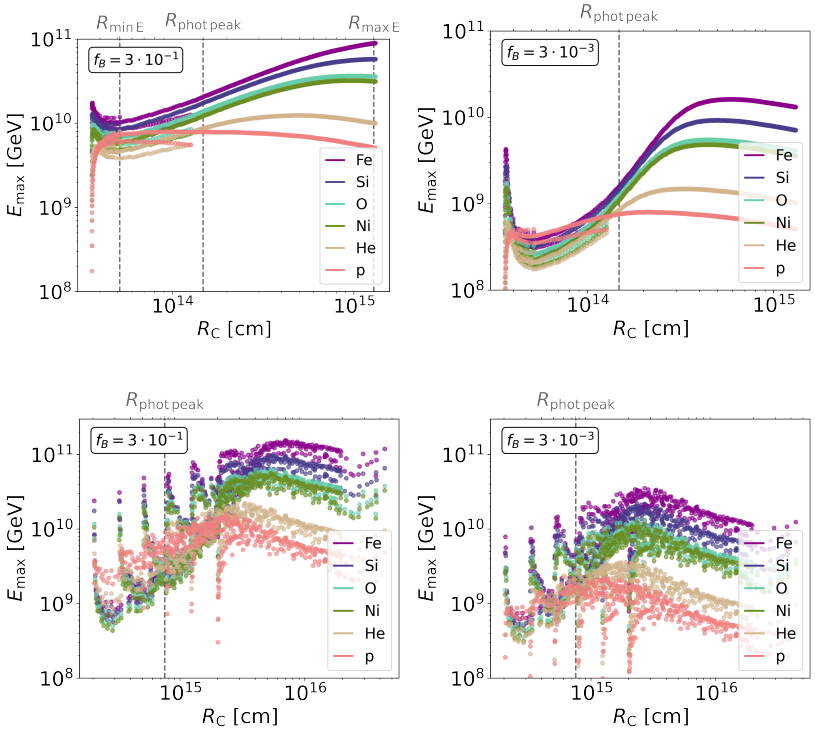

Figure 6.8: Maximal energies of cosmic-ray nuclei (in the source frame) as a function of collision radius for GRB-SP (upper panel) and GRB-UL (lower panel). For both prototypes we explore $f_B = 3 \cdot 10^{-1}$ and $f_B = 3 \cdot 10^{-3}$. Each 'dot' represents one collision. For all scenarios we indicate the radius of maximal photon emission as $R_{\mathrm{phot,peak}}$ (defined as maximum of $\epsilon'_{\mathrm{diss}}$, see Figure 6.4). For GRB-SP and $f_B = 3 \cdot 10^{-1}$ we mark the radii where iron nuclei reach the highest/lowest energies as $R_{\mathrm{min\,E}}$ and $R_{\mathrm{max\,E}}$.

as UHECRs to 10%. This implies a relatively high total luminosity of the bursts that naturally may reflect in high optical fluxes in contradiction with observational constraints.

In reference to their findings and methods, we calculate the maximal energies of different cosmic-ray nuclei for each collision using the simulated photon spectra and fireball evolutions presented earlier. Our procedure is still similar to [272, 278–280]: We balance the acceleration rate ($t'^{-1}_{\mathrm{acc}} = c/R'_{\mathrm{L}}$, see Eq. 3.5) with the energy losses (photo-hadronic cooling, photo-disintegration cooling, synchrotron cooling and adiabatic cooling) with NeuCosmA.

In contrast to [272] our approach thus accounts for different emission regions along the jet (represented by different collisions). We further explicitly reproduce the observed properties of our reference models. Finally, our results are independent of the baryonic loading $f_p = \epsilon_{\mathrm{CR}}/\epsilon_e$ as long as the photon fields are not perturbed by hadronic processes; note that proton-proton interactions are not taken into account given their comparatively low efficiency in these environments.

We limit ourselves to studying GRB-SP (representing normal duration, single-peaked LL-GRBs) and GRB-UL (representing the sub-class of ultra-long GRBs studied in [272]). We proceed similar to before and impose different magnetic field strengths (set by f_B) that will impact the target photon fields but also the acceleration efficiency and synchrotron cooling rate. The maximal energies of different cosmic-ray nuclei for the two prototypes are shown in Figure 6.8, where each dot represents one collision and each colour an element group. We further indicate

[272]: Samuelsson et al. (2020), "Constraining Low-luminosity Gamma-Ray Bursts as Ultra-high-energy Cosmic Ray Sources Using GRB 060218 as a Proxy"
[278]: Zhang et al. (2018), "Low-luminosity gamma-ray bursts as the sources of ultrahigh-energy cosmic ray nuclei"
[279]: Boncioli et al. (2019), "On the common origin of cosmic rays across the ankle and diffuse neutrinos at the highest energies from low-luminosity Gamma-Ray Bursts"
[280]: Samuelsson et al. (2019), "The Limited Contribution of Low- and High-Luminosity Gamma-Ray Bursts to Ultra-High Energy Cosmic Rays"

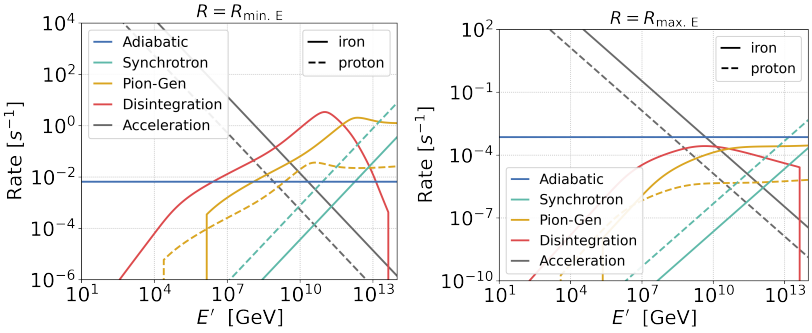

Figure 6.9: Interaction rates (in the co-moving frame) for proton and iron nuclei for GRB-SP ($f_B = 3 \cdot 10^{-1}$) for the collision where iron nuclei reach the highest/lowest energies ($R_{\mathrm{min\,E}}/R_{\mathrm{max\,E}}$), see also Figure 6.8.

the collision radius where the energy dissipated per unit mass $\epsilon'_{\mathrm{diss}}$ is maximal as $R_{\mathrm{phot,peak}}$. For GRB-SP and $f_B = 3 \cdot 10^{-1}$ this is complemented by the radii where iron nuclei reach the highest/lowest energies, labelled as $R_{\mathrm{min\,E}}$ and $R_{\mathrm{max\,E}}$.

We find that iron nuclei (protons) can reach energies up to $\simeq 10^{11}$ GeV (10^{10} GeV), where high f_B (which increase the acceleration rate) yield higher maximal energies. The largest maximal energies are typically found at intermediate to large collision radii above $R_{\mathrm{phot,peak}}$. This again questions the validity of one-zone models where typically the parameters of the collision at $R_{\mathrm{phot,peak}}$ are considered to be representative of the complete burst.

At low collision radii, the maximal energies of nuclear species heavier than protons are low. This can be understood by comparing the loss rates for different processes shown in Figure 6.9 for iron and proton nuclei at $R_{\mathrm{min\,E}}$ and $R_{\mathrm{max\,E}}$ for GRB-SP and $f_B = 3 \cdot 10^{-1}$: The plots demonstrate that iron nuclei are subject to efficient disintegration at $R_{\mathrm{min\,E}}$. This process is experienced by all nuclei heavier than protons, which is the reason for their low maximal energies at small radii. For protons, which suffer pion-generation losses but no photo-disintegration, the radial dependence is not as pronounced. At large radii low target photon densities make adiabatic cooling the dominating energy loss process for all nuclei.

We close this chapter by putting our results in context with literature and the results of the leptonic radiation modelling:

Overall, our findings are compatible with earlier studies (considering that the assumptions and parameters used differ slightly). First we compare to [272, 280]: [280] found that the "highest obtainable energies are $< 10^{19}$ eV and $< 10^{20}$ eV for protons an iron respectively, regardless of the model" for LL-GRBs. This is in agreement with our results for $f_B = 3 \cdot 10^{-1}$ for both prototypes. [272] argue that optical constraints for GRB 060218 limit the maximal energies to even lower values. Indeed, for GRB-UL the optical limits from *Swift*-UVOT non-detection also may favour a low-f_B scenario (as detailed above). This low f_B scenario would however imply low(er) maximal cosmic-ray energies. [272] further report that for a number fraction of accelerated electrons $\zeta_e < 10^{-2}$ and a Lorentz factor

[272]: Samuelsson et al. (2020), "Constraining Low-luminosity Gamma-Ray Bursts as Ultra-high-energy Cosmic Ray Sources Using GRB 060218 as a Proxy"
[280]: Samuelsson et al. (2019), "The Limited Contribution of Low- and High-Luminosity Gamma-Ray Bursts to Ultra-High Energy Cosmic Rays"

of $\Gamma \simeq 30$ their method cannot constrain UHECR acceleration – which however corresponds to the parameter-space region explored by our models.

A fit to UHECR data (spectrum and composition measured by the Pierre Auger observatory) from LL-GRBs are explicitly was presented in [278, 279]. The best fit of [279] requires a comoving maximum silicon energy of $E'_{\rm max} \simeq 10^{9.7}$ GeV (see their Fig. 2, left panel). This is in consistency with the maximal silicon energy of our $f_B = 3 \cdot 10^{-1}$ examples (at large enough distances to the source). We thus infer that under the assumption of efficient acceleration, the maximal energies suffice to describe UHECRs.

Connecting the findings of this section with the leptonic radiation modelling we conclude that a LL-GRB can **either** have a leptonic SSC VHE component in the photon spectrum (for low f_B) **or** accelerate cosmic rays to the highest energies (for high f_B). We point out that a VHE spectral component could alternatively be introduced by hadronic processes. Finally, to test whether LL-GRBs can power the UHECR flux in spite of multi-messenger observations, the maximal baryonic loading compatible with both neutrino limits and photon spectra should be tested. This may be addressed in a future study including self-consistent lepto-hadronic radiation models.

[278]: Zhang et al. (2018), "Low-luminosity gamma-ray bursts as the sources of ultrahigh-energy cosmic ray nuclei"

[279]: Boncioli et al. (2019), "On the common origin of cosmic rays across the ankle and diffuse neutrinos at the highest energies from low-luminosity Gamma-Ray Bursts"

Lepto-hadronic GRB models and application to *Fermi*-LAT detected events

7

7.1 Methods 85

7.2 Educative example: Leptonic models 88

7.3 Educative example: Lepto-hadronic models 93

7.4 Secondary pion/muon cooling and relevance for neutrino spectra 101

7.5 The sample of LAT-detected bursts and reference events 104

7.6 Simulated results for the *Fermi*-LAT inspired prototypes 107

In addition to neutrinos, hadronic signatures in the electromagnetic spectrum could provide evidence for the presence of cosmic rays in GRB outflows. A typical and clear signature would be a peak from neutral pion decays at the highest energies, but also secondary particle cascades can reshape multi-wavelength spectra. Their signatures may be visible at low to intermediate energies that are not subject to strong EBL absorption.

Examining these possible signatures, this chapter focuses on lepto-hadronic radiation models for a multi-zone internal shock scenario. Our methods and the characteristics of an academic example GRB referred to as 'educative example' are introduced in Section 7.1. On leptonic scenarios for this educative example we study the impact of parameter choices in Section 7.2 before turning to lepto-hadronic scenarios in Section 7.3. We complement these results by reviewing secondary pion/muon cooling and its impact on neutrino spectra in Section 7.4. Hadronic signatures have been explored as the origin of a high-energy component observed for some GRBs by the *Fermi*-LAT. Following this idea, we introduce the sample of *Fermi*-LAT detected bursts in Section 7.5 and select two reference events. We present prototypes with characteristics similar to these events in Section 7.6 and discuss whether the results obtained for our educative example are valid in a larger parameter-space region.
The results presented in this section are part of an upcoming publication prepared in collaboration with Maria Petropoulou, Željka Bošnjak and Walter Winter. Furthermore, my collaborator Shan Gao implemented pion/muon cooling and quantum synchrotron emission in AM3 (for details see Appendix A), which are necessary for the numerical modelling of hadronic interactions in GRBs. I then verified these modifications of AM3 by applying the code to a lepto-hadronic GRB model and comparing the results to the literature.

While we followed the simulation procedure proposed in the literature in Chapter 6, this chapter explicitly examines the impact of modelling assumptions and parameter sets. This will allow to critically review the fine-tuning of parameter choices necessary to accommodate typical observational characteristics within a multi-collision model for the GRB prompt phase.

7.1 Methods

We apply the internal shock model of Daigne and Mochkovitch to the outflow. The full description of a collision between a fast (subscript f)

and slow (subscript s) shell can be found in Section 5.1. We modify this model such that the full dissipated energy per collision is accounted for (instead of assuming that the majority of energy is dissipated as the lighter of the two shells sweeps up a mass comparable to its own). The mass and density of the plasma during the collision are then given by

$$m_C = m_f + m_s \,, \tag{7.1}$$

$$\rho' = \frac{m_C}{V'} = \frac{m_C}{4\pi R_C^2 \Gamma_C c \, \mathrm{d}\tau} \,, \tag{7.2}$$

and the dissipated energy as

$$E_{\mathrm{diss}} = m_f \Gamma_f + m_s \Gamma_s - m_C \Gamma_C \,. \tag{7.3}$$

Here we have used the collision parameter symbols from Section 5.1.

Again, our simulations will be guided by gamma-ray observables, namely the isotropic emitted gamma-ray energy $E_{\gamma,\mathrm{iso}}$ and the peak energy E_{peak} of the $E_{\mathrm{obs}}\mathcal{F}_{E_{\mathrm{obs}}}$ spectrum. In our leptonically dominated radiation model, the observed flux around the peak is powered by synchrotron radiation of accelerated electrons. Hence, we normalise to a fixed total energy transferred to non-thermal electrons ($E_{e,\mathrm{tot}} = \sum \epsilon_e E_{\mathrm{diss}}$, summing over all collisions) to reproduce a given $E_{\gamma,\mathrm{iso}}$. When varying the magnetic field strength (through ϵ_B) and/or the fraction of energy transferred to non-thermal baryons (through ϵ_p), we have to keep in mind that energy conservation dictates $\epsilon_\mathrm{p} + \epsilon_e + \epsilon_B \lesssim 1$. From this constraint and the normalisation to $E_{e,\mathrm{tot}}$ it is consistent to relate the microphysics parameters ϵ_B and ϵ_p to ϵ_e: $f_B = \epsilon_B/\epsilon_e$ and the baryonic loading $f_p = \epsilon_p/\epsilon_e$. From the overall dissipation of the fireball ($\varepsilon = E_{\mathrm{diss,tot}}/E_{\mathrm{kin,initial}}$), we can calculate the **minimal** initial kinetic energy of the fireball as

$$E_{\mathrm{kin,min}} = \frac{1}{\varepsilon}(1 + f_B + f_p) E_{e,\mathrm{tot}} \,. \tag{7.4}$$

This is the minimal initial kinetic energy as it does not include the energy transferred to thermal particles. The minimal wind luminosity can be calculated as $L_{\mathrm{wind,min}} = E_{\mathrm{kin,min}}/t_{\mathrm{eng}}$. In each collision the magnetic field is given from the energy density of non-thermal electrons $u'_{\mathrm{ele,NT}} = \epsilon_e u'_{E'}$ as

$$B' = \sqrt{8\pi f_B u'_{\mathrm{ele,NT}}} \,. \tag{7.5}$$

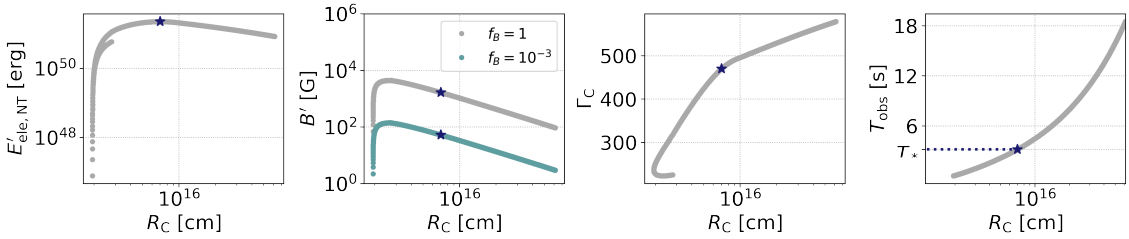

Figure 7.1: Evolution of fireball parameters with collision radius R_C for our educative example. From left to right we show the energy transferred to non-thermal electrons $E'_{\mathrm{ele,NT}} = \epsilon_e u'_{E'} V'_C$ (which remains equal for all choices of f_B and f_p, in the comoving frame), the comoving magnetic field B' for $f_B = 1$ and $f_B = 10^{-3}$, the Lorentz factor Γ_C and the observed time T_{obs}.
We indicate the collision where the dissipated energy is maximal with a star symbol; it will also be labelled 'representative collision' in the following.

Radiation modelling

The radiation modelling is performed with AM3. In contrast to earlier versions of the software, the applied code accounts for muon and pion synchrotron radiation/ cooling and adiabatic cooling of charged particles. Furthermore, quantum synchrotron radiation was implemented following [281]; for more details see Appendix A.

[281]: Brainerd (1987), "Quantum Synchrotron Spectra from Semirelativistic Electrons in Teragauss Magnetic Fields"

For an injection time t'_{inject} of primary particles, we evolve the comoving spectra until $t'_{\mathrm{final}} = t'_{\mathrm{inject}} + t'_{\mathrm{dyn}}$ (where $t'_{\mathrm{dyn}} = t'_{\mathrm{esc}}$ is the dynamical timescale of the system). It is reasonable to believe that after this time the comoving particle spectra will not be subject to substantial change, as the bulk of particles has either cooled or escaped.
In contrast to before, we further account for escape of neutral particles (charged particles remain confined). For an escape timescale t'_{esc}, the spectrum of particles escaped until a simulation time t' can be calculated from the time-dependent comoving energy density $u'_{E'}(t')$ as

$$u'_{E',\mathrm{escaped}} = \frac{1}{t'_{\mathrm{esc}}} \int_{\hat{t}'=0}^{\hat{t}'=t'} u'_{E'}(\hat{t}')\mathrm{d}\hat{t}' \,. \tag{7.6}$$

Consequently, the full time-integrated emitted spectrum $u'_{E',\mathrm{emitted}}$ (of a single collision) is given as

$$u'_{E',\mathrm{emitted}} = \frac{1}{t'_{\mathrm{esc}}} \int_{\hat{t}'=0}^{\hat{t}'=t'_{\mathrm{final}}} u'_{E'}(\hat{t}')\mathrm{d}\hat{t}' + u'_{E'}(t'_{\mathrm{final}}) \,. \tag{7.7}$$

For these spectra we follow the same procedure outlined in Section 6.3 for the calculation of observed quantities (such as light curves and spectra in the observers frame).

Introducing an educative example

Before moving to more complex setups, we will examine the impact of modelling choices and hadronic signatures at a simple, academic GRB,

dubbed the 'educative example'. We choose a burst with a relatively high photon luminosity, for two reasons: First, a high kinetic energy of the outflow is advantageous to power the UHECR flux (from simple energy requirements, see discussion in Section 5.3). Second, *Fermi*-LAT detected events (that will be examined later on in this chapter) populate the upper range of the $E_{\gamma,\mathrm{iso}}$ distribution. For simplicity, we further assume a smooth single-peaked light curve without stochastic engine behaviour. The initial Lorentz factor distribution is thus given by the same profile as for GRB-SP and GRB-HL in Chapter 6 Figure 6.3 and can be characterised by its maximum and minimum Lorentz factor and the engine active t_{eng}. The observational burst characteristics and fiducial fireball parameters of our educative example are summarised in Table 7.1 (complemented by Table B.2).

Table 7.1: Characteristics of the educative example.
Burst characteristics: Isotropic emitted gamma-ray energy $E_{\gamma,\mathrm{iso}}$ (between 1 and 10000 keV), redshift z, peak energy E_{peak} and approximate observed duration T_{dur}.
Fiducial fireball parameters: Total energy transferred to non-thermal electrons $E_{\mathrm{e,tot}}$, fireball efficiency ε, minimum and maximum Lorentz factor of the initial shell distribution ($\Gamma_{\mathrm{min}}^{\mathrm{initial}}$, $\Gamma_{\mathrm{max}}^{\mathrm{initial}}$), number of initial plasma shells $N_{\mathrm{shells}}^{\mathrm{initial}}$ and engine active time t_{eng}.

Burst characteristics	
$E_{\gamma,\mathrm{iso}}$	10^{54} erg
z	2
E_{peak}	400 keV
T_{dur}	15 s
Fiducial fireball parameters	
$E_{\mathrm{e,tot}}$	$1.3 \cdot 10^{54}$ erg
ε	7.8 %
$\Gamma_{\mathrm{min}}^{\mathrm{initial}}$, $\Gamma_{\mathrm{max}}^{\mathrm{initial}}$	200, 700
$N_{\mathrm{shells}}^{\mathrm{initial}}$	1000
t_{eng}	5 s

7.2 Educative example: Leptonic models

Within a purely leptonic radiation model we explore the impact of the following parameter assumptions and modelling choices: *(a)* The injection timescale of accelerated particles, *(b)* the scaling of the number fraction of accelerated electrons throughout the fireball evolution, *(c)* the maximum and minimum (initial) Lorentz factor of the outflow, *(d)* the magnetic field strength (set through f_B) and *(e)* EBL absorption. This will allow to critically review the parameter and model choices generally applied in GRB radiation models. The simulated spectra examining these aspects are shown in Figure 7.2.

(a) Injection timescale of accelerated particles
In Chapter 6 (guided by the model applied in [184, 234, 235]), the injection timescale of primary electrons (for each single-collision radiation calculation) was infinitesimally small. Simply spoken this corresponds to separate acceleration and radiation zones, and means that no assumptions on the details of the acceleration process are made. On the other hand it is unclear how the radiation zone can be filled on an infinitesimally small timescale without any particle interactions. To scrutinise the implications of different choices of the injection timescale, we show the simulated spectra for $t'_{\mathrm{inject}} = t'_{\mathrm{dyn}}$ and $t'_{\mathrm{inject}} = 0.01 t'_{\mathrm{dyn}}$ (labelled as $\delta t'_{\mathrm{inject}} \rightarrow 0$) in Figure 7.2.
We find that the results for the two injection timescale agree well for strong magnetic fields (high f_B). For low f_B, several differences between the results for the two injection timescales manifest: The most noticeable one is the lower fluence around the keV synchrotron peak for $t'_{\mathrm{inject}} = t'_{\mathrm{dyn}}$. We further report a more intense (V)HE component and enhanced low-energy fluences for $t'_{\mathrm{inject}} = t'_{\mathrm{dyn}}$. Finally, the systematic dependence of the low-energy photon index reported for LL-GRBs and for $\delta t'_{\mathrm{inject}} \rightarrow 0$

[184]: Daigne et al. (2011), "Reconciling observed GRB prompt spectra with synchrotron radiation ?"
[234]: Bosnjak et al. (2009), "Prompt high-energy emission from gamma-ray bursts in the internal shock model"
[235]: Bošnjak et al. (2014), "Spectral evolution in gamma-ray bursts: predictions of the internal shock model and comparison to observations"

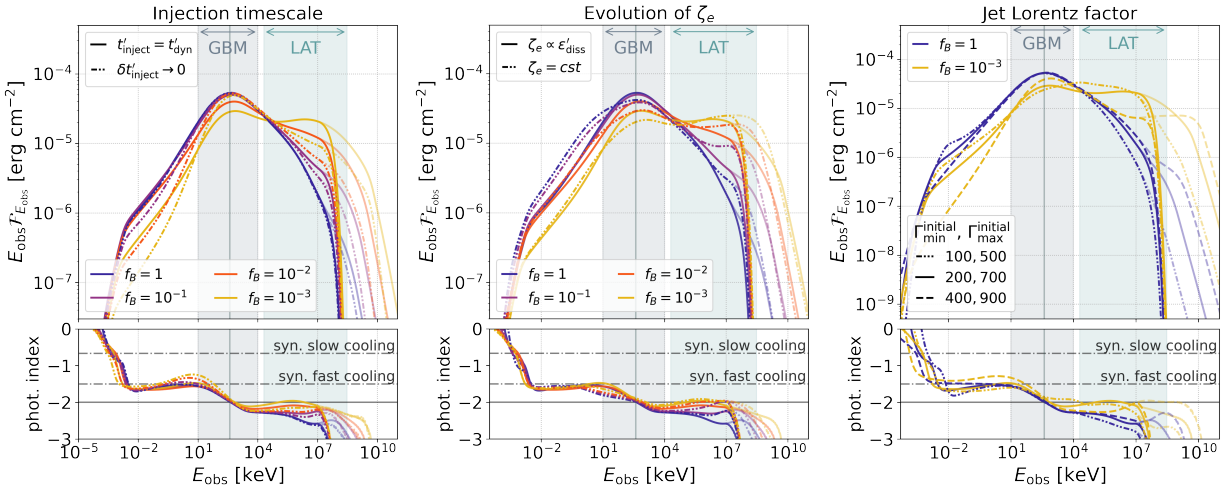

Figure 7.2: Educative example leptonic scenarios: Simulated spectra exploring the impact of *(left)* the injection timescale of accelerated particles $t'_{\rm inject}$, *(middle)* the scaling of the number fraction of accelerated electrons ζ_e throughout the fireball evolution and *(right)* the minimum and maximum Lorentz factors of the initial Lorentz factor distribution ($\Gamma^{\rm initial}_{\rm min}$, $\Gamma^{\rm initial}_{\rm max}$). In all scenarios we study the impact of the magnetic field strength by setting different $f_B = \epsilon_B/\epsilon_e$.
Upper panels: Simulated spectra $E_{\rm obs}\mathcal{F}_{E_{\rm obs}}$. The vertical lines mark the chosen peak energy of 400 keV, the shaded regions indicate the energy ranges of the *Fermi*-GBM and *Fermi*-LAT. Thin lines correspond to the results without EBL absorption.
Lower panels: Photon index (defined as spectral index of $\mathcal{F}_{E_{\rm obs}}/E_{\rm obs}$). Dashed lines indicate the synchrotron predictions for the slow- and fast-cooling regime ($-2/3$ and -1.5); the solid line corresponds to a photon index of -2, where $E_{\rm obs}\mathcal{F}_{E_{\rm obs}}$ is maximal/minimal.

cannot be reproduced in the case of a long(er) injection timescale. As these effects increase with decreasing f_B, we attribute them to inverse Compton scatterings that are more efficient in case of low f_B. The exact reason for these behaviours will be examined later; for now we state that high-f_B synchrotron-dominated models are robust against variations of the injection timescale of energetic particles, whereas low-f_B scenarios are sensitive to the choice of $t'_{\rm inject}$.

(b) Evolution of the number fraction of accelerated electrons ζ_e

GRB synchrotron models within the internal shock scenario commonly set the number fraction of accelerated electrons proportional to the dissipated energy per unit mass ($\zeta_e \propto \varepsilon'_{\rm diss}$). The intention is to keep the minimum Lorentz factor of electrons $\gamma_{e,\rm min}$ constant throughout the fireball evolution (see Eq. 6.3) which is thought to result in narrow(er) spectra. In the middle panel of Figure 7.2, we show the results of for $\zeta_e \propto \varepsilon'_{\rm diss}$ and ζ_e = cst., under the assumption that $t'_{\rm inject} = t'_{\rm dyn}$ (for parameters see Table B.2). Independent of f_B the simulations with ζ_e = cst. are different in two main points: First, the synchrotron peak is broadened and reduced in energy fluence. Second, the low-energy and high-energy fluences are enhanced. The broad synchrotron peak reflects in the photon indexes, which are relatively flat around the peak. With values that are overall below -1.5, it is questionable whether ζ_e = cst. can produce narrow spectra compatible with observations.

We conclude that $\zeta_e \propto \varepsilon'_{\rm diss}$ (which yields a constant minimum Lorentz factor of electrons $\gamma_{e,\rm min}$ throughout the fireball evolution) is necessary to reproduce spectra compatible with observed ones within a multi-

collision model. We point out that this is a somewhat fine-tuned choice and should be confirmed by simulations of particle acceleration in (mildly) relativistic shocks for a broad range of shock strengths and comoving energy densities.

(c) Initial jet Lorentz factor
Next, we examine the impact of the jet Lorentz factor. We choose three different initial Lorentz factor distributions, characterised by their minimal and maximal Γ:

$$(\Gamma_{\mathrm{min}}^{\mathrm{inital}}, \Gamma_{\mathrm{max}}^{\mathrm{inital}}) \in \{(100, 500), (200, 700), (400, 900)\}\,.$$

For the sake of simplicity, we only show the results for $f_B = 1$ and $f_B = 10^{-3}$. We find that for a synchrotron-dominated scenario with negligible inverse Compton contributions ($f_B = 1$), the results are robust against variations of the initial Lorentz factor distribution. However, the $f_B = 10^{-3}$ scenario with dominant inverse Compton contributions shows strong dependence on the Lorentz factor distribution: The lower the Lorentz factors, the stronger the distortions of the spectrum. A natural explanation for this behaviour is the impact of lepton pairs produced in $\gamma\gamma$-annihilation, which are produced in dense environments and distort the spectrum by synchrotron radiation at low energies and inverse Compton radiation at high energies. For low Lorentz factors, the comoving densities are higher (due to smaller collision radii and a smaller effect of boosting). Consequently, the $\gamma\gamma$-annihilation efficiency is increased and a large number of pairs reshape the spectrum.

(d) Magnetic field strength
We proceed by reviewing the impact of the magnetic field strength (through $f_B = \epsilon_B/\epsilon_e$), which we varied for all scenarios presented above. In Chapter 6, we found a systematic dependence of the VHE and LE fluence as well as the low-energy photon index on f_B.
Overall, we confirm the dependence of the (V)HE fluence on f_B that is common to all parameter and modelling choices. Also the LE (optical and UV) fluences are generally enhanced with respect to the sub-MeV peak for low values of f_B. However, as outlined above, we cannot generally confirm the systematic dependence of the photon index below the peak on f_B.

(e) EBL absorption
The high redshift of $z = 2$ assumed for our educative example further allows to study the impact of EBL absorption on (V)HE spectra. In Section 6.4, we found a suppression of the VHE fluence for $z > 0.5$. This is in agreement with our results in Figure 7.2 where the fluence above 10^8 keV = 10^{11} eV is EBL-absorbed. We thus conclude that for $z > 2$, any signatures beyond the energy range of the LAT will not be observable.

From here on we will use $t'_{\mathrm{inject}} = t'_{\mathrm{dyn}}$ and $\zeta_e \propto \varepsilon'_{\mathrm{diss}}$ in all simulations.

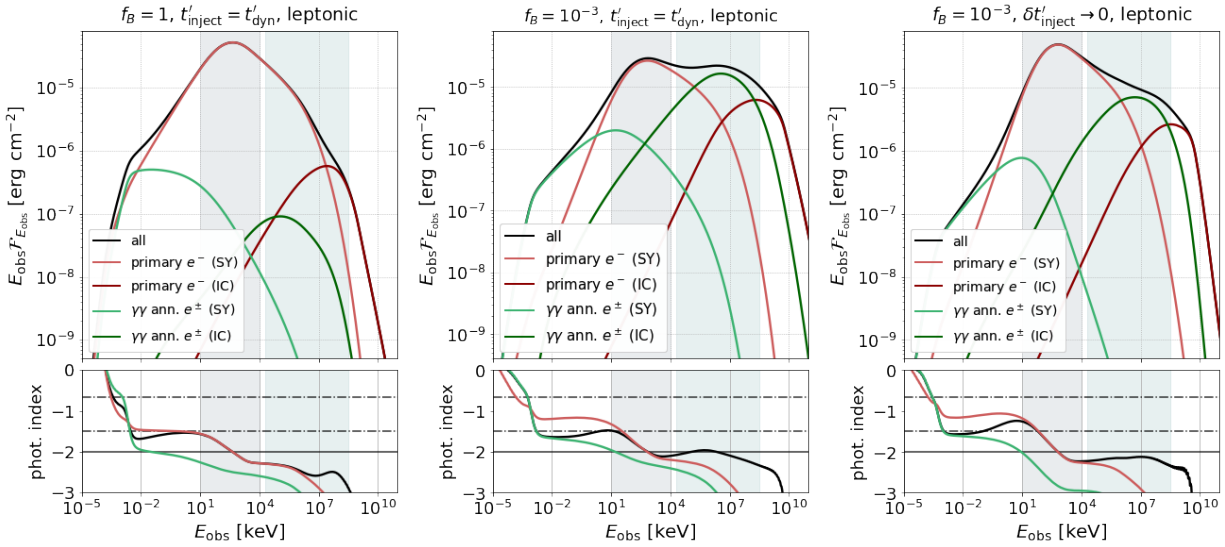

Figure 7.3: Decomposed spectra and photon indices for the educative example, with parameter choices indicated above the single plots. We show the synchrotron (SY) and inverse Compton (IC) contributions of primary electrons and secondary lepton pairs from $\gamma\gamma$-pair annihilation.
Upper panels: Simulated spectra $E_{\rm obs}\mathcal{F}_{E_{\rm obs}}$. The shaded regions indicate the energy ranges of the *Fermi*-GBM and *Fermi*-LAT.
Lower panels: Photon index (defined as spectral index of $\mathcal{F}_{E_{\rm obs}}/E_{\rm obs}$). Dashed lines indicate the synchrotron predictions for the slow- and fast-cooling regime ($-2/3$ and -1.5); the solid line corresponds to a photon index of -2, where $E_{\rm obs}\mathcal{F}_{E_{\rm obs}}$ is maximal/minimal. For the sake of simplicity, we show only the spectral indices of the synchrotron components and the overall photon index.

We further neglect the effect of EBL absorption for the remainder of this section.

Decomposition into emission processes

Our results for $t'_{\rm inj} = t'_{\rm dyn}$ do not reproduce the low-energy photon index of up to $\alpha \simeq -1$ found in Chapter 6 and reported *e.g.* in [184]. For further investigation we decompose the spectra by emitting particle species (primary electrons or secondary lepton pairs from $\gamma\gamma$-annihilation) and radiation process (synchrotron or inverse Compton). The inverse Compton component of a particle distribution is defined as the emission produced by those particles scattering on the complete photon distribution. Figure 7.3 shows the decomposed simulated spectra $E_{\rm obs}\mathcal{F}_{E_{\rm obs}}$ for $f_B = 1$ and $f_B = 10^{-3}$ (for $t'_{\rm inject} = t'_{\rm dyn}$ and $\delta t'_{\rm inject} \to 0$).
For $f_B = 1$ inverse Compton of primary electrons and the contribution of secondary leptons are negligible and the observed spectrum is dominated by synchrotron radiation of primary electrons.
In contrast to this, the radiation of secondary lepton pairs as well as inverse Compton emission of primary electrons produce distinct spectral features for $f_B = 10^{-3}$. It is noteworthy to report that contributions of secondary lepton pairs (at low and high energies) have not been captured by past publications such as [234]. In this sense, those studies may not have provided accurate results for these energy ranges for parameter sets and scenarios with a high $\gamma\gamma$-annihilation efficiency.

[184]: Daigne et al. (2011), "Reconciling observed GRB prompt spectra with synchrotron radiation ?"

[234]: Bosnjak et al. (2009), "Prompt high-energy emission from gamma-ray bursts in the internal shock model"

The injection timescale $t'_{\rm inj}$ affects the normalisation of the sub-MeV synchrotron peak: For $\delta t'_{\rm inj} \to 0$, the fluence around the peak is similar to high-f_B scenarios, for $t'_{\rm inj} = t'_{\rm dyn}$ it is lower. This may be related to the dominating energy loss mechanism of primary electrons at $\gamma_{e,\rm min}$: For $\delta t'_{\rm inj} \to 0$, energetic primaries are present only at early t'. However, at this point the photon spectra are just building up and cannot serve as target fields for inverse Compton scatterings. Consequently, the efficiency of inverse Compton scatterings is low(er) and primary electrons at $\gamma_{e,\rm min}$ predominantly cool through synchrotron emission. For $t'_{\rm inj} = t'_{\rm dyn}$, high-energy electrons are available for longer times, facilitating efficient inverse Compton scatterings and reducing the synchrotron cooling and emission of electrons at $\gamma_{e,\rm min}$.

The shape of the primary electron synchrotron spectrum is very similar for both injection timescales and the primary synchrotron photon index (lower panel of Figure 7.3) deviates from the synchrotron fast-cooling prediction at low energies. However, for $t'_{\rm inj} = t'_{\rm dyn}$, the synchrotron contribution of secondary leptons effectively softens the spectrum to a photon index of $\simeq -1.5$. In this sense, our results remain compatible with the findings of [184, 187, 188], who predicted a low-energy photon index of up to $\alpha \simeq -1$ due to inverse Compton scatterings in the Klein-Nishina regime. The presented results however highlight the importance of a complete radiation treatment invoking also secondary particles and their emission, that can reshape the photon spectra.

[184]: Daigne et al. (2011), "Reconciling observed GRB prompt spectra with synchrotron radiation ?"
[187]: Nakar et al. (2009), "Klein-Nishina effects on Synchrotron and Synchrotron self-Compton spectrum"
[188]: Duran et al. (2012), "Inverse Compton cooling in Klein-Nishina regime and GRB prompt spectrum"

Comoving evolution of the representative collision

For a better understanding of the physical processes shaping the multi-wavelength spectra we examine the collision in which most of the energy is dissipated (the 'representative collision', marked with a star symbol ($\star$) in Figure 7.1). For this collision we show the emitted (decomposed) spectrum and the loss rates for leptons and photons in Figure 7.4, for $f_B = 1$ (upper panel) and $f_B = 10^{-3}$ (lower panel). The relative contributions of the single components to the emitted spectra of the representative collision (left plots of Figure 7.4) are similar to the full time-integrated spectrum. This underlines that despite the contributions of other collisions, the results for this collision are somewhat representative for the complete burst.

The middle and right plots of Figure 7.4 show the loss rates for photons and electrons. For photons we further indicate the emitted photon spectrum on the right y-axis, for electrons the injected primary distribution. Loss rates of time-dependent processes are shown at $t' \in \{0.25, 0.5, 0.75\} t'_{\rm dyn}$ with different line styles. Naturally, the weaker magnetic field for $f_B = 10^{-3}$ demands a larger minimum Lorentz factor to reproduce the same synchrotron peak energy (recall that $E_{\rm syn} \propto \gamma^2_{e,\rm min} B'$). However, as the synchrotron cooling rate scales with B'^{-2}, in this scenario electrons can be accelerated to higher Lorentz factors. Consequently, the primary electron distribution is shifted to higher energies. We further

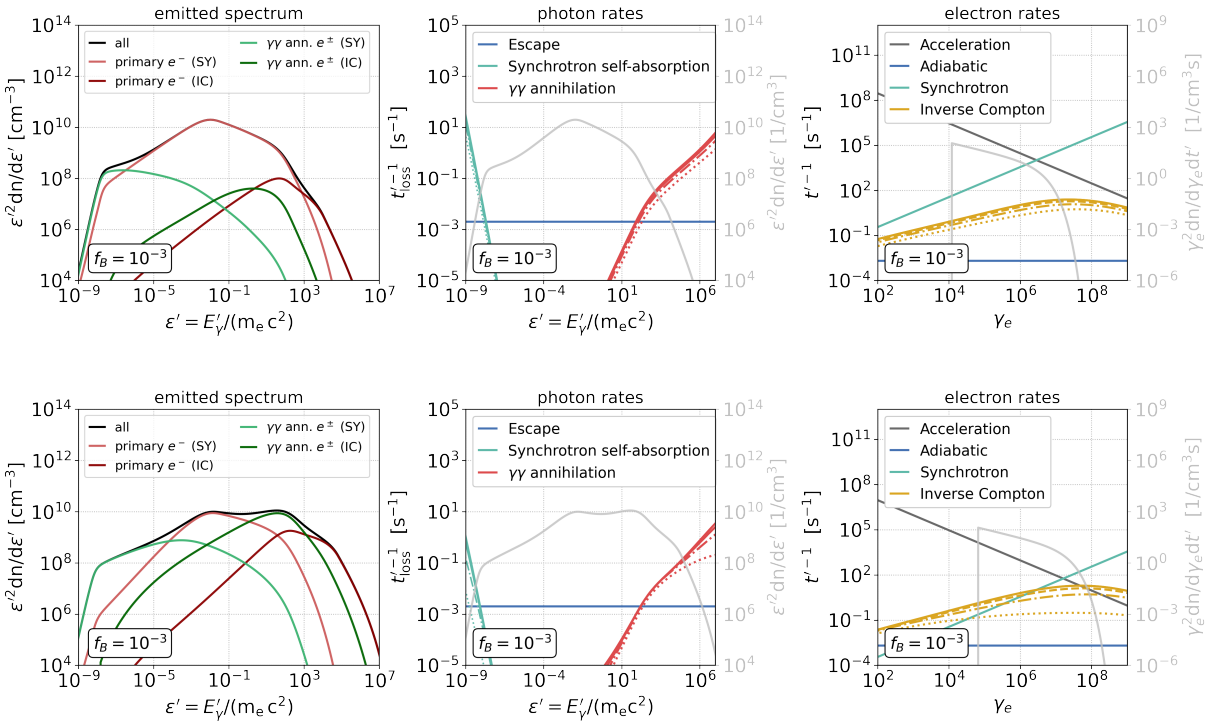

Figure 7.4: Examining the representative collision in a leptonic scenario for $t'_{\rm inject} = t'_{\rm dyn}$ and $f_B = 1$ (top)/ $f_B = 10^{-3}$ (bottom).
Left: Decomposed emitted spectrum with synchrotron (SY) and inverse Compton (IC) contributions of primary electrons and secondary lepton pairs from $\gamma\gamma$-annihilation.
Middle and right: Loss and acceleration rates t'^{-1} for photons and electrons. For processes evolving with time we show the results at $0.25t'_{\rm dyn}$ (dotted), $0.5t'_{\rm dyn}$ (dash-dotted), $0.75t'_{\rm dyn}$ (dashed), $1.0t'_{\rm dyn}$ (solid). The second y-axes show the emitted photon spectrum and the distribution of injected primary electrons.

notice that while inverse Compton scatterings are sub-dominant for all times and energy ranges for $f_B = 1$, they are the dominating energy loss mechanism for low- to medium-energy electrons for $f_B = 10^{-3}$. Indeed, the electrons around $\gamma_{e,\rm min}$ cool predominantly through inverse Compton scatterings for $t' \gtrsim 0.25t'_{\rm dyn}$. The scaling of the cooling rate which differs from the synchrotron one reflects in the shape of the cooled electron spectrum. This spectrum, in turn, is reflected in the photon index – as shown in Figure 7.3, where for the primary synchrotron emission photon indices of up to ~ -1 were achieved.
The photon fields are shaped by synchrotron self-absorption at the lowest and $\gamma\gamma$-annihilation at the highest energies, where both loss rates evolve little with simulation time. The position of the spectral breaks can be inferred from the intersection of the respective loss rates with the escape rate.

7.3 Educative example: Lepto-hadronic models

To power the UHECR flux from GRBs, UHECR fits usually demand a relatively high baryonic loading f_p. For example, the fit presented in [215] (summarised in Chapter 5) required a baryonic loading of the order

[215]: Heinze et al. (2020), "Systematic parameter space study for the UHECR origin from GRBs in models with multiple internal shocks"

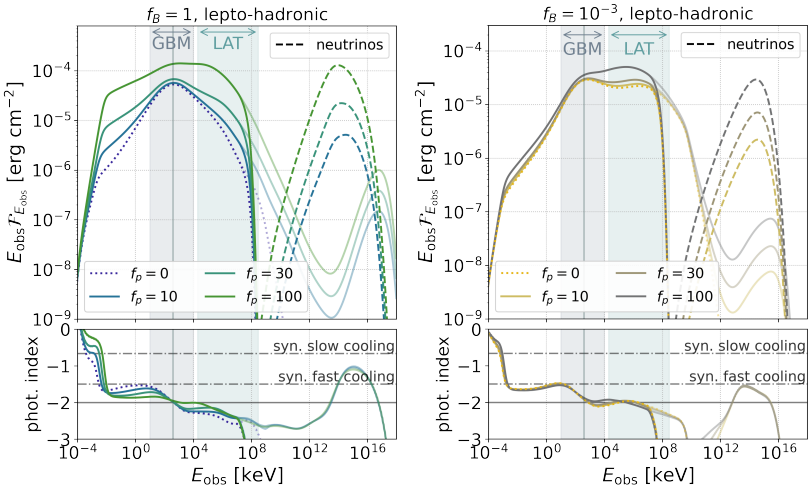

Figure 7.5: Simulated photon and all-flavour neutrino spectra for the educative example, exploring different f_p for *(left)* $f_B = 1$ and *(right)* $f_B = 10^{-3}$. **Upper panels**: Simulated spectra $E_{\rm obs}\mathcal{F}_{E_{\rm obs}}$ for different values of f_p. Shaded regions indicate the energy ranges of the *Fermi*-GBM and *Fermi*-LAT, the vertical line marks the chosen peak energy of 400 keV. **Lower panels:** Photon index (defined as spectral index of $\mathcal{F}_{E_{\rm obs}}/E_{\rm obs}$). Dashed lines indicate the synchrotron predictions for the slow- and fast-cooling regime ($-2/3$ and -1.5); the solid line corresponds to a photon index of -2, where $E_{\rm obs}\mathcal{F}_{E_{\rm obs}}$ is maximal/minimal.

of 50-100. This is in consistency with the findings of other publications such as [212] and the $f_p \simeq 25$ estimated in [233]. Within a self-consistent model, a crucial puzzle piece confirming the validity of GRB UHECR fits is thus to prove that typical f_p are compatible with observed spectra.
In this context, [189, 191] explored internal shock models with $f_p > 0$ in a steady-state models. The results were extended in time-dependent models in [282, 283]. While those studies self-consistently calculate the keV-range observed spectrum from primary electrons, [213, 284] studied hadronic interactions on a more generic spectrum motivated by observations (*i.e.* a Band function or grey body).

In [282, 284], hadronic signatures were explored as potential origin of a HE component that was in some cases observed by the *Fermi*-LAT. In the same spirit as those studies, we investigate lepto-hadronic scenarios of our educative example paying special attention to a HE component.
In our leptonic study, no HE enhancement was found for the synchrotron dominated scenario of $f_B = 1$. In contrast to this, low-f_B scenarios showed an increased HE fluence due to inverse Compton scatterings of primary and secondary leptons. Motivated by these findings, we select $f_B = 1$ and $f_B = 10^{-3}$ to investigate the impact of the magnetic field strength on a potential HE component in a lepto-hadronic model. We impose again $t'_{\rm inject} = t'_{\rm dyn}$ and $\zeta_e \propto \varepsilon'_{\rm diss}$) and explore $f_p \in \{0, 10, 30, 100\}$.
For all realisations we choose a minimum Lorentz factor of protons of $\gamma_{p,\rm min} = 10$ and determine the maximal proton Lorentz factor $\gamma_{p,\rm max}$ by balancing acceleration (in the Bohm limit, as for electrons) with all hadronic loss processes at each timestep of the radiation calculations.

The simulated photon and neutrino spectra are shown in Figure 7.5.
For $f_B = 1$, we report two main effects on the SED: First, a wing-like broadening of the sub-MeV peak which increases with f_p. This feature was also found in other publications [213, 283, 284]. The second feature is a VHE bump (which we attribute to π^0 decays) that again scales with

[212]: Globus et al. (2015), "UHECR acceleration at GRB internal shocks"
[233]: Rudolph et al. (2022), "Multi-wavelength radiation models for low-luminosity GRBs and the implications for UHECRs"
[189]: Asano et al. (2007), "Prompt GeV-TeV Emission of Gamma-Ray Bursts Due to High-Energy Protons, Muons and Electron-Positron Pairs"
[191]: Asano et al. (2009), "Prompt High-Energy Emission from Proton-Dominated Gamma-Ray Bursts"
[282]: Asano et al. (2012), "Delayed Onset of High-Energy Emissions in Leptonic and Hadronic Models of Gamma-Ray Bursts"
[283]: Asano et al. (2014), "Neutrino and Cosmic-Ray Release from Gamma-Ray Bursts: Time-Dependent Simulations"
[213]: Petropoulou (2014), "The role of hadronic cascades in GRB models of efficient neutrino production"
[284]: Wang et al. (2018), "Hadronic origin of prompt high-energy emission of gamma-ray bursts revisited: in the case of a limited maximum proton energy"
[282]: Asano et al. (2012), "Delayed Onset of High-Energy Emissions in Leptonic and Hadronic Models of Gamma-Ray Bursts"
[284]: Wang et al. (2018), "Hadronic origin of prompt high-energy emission of gamma-ray bursts revisited: in the case of a limited maximum proton energy"

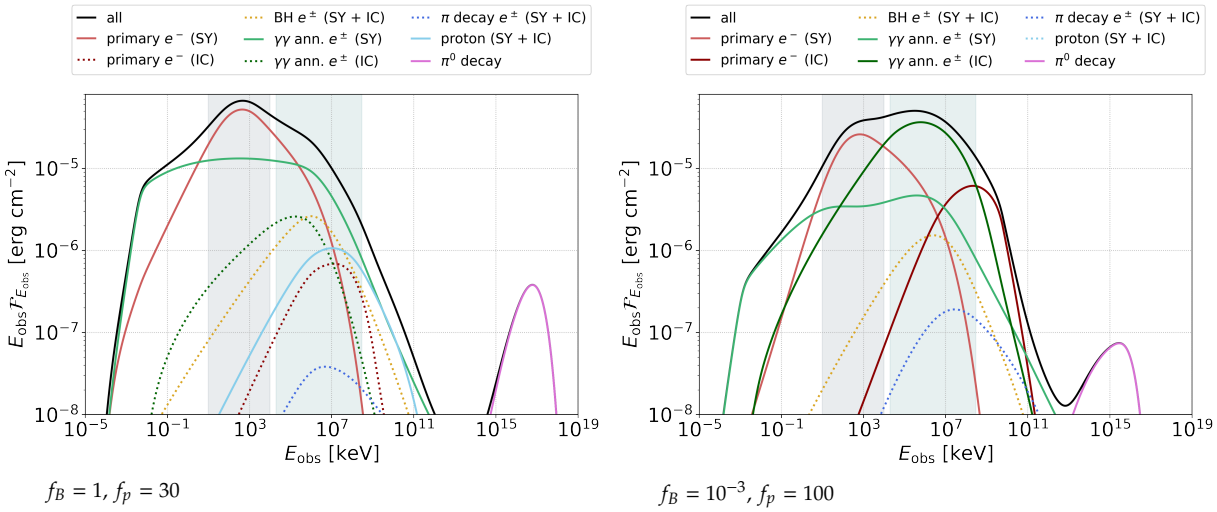

Figure 7.6: Decomposed lepto-hadronic spectra $E_{\rm obs}\mathcal{F}_{E_{\rm obs}}$ for lepto-hadronic scenarios of the educative example.
We show contributions of the following particle species: primary electrons, photo-pair produced $e^\pm$ (labeled as Bethe-Heitler, BH), secondary $e^\pm$ from $\gamma\gamma$-annihilation, $e^\pm$ from pion decays, primary protons and photons from neutral pion decays. For charged particles we indicate the synchrotron (SY) and inverse Compton (IC) emission; dominant contributions are shown as solid lines, sub-dominant contributions as dotted lines.
Shaded regions indicate the energy ranges of the *Fermi*-GBM and *Fermi*-LAT.

f_p in intensity. The neutrino peak energies are shifted to slightly lower energies with respect to this high-energy peak, the neutrino fluxes also scale with f_p in intensity.

For $f_B = 10^{-3}$, only the spectrum **above** the sub-MeV peak is affected. Here, $f_p = 100$ is the only case for which a significant deviation from the purely leptonic scenario is found in the *Fermi*-LAT range. Both the VHE peak and the neutrino peak are at lower energies than for $f_B = 1$, and the cut-off in the neutrino spectrum is close to the photon spectrum cut-off. In both scenarios, the VHE peak is absorbed due to interactions with the EBL. In this sense, only secondary cascade emission up to the LAT energy range or neutrinos could serve as probes of hadronic interactions. From here on, we will again show results without EBL absorption.

[213]: Petropoulou (2014), "The role of hadronic cascades in GRB models of efficient neutrino production"
[283]: Asano et al. (2014), "Neutrino and Cosmic-Ray Release from Gamma-Ray Bursts: Time-Dependent Simulations"
[284]: Wang et al. (2018), "Hadronic origin of prompt high-energy emission of gamma-ray bursts revisited: in the case of a limited maximum proton energy"

Decomposition into emission processes

We follow the same procedure as for the leptonic scenarios and first decompose the full time-integrated spectra by emission process in Figure 7.6 (for $f_B = 1$, $f_p = 30$ and $f_B = 10^{-3}$, $f_p = 100$). The Figure shows contributions of the following particle species: primary electrons, photo-pair produced $e^\pm$ (labelled as Bethe-Heitler, BH), secondary $e^\pm$ from $\gamma\gamma$-annihilation, $e^\pm$ from pion decays, primary protons and photons from neutral pion decays. For charged particles we indicate the synchrotron (SY) and inverse Compton (IC) emission; dominant contributions are shown as solid lines, sub-dominant contributions as dotted lines.

For $f_B = 1$, we can clearly identify the mechanism responsible for the broadening of the sub-MeV peak as synchrotron emission of lepton pairs

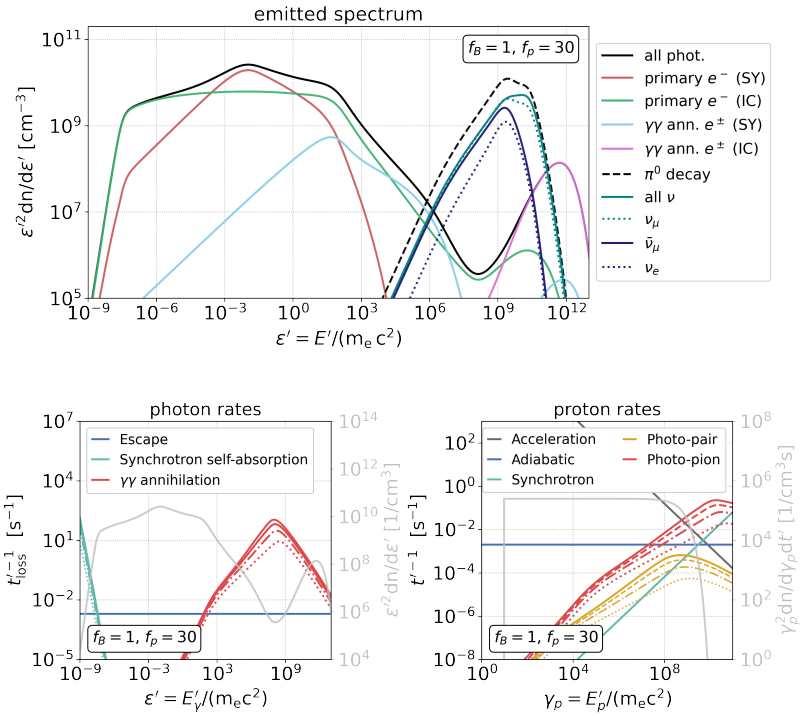

Figure 7.7: Top: Decomposition of the emitted spectrum of the representative collision for $f_B = 1$, $f_p = 30$. For photons we show only the dominant contributions identified in Figure 7.6. The neutrino spectra are shown per flavour (ν_μ, $\bar{\nu}_\mu$, ν_e, $\bar{\nu}_e$) and all-flavour (dashed). **Bottom:** Loss and acceleration rates for photons and protons. For processes evolving with time we show the results at $0.25t'_{dyn}$ (dotted), $0.5t'_{dyn}$ (dash-dotted), $0.75t'_{dyn}$ (dashed), $1.0t'_{dyn}$ (solid). The second y-axes show the emitted photon spectrum and the distribution of injected primary protons at $t' = t'_{dyn}$.

from $\gamma\gamma$-annihilation. The flat synchrotron spectrum is produced by secondary lepton pairs following a $n(\gamma_e) \propto \gamma_e^{-3}$ distribution. A secondary particle distribution of that shape is equally found in [284] and may be interpreted as a common phenomenon in these environments. The VHE peak is confirmed to be produced by π^0 decays; at intermediate energies primary proton synchrotron emission is visible.

For $f_B = 10^{-3}$, the synchrotron radiation of $\gamma\gamma$-annihilation produced leptons dominates only at the lowest energies. The sub-MeV peak is (as in all scenarios) produced by primary synchrotron, with the steeper slope reported also for the leptonic scenario. Pairs from $\gamma\gamma$-annihilation further enhance the fluence above the peak through inverse Compton scatterings, outshining the primary inverse Compton emission. The VHE peak, which is less intense and at lower energies compared to the high-f_B scenario, is again produced by decays of neutral pions.

Evolution of comoving quantities for the representative collision

Again proceeding similarly to the leptonic models we move from the full, time-integrated spectrum to the representative collision.

We first discuss the $f_B = 1$-scenario: The emitted spectrum and the photon and proton loss rates and comoving distributions are shown Figure 7.7. For the photon spectra we indicate only the dominant contributions identified in Figure 7.6; the neutrino spectra are shown as all-flavour and per-flavour (ν_μ, $\bar{\nu}_\mu$,ν_e, $\bar{\nu}_e$). In concordance with the full-burst spectra in Figure 7.5, the neutrino spectra peak at lower energy with respect to the π^0-decay photons. The neutrino peak energy and spectral shape differ by species, where ν_μ have the highest peak energies. The $\bar{\nu}_\mu$ spectrum extends to equal energies as the ν_μ spectrum, but peaks at a lower energy.

[284]: Wang et al. (2018), "Hadronic origin of prompt high-energy emission of gamma-ray bursts revisited: in the case of a limited maximum proton energy"

The two electron neutrino spectra are similar to each other and have peak energies similar to the $\bar{\nu}_\mu$ spectrum – although not extending to similarly high energies.
We attribute the lower peak energies of neutrinos with respect to the π^0-decay peak in the photon SED to two effects:

* *Cooling of intermediate pions and muons*: Charged intermediate secondaries are subject to adiabatic and synchrotron cooling. For the high magnetic fields in our $f_B = 1$ scenario, both species synchrotron-cool before decaying. This introduces a cooling break in the neutrino spectra [285] and reduces their energy with respect to the parent proton energy. The longer decay time of muons and their larger synchrotron cooling rate enhance this effect on the spectra of electron neutrinos (produced in muon decays). This effect and its manifestation throughout the fireball evolution will be discussed in detail in Section 7.4.
* *Attenuation of photons vs. neutrinos*: Neutrinos as free-streaming particles reflect the in-source distribution throughout the complete evolution. This is different for photons, which are subject to $\gamma\gamma$-annihilation. In a single collision, VHE photons can escape more easily at small t' (when the radiation densities are low), see dotted cooling rates in Figure 7.7. At these early t', the low radiation densities also result in a low pion-production efficiency. This in turn enables large proton maximal energies, which evolve to lower energies as the densities increase (see proton spectra and photo-pion rates in Figure 7.7). Thus, the escaping VHE photon spectrum is dominated by early in-source spectra with high maximal proton energies, whereas the neutrino spectra capture the complete evolution up to late t' when the maximal proton energies are lower.

[285]: Baerwald et al. (2012), "Systematics in the Interpretation of Aggregated Neutrino Flux Limits and Flavor Ratios from Gamma-Ray Bursts"

We now move the the $f_B = 10^{-3}$ results, displayed in Figure 7.8. As acceleration is less efficient for weak magnetic fields, proton energies are now equally limited by adiabatic cooling and photo-pion production (see loss rates in Figure 7.8). This has two implications: First, the maximal proton energy remains almost constant throughout the simulation time. Second, photo-pion production is inefficient compared to adiabatic cooling which implies that protons cannot efficiently convert their energy into secondaries. This may be the reason why the photon spectra in the keV-regime are less distorted.
We further point out that the neutrino spectra are not shifted to lower energies with respect to the π^0-decay photons. Staying in the same line of argumentation as before, this can easily be explained: First, cooling effects of pions and muons are negligible since the low magnetic field strengths reduce the synchrotron cooling rate and the lower maximal proton energies result in low-energy secondaries which do not cool before decaying. We again point to Section 7.4 for an in-depth discussion of these effects. Second, the (almost) constant maximal proton energies imply

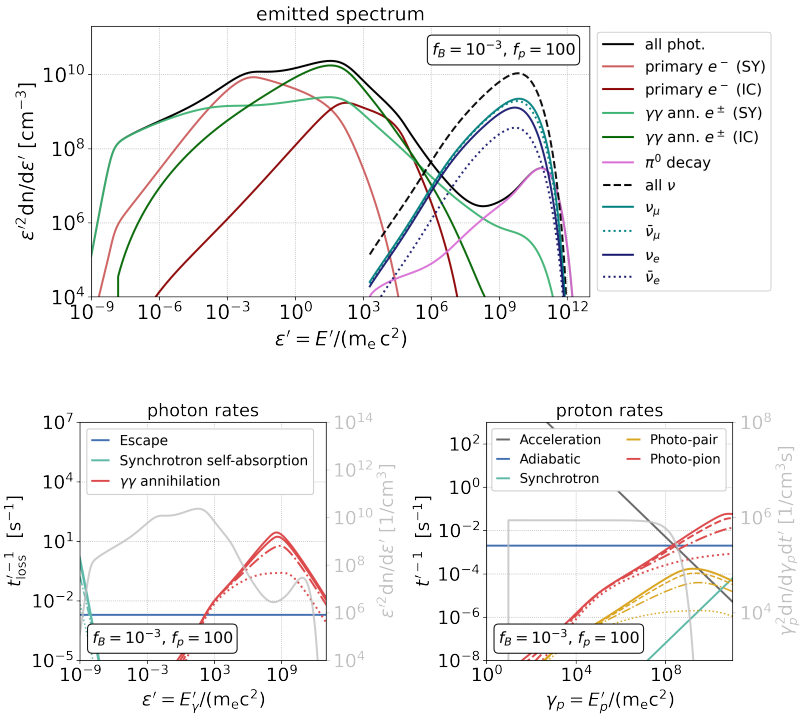

Figure 7.8: Same as Figure 7.7, but for $f_B = 10^{-3}$, $f_p = 100$.

that the neutrino spectra do not evolve to lower energies throughout the evolution. We conclude that for low f_B, the low maximal proton energies inhibit efficient photo-pion production and hence enable larger f_p without affecting the keV spectrum. The lower maximal energies further shift the pion-decay photons to lower energies.

Time-dependent signatures

Besides the question at which energy hadronic signatures show up, one may ask *when* they appear. To investigate this aspect, we show the time-dependent energy fluxes for $f_B = 1$, $f_p = 30$ and $f_B = 10^{-3}$, $f_p = 100$ in Figure 7.10, calculated with Eq. 6.10. The decomposition into emission processes is similar to before, for better overview we show dominant contributions only. EBL absorption was neglected. We normalise the energy flux for each component by dividing by the maximum energy flux of that component $\max(E_{\mathrm{obs}} F(T_{\mathrm{obs}}))$; we further recall from Figure 7.1 that small T_{obs} correspond to small collision radii R_{C} and small shell volumes V' / large densities.

We first discuss the results for $f_B = 1$, $f_p = 30$: The first peak is from synchrotron radiation by secondary lepton pairs from $\gamma\gamma$-annihilation. This early emission originates from close to the source where radiation densities are high, which naturally enhances the efficiency of density-dependent processes such as $\gamma\gamma$-annihilation. The primary electron synchrotron peaks at T_* (which is when most energy is transferred to primary electrons). Finally, the photons produced by π^0 decays peak a

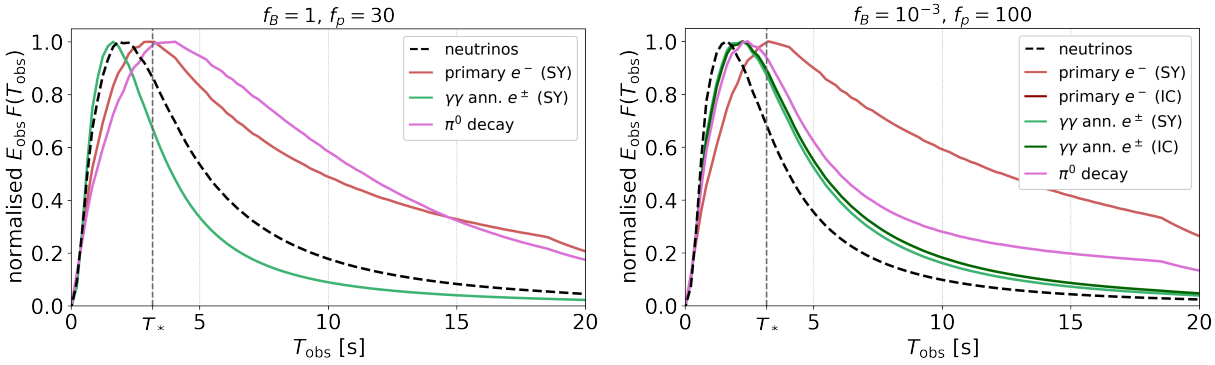

Figure 7.9: Decomposed simulated energy fluxes $E_{\rm obs}F(T_{\rm obs})$ (not accounting for EBL absorption) for the educative example, for *(left)* $f_B = 1$, $f_p = 30$ and *(right)* $f_B = 10^{-3}$, $f_p = 100$. We normalise the energy flux of each component by dividing by the maximum energy flux of that component $\max(E_{\rm obs}F(T_{\rm obs}))$. We show only dominant contributions identified in Figure 7.6. The all-flavour neutrino energy fluxes are shown as black, dashed lines.
The dashed vertical line indicates the observed time of the representative collision.

little later, when lower radiation densities decrease the suppression due to in-source $\gamma\gamma$-annihilation. The neutrino spectra also peak at relatively early times when high densities enable efficient photo-pion production. This is in agreement with findings *e.g.* in [18], where neutrinos were shown to originate from small and VHE gamma-rays from large radii.
From this, we move to the results for $f_B = 10^{-3}$, $f_p = 100$: Here again, the synchrotron and inverse Compton emission from secondary lepton pairs generated in $\gamma\gamma$-annihilation peak at early times when the densities are high. By construction the primary synchrotron emission again peaks at T_*. The most noticeable differences arise for the secondaries from photo-pion production: Neutrinos and photons from π^0-decays peak substantially earlier than for the $f_B = 1$ scenario. We attribute this effect to the lower maximal proton energies in this scenario which limit the photo-pion production efficiency. Close to the source, magnetic fields are stronger and protons can reach higher energies. This increases the photo-pion production efficiency and subsequently the flux of secondaries.

[18]: Bustamante et al. (2017), "Multi-messenger light curves from gamma-ray bursts in the internal shock model"

Dominance of secondary emission in the *Fermi*-GBM and LAT band

The maximum baryonic loading f_p compatible with observed spectra has been studied in a range of publications such as [191, 213, 283]. A summary of their findings can be found in [213] Figure 11, as a function of comoving photon compactness l_γ (defined as $l_\gamma = \frac{\sigma_T L_\gamma}{4\pi R_C^2 \Gamma_C^4 m_e c^2}$). Please note that this quantity depends on all parameters that affect the comoving density (like the observed luminosity, the collision radius and the Lorentz factor).
Overall, they conclude that for low compactness ($l_\gamma = 0.1$) the baryonic loading should be below $f_p \lesssim 10^{1.5} \simeq 30$, whereas in high-compactness scenarios ($l_\gamma = 100$) the baryonic loading is limited to $f_p \lesssim 10^{0.25} \simeq 1.8$. Extending this work, we review the impact of f_p on spectra in the *Fermi*-

[191]: Asano et al. (2009), "Prompt High-Energy Emission from Proton-Dominated Gamma-Ray Bursts"
[213]: Petropoulou (2014), "The role of hadronic cascades in GRB models of efficient neutrino production"
[283]: Asano et al. (2014), "Neutrino and Cosmic-Ray Release from Gamma-Ray Bursts: Time-Dependent Simulations"

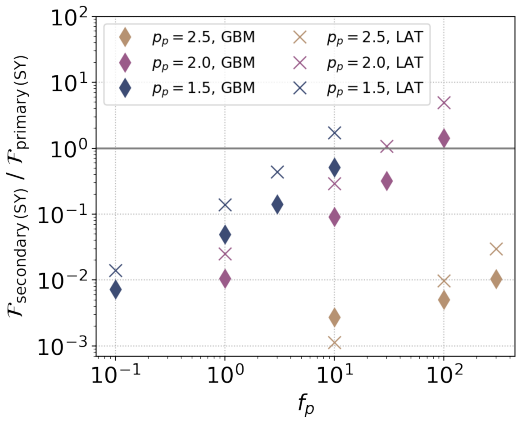

Figure 7.10: Ratio of fluences $\mathcal{F}_{\rm primary\,(SY)}$ and $\mathcal{F}_{\rm seconday\,(SY)}$ (without accounting for EBL absorption). We calculate the fluence in the energy bands of the *Fermi*-GBM (10 keV to 10 MeV, marked as diamonds) and the *Fermi*-LAT (20 MeV to 300 GeV, marked as crosses) from Eq. 7.8 for different values of f_p and primary proton power-law indices p_p. In all examples we chose $f_B = 1$, the solid line indicates where $\mathcal{F}_{\rm primary\,(SY)} = \mathcal{F}_{\rm secondary\,(SY)}$).

GBM and LAT energy ranges for our educative example. For the first time we explicitly study the impact of different primary proton power-law indices $-p_p$. For equal energy budget of non-thermal protons and minimum proton Lorentz factor $\gamma_{p,\rm min}$, p_p defines the energy transferred to protons at the highest energies: The lower p_p, the larger the amount of energy transferred to high-energy protons.

In order to study for which parameters emission from secondary particles outshines the primary electron synchrotron radiation, we show the ratio of synchrotron fluences of primary electrons $\mathcal{F}_{\rm primary\,(SY)}$ and secondary leptons from $\gamma\gamma$-annihilation $\mathcal{F}_{\rm secondary\,(SY)}$ in the *Fermi*-GBM and -LAT range for different (f_p,p_p)-pairs in Figure 7.10. For all scenarios we choose $f_B = 1$ and neglect EBL absorption. The Fluences are obtained by integrating the differential $\mathcal{F}_{E_{\rm obs}}$ in the energy ranges of the *Fermi*-GBM (10 keV to 10 MeV, marked as diamonds) and the *Fermi*-LAT (20 MeV to 300 GeV, marked as crosses):

$$\mathcal{F} = \int_{E_{\rm min}}^{E_{\rm min}} \mathcal{F}_{E_{\rm obs}} {\rm d}E_{\rm obs}\,. \tag{7.8}$$

The horizontal line indicates where $\mathcal{F}_{\rm primary\,(SY)} = \mathcal{F}_{\rm secondary\,(SY)}$; noticeable distortions of the primary synchrotron spectrum may be expected for $\mathcal{F}_{\rm secondary\,(SY)}/\mathcal{F}_{\rm primary\,(SY)} \gtrsim 0.5$.

Due to the larger luminosity in high-energy protons, the secondary emission outshines the primary emission already for low f_p for $-p_p = -1.5$. With increasing p_p, larger f_p can be sustained. The linear increase (in log-log space) is common to all choices of p_p and may therefore be interpreted as a general feature. From the Figure we conclude that in our example, for a typical proton index of $-p_p = -2.0$ the secondary emission outshines the primary one for baryonic loadings of $f_p \gtrsim 30$.

We point out that the results presented here are sensitive to the comoving particle/photon densities, and may deviate *e.g.* for different Lorentz factors of the outflow. On the other hand, the fact that overall similar results were obtained in [213] with more generic sub-MeV photon fields indicate that our results can be generalised for other target photon spectra.

7.4 Secondary pion/muon cooling and relevance for neutrino spectra

We close the study of our educative example by assessing charged pion and muon cooling and its impact on neutrino spectra in detail. For a particle of species i and Lorentz factor γ (with corresponding mass m_i, charge number Z_i and rest-frame lifetime $\tau_{0,i}$) the synchrotron and adiabatic cooling time and the decay time in the plasma rest frame are

$$t'_{\mathrm{sy,i}}(\gamma) = \frac{6\pi}{Z_i^4 \sigma_t} \frac{m_i c^2}{c} \left(\frac{m_i}{m_e}\right)^2 \frac{1}{B'^2 \gamma} \,, \tag{7.9}$$

$$t'_{\mathrm{ad,i}} = t'_{\mathrm{ad}} \,, \tag{7.10}$$

$$t'_{\mathrm{dec,i}}(\gamma) = \tau_{0,i} \gamma \,, \tag{7.11}$$

with corresponding loss rates $t'^{-1}_{\mathrm{sy,i}}(\gamma)$, $t'^{-1}_{\mathrm{ad,i}}$ and $t'^{-1}_{\mathrm{dec,i}}(\gamma)$.
We label the energies at which the timescales of two different processes are equal as *critical* energies; they mark the intersections of timescales/loss rates in the respective plots. Three processes imply three critical energies: $E'_{\mathrm{c,ad/dec}}$ (where $t'_{\mathrm{ad}} = t'_{\mathrm{dec}}$), $E'_{\mathrm{c,sy/dec}}$ (where $t'_{\mathrm{sy}} = t'_{\mathrm{dec}}$) and $E'_{\mathrm{c,ad/sy}}$ (where $t'_{\mathrm{ad}} = t'_{\mathrm{sy}}$). Decay (with $t'^{-1}_{\mathrm{dec}} \propto \gamma^{-1}$ can be assumed to be the dominating loss process at the lowest energies. Depending on the relative importance of the three processes, two cases (visualised in the left panel of Figure 7.11) are possible:

(1) Synchrotron cooling dominates at the highest, adiabatic cooling at intermediate and decay at the lowest energies.
It is realised if $E'_{\mathrm{c,ad/dec}} < E'_{\mathrm{c,sy/dec}} < E'_{\mathrm{c,ad/sy}}$.
(2) Adiabatic cooling is subdominant. At high energies, particles cool via synchrotron cooling, at lower energies decay dominates. In a GRB/astrophysical context, this was examined *e.g.* in [285].
It is realised if $E'_{\mathrm{c,ad/sy}} < E'_{\mathrm{c,sy/dec}} < E'_{\mathrm{c,ad/dec}}$.

[285]: Baerwald et al. (2012), "Systematics in the Interpretation of Aggregated Neutrino Flux Limits and Flavor Ratios from Gamma-Ray Bursts"

Pion/muon cooling in the representative collision

We study the cooling of pions and muons first at the example of the representative collision. Given that the synchrotron cooling rate scales with B'^2 we select $f_B = 1$ and $f_B = 10^{-3}$ to evaluate the impact of the magnetic field strength. The loss rates for pions and muons are shown in the right panel of Figure 7.11, calculated from Eq. 7.9 to Eq. 7.11.
For $f_B = 10^{-3}$, pions are only just in case (2) while for muons adiabatic cooling dominates at intermediate energies (corresponding to case (1)). For $f_B = 1$, synchrotron cooling and acceleration are more efficient and adiabatic cooling is sub-dominant at all energies (corresponding to case (2)). Independent of f_B the longer decay time of muons shifts their critical

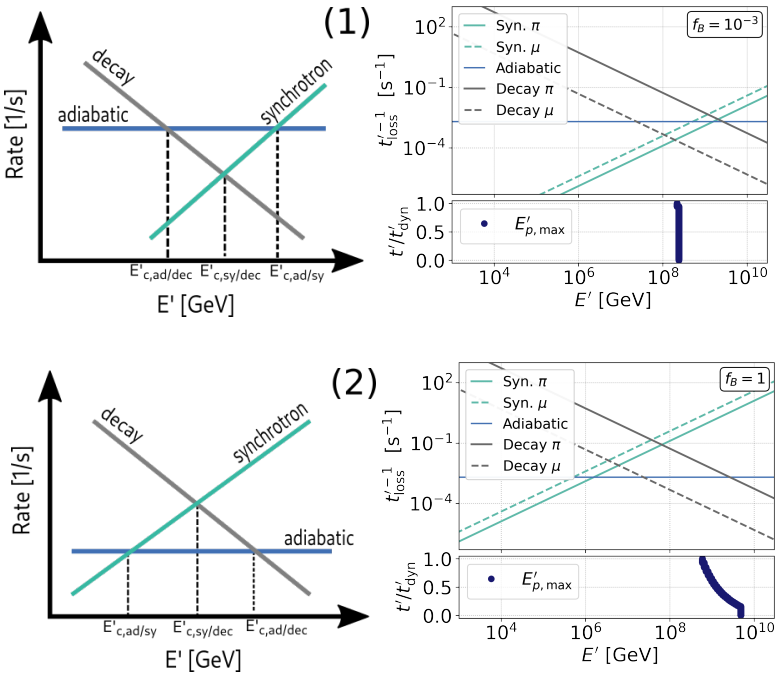

Figure 7.11: Left: Illustration of cooling cases for pions and muons:
(1) $E'_{\rm c,ad/dec} < E'_{\rm c,sy/dec} < E'_{\rm c,ad/sy}$. At the highest energies, synchrotron cooling dominates, at intermediate ones adiabatic cooling and at low energies particles decay without prior cooling.
(2) $E'_{\rm c,ad/sy} < E'_{\rm c,sy/dec} < E'_{\rm c,ad/dec}$. Adiabatic cooling is always subdominant, high-energy particles synchrotron cool before decaying.
Right: Pion and muon loss rates $t'^{-1}_{\rm loss}$ for the representative collision, for *(top)* $f_B = 10^{-3}$ and *(bottom)* $f_B = 1$. The bottom panel shows the evolution of (comoving) maximal proton energies obtained throughout the radiation calculations until $t'_{\rm dyn}$.

energies to lower energies compared to pions.
The Figure further displays the maximum proton energies as a function of $t'/t'_{\rm dyn}$ (recall that the injection time was set to $t'_{\rm inj} = t'_{\rm dyn}$). For $f_B = 1$, the maximal energies decrease with simulation time. This can be understood as follows: Initially, the maximum proton energies are limited adiabatic cooling (*cf.* Figure 7.7). As the photon fields build up, photo-pion production becomes efficient and reduces the maximal proton energies. For $f_B = 10^{-3}$, the maximum proton energy is dominated by adiabatic cooling until almost $t'_{\rm dyn}$ and remains approximately constant (*cf.* Figure 7.8).
We compare the maximum proton energies to the pion and muon loss rates: For $f_B = 1$, secondaries are produced at high enough energies to cool prior to their decay. In contrast to this, in the $f_B = 10^{-3}$ scenario only the secondary muons cool before decaying.

Cooling regimes during the fireball dynamical evolution

From the representative collision we move to the complete fireball dynamical evolution. We define the critical energy as

$$E'_{\rm c} = \min\{E'_{\rm c,sy/dec}, E'_{\rm c,ad/dec}\}\,. \tag{7.12}$$

It may be understood as the energy below which particles do not cool prior to their decay.
The evolution of critical energy as a function of collision radius for our educative example is shown in Figure 7.12. The colour-coding further indicates if above the critical energy, adiabatic or synchrotron cooling

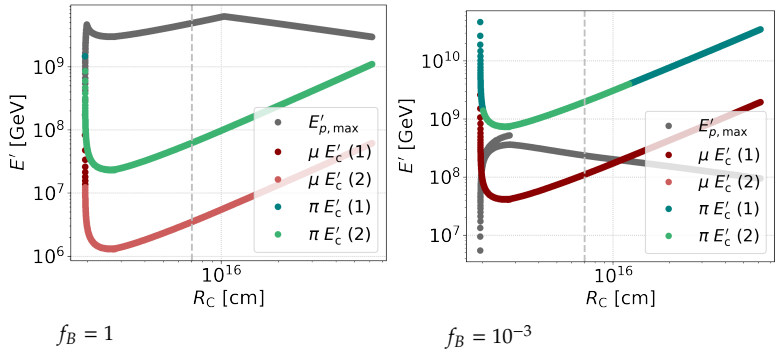

Figure 7.12: Critical energies E'_c (Eq. 7.12) as a function of R_C for pions and muons, for *(left)* $f_B = 1$ and *(right)* $f_B = 10^{-3}$. The number indicates if particles are in case (1) or (2) of the left panel of Figure 7.11. For reference we further indicate the maximal proton energies obtained by balancing acceleration with adiabatic and synchrotron losses (in contrast to Figure 7.11 where also photo-pion and photo-pair production were taken into account). The dashed line indicates the radius of the representative collision.

dominates (corresponding to case (1) and (2) in the left panel of Figure 7.11). For comparison we further indicate the maximal proton energy obtained by balancing synchrotron and adiabatic losses with acceleration. We point out that this is an upper limit on $E'_{p,\max}$ since photo-pair or photo-pion production may further reduce the maximal energy attainable.

For $f_B = 1$, pions and muons are in case (1) for almost all collisions. Further, the critical energies lie several orders of magnitude below $E'_{\mathrm{p,max}}$. In this scenario we thus predict a strong impact of pion and muon cooling throughout the complete fireball evolution.

For $f_B = 10^{-3}$, pions are partially in case (1), partially in case (2). Muons are always in case (2). In this scenario, the maximum proton energies are smaller than the pion critical energies for all collisions. Pions will thus not cool before decaying. Muon critical energies are below $E'_{p,\max}$ for some part of the fireball evolution, the difference in energy is however one order of magnitude at most.

We conclude for strong magnetic fields (high f_B) pions and muons synchrotron-cool prior to their decay. This introduces a spectral break and reshapes the energy distribution of secondaries such as lepton pairs and neutrinos. For weak magnetic fields (low f_B) on the other hand, the maximal proton energies are too low to enable pion cooling prior to their decay. Muons may cool adiabatically before their decay. Overall, the cooling effects of pions and muons hardly impact secondary lepton and neutrino spectra.

Impact on neutrino spectra

Finally, we illustrate the impact of muon and pion cooling on neutrino spectra of the representative collision for $f_B = 1$ and $f_p = 30$ (as in Figure 7.6 and Figure 7.7). We show the evolution of comoving photon and neutrino spectra as a function of t' until $t'_{\mathrm{final}} = 2t'_{\mathrm{dyn}}$ in the left plot of Figure 7.13. Throughout the evolution, neutrino spectra peak at lower energies than the high-energy photons from π^0-decays. The right plot shows the evolution of neutrino spectra *(1)* with full treatment of pions/muons, *(2)* without pion and muon cooling and *(3)* for an infinitesimally small decay time of muons and pions (which implicitly

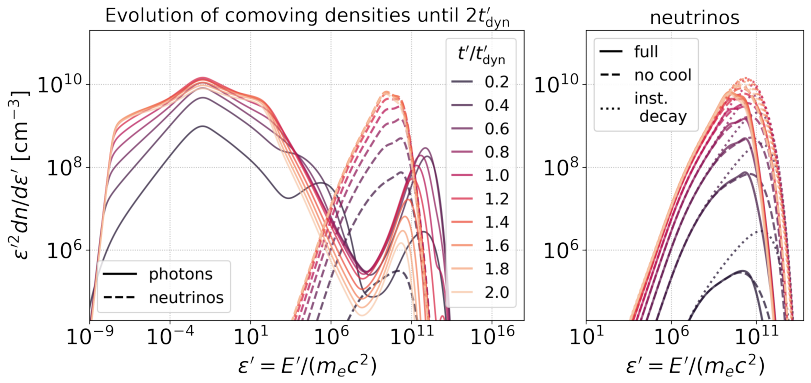

Figure 7.13: Left: Evolution of comoving photon and neutrino spectra until $t'_{\rm final} = 2t'_{\rm dyn}$ for the representative collision and $f_B = 1$, $f_p = 30$.
Right: Evolution of comoving neutrino spectra examining the effect of muon and pion cooling. We run the following scenarios: *(full)* full treat of pions/muons, *(no cool)* no pion and muon cooling and *(inst. decay)* assuming an infinitesimally small decay time of muons and pions. The latter implicitly means that pion and muon cooling are not accounted for.

means that pion and muon cooling are not accounted for).
For the first snapshot at $t' = 0.2t'_{\rm dyn}$, the scenarios with/without pion and muon cooling are little different and do not extend to the highest energies. If however, pions and muons are assumed to decay instantaneously (dotted lines in the right plot), energies comparable to the photons from π^0-decays are reached. This means that at early times t' the maximal energies of neutrinos are limited by the longer decay times of high-energy pions and muons (recall the dependency of the decay time on particle Lorentz factor, Eq. 7.11). As the system evolves, the decay time of high-energy particles is smaller than t' and the dash-dotted and dotted lines in Figure 7.13 extend to similarly high energies. We point out that the effect of the decay timescale is not as relevant if pion and muon cooling are accounted for: By cooling down, particles move to shorter decay times. Overall, Figure 7.13 confirms that the lower peak energies of neutrino spectra for $f_B = 1$ can be attributed to cooling effects of intermediate pions and muons.

7.5 The sample of LAT-detected bursts and reference events

From our educative example we now move to prototypes inspired by real GRBs. This way, we will verify that our results obtained before are valid also for parameter choices reproducing the properties of real events. As detailed above, the HE-emission observed by the *Fermi*-LAT that was reported for a number of bursts has been proposed to be of hadronic origin in a range of publications. Following this idea, we will study the sample of GRBs detected by the *Fermi*-LAT and select reference events for which an internal dissipation origin is likely – in contrast to those events where the LAT detection most surely can be attributed to the afterglow of the event.

The second *Fermi*-LAT GRB catalogue [287] spans 10 years of operation between 2008 and 2018 and lists 186 GRBs. Only 34 (19%) have measured redshifts that allow to calculate source-frame properties. To

[287]: Ajello et al. (2019), "A Decade of Gamma-Ray Bursts Observed by Fermi-LAT: The Second GRB Catalog"

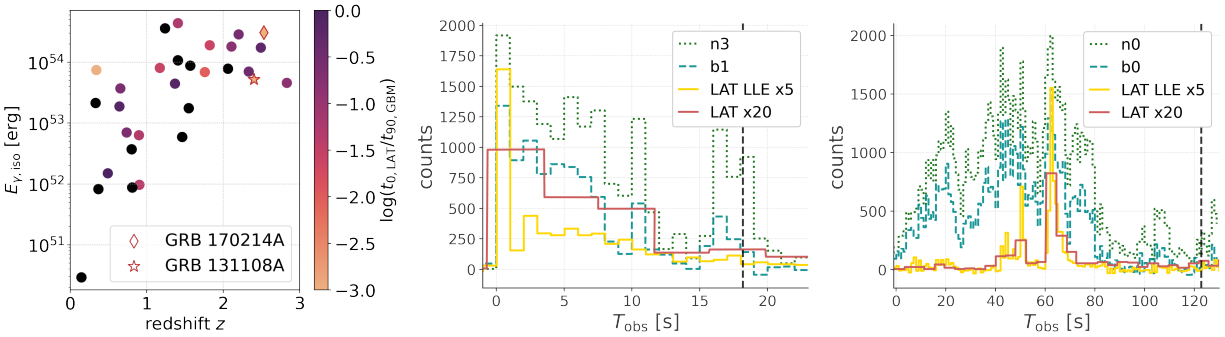

LAT-GRB redshift sample | GRB 131108A light curve | GRB 170214A light curve

Figure 7.14: Left: Sample of *Fermi*-LAT detected bursts with measured redshift in the z-$E_{\gamma,\mathrm{iso}}$ -plane. The colour-coding represents the ratio of the LAT onset time $T_{0,\mathrm{LAT}}$ and the observation time interval during which 90 % of the photons were detected by *Fermi*-GBM ($T_{90,\mathrm{GBM}}$). For GRBs symbolised by black dots, the LAT onset was after the GBM T_{90}. We further indicate our selected reference events. **Right:** Light curves in different energy bands for the reference events, produced with ThreeML [286] and Gtburst. We show the brightest GBM NaI detector (sensitive between a 8 keV and 900 keV), the brightest GBM BGO detector (sensitive between 250 keV and 40 MeV), the LAT Low-Energy extension (LLE, 30 MeV-100 MeV) and the conventional LAT (100 MeV-300 GeV). The dashed vertical line indicates the reported GBM T_{90}.

study potential candidates for a internal dissipation origin, we select these 34 GRBs and study their *Fermi*-LAT onset time $t_{0,\mathrm{LAT}}$ with respect to the *Fermi*-GBM/Konus-Wind T_{90} (a internal dissipation is favoured for $t_{0,\mathrm{LAT}} < T_{90}$). The result is shown in Figure 7.14 which contains a representation of these bursts in the z-$E_{\gamma,\mathrm{iso}}$ plane. The emitted isotropic energy was calculated with the reported GBM Band-function fit and observed fluence, accounting for k-correction [288, 289]. The colour-coding represents the ratio of the LAT onset time $T_{0,\mathrm{LAT}}$ and the *Fermi*-GBM $T_{90,\mathrm{GBM}}$. Bursts for which $T_{0,\mathrm{LAT}} > T_{90,\mathrm{GBM}}$ are marked black. As can be inferred from the Figure, a relatively high $E_{\gamma,\mathrm{iso}}$ is common to all events of the sample

We further indicate our selected reference events. In addition to an early LAT onset time, those two GRBs exhibit temporal variability in both the LAT and GBM band that supports an internal-shock origin of the LAT emission. Their photon light curves (in different energy bands) are shown in the middle and right plot of Figure 7.14, other observational and spectral characteristics are summarised in Table 7.2. We discuss their properties and temporal structure qualitatively:

* GRB 131108A directly triggered both the LAT and the GBM. The first bright pulse is followed by smaller peaks/oscillations, for which [290] fit a double peaked cut-off power law. In the same paper, the first bright peak is described by a single power law, the late time emission by a band function. The burst was also observed by the AGILE satellite, with spectral properties pointing to a multi-component SED [291].

  The GBM time integrated spectral analysis reports a Band function fit with a high $\alpha = -0.91$, a low-energy photon index of $\beta = -2.51$ and $E_{\mathrm{peak}} = 367$ keV.
* GRB 170214A is a multi-peaked burst with short-time variability on

[288]: Bloom et al. (2001), "The prompt energy release of gamma-ray bursts using a cosmological k-correction"
[289]: Kovacs et al. (2012), "Cosmology with Gamma-Ray Bursts Using k-correction"

Table 7.2: Reported properties of the two reference GRB: Band-function fit parameters (α, β, E_{peak}), observed Fluence, T_{90}, isotropic emitted gamma-ray energy $E_{\gamma,\mathrm{iso}}$ (between 1 and 10000 keV) and redshift z.

GRB 131108A	
α	-0.91 ± 0.02
β	-2.46 ± 0.19
E_{peak} [keV]	367 ± 16
Fluence [erg/cm^2]	$(3.56 \pm 0.01) \cdot 10^{-5}$
T_{90} [s]	18.18 ± 0.57
$E_{\gamma,\mathrm{iso}}$ [erg]	$5.37 \cdot 10^{53}$
z	2.4
GRB 170214A	
α	-0.98 ± 0.009
β	-2.51 ± 0.01
E_{peak} [keV]	481 ± 11
Fluence [erg/cm^2]	$(1.8 \pm 0.001) \cdot 10^{-4}$
T_{90} [s]	122.8 ± 0.7
$E_{\gamma,\mathrm{iso}}$ [erg]	$2.9 \cdot 10^{54}$
z	2.53

[290]: Ajello et al. (2019), "Bright γ-Ray Flares Observed in GRB 131108A"
[291]: Giuliani et al. (2014), "A prompt extra component in the high energy spectrum of GRB 131108A"

top of an underlying structure of longer-timescale peaks. Between $0 - 53$ s, no LAT detection was reported while the GBM light curve is pulsed with temporal variability. A broad joint peak is observed around 60 s, with some pulsed structures afterwards.
A analysis of the combined GBM and LAT spectra has been published in [292], where no deviation from a single-component Band function was found. The time-integrated GBM Band function fit reports $\alpha = -0.98$, $\beta = -2.51$ and a peak energy of $E_{\rm peak} = 481$ keV.

[292]: Tang et al. (2017), "Evidence of an Internal Dissipation Origin for the High-energy Prompt Emission of GRB 170214A"

Bulk Lorentz factor estimates

As discussed before, the Lorentz factor of the outflow can have a crucial impact on multi-wavelength spectra shaped by density-dependent processes relevant for low-f_B/high-f_p scenarios. The observational constraints on the Lorentz factor of the outflow mostly refer to the bulk Lorentz factor Γ_0, that approximately represents the mean Lorentz factor. Bulk Lorentz factor estimates usually rely on the peak time of the afterglow $T_{\rm p}$ and the density profile of the medium surrounding the GRB. A summary of different approaches has been provided in [236]. We calculate the Lorentz factor from the methods introduced in that publication, extended by the method of [293]. The exact value of $T_{\rm p}$ is not reported for our reference GRBs. We restrict the possible range for Γ_0 by taking into account the upper limit on $T_{\rm p}$ (given by the first observation of the associated afterglow) and the lower limit on $T_{\rm p}$ (given by the first peak of the prompt phase). We calculate $\Gamma_{0,\rm min}$ and $\Gamma_{0,\rm max}$ following [294] ('SP99'), [295] ('M07'), [296] ('G10'), [297] ('G12'), [298] ('N13'), [299] ('N14') and [293] ('H14').
For the external medium we consider a wind-like density profile ($\rho(r) = \rho_0 \cdot r^{-2}$ where r is the distance from the source) and a constant density profile ($\rho(r) = \rho_0 \cdot r^0$). The profiles are normalised as follows: $\rho_0 = 1\mathrm{cm}^{-3} \cdot m_p$ for the constant profile and $\rho_0 = \dot{M}/(4\pi v_w)$ with $\dot{M} = 10^{-5}\mathrm{M}_\odot/\mathrm{yr}$ and $v_w = 10^3\mathrm{km/s}$ for the wind-like profile.
The most conservative *upper limit* on the attainable Lorentz factor comes from setting the acceleration radius equal to the transparency radius [300]. As we study GRBs with *Fermi*-LAT detection, we can find an additional *lower limit* from the transparency condition for HE photons [273]. For this, we take use the most energetic photon associated with the prompt phase. The method allows to account for emission radii of the bulk of the prompt emission (R_0) and the high-energy emission ($R_{\rm e}$) which might be decoupled (see also *e.g.* [18]).
The results for the different methods are shown in Figure 7.15, for an upper limit of the onset time of 1147 s (10935 s) and a lower limit of 0.075 s (16 s) for GRB 131108A (GRB 170214A), all redshift-corrected. For the lower limit from the transparency emission we chose an exemplary emission radius of $R_{\rm e} = 10^{17}$ cm for the 7.6 GeV LAT photon and an

[236]: Ghirlanda et al. (2018), "Bulk Lorentz factors of Gamma-Ray Bursts"

[293]: Hascoet et al. (2013), "Prompt thermal emission in gamma-ray bursts"

[294]: Sari et al. (1999), "Predictions for the very early afterglow and the optical flash"
[295]: Molinari et al. (2007), "A direct measurement of the relativistic expansion velocity of gamma-ray burst fireballs"
[296]: Ghisellini et al. (2009), "A unifying view of Gamma Ray Burst Afterglows"
[297]: Ghirlanda et al. (2012), "Gamma Ray Bursts in the comoving frame"
[298]: Nava et al. (2013), "Afterglow emission in Gamma-Ray Bursts: I. Pair-enriched ambient medium and radiative blast waves"
[299]: Nava et al. (2014), "Clustering of LAT light curves: a clue to the origin of high-energy emission in Gamma-Ray Bursts"
[300]: Daigne et al. (2002), "The Expected thermal precursors of gamma-ray bursts in the internal shock model"
[273]: Hascoet et al. (2012), "Do Fermi-LAT observations imply very large Lorentz factors in GRB outflows ?"
[18]: Bustamante et al. (2017), "Multi-messenger light curves from gamma-ray bursts in the internal shock model"

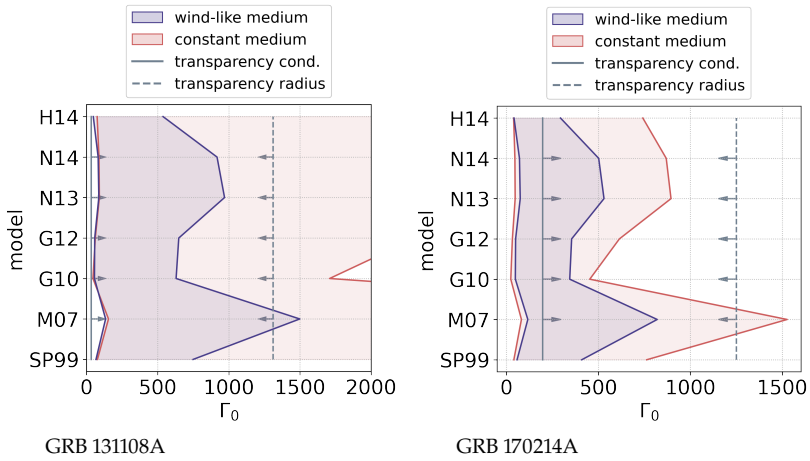

Figure 7.15: Limits for the bulk Lorentz factor Γ_0 of our two reference events. We show the range between the upper and lower limit derived following [294] ('SP99'), [295] ('M07'), [296] ('G10'), [297] ('G12'), [298] ('N13'), [299] ('N14') and [293] ('H14'), for a wind-like and constant-density medium (blue and red shading). This is complemented by the upper limit from the transparency radius [300] and the lower limit from the transparency condition [273].

exemplary bulk emission radius of $R_0 = 5 \cdot 10^{15}$ cm for GRB 170214A. For GRB 131108A, where the first, bright pulse is seen both by LAT and GBM, we assume $R_0 = R_e = 10^{15}$ cm for the 900 MeV photon observed by LAT. Comparable results are obtained with the 100 MeV photon observed 1 s after the trigger reported by the MCAL instrument onboard the AGILE satellite [291]. We have verified that those radii are in both scenarios compatible with the estimates of the deceleration radius (at which the initial jet has swept up a mass comparable to its own). Note that the obtained limits for this method may deviate if different emission radii are chosen. The long duration of both GRBs favours a massive star progenitor for both events and thus a wind-like medium surrounding the bursts. We will consequently choose Lorentz factor distributions approximately within the blue region in Figure 7.15. To ensure that the outflow is optically thin during most of the internal shock phase, we impose relatively high Lorentz factors close to the upper limit for our prototypes.

[291]: Giuliani et al. (2014), "A prompt extra component in the high energy spectrum of GRB 131108A"

7.6 Simulated results for the *Fermi*-LAT inspired prototypes

Finally, we present the simulated results for the prototypes inspired by GRBs 131108A and 170214A. Our parameters are chosen such that the reported E_{peak}, high-energy photon index β, fluence and light curve structure are reproduced. The fiducial fireball characteristics are summarised in Table 7.3 (complemented by Table B.2) and the initial Lorentz factor distributions are displayed in the left plot of Figure 7.16. As outlined in the last section, we choose Lorentz factors close to the upper limit obtained for the wind-like scenario in Figure 7.15. EBL absorption is included in all calculations. We impose $t'_{\mathrm{inject}} = t'_{\mathrm{dyn}}$ and $\zeta_e \propto \epsilon'_{\mathrm{diss}}$ in all simulations and again study different choices of f_B and f_p while adjusting $\zeta_{e,0}$ such that the observed peak is reproduced.

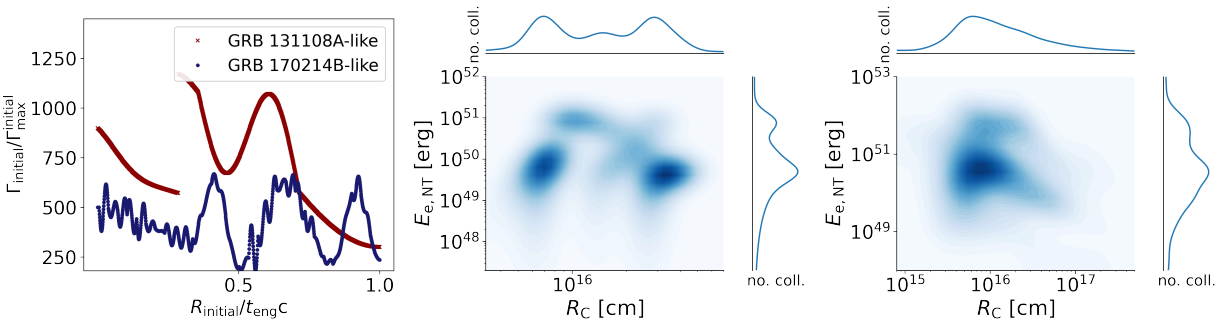

Initial Γ distribution | GRB 131108A-like | GRB 170214A-like

Figure 7.16: Left: Initial Lorentz factor distributions for the two *Fermi*-LAT inspired prototypes.
Middle and right: Density plot of the distribution of collisions for the two prototypes in the parameter space of $E_{\rm NT,e}$ (energy transferred to non-thermal electrons, in the source frame) and $R_{\rm C}$ (collision radius).

The middle and right plot of Figure 7.16 show a density map of the distribution of collisions in $E_{\rm e,NT}$ -$R_{\rm C}$ parameter space. In contrast to our educative example, collisions of different pulses occur at the same radius and the distribution of collisions deviates from the simple behaviour displayed in Figure 7.1.

In Figure 7.17 and Figure 7.18, we show the simulated time-integrated spectra and photon light curves (in energy ranges corresponding to different instruments, see plot description) for the two prototypes. Besides the simulation results, we indicate the Band-function fit parameters (α, β and $E_{\rm peak}$) of the reference events.
We first discuss the results for the GRB 131108A-like prototype (Figure 7.17): By construction, the $f_B = 1$ leptonic scenario reproduces the peak energy and high-energy photon index β of the reference event. None of the parameter sets can reproduce the low-energy photon index α reported for the reference GRB. For $f_B = 1$, we find a wing-like broadening for the lepto-hadronic scenarios. This is also mirrored in the light curves, where the fluences in all wavelength bands increase with f_p. For $f_B = 10^{-3}$, only the fluences above $E_{\rm peak}$ vary with f_p. This reflects also in the light curves that show no dependence on f_p for the low-energy (ZTF, ULTRASAT and XRT) instrumental ranges. The light curve has two peaks, with the first peak is more intense than the second one.
Let us now discuss the results for the GRB 170214A-like prototype (Figure 7.18): Again, the high-energy photon index β and the peak energy of the reference event are reproduced in the $f_B = 1$ leptonic scenario and none of the simulations reach the reported α. For $f_B = 1$ we find the usual wing-like broadening of the spectra with increasing f_p. Again, for $f_B = 10^{-3}$ the low-energy spectra are similar for all choices of f_p. The light curves exhibit short-time variability on top of an underlying structure of broader peaks for all parameter choices. For $f_B = 10^{-3}$, the low-energy light curves up to the XRT band are independent of f_p; for higher energy bands the photon flux increases with f_p. For $f_B = 1$, the photon flux increases with f_p for all energy bands.

Table 7.3: Fireball characteristics for the two *Fermi*-LAT inspired prototypes: Total energy transferred to non-thermal electrons $E_{\rm e,tot}$, fireball efficiency ε, number of initial plasma shells $N^{\rm initial}_{\rm shells}$, engine active time $t_{\rm eng}$ and primary electron power-law index p_e.

GRB 131108A-like	
$E_{\rm e,tot}$	$5.94 \cdot 10^{53}$ erg
ε	6.17 %
$N^{\rm initial}_{\rm shells}$	1300
$t_{\rm eng}$	4.41 s
p_e	2.92
GRB 170214A-like	
$E_{\rm e,tot}$	$3.52 \cdot 10^{54}$ erg
ε	2.98 %
$N^{\rm initial}_{\rm shells}$	1297
$t_{\rm eng}$	34 s
p_e	3.02

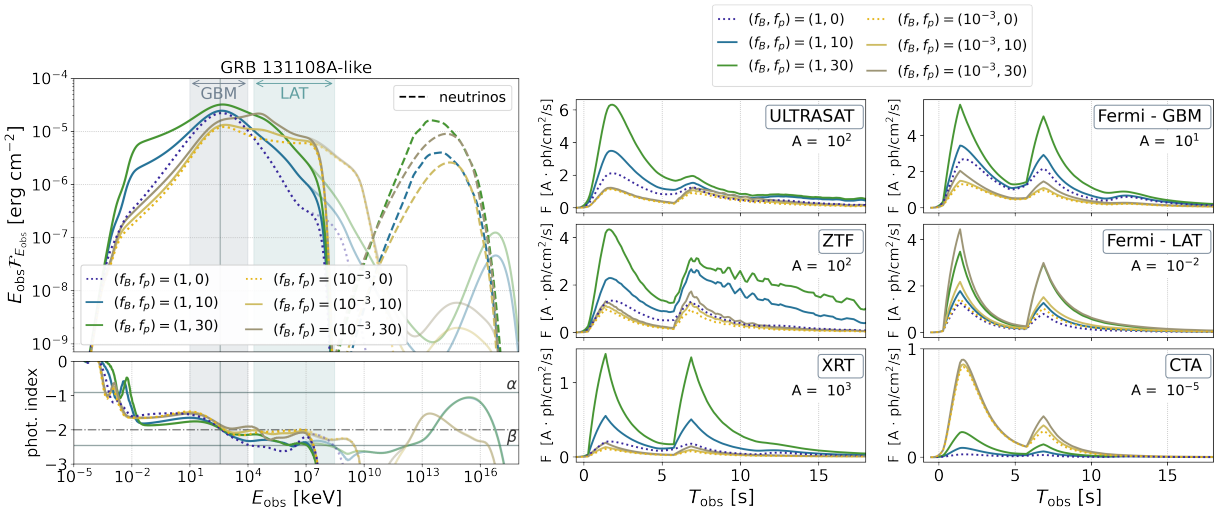

Figure 7.17: Results for the GRB131108A-like prototype exploring different f_B and f_p.
Left: Simulated spectra $E_{\rm obs}\mathcal{F}_{E_{\rm obs}}$ as a function of observed energy. The vertical lines mark the reported peak energy of the reference event, the shaded regions the energy ranges of the *Fermi*-GBM and *Fermi*-LAT. Thin lines correspond to the results without EBL absorption. The lower panel shows the photon indexes (spectral slope of $\mathcal{F}_{E_{\rm obs}}/E_{\rm obs}$). We indicate the reported α and β for the reference event; the dashed line corresponds to a photon index of -2, where $E_{\rm obs}\mathcal{F}_{E_{\rm obs}}$ is maximal/minimal.
Right: Photon light curve in energy bands corresponding to the ULTRASAT satellite (220 - 280 nm), the ZTF r-band (560 - 730 nm), Swift-XRT (0.2 - 10 keV), *Fermi*-GBM (10 keV - 10 MeV), *Fermi*-LAT (20 MeV - 600 GeV) and CTA (20 GeV - 20 TeV).

Overall, the simulated spectra of the prototypes exhibit the similar behaviour as found for the educative example: For strong magnetic fields ($f_B = 1$), high f_p introduce a wing-like broadening of the sub-MeV peak. For weak magnetic fields (low f_B) high f_p enhance the fluence above the sub-MeV peak, whereas the LE fluence remains unaffected. In those scenarios the pion decay and neutrino peaks are at lower energies compared to the high-f_B results. For high f_B, the neutrino spectra peak at lower energies compared to the π^0-decay photons. Finally, photon signatures beyond the *Fermi*-LAT energy range are suppressed due to EBL absorption. From this we infer that the general trends found for the educative example are valid in a larger parameter-space region and for bursts with properties inspired by real events, as well as temporally variable light curves.
The simulated light curves exhibit similar temporal variability in all energy ranges/wavelength bands. Thus, within our internal shock framework, a time-variability in the LAT band tracing the GBM band is strongly suggested for an internal dissipation origin of HE emission. For the GRB 131108A-like prototype, the first broad peak is reproduced in all energy bands, which is consistent with the direct LAT-trigger. For the GRB 170214A-like prototype, the first peak is very weak in the LAT band with respect to the GBM band, which may be interpreted as consistent with the delayed LAT-detection onset for the reference event.

We conclude that by choosing adequate fireball parameters and microphysics parameters the peak energy $E_{\rm peak}$, the high-energy photon index β and the light curve structure of given GRBs can be reproduced. As

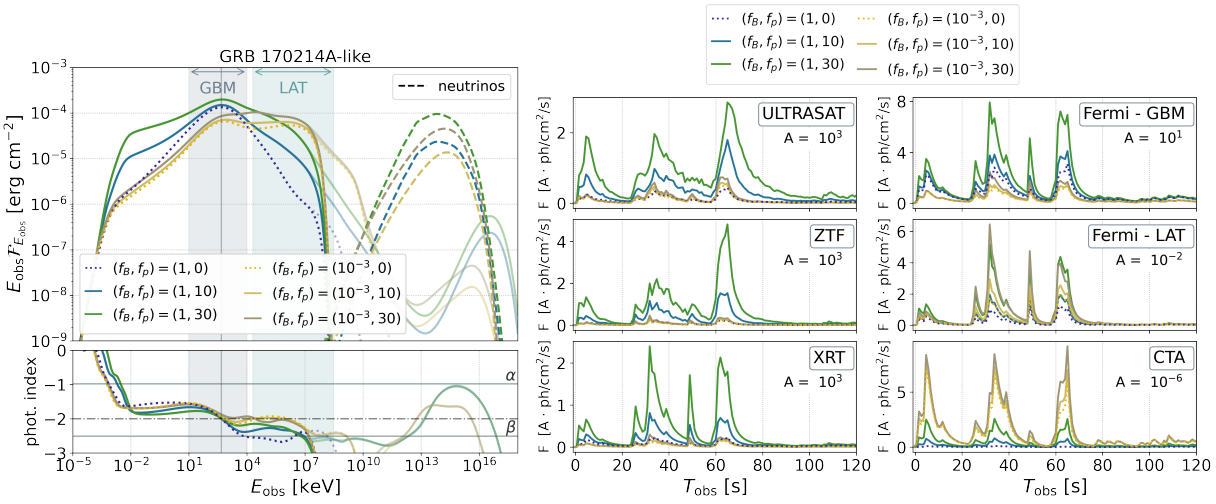

Figure 7.18: Same as Figure 7.17 for the GRB 170214A-like prototype.

detailed in Section 7.2, this requires some fine-tuning of parameters (*e.g.* ζ_e scaling with $\varepsilon'_{\rm diss}$). However, high $\alpha \simeq -1$ (as reported for both reference events) are difficult to reconcile with our optically thin internal shock scenarios. Here we again stress that we cannot reproduce the hard α found for low f_B that was reported past numerical studies [184]. Additionally, both low-f_B and high-f_p scenarios are found to increase the high-energy spectral photon index β which results in broad spectra around $E_{\rm peak}$.

From our selected reference GRBs, the combined *Fermi*-GBM and LAT spectrum of GRB 170214A was fitted with a single power-law in [292]. In principle, all our simulations do not predict a double-peaked structure and would be in agreement with this; however high f_p and/or low f_B are incompatible with the reported β. In this sense, our modelling favours a high-f_B/low-f_p scenario for that burst. On the other hand, a two-component scenario has been proposed for GRB 131108A. Within our modelling, this may point to a low-f_B and low-f_p scenario.

We point out that these results are sensitive to the bulk Lorentz factor of the outflow. This underlines the importance of accurate bulk Lorentz factor estimates which rely on measurements of the afterglow peak time $T_{\rm p}$.

Out of other LAT-detected GRBs discussed in the literature, GRB 09092B is an interesting example. For this event, the *Fermi*-LAT spectrum was fit by a power law of index 1.94. The burst further exhibited excesses both at high and low energies. As pointed out in [284], these features can be explained well within a lepto-hadronic scenario wing-like structure as also found in our simulations.

[184]: Daigne et al. (2011), "Reconciling observed GRB prompt spectra with synchrotron radiation ?"

[292]: Tang et al. (2017), "Evidence of an Internal Dissipation Origin for the High-energy Prompt Emission of GRB 170214A"

[284]: Wang et al. (2018), "Hadronic origin of prompt high-energy emission of gamma-ray bursts revisited: in the case of a limited maximum proton energy"

8 Conclusion and Outlook

Only a handful of objects in the Universe are believed to be powerful enough to accelerate particles to ultra-high energies. Among the few candidates are GRBs, which we have examined as a potential source of UHECRs and (V)HE radiation in this thesis. Focussing on the prompt phase of the event, we have applied the internal shock model to the relativistic outflow and calculated particle interactions and spectra with numerical codes. Our aim was to assess under which conditions GRBs can account for UHECR measurements while obeying multi-messenger constraints, which radiation processes may induce a (V)HE gamma-ray component and which multi-wavelength signatures are introduced by hadronic interactions.
Our radiation modelling was mainly carried out with the time-dependent numerical code AM3. As the code was originally designed for AGN, this required software modifications such as the inclusion of adiabatic cooling, pion and muon cooling and quantum synchrotron emission. I implemented and tested the numerical calculation of these processes in collaboration with Shan Gao. Additionally, I implemented a framework to calculate time-dependent quantities from different regions of the jet taking into account the curvature of the emitting surface.
We briefly summarise the main findings, ordered by chapter:

For context, Chapter 3 reviewed leptonic and hadronic processes relevant for high-energy astrophysics using scenarios that I developed as part of the Hadronic Code Comparison Project, HCCP. For the examined scenarios, all participating codes predicted comparable multi-wavelength and neutrino spectra even in extreme parameter-space regions like the inverse Compton catastrophe and the photo-pair synchrotron loop (also referred to as hadronic supercriticality). The results were further compared with analytical estimates.

Two different frameworks of the internal shock scenario for the relativistic outflow in GRBs were introduced in Chapter 5. Testing the robustness of multi-messenger predictions against model variations, we showed that modified collision dynamics within the internal shock scenario do not impact neutrino predictions (under the assumption of similar gamma-ray observables).
We further presented a fit to the UHECR energy spectrum and composition as observed by the Pierre Auger Observatory that was performed in a scan over different initial Lorentz factor distributions of the outflow, dubbed 'engine realisations'. A comparable GRB-UHECR-fit had previously been presented in [212], but here we introduced the possibility of a variable engine setup. This allowed the model to predict light curves with

[212]: Globus et al. (2015), "UHECR acceleration at GRB internal shocks"

multi-timescale variability, closer to the stochastic behaviour observed in real GRBs. Our results indicate that GRBs can describe UHECRs for a large range of engine realisations. Generally, this however requires large engine kinetic energies and a high percentage of the energy being transferred to non-thermal cosmic rays. The latter was quantified by the baryonic loading $f_p = \epsilon_{\mathrm{CR}}/\epsilon_e$, the energy transferred to non-thermal cosmic rays divided by the energy transferred to non-thermal electrons; our UHECR fit required $f_p \sim 50 - 100$. The post-dicted neutrino fluxes were shown to be below current IceCube limits but in reach of future neutrino experiments like the planned IceCube Gen2.
We pointed out that a pure, heavy composition as demanded by $\sigma(X_{\mathrm{max}})$ measurements is challenging to reproduce with stochastic engine setups. This may be in contradiction with typical observed variability timescales as investigated in [228]. A caveat of our study is further the assumed redshift distribution of identical GRBs that does not represent the wealth of observed events. However, in a more realistic setup of non-similar sources contributing to the overall flux, a pure composition as suggested by $\sigma(X_{\mathrm{max}})$ measurements may even be challenging to reproduce for smooth light-curve/engine setups.

[228]: Golkhou et al. (2014), "Uncovering the Intrinsic Variability of Gamma-ray Bursts"

While the aforementioned results did not include self-consistent calculations of the photon spectra, in Chapter 6 we demonstrated the applicability of AM3 to GRBs using the example of low-luminosity events. Within a purely leptonic radiation modelling we found that a VHE inverse Compton component can be realised if a small part of the dissipated energy is transferred to magnetic fields. The latter was quantified by $f_B = \epsilon_B/\epsilon_e$, the energy transferred to magnetic fields divided by the energy transferred to non-thermal electrons. Given the high local rate of LL-GRBs, this VHE component makes LL-GRBs a potential target for IACTs. We demonstrated that LE fluence and photon index may be additional probes of f_B.
As a next step, we used the results of the radiation modelling and the fireball evolution to calculate the maximal energies attainable for different cosmic-ray nuclei with NeuCosmA. We demonstrated that high cosmic-ray energies compatible with UHECR fits from LL-GRBs in the literature are possible if a large part of the energy is transferred to magnetic fields (large f_B). We thus conclude that within our framework, a LL-GRB may either accelerate cosmic rays to the highest energies or produce a leptonic VHE component potentially observable by IACTs. We emphasize that a (V)HE component induced by hadronic processes and the maximal baryonic loading compatible with photon and neutrino observations remain to be addressed in a future study.

Finally, in Chapter 7 we presented lepto-hadronic radiation models of high-luminosity GRBs invoking both primary electrons and protons. We first examined the contribution of different radiation processes and the impact of parameter choices on observed spectra at an simple academic

GRB referred to as 'educative example'. For SSC scenarios with high inverse Compton efficiency realised for low f_B, inverse Compton emission of lepton pairs from $\gamma\gamma$-annihilation was shown to enhance the fluence in the *Fermi*-LAT band. In contrast to this, primary electron inverse Compton was subdominant and showed up at higher energies. In high-f_B scenarios with a baryonic loading $f_p \gtrsim 10$, synchrotron radiation of secondary lepton pairs introduced a wing-like broadening of the sub-MeV peak. This feature had previously been reported in the literature, including for setups with generic sub-MeV target photon fields [213, 284] – which indicates that the feature is not specific to our synchrotron model for the sub-MeV peak. For our educative example, $f_B = 1$ and a fiducial proton power-law index of $-p_p = -2.0$ we found an upper limit on the baryonic loading of $f_p \lesssim 30$ if synchrotron emission of the secondary particle cascade should not outshine the primary electron synchrotron emission in the GBM/LAT band. For high f_B we demonstrated that secondary pion and muon cooling effects reduce the neutrino peak energy and reshape the spectra of secondaries.

[213]: Petropoulou (2014), "The role of hadronic cascades in GRB models of efficient neutrino production"
[284]: Wang et al. (2018), "Hadronic origin of prompt high-energy emission of gamma-ray bursts revisited: in the case of a limited maximum proton energy"

We further review the conditions necessary to reproduce narrow spectra similar to observed ones: First, a narrow synchrotron peak can only be generated if the minimum Lorentz factor of electrons remains constant throughout the fireball evolution. This can be realised by setting the number fraction of accelerated electrons ζ_e as $\zeta_e \propto \epsilon'_{\rm diss}$. Second, both low f_B and high f_p result in a broadening of the sub-MeV synchrotron peak. In this sense, the pure synchrotron is the narrowest spectrum that can be produced. Here we note that the low-energy photon index $\alpha \simeq -1$ for low f_B reported in [184] could only be reproduced if electrons are injected into the radiation zone on a timescale much shorter than the dynamical timescale of the system. We point out that the spectra of low-f_B/high-f_p scenarios that have large contributions of secondaries from $\gamma\gamma$-annihilation strongly depend on the bulk Lorentz factor of the outflow. To summarize, our optically thin SSC model requires some fine-tuning of parameters in order to be compatible with observations.

[184]: Daigne et al. (2011), "Reconciling observed GRB prompt spectra with synchrotron radiation ?"

From the educative example we turned to real GRBs with a high-energy component detected by the *Fermi*-LAT. Selecting two events of this sample, we showed that the behaviour found for the educative example was also reproduced for prototypes with observed properties similar to detected GRBs. Within our models, it was challenging to reproduce the low-energy photon index $\alpha \simeq -1$ reported for the selected reference events. As detailed above, the narrowest spectra were found for scenarios dominated by primary electron synchrotron radiation.

In the remainder of this conclusion, I provide an outlook on future developments, putting our results in context of selected scientific questions:

Do these findings imply that GRBs cannot be UHECR sources? Our results suggest that within the internal shock model it is indeed questionable whether the high baryonic loading of order 10-100 demanded by UHECR

fits is compatible with observed spectra. However, this does not mean that GRB jets are generally excluded to be baryon-loaded; in fact, it may simply be the case that they are not the sole sources of the UHECRs. This would entail a multi-component model for UHECRs, as presented *e.g.* in [301] or [302]. We further point out that UHECR fits often assume a generic baryonic loading common to all events. However, in the context of AGN it has been demonstrated that a fit to the UHECR spectrum compatible with IceCube neutrino limits is possible if the baryonic loading is high only for low-luminosity sources [303]. For GRBs a similar conclusion may be drawn from the strong constraints on the baryonic loading derived for selected bright events [304, 305]. This would strengthen the case for LL-GRBs as UHECR sources, as discussed in Chapter 6.
We stress that from source physics a certain baryon contamination of the jet may be reasonable, especially for long GRBs that originate from heavy stars containing nuclei up to iron (see *e.g.* [173]).

How can theoretical models be improved? For more robust constraints, lepto-hadronic GRB models should be tested within a broader variety of models including photospheric or reconnection scenarios. This could be complemented by multi-epoch studies from early photospheric to afterglow emission as *e.g.* in [306]. In the context of cosmic rays, one should further include nuclei heavier than protons into the full radiation calculations (given that UHECR fits require nuclear masses up to iron), where also the maximal energies attainable for different nuclear species should be carefully reviewed.
Finally, the presented models would benefit from a closer connection to (R)MHD jet simulations that provide a more realistic picture of the 3D plasma conditions. In a cosmic-ray and neutrino context such a combined model was presented in [307]. A first step may be to invoke a more complex, although still parametrised geometry of the jet (*e.g.* structured jets, as also favoured from afterglow measurements of GRB 170817A [98]).

What can we learn from comparing our models to multi-wavelength data? An emphasis of our modelling lies on electromagnetic (V)HE and LE signatures. Our results underline the importance of state-of-the-art radiation models that fully account for the emission of secondary particles. For example, lepton pairs produced in (source-internal) $\gamma\gamma$-annihilation shine in low-energy (optical to UV) and high-energy (MeV to GeV) bands. Both those signatures are not attenuated due to EBL absorption and may also be observed at higher redshifts. In this sense, our models may be tested by comparing to multi-wavelength data down to low energies.
An apparent issue of our optically thin internal shock models are the spectral shapes which are difficult to reconcile with the low-energy photon indexes $\alpha \simeq -1$ reported in (some) Band-function fits and the generally narrow spectra [162, 163]. We point out that a direct comparison to data would be an essential next step: [183] showed that by forward-

[301]: Das et al. (2021), "Modeling the spectrum and composition of ultrahigh-energy cosmic rays with two populations of extragalactic sources"
[302]: Muzio et al. (2019), "Progress towards characterizing ultrahigh energy cosmic ray sources"
[303]: Rodrigues et al. (2021), "Active Galactic Nuclei Jets as the Origin of Ultrahigh-Energy Cosmic Rays and Perspectives for the Detection of Astrophysical Source Neutrinos at EeV Energies"
[304]: Fraija et al. (2017), "Theoretical Description Of GRB 160625B with Wind-to-ISM Transition and Implications for a Magnetized Outflow"
[305]: Gao et al. (2013), "On the neutrino non-detection of GRB 130427A"
[173]: Gottlieb et al. (2019), "High efficiency photospheric emission entailed by formation of a collimation shock in gamma-ray bursts"
[306]: Pitik et al. (2021), "Neutrino signal dependence on gamma-ray burst emission mechanism"
[307]: Gottlieb et al. (2021), "The Role of Jet–Cocoon Mixing, Magnetization, and Shock Breakout in Neutrino and Cosmic-Ray Emission from Short Gamma-Ray Bursts"
[98]: Troja et al. (2019), "A year in the life of GW 170817: the rise and fall of a structured jet from a binary neutron star merger"
[162]: Axelsson et al. (2015), "The width of gamma-ray burst spectra"
[163]: Yu et al. (2015), "The sharpness of gamma-ray burst prompt emission spectra"
[183]: Burgess et al. (2019), "Gamma-ray bursts as cool synchrotron sources"

folding of synthetic spectra with detector response, GRB prompt spectra may be fitted well by a synchrotron model. This implies that a comparison to (over-)simplified Band-function fits can not unambiguously rule out models. A further caveat of these fits is their sensitivity to the position of the peak energy $E_{\rm peak}$ within the energy range of the instrument.
As pointed out in [208], the energy dissipation and radiation mechanism at play may differ between GRBs. In this sense, the narrow spectra of some GRBs may point to a photospheric origin of their prompt emission while broader spectra may be accommodated in optically-thin internal-shock models.

[208]: Acuner et al. (2018), "Clustering of gamma-ray burst types in the Fermi-GBM catalogue: indications of photosphere and synchrotron emissions during the prompt phase"

Which experimental advances may contribute to constraining multi-messenger GRB prompt phase models? First, a neutrino signal from GRBs from future experiments such as IceCube Gen2 [55] could evidently confirm a baryonic loading of GRB jets. Further constraints may come from multi-wavelength coverage. As detailed above, lepto-hadronic models predict an enhancement of the LE flux due to cascade-produced secondary leptons. In this energy range, a variety of experiments have been recently launched, and even more are scheduled for future deployment. Without claiming completeness, we list the Zwicky Transient Facility (ZTF) [106], Vera Rubin Observatory (former LSST) [107] and Ultraviolet Transient Astronomy Satellite (ULTRASAT) [108]. A challenging aspect of optical and UV measurements/limits is that they have to be corrected for absorption in the host galaxy which is often poorly constrained. Despite these challenges, already data from current experiments such as *Swift*-UVOT can constrain the mechanisms at play during the prompt phase, as shown *e.g.* in [186]. For close-by objects such as LL-GRBs, this could be complemented by future IACTs like CTA [76]; objects at larger distances rely on HE measurements by instruments like *Fermi*-LAT – which is however still lacking a successor mission. Finally, precision measurements of the composition at the highest energies will further slim the list of potential UHECR sources. Here we point out that a major uncertainty comes from hadronic interaction models that are an input for air-shower reconstruction and in-source interaction models. A recent discussion highlighting those uncertainties is the 'cosmic-ray muon puzzle' (*e.g.* [308]), a deficit of predicted muons in air showers with respect to measurements. Advances in air-shower modelling in the upcoming years may be expected from new experimental data of nuclear interactions, *e.g.* by including oxygen and lead in LHC Run 3 and Run 4 [309]. This will be complemented by more accurate measurements of the muon and electron components by the upgraded Auger Prime Observatory [39].

[55]: Aartsen et al. (2021), "IceCube-Gen2: the window to the extreme Universe"

[106]: Graham et al. (2019), "The Zwicky Transient Facility: Science Objectives"

[107]: Ivezić et al. (2019), "LSST: from Science Drivers to Reference Design and Anticipated Data Products"

[108]: Sagiv et al. (2014), "Science with a wide-field UV transient explorer"

[186]: Oganesyan et al. (2019), "Prompt optical emission as a signature of synchrotron radiation in gamma-ray bursts"

[76]: Actis et al. (2011), "Design concepts for the Cherenkov Telescope Array CTA: An advanced facility for ground-based high-energy gamma-ray astronomy"

[308]: Dembinski et al. (2021), "The Muon Puzzle in air showers and its connection to the LHC"

[309]: Citron et al. (2019), "Report from Working Group 5: Future physics opportunities for high-density QCD at the LHC with heavy-ion and proton beams"

[39]: Aab et al. (2016), "The Pierre Auger Observatory Upgrade - Preliminary Design Report"

All things considered, both new experimental data and theoretical approaches are expected to bring real progress in the next years and decades. Together they will reveal more and more about the nature of the mysterious events called gamma-ray bursts – and possibly unveil whether they are sources of high-energy cosmic rays and neutrinos.

Bibliography

[1] Victor F. Hess. "Über Beobachtungen der durchdringenden Strahlung bei sieben Freiballonfahrten". In: *Phys. Z.* 13 (1912), pp. 1084–1091 (cited on pages 1, 6).

[2] S. H. Neddermeyer and C. D. Anderson. "Note on the Nature of Cosmic Ray Particles". In: *Phys. Rev.* 51 (1937), pp. 884–886. DOI: 10.1103/PhysRev.51.884 (cited on page 1).

[3] C. M. G. Lattes et al. "Processes involving charged mesons". In: *Nature* 159 (1947), pp. 694–697. DOI: 10.1038/159694a0 (cited on page 1).

[4] Karl G. Jansky. "Radio Waves from Outside the Solar System". In: *Nature* 132.3323 (July 1933), p. 66. DOI: 10.1038/132066a0 (cited on page 1).

[5] W. L. Kraushaar and G. W. Clark. "Search for Primary Cosmic Gamma Rays with the Satellite Explorer XI". In: *Phys. Rev. Lett.* 8.3 (Feb. 1962), pp. 106–109. DOI: 10.1103/PhysRevLett.8.106 (cited on page 1).

[6] John N. Bahcall and R. Davis. "Solar Neutrinos - a Scientific Puzzle". In: *Science* 191 (1976), pp. 264–267. DOI: 10.1126/science.191.4224.264 (cited on page 1).

[7] M. G. Aartsen et al. "Evidence for High-Energy Extraterrestrial Neutrinos at the IceCube Detector". In: *Science* 342 (2013), p. 1242856. DOI: 10.1126/science.1242856 (cited on pages 1, 13).

[8] B. P. Abbott et al. "Observation of Gravitational Waves from a Binary Black Hole Merger". In: *Phys. Rev. Lett.* 116.6 (2016), p. 061102. DOI: 10.1103/PhysRevLett.116.061102 (cited on pages 1, 7).

[9] Alexander Aab et al. "The Pierre Auger Cosmic Ray Observatory". In: *Nucl. Instrum. Meth. A* 798 (2015), pp. 172–213. DOI: 10.1016/j.nima.2015.06.058 (cited on pages 1, 10).

[10] M. Fukushima. "Telescope array project for extremely high energy cosmic rays". In: *Prog. Theor. Phys. Suppl.* 151 (2003). Ed. by T. Hatsuda et al., pp. 206–210. DOI: 10.1143/PTPS.151.206 (cited on pages 1, 10).

[11] M. G. Aartsen et al. "The IceCube Neutrino Observatory: Instrumentation and Online Systems". In: *JINST* 12.03 (2017), P03012. DOI: 10.1088/1748-0221/12/03/P03012 (cited on pages 1, 12).

[12] A. M. Hillas. "The Origin of Ultrahigh-Energy Cosmic Rays". In: *Ann. Rev. Astron. Astrophys.* 22 (1984), pp. 425–444. DOI: 10.1146/annurev.aa.22.090184.002233 (cited on pages 2, 16, 17).

[13] Eli Waxman. "Cosmological gamma-ray bursts and the highest energy cosmic rays". In: *Phys. Rev. Lett.* 75 (1995), pp. 386–389. DOI: 10.1103/PhysRevLett.75.386 (cited on pages 2, 42, 52).

[14] Eli Waxman and John N. Bahcall. "High-energy neutrinos from cosmological gamma-ray burst fireballs". In: *Phys. Rev. Lett.* 78 (1997), pp. 2292–2295. DOI: 10.1103/PhysRevLett.78.2292 (cited on pages 2, 53).

[15] M. G. Aartsen et al. "An All-Sky Search for Three Flavors of Neutrinos from Gamma-Ray Bursts with the IceCube Neutrino Observatory". In: *Astrophys. J.* 824.2 (2016), p. 115. DOI: 10.3847/0004-637X/824/2/115 (cited on pages 2, 14, 42, 53).

[16] M. G. Aartsen et al. "Extending the search for muon neutrinos coincident with gamma-ray bursts in IceCube data". In: *Astrophys. J.* 843.2 (2017), p. 112. DOI: 10.3847/1538-4357/aa7569 (cited on pages 2, 14, 42, 53).

[17] Daniel Biehl et al. "Cosmic-Ray and Neutrino Emission from Gamma-Ray Bursts with a Nuclear Cascade". In: *Astron. Astrophys.* 611 (2018), A101. DOI: 10.1051/0004-6361/201731337 (cited on pages 2, 52, 53, 63, 81).

[18] Mauricio Bustamante et al. "Multi-messenger light curves from gamma-ray bursts in the internal shock model". In: *Astrophys. J.* 837.1 (2017), p. 33. DOI: 10.3847/1538-4357/837/1/33 (cited on pages 2, 53, 65, 79, 81, 99, 106).

[19] Alessandro De Angelis, Giorgio Galanti, and Marco Roncadelli. "Transparency of the Universe to gamma rays". In: *Mon. Not. Roy. Astron. Soc.* 432 (2013), pp. 3245–3249. DOI: 10.1093/mnras/stt684 (cited on page 6).

[20] W. Pauli. "Dear radioactive ladies and gentlemen". In: *Open letter to the group of radioactive people at the Gauverein meeting in Tübingen* (Dec. 1930) (cited on page 7).

[21] E. Fermi. "An attempt of a theory of beta radiation. 1." In: *Z. Phys.* 88 (1934), pp. 161–177. DOI: 10.1007/BF01351864 (cited on page 7).

[22] R. M. Bionta et al. "Observation of a Neutrino Burst in Coincidence with Supernova SN 1987a in the Large Magellanic Cloud". In: *Phys. Rev. Lett.* 58 (1987), p. 1494. DOI: 10.1103/PhysRevLett.58.1494 (cited on page 7).

[23] K. Hirata et al. "Observation of a Neutrino Burst from the Supernova SN 1987a". In: *Phys. Rev. Lett.* 58 (1987). Ed. by K. C. Wali, pp. 1490–1493. DOI: 10.1103/PhysRevLett.58.1490 (cited on page 7).

[24] R. A. Hulse and J. H. Taylor. "Discovery of a pulsar in a binary system". In: *Astrophys. J. Lett.* 195 (1975), pp. L51–L53. DOI: 10.1086/181708 (cited on page 7).

[25] Pau Amaro-Seoane et al. “Laser Interferometer Space Antenna”. In: *arXiv e-prints* (Feb. 2017) (cited on page 7).

[26] M. G. Aartsen et al. “The IceCube Realtime Alert System”. In: *Astropart. Phys.* 92 (2017), pp. 30–41. DOI: 10.1016/j.astropartphys.2017.05.002 (cited on page 8).

[27] M. W. E. Smith et al. “The Astrophysical Multimessenger Observatory Network (AMON)”. In: *Astropart. Phys.* 45 (2013), pp. 56–70. DOI: 10.1016/j.astropartphys.2013.03.003 (cited on page 8).

[28] P. A. Zyla et al. “Review of Particle Physics”. In: *PTEP* 2020.8 (2020), p. 083C01. DOI: 10.1093/ptep/ptaa104 (cited on page 9).

[29] Jorg R. Horandel. “Cosmic rays from the knee to the second knee: 10^{14} to 10^{18}-eV”. In: *Mod. Phys. Lett. A* 22 (2007). Ed. by Maurice M. Shapiro, Todor Stanev, and John P. Wefel, pp. 1533–1552. DOI: 10.1142/S0217732307024139 (cited on page 8).

[30] Kenneth Greisen. “End to the cosmic ray spectrum?” In: *Phys. Rev. Lett.* 16 (1966), pp. 748–750. DOI: 10.1103/PhysRevLett.16.748 (cited on page 9).

[31] G. T. Zatsepin and V. A. Kuz’min. “Upper limit of the spectrum of cosmic rays”. In: *JETP Lett.* 4 (1966), pp. 78–80 (cited on page 9).

[32] J. L. Puget, F. W. Stecker, and J. H. Bredekamp. “Photonuclear Interactions of Ultrahigh-Energy Cosmic Rays and their Astrophysical Consequences”. In: *Astrophys. J.* 205 (1976), pp. 638–654. DOI: 10.1086/154321 (cited on page 9).

[33] Beetjedwars from nl. *Air Shower Illustration — Wikipedia, The Free Encyclopedia*. [Online; accessed 30-August-2021]. 2010. URL: https://commons.wikimedia.org/wiki/File:AirShower.svg (cited on page 9).

[34] A. U. Abeysekara et al. “The 2HWC HAWC Observatory Gamma Ray Catalog”. In: *Astrophys. J.* 843.1 (2017), p. 40. DOI: 10.3847/1538-4357/aa7556 (cited on page 9).

[35] T Antoni et al. “The Cosmic ray experiment KASCADE”. In: *Nucl. Instrum. Meth. A* 513 (2003), pp. 490–510. DOI: 10.1016/S0168-9002(03)02076-X (cited on page 10).

[36] W. D. Apel et al. “The KASCADE-Grande experiment”. In: *Nucl. Instrum. Meth. A* 620 (2010), pp. 202–216. DOI: 10.1016/j.nima.2010.03.147 (cited on page 10).

[37] T. Abu-Zayyad et al. “The prototype high-resolution Fly’s Eye cosmic ray detector”. In: *Nucl. Instrum. Meth. A* 450 (2000), pp. 253–269. DOI: 10.1016/S0168-9002(00)00307-7 (cited on page 10).

[38] R. U. Abbasi et al. “First observation of the Greisen-Zatsepin-Kuz’min suppression”. In: *Phys. Rev. Lett.* 100 (2008), p. 101101. DOI: 10.1103/PhysRevLett.100.101101 (cited on page 10).

[39] Alexander Aab et al. "The Pierre Auger Observatory Upgrade - Preliminary Design Report". In: *ArXiv eprints* (Apr. 2016) (cited on pages 10, 115).

[40] Bjarni Pont. "A Large Radio Detector at the Pierre Auger Observatory - Measuring the Properties of Cosmic Rays up to the Highest Energies". In: *PoS* ICRC2019 (2021), p. 395. DOI: 10.22323/1.358.0395 (cited on page 10).

[41] Eiji Kido. "The TAx4 experiment". In: *PoS* ICRC2017 (2018), p. 386. DOI: 10.22323/1.301.0386 (cited on page 10).

[42] Antonella Castellina. "Highlights from the Pierre Auger Observatory". In: *PoS* ICRC2019 (2021), p. 004. DOI: 10.22323/1.358.0004 (cited on pages 11, 16).

[43] William Hanlon. "Telescope Array 10 Year Composition". In: *PoS* ICRC2019 (2021), p. 280. DOI: 10.22323/1.358.0280 (cited on page 11).

[44] Alexander Aab et al. "Observation of a Large-scale Anisotropy in the Arrival Directions of Cosmic Rays above 8×10^{18} eV". In: *Science* 357.6537 (2017), pp. 1266–1270. DOI: 10.1126/science.aan4338 (cited on page 11).

[45] Alexander Aab et al. "Searches for Anisotropies in the Arrival Directions of the Highest Energy Cosmic Rays Detected by the Pierre Auger Observatory". In: *Astrophys. J.* 804.1 (2015), p. 15. DOI: 10.1088/0004-637X/804/1/15 (cited on page 11).

[46] Alexander Aab et al. "An Indication of anisotropy in arrival directions of ultra-high-energy cosmic rays through comparison to the flux pattern of extragalactic gamma-ray sources". In: *Astrophys. J. Lett.* 853.2 (2018), p. L29. DOI: 10.3847/2041-8213/aaa66d (cited on page 11).

[47] Thomas K. Gaisser, Francis Halzen, and Todor Stanev. "Particle astrophysics with high-energy neutrinos". In: *Phys. Rept.* 258 (1995). [Erratum: Phys.Rept. 271, 355–356 (1996)], pp. 173–236. DOI: 10.1016/0370-1573(95)00003-Y (cited on page 12).

[48] Eli Waxman and John N. Bahcall. "High-energy neutrinos from astrophysical sources: An Upper bound". In: *Phys. Rev. D* 59 (1999), p. 023002. DOI: 10.1103/PhysRevD.59.023002 (cited on page 12).

[49] M. Ageron et al. "ANTARES: the first undersea neutrino telescope". In: *Nucl. Instrum. Meth. A* 656 (2011), pp. 11–38. DOI: 10.1016/j.nima.2011.06.103 (cited on page 12).

[50] A. D. Avrorin et al. "Baikal-GVD: status and prospects". In: *EPJ Web Conf.* 191 (2018). Ed. by V. E. Volkova et al., p. 01006. DOI: 10.1051/epjconf/201819101006 (cited on page 12).

[51] S. Adrian-Martinez et al. “Letter of intent for KM3NeT 2.0”. In: *J. Phys. G* 43.8 (2016), p. 084001. DOI: 10.1088/0954-3899/43/8/084001 (cited on page 12).

[52] Francis Halzen et al. “The AMANDA neutrino telescope”. In: *Nucl. Phys. B Proc. Suppl.* 77 (1999). Ed. by N. J. C. Spooner and V. Kudryavtsev, pp. 474–485. DOI: 10.1016/S0920-5632(99)00469-7 (cited on page 12).

[53] R. Abbasi et al. “IceTop: The surface component of IceCube”. In: *Nucl. Instrum. Meth. A* 700 (2013), pp. 188–220. DOI: 10.1016/j.nima.2012.10.067 (cited on page 12).

[54] R. Abbasi et al. “The Design and Performance of IceCube DeepCore”. In: *Astropart. Phys.* 35 (2012), pp. 615–624. DOI: 10.1016/j.astropartphys.2012.01.004 (cited on page 12).

[55] M. G. Aartsen et al. “IceCube-Gen2: the window to the extreme Universe”. In: *J. Phys. G* 48.6 (2021), p. 060501. DOI: 10.1088/1361-6471/abbd48 (cited on pages 12, 115).

[56] M. G. Aartsen et al. “Detection of a particle shower at the Glashow resonance with IceCube”. In: *Nature* 591.7849 (2021). [Erratum: Nature 592, E11 (2021)], pp. 220–224. DOI: 10.1038/s41586-021-03256-1 (cited on page 13).

[57] R. Abbasi et al. “Measurement of Astrophysical Tau Neutrinos in IceCube’s High-Energy Starting Events”. In: *arXiv e-prints* (Nov. 2020) (cited on page 13).

[58] Markus Ahlers, Klaus Helbing, and Carlos Pérez de los Heros. “Probing Particle Physics with IceCube”. In: *Eur. Phys. J. C* 78.11 (2018), p. 924. DOI: 10.1140/epjc/s10052-018-6369-9 (cited on page 13).

[59] R. Abbasi et al. “The IceCube high-energy starting event sample: Description and flux characterization with 7.5 years of data”. In: *Phys. Rev. D* 104.2, 022002 (July 2021), p. 022002. DOI: 10.1103/PhysRevD.104.022002 (cited on pages 13, 14).

[60] R. Abbasi et al. “Improved Characterization of the Astrophysical Muon-Neutrino Flux with 9.5 Years of IceCube Data”. In: *arXiv e-prints* (Nov. 2021) (cited on pages 13, 14).

[61] M. G. Aartsen et al. “Characteristics of the diffuse astrophysical electron and tau neutrino flux with six years of IceCube high energy cascade data”. In: *Phys. Rev. Lett.* 125.12 (2020), p. 121104. DOI: 10.1103/PhysRevLett.125.121104 (cited on pages 13, 14).

[62] Rasha Abbasi et al. “A Combined Fit of the Diffuse Neutrino Spectrum using IceCube Muon Tracks and Cascades”. In: *PoS* ICRC2021 (2021), p. 1129. DOI: 10.22323/1.395.1129 (cited on pages 13, 14).

[63] Markus Ackermann et al. "Astrophysics Uniquely Enabled by Observations of High-Energy Cosmic Neutrinos". In: *Bull. Am. Astron. Soc.* 51 (2019), p. 185 (cited on page 14).

[64] M. G. Aartsen et al. "The contribution of Fermi-2LAC blazars to the diffuse TeV-PeV neutrino flux". In: *Astrophys. J.* 835.1 (2017), p. 45. DOI: 10.3847/1538-4357/835/1/45 (cited on page 14).

[65] Daniel Smith, Dan Hooper, and Abigail Vieregg. "Revisiting AGN as the source of IceCube's diffuse neutrino flux". In: *JCAP* 03 (2021), p. 031. DOI: 10.1088/1475-7516/2021/03/031 (cited on page 14).

[66] Keith Bechtol et al. "Evidence against star-forming galaxies as the dominant source of IceCube neutrinos". In: *Astrophys. J.* 836.1 (2017), p. 47. DOI: 10.3847/1538-4357/836/1/47 (cited on page 14).

[67] M. G. Aartsen et al. "Constraints on minute-scale transient astrophysical neutrino sources". In: *Phys. Rev. Lett.* 122.5 (2019), p. 051102. DOI: 10.1103/PhysRevLett.122.051102 (cited on pages 14, 81).

[68] Andrea Palladino et al. "Interpretation of the diffuse astrophysical neutrino flux in terms of the blazar sequence". In: *Astrophys. J.* 871.1 (2019), p. 41. DOI: 10.3847/1538-4357/aaf507 (cited on page 14).

[69] Andrea Palladino and Walter Winter. "A multi-component model for observed astrophysical neutrinos". In: *Astron. Astrophys.* 615 (2018), A168. DOI: 10.3204/PUBDB-2018-01376 (cited on page 14).

[70] I. Bartos et al. "The IceCube Pie Chart: Relative Source Contributions to the Cosmic Neutrino Flux". In: *Astrophys. J.* 921.1 (2021), p. 45. DOI: 10.3847/1538-4357/ac1c7b (cited on pages 14, 21).

[71] C. E. Fichtel et al. "High-energy gamma-ray results from the second Small Astronomy Satellite." In: *Astrophys. J.* 198 (May 1975), pp. 163–182. DOI: 10.1086/153590 (cited on page 15).

[72] W. B. Atwood et al. "The Large Area Telescope on the Fermi Gamma-ray Space Telescope Mission". In: *Astrophys. J.* 697 (2009), pp. 1071–1102. DOI: 10.1088/0004-637X/697/2/1071 (cited on pages 15, 42).

[73] Jamie Holder et al. "The first VERITAS telescope". In: *Astropart. Phys.* 25 (2006), pp. 391–401. DOI: 10.1016/j.astropartphys.2006.04.002 (cited on page 15).

[74] F. Aharonian et al. "Observations of the Crab Nebula with H.E.S.S". In: *Astron. Astrophys.* 457 (2006), pp. 899–915. DOI: 10.1051/0004-6361:20065351 (cited on page 15).

[75] J. Aleksić et al. “The major upgrade of the MAGIC telescopes, Part II: A performance study using observations of the Crab Nebula”. In: *Astropart. Phys.* 72 (2016), pp. 76–94. DOI: 10.1016/j.astropartphys.2015.02.005 (cited on page 15).

[76] M. Actis et al. “Design concepts for the Cherenkov Telescope Array CTA: An advanced facility for ground-based high-energy gamma-ray astronomy”. In: *Exper. Astron.* 32 (2011), pp. 193–316. DOI: 10.1007/s10686-011-9247-0 (cited on pages 15, 115).

[77] Zhen Cao. “A future project at Tibet: The large high altitude air shower observatory (LHAASO)”. In: *Chin. Phys. C* 34 (2010), pp. 249–252. DOI: 10.1088/1674-1137/34/2/018 (cited on page 15).

[78] S. Abdollahi et al. “*Fermi* Large Area Telescope Fourth Source Catalog”. In: *Astrophys. J. Suppl.* 247.1 (2020), p. 33. DOI: 10.3847/1538-4365/ab6bcb (cited on page 15).

[79] H. Abdalla et al. “The H.E.S.S. Galactic plane survey”. In: *Astron. Astrophys.* 612 (2018), A1. DOI: 10.1051/0004-6361/201732098 (cited on page 16).

[80] M. Ackermann et al. “The spectrum of isotropic diffuse gamma-ray emission between 100 MeV and 820 GeV”. In: *Astrophys. J.* 799 (2015), p. 86. DOI: 10.1088/0004-637X/799/1/86 (cited on page 16).

[81] J. Stettner. “Measurement of the Diffuse Astrophysical Muon-Neutrino Spectrum with Ten Years of IceCube Data”. In: *PoS* ICRC2019 (2020), p. 1017. DOI: 10.22323/1.358.1017 (cited on page 16).

[82] Markus Ahlers and Francis Halzen. “Opening a New Window onto the Universe with IceCube”. In: *Prog. Part. Nucl. Phys.* 102 (2018), pp. 73–88. DOI: 10.1016/j.ppnp.2018.05.001 (cited on page 16).

[83] Rafael Alves Batista et al. “Open Questions in Cosmic-Ray Research at Ultrahigh Energies”. In: *Front. Astron. Space Sci.* 6 (2019), p. 23. DOI: 10.3389/fspas.2019.00023 (cited on page 17).

[84] C. Megan Urry and Paolo Padovani. “Unified schemes for radio-loud active galactic nuclei”. In: *Publ. Astron. Soc. Pac.* 107 (1995), p. 803. DOI: 10.1086/133630 (cited on page 18).

[85] Gustavo E. Romero, Ana Laura Müller, and Markus Roth. “Particle acceleration in the superwinds of starburst galaxies”. In: *Astron. Astrophys.* 616 (2018), A57. DOI: 10.1051/0004-6361/201832666 (cited on page 18).

[86] Suvi Gezari. “Tidal Disruption Events”. In: *Ann. Rev. Astron. Astrophys.* 59 (2021), pp. 21–58. DOI: 10.1146/annurev-astro-111720-030029 (cited on page 19).

[87] Lixin Dai et al. "A unified model for tidal disruption events". In: *Astrophys. J. Lett.* 859.2 (2018), p. L20. DOI: 10.3847/2041-8213/aab429 (cited on page 19).

[88] Robert Stein. "Tidal Disruption Events and High-energy Neutrinos". In: *PoS* ICRC2021 (2021), p. 009. DOI: 10.22323/1.395.0009 (cited on page 19).

[89] ENRICO Fermi. "On the Origin of the Cosmic Radiation". In: *Phys. Rev.* 75 (8 Apr. 1949), pp. 1169–1174. DOI: 10.1103/PhysRev.75.1169 (cited on page 20).

[90] James Matthews, Anthony Bell, and Katherine Blundell. "Particle acceleration in astrophysical jets". In: *New Astron. Rev.* 89 (2020), p. 101543. DOI: 10.1016/j.newar.2020.101543 (cited on page 20).

[91] Martin Pohl, Masahiro Hoshino, and Jacek Niemiec. "PIC Simulation Methods for Cosmic Radiation and Plasma Instabilities". In: *Prog. Part. Nucl. Phys.* 111 (2020), p. 103751. DOI: 10.1016/j.ppnp.2019.103751 (cited on page 20).

[92] A. Marcowith et al. "Multi-scale simulations of particle acceleration in astrophysical systems". In: *Liv. Rev. Comput. Astrophys.* 6 (2020), p. 1. DOI: 10.1007/s41115-020-0007-6 (cited on page 20).

[93] Kenichi Nishikawa et al. "PIC methods in astrophysics: Simulations of relativistic jets and kinetic physics in astrophysical systems". In: *Liv. Rev. Comput. Astrophys.* 7 (2021), p. 1. DOI: 10.1007/s41115-021-00012-0 (cited on page 20).

[94] B. P. Abbott et al. "Gravitational Waves and Gamma-rays from a Binary Neutron Star Merger: GW170817 and GRB 170817A". In: *Astrophys. J. Lett.* 848.2 (2017), p. L13. DOI: 10.3847/2041-8213/aa920c (cited on pages 20, 21, 44).

[95] Iair Arcavi et al. "Optical emission from a kilonova following a gravitational-wave-detected neutron-star merger". In: *Nature* 551 (2017), p. 64. DOI: 10.1038/nature24291 (cited on page 21).

[96] B. P. Abbott et al. "Multi-messenger Observations of a Binary Neutron Star Merger". In: *Astrophys. J. Lett.* 848.2 (2017), p. L12. DOI: 10.3847/2041-8213/aa91c9 (cited on page 21).

[97] Jonathan Granot, Dafne Guetta, and Ramandeep Gill. "Lessons from the Short GRB 170817A: The First Gravitational-wave Detection of a Binary Neutron Star Merger". In: *Astrophys. J. Lett.* 850.2 (2017), p. L24. DOI: 10.3847/2041-8213/aa991d (cited on page 21).

[98] E. Troja et al. "A year in the life of GW 170817: the rise and fall of a structured jet from a binary neutron star merger". In: *Mon. Not. Roy. Astron. Soc.* 489.2 (2019), pp. 1919–1926. DOI: 10.1093/mnras/stz2248 (cited on pages 21, 114).

[99] E. Pian et al. “Spectroscopic identification of r-process nucleosynthesis in a double neutron star merger”. In: *Nature* 551 (2017), pp. 67–70. DOI: 10.1038/nature24298 (cited on page 21).

[100] N. R. Tanvir et al. “The Emergence of a Lanthanide-Rich Kilonova Following the Merger of Two Neutron Stars”. In: *Astrophys. J. Lett.* 848.2 (2017), p. L27. DOI: 10.3847/2041-8213/aa90b6 (cited on page 21).

[101] M. G. Aartsen et al. “Multimessenger observations of a flaring blazar coincident with high-energy neutrino IceCube-170922A”. In: *Science* 361.6398 (2018), eaat1378. DOI: 10.1126/science.aat1378 (cited on page 21).

[102] M. G. Aartsen et al. “Neutrino emission from the direction of the blazar TXS 0506+056 prior to the IceCube-170922A alert”. In: *Science* 361.6398 (2018), pp. 147–151. DOI: 10.1126/science.aat2890 (cited on page 21).

[103] Xavier Rodrigues et al. “Leptohadronic Blazar Models Applied to the 2014–2015 Flare of TXS 0506+056”. In: *Astrophys. J. Lett.* 874.2 (2019), p. L29. DOI: 10.3847/2041-8213/ab1267 (cited on page 21).

[104] Maria Petropoulou et al. “Multi-Epoch Modeling of TXS 0506+056 and Implications for Long-Term High-Energy Neutrino Emission”. In: *Astrophys. J.* 891 (2020), p. 115. DOI: 10.3847/1538-4357/ab76d0 (cited on page 21).

[105] Robert Stein et al. “A tidal disruption event coincident with a high-energy neutrino”. In: *Nature Astron.* 5.5 (2021), pp. 510–518. DOI: 10.1038/s41550-020-01295-8 (cited on page 21).

[106] Matthew J. Graham et al. “The Zwicky Transient Facility: Science Objectives”. In: *Publ. Astron. Soc. Pac.* 131.1001 (2019), p. 078001. DOI: 10.1088/1538-3873/ab006c (cited on pages 22, 115).

[107] Željko Ivezić et al. “LSST: from Science Drivers to Reference Design and Anticipated Data Products”. In: *Astrophys. J.* 873.2 (2019), p. 111. DOI: 10.3847/1538-4357/ab042c (cited on pages 22, 115).

[108] I. Sagiv et al. “Science with a wide-field UV transient explorer”. In: *Astron. J.* 147 (2014), p. 79. DOI: 10.1088/0004-6256/147/4/79 (cited on pages 22, 115).

[109] A. Abramowski et al. “Acceleration of petaelectronvolt protons in the Galactic Centre”. In: *Nature* 531 (2016), p. 476. DOI: 10.1038/nature17147 (cited on page 22).

[110] A. Albert et al. “HAWC J2227+610 and its association with G106.3+2.7, a new potential Galactic PeVatron”. In: *Astrophys. J. Lett.* 896 (2020), p. L29. DOI: 10.3847/2041-8213/ab96cc (cited on page 22).

[111] M. Amenomori et al. "Potential PeVatron supernova remnant G106.3+2.7 seen in the highest-energy gamma rays". In: *Nature Astron.* 5.5 (2021), pp. 460–464. DOI: 10.1038/s41550-020-01294-9 (cited on page 22).

[112] F. Aharonian et al. "Discovery of very high energy gamma-ray emission from Centaurus A with H.E.S.S". In: *Astrophys. J. Lett.* 695 (2009), pp. L40–L44. DOI: 10.1088/0004-637X/695/1/L40 (cited on page 22).

[113] H. Abdalla et al. "Resolving acceleration to very high energies along the jet of Centaurus A". In: *Nature* 582.7812 (2020). [Erratum: Nature 583, E23 (2020)], pp. 356–359. DOI: 10.1038/s41586-020-2354-1 (cited on page 22).

[114] Zhen Cao et al. "Discovery of the Ultra-high energy gamma-ray source LHAASO J2108+5157". In: (June 2021). DOI: 10.3847/2041-8213/ac2579 (cited on page 22).

[115] Zhen Cao et al. "Discovery of a New Gamma-Ray Source, LHAASO J0341+5258, with Emission up to 200 TeV". In: *Astrophys. J. Lett.* 917.1 (2021), p. L4. DOI: 10.3847/2041-8213/ac0fd5 (cited on page 22).

[116] H. Abdalla et al. "A very-high-energy component deep in the γ-ray burst afterglow". In: *Nature* 575.7783 (2019), pp. 464–467. DOI: 10.1038/s41586-019-1743-9 (cited on pages 22, 68).

[117] V. A. Acciari et al. "Observation of inverse Compton emission from a long γ-ray burst". In: *Nature* 575.7783 (2019), pp. 459–463. DOI: 10.1038/s41586-019-1754-6 (cited on page 22).

[118] V. A. Acciari et al. "Teraelectronvolt emission from the γ-ray burst GRB 190114C". In: *Nature* 575.7783 (2019), pp. 455–458. DOI: 10.1038/s41586-019-1750-x (cited on page 22).

[119] H. Abdalla et al. "Revealing x-ray and gamma ray temporal and spectral similarities in the GRB 190829A afterglow". In: *Science* 372.6546 (2021), pp. 1081–1085. DOI: 10.1126/science.abe8560 (cited on pages 22, 70).

[120] Yusuke Suda et al. "Observation of a relatively low luminosity long duration GRB 201015A by the MAGIC telescopes". In: *PoS* ICRC2021 (2021), p. 797. DOI: 10.22323/1.395.0797 (cited on pages 22, 70).

[121] Satoshi Fukami et al. "Very-high-energy gamma-ray emission from GRB 201216C detected by MAGIC". In: *PoS* ICRC2021 (2021), p. 788. DOI: 10.22323/1.395.0788 (cited on page 22).

[122] Sarira Sahu and Carlos E. López Fortıén. "Origin of sub-TeV afterglow emission from gamma-ray bursts GRB 190114C and GRB 180720B". In: *Astrophys. J. Lett.* 895.2 (2020), p. L41. DOI: 10.3847/2041-8213/ab93da (cited on page 22).

[123] Matteo Cerruti et al. “The Blazar Hadronic Code Comparison Project”. In: *PoS* ICRC2021 (2021), p. 979. DOI: 10.22323/1.395.0979 (cited on page 23).

[124] Shan Gao, Martin Pohl, and Walter Winter. “On the direct correlation between gamma-rays and PeV neutrinos from blazars”. In: *Astrophys. J.* 843.2 (2017), p. 109. DOI: 10.3847/1538-4357/aa7754 (cited on pages 23, 26, 74, 145–147).

[125] M. Boettcher et al. “Leptonic and Hadronic Modeling of Fermi-Detected Blazars”. In: *Astrophys. J.* 768 (2013), p. 54. DOI: 10.1088/0004-637X/768/1/54 (cited on page 26).

[126] M. Cerruti et al. “A hadronic origin for ultra-high-frequency-peaked BL Lac objects”. In: *Mon. Not. Roy. Astron. Soc.* 448.1 (2015), pp. 910–927. DOI: 10.1093/mnras/stu2691 (cited on page 26).

[127] A. Mastichiadis and J. G. Kirk. “Self-consistent particle acceleration in active galactic nuclei”. In: *Astron. Astrophys.* 295 (Mar. 1995), p. 613 (cited on pages 26, 32, 33).

[128] A. Mastichiadis, R. J. Protheroe, and John G. Kirk. “Spectral and temporal signatures of ultrarelativistic protons in compact sources. 1. Effects of Bethe-Heitler pair production”. In: *Astron. Astrophys.* 433 (2005), p. 765. DOI: 10.1051/0004-6361:20042161 (cited on page 26).

[129] S. Dimitrakoudis et al. “The time-dependent one-zone hadronic model - First principles”. In: *Astron. Astrophys.* 546 (2012), A120. DOI: 10.1051/0004-6361/201219770 (cited on page 26).

[130] Maria Petropoulou, Dimitrios Giannios, and Stavros Dimitrakoudis. “Implications of a PeV neutrino spectral cutoff in GRB models”. In: *Mon. Not. Roy. Astron. Soc.* 445.1 (2014), pp. 570–580. DOI: 10.1093/mnras/stu1757 (cited on page 26).

[131] M. S. Longair, ed. *High-energy astrophysics. Vol. 1: Particles, photons and their detection*. 1992 (cited on page 27).

[132] Charles D. Dermer and Govind Menon. *High energy radiation from black holes: Gamma rays, cosmic rays and neutrinos*. Princeton, USA: Princeton U. Pr., 2009 (cited on pages 27, 32, 75).

[133] Gabriele Ghisellini. *Radiative Processes in High Energy Astrophysics*. Vol. 873. 2013 (cited on pages 27, 31).

[134] S. R. Kelner and F. A. Aharonian. “Energy spectra of gamma-rays, electrons and neutrinos produced at interactions of relativistic protons with low energy radiation”. In: *Phys. Rev. D* 78 (2008). [Erratum: Phys.Rev.D 82, 099901 (2010)], p. 034013. DOI: 10.1103/PhysRevD.82.099901 (cited on pages 32, 33, 35, 147).

[135] Leonel Morejon et al. “Improved photomeson model for interactions of cosmic ray nuclei”. In: *JCAP* 11 (2019), p. 007. DOI: 10.1088/1475-7516/2019/11/007 (cited on page 32).

[136] R. J. Protheroe and P. A. Johnson. "Propagation of ultrahigh-energy protons over cosmological distances and implications for topological defect models". In: *Astropart. Phys.* 4 (1996), p. 253. DOI: 10.1016/0927-6505(95)00039-9 (cited on page 35).

[137] A. Mucke et al. "SOPHIA: Monte Carlo simulations of photohadronic processes in astrophysics". In: *Comput. Phys. Commun.* 124 (2000), pp. 290–314. DOI: 10.1016/S0010-4655(99)00446-4 (cited on page 35).

[138] S. Hummer et al. "Simplified models for photohadronic interactions in cosmic accelerators". In: *Astrophys. J.* 721 (2010), pp. 630–652. DOI: 10.1088/0004-637X/721/1/630 (cited on pages 35, 146).

[139] Malcolm S. Longair. *High Energy Astrophysics*. 2011 (cited on page 37).

[140] Anthony C. S. Readhead. "Equipartition brightness temperature and the inverse Compton catastrophe". In: *Astrophys. J.* 426 (1994), pp. 51–59. DOI: 10.1086/174038 (cited on page 38).

[141] Olivia Tsang and J. G. Kirk. "The inverse Compton catastrophe and high brightness temperature radio sources". In: *Astron. Astrophys.* 463 (2007), p. 145. DOI: 10.1051/0004-6361:20066502 (cited on page 38).

[142] Maria Petropoulou, Tsvi Piran, and Apostolos Mastichiadis. "Spectral signatures of compact sources in the inverse Compton catastrophe limit". In: *Mon. Not. Roy. Astron. Soc.* 452.3 (2015), pp. 3226–3245. DOI: 10.1093/mnras/stv1523 (cited on page 38).

[143] J. G. Kirk and A. Mastichiadis. "X-ray flares from runaway pair production in active galactic nuclei". In: *Nature* 360.6400 (1992), pp. 135–137. DOI: 10.1038/360135a0 (cited on page 38).

[144] Maria Petropoulou et al. "Hadronic supercriticality as a trigger for γ-ray burst emission". In: *Mon. Not. Roy. Astron. Soc.* 444.3 (2014), pp. 2186–2199. DOI: 10.1093/mnras/stu1362 (cited on pages 38, 51).

[145] Apostolos Mastichiadis et al. "A roadmap to hadronic supercriticalities: a comprehensive study of the parameter space for high-energy astrophysical sources". In: *Mon. Not. Roy. Astron. Soc.* 495.2 (2020), pp. 2458–2474. DOI: 10.1093/mnras/staa1308 (cited on page 39).

[146] Chryssa Kouveliotou et al. "Identification of two classes of gamma-ray bursts". In: *Astrophys. J. Lett.* 413 (1993), pp. L101–104. DOI: 10.1086/186969 (cited on page 41).

[147] Ray W. Klebesadel, Ian B. Strong, and Roy A. Olson. "Observations of Gamma-Ray Bursts of Cosmic Origin". In: *Astrophys. J.* 182 (1973), pp. L85–L88. DOI: 10.1086/181225 (cited on page 41).

[148] D. Band et al. “BATSE observations of gamma-ray burst spectra. 1. Spectral diversity.” In: *Astrophys. J.* 413 (1993), pp. 281–292. DOI: 10.1086/172995 (cited on pages 42, 44).

[149] C. A. Meegan et al. “Spatial distribution of gamma-ray bursts observed by BATSE”. In: *Nature* 355 (1992), pp. 143–145. DOI: 10.1038/355143a0 (cited on page 42).

[150] E. Costa et al. “Discovery of an X-ray afterglow associated with the gamma-ray burst of 28 February 1997”. In: *Nature* 387 (1997), pp. 783–785. DOI: 10.1038/42885 (cited on page 42).

[151] S. D. Barthelmy et al. “The Burst Alert Telescope (BAT) on the Swift MIDEX mission”. In: *Space Sci. Rev.* 120 (2005), p. 143. DOI: 10.1007/s11214-005-5096-3 (cited on page 42).

[152] Charles Meegan et al. “The Fermi Gamma-Ray Burst Monitor”. In: *Astrophys. J.* 702 (2009), pp. 791–804. DOI: 10.1088/0004-637X/702/1/791 (cited on page 42).

[153] M. J. Rees and P. Meszaros. “Relativistic fireballs - energy conversion and time - scales”. In: *Mon. Not. Roy. Astron. Soc.* 258 (1992), pp. 41–43 (cited on page 43).

[154] R. D. Blandford and R. L. Znajek. “Electromagnetic extractions of energy from Kerr black holes”. In: *Mon. Not. Roy. Astron. Soc.* 179 (1977), pp. 433–456 (cited on page 44).

[155] R. D. Blandford and D. G. Payne. “Hydromagnetic flows from accretion discs and the production of radio jets”. In: *Mon. Not. Roy. Astron. Soc.* 199 (1982), p. 883 (cited on page 44).

[156] John F. Hawley et al. “Disks and Jets - Gravity, Rotation and Magnetic Fields”. In: *Space Sci. Rev.* 191.1-4 (2015), pp. 441–469. DOI: 10.1007/s11214-015-0174-7 (cited on page 44).

[157] Serguei Komissarov and Oliver Porth. “Numerical simulations of jets”. In: *New Astronomy Reviews* 92, 101610 (2021), p. 101610. DOI: 10.1016/j.newar.2021.101610 (cited on page 44).

[158] Omer Bromberg and Alexander Tchekhovskoy. “Relativistic MHD simulations of core-collapse GRB jets: 3D instabilities and magnetic dissipation”. In: *Mon. Not. Roy. Astron. Soc.* 456.2 (2016), pp. 1739–1760. DOI: 10.1093/mnras/stv2591 (cited on pages 44, 47).

[159] Jonathan Granot, Serguei Komissarov, and Anatoly Spitkovsky. “Impulsive Acceleration of Strongly Magnetized Relativistic Flows”. In: *Mon. Not. Roy. Astron. Soc.* 411 (2011), p. 1323. DOI: 10.1111/j.1365-2966.2010.17770.x (cited on page 44).

[160] Jonathan Granot. “The effects of sub-shells in highly magnetized relativistic flows”. In: *Mon. Not. Roy. Astron. Soc.* 421 (2012), pp. 2467–2477. DOI: 10.1111/j.1365-2966.2012.20474.x (cited on page 44).

[161] S. Poolakkil et al. "The Fermi-GBM Gamma-Ray Burst Spectral Catalog: 10 yr of Data". In: *Astrophys. J.* 913.1 (2021), p. 60. DOI: 10.3847/1538-4357/abf24d (cited on pages 44, 50).

[162] Magnus Axelsson and Luis Borgonovo. "The width of gamma-ray burst spectra". In: *Mon. Not. Roy. Astron. Soc.* 447 (2015), pp. 3150–3154. DOI: 10.1093/mnras/stu2675 (cited on pages 44, 114).

[163] Hoi-Fung Yu et al. "The sharpness of gamma-ray burst prompt emission spectra". In: *Astron. Astrophys.* 583 (2015), A129. DOI: 10.1051/0004-6361/201527015 (cited on pages 44, 114).

[164] Xiang-Gao Wang et al. "Gamma-ray burst jet breaks revisited". In: *Astrophys. J.* 859.2 (2018), p. 160. DOI: 10.3847/1538-4357/aabc13 (cited on page 45).

[165] Bing Zhang. *The Physics of Gamma-Ray Bursts*. Cambridge University Press, Dec. 2018 (cited on pages 45, 51).

[166] M. J. Rees and P. Meszaros. "Unsteady outflow models for cosmological gamma-ray bursts". In: *Astrophys. J.* 430 (1994), pp. L93–L96. DOI: 10.1086/187446 (cited on pages 45, 55).

[167] Shiho Kobayashi, Tsvi Piran, and Re'em Sari. "Can internal shocks produce the variability in GRBs?" In: *Astrophys. J.* 490 (1997), pp. 92–98. DOI: 10.1086/512791 (cited on pages 45, 55, 56, 59, 61, 65).

[168] F. Daigne and R. Mochkovitch. "Gamma-ray bursts from internal shocks in a relativistic wind: temporal and spectral properties". In: *Mon. Not. Roy. Astron. Soc.* 296 (1998), p. 275. DOI: 10.1046/j.1365-8711.1998.01305.x (cited on pages 45, 55, 57–59, 73, 149).

[169] Patrick Crumley et al. "Kinetic simulations of mildly relativistic shocks – I. Particle acceleration in high Mach number shocks". In: *Mon. Not. Roy. Astron. Soc.* 485.4 (2019), pp. 5105–5119. DOI: 10.1093/mnras/stz232 (cited on page 45).

[170] Dimitrios Giannios and Henk C. Spruit. "Poynting - flux powered GRB outflows: Spectral predictions". In: *Astron. Astrophys.* 430 (2005), pp. 1–7. DOI: 10.1051/0004-6361:20047033 (cited on page 46).

[171] Jonathan C. McKinney and Dmitri A. Uzdensky. "A Reconnection Switch to Trigger Gamma-Ray Burst Jet Dissipation". In: *Mon. Not. Roy. Astron. Soc.* 419 (2012), pp. 573–607. DOI: 10.1111/j.1365-2966.2011.19721.x (cited on page 46).

[172] Bing Zhang and Huirong Yan. "The Internal-Collision-Induced Magnetic Reconnection and Turbulence (ICMART) Model of Gamma-Ray Bursts". In: *Astrophys. J.* 726 (2011), p. 90. DOI: 10.1088/0004-637X/726/2/90 (cited on page 46).

[173] Ore Gottlieb, Amir Levinson, and Ehud Nakar. "High efficiency photospheric emission entailed by formation of a collimation shock in gamma-ray bursts". In: *Mon. Not. Roy. Astron. Soc.* 488.1 (2019), pp. 1416–1426. DOI: 10.1093/mnras/stz1828 (cited on pages 46, 47, 114).

[174] Ore Gottlieb et al. "The structure of weakly magnetized γ-ray burst jets". In: *Mon. Not. Roy. Astron. Soc.* 498.3 (2020), pp. 3320–3333. DOI: 10.1093/mnras/staa2567 (cited on pages 46, 47).

[175] Ore Gottlieb, Amir Levinson, and Ehud Nakar. "Intermittent hydrodynamic jets in collapsars do not produce GRBs". In: *Mon. Not. Roy. Astron. Soc.* 495.1 (2020), pp. 570–577. DOI: 10.1093/mnras/staa1216 (cited on pages 46, 47).

[176] Ore Gottlieb et al. "Intermittent mildly magnetized jets as the source of GRBs". In: *Mon. Not. Roy. Astron. Soc.* 504.3 (2021), pp. 3947–3955. DOI: 10.1093/mnras/stab1068 (cited on pages 46, 47).

[177] A. M. Beloborodov and P. Mészáros. "Photospheric Emission of Gamma-Ray Bursts". In: *Space Sci. Rev.* 207.1-4 (2017), pp. 87–110. DOI: 10.1007/s11214-017-0348-6 (cited on pages 48, 51, 52).

[178] Tsvi Piran. "The physics of gamma-ray bursts". In: *Rev. Mod. Phys.* 76 (2004), pp. 1143–1210. DOI: 10.1103/RevModPhys.76.1143 (cited on page 48).

[179] Re'em Sari, Tsvi Piran, and Ramesh Narayan. "Spectra and light curves of gamma-ray burst afterglows". In: *Astrophys. J. Lett.* 497 (1998), p. L17. DOI: 10.1086/311269 (cited on page 48).

[180] R. D. Preece et al. "On the Consistency of Gamma-Ray Burst Spectral Indices with the Synchrotron Shock Model". In: *The Astrophysical Journal* 581.2 (2002), p. 1248 (cited on page 50).

[181] Gabriele Ghisellini, Annalisa Celotti, and Davide Lazzati. "Constraints on the emission mechanisms of gamma-ray bursts". In: *Mon. Not. Roy. Astron. Soc.* 313 (2000), p. 1. DOI: 10.1046/j.1365-8711.2000.03354.x (cited on page 50).

[182] Amy Lien et al. "The Third Swift Burst Alert Telescope Gamma-Ray Burst Catalog". In: *Astrophys. J.* 829.1 (2016), p. 7. DOI: 10.3847/0004-637X/829/1/7 (cited on page 50).

[183] J. Michael Burgess et al. "Gamma-ray bursts as cool synchrotron sources". In: *Nature Astron.* 4.2 (2019), pp. 174–179. DOI: 10.1038/s41550-019-0911-z (cited on pages 50, 52, 114).

[184] F. Daigne, Z. Bosnjak, and Guillaume Dubus. "Reconciling observed GRB prompt spectra with synchrotron radiation ?" In: *Astron. Astrophys.* 526 (2011), A110. DOI: 10.1051/0004-6361/201015457 (cited on pages 50, 69, 77–79, 88, 91, 92, 110, 113, 154).

[185] Gor Oganesyan et al. “Detection of Low-energy Breaks in Gamma-Ray Burst Prompt Emission Spectra”. In: *Astrophys. J.* 846 (2017), p. 137. DOI: 10.3847/1538-4357/aa831e (cited on page 50).

[186] Gor Oganesyan et al. “Prompt optical emission as a signature of synchrotron radiation in gamma-ray bursts”. In: *Astron. Astrophys.* 628 (2019), A59. DOI: 10.1051/0004-6361/201935766 (cited on pages 50, 79, 115).

[187] Ehud Nakar, Shin’ichiro Ando, and Re’em Sari. “Klein-Nishina effects on Synchrotron and Synchrotron self-Compton spectrum”. In: *Astrophys. J.* 703 (2009), pp. 675–691. DOI: 10.1088/0004-637X/703/1/675 (cited on pages 50, 92, 154).

[188] R.Barniol Duran, Z. Bosnjak, and P. Kumar. “Inverse Compton cooling in Klein-Nishina regime and GRB prompt spectrum”. In: *Mon. Not. Roy. Astron. Soc.* 424 (2012), pp. 3192–3200. DOI: 10.1111/j.1365-2966.2012.21533.x (cited on pages 50, 92).

[189] Katsuaki Asano and Susumu Inoue. “Prompt GeV-TeV Emission of Gamma-Ray Bursts Due to High-Energy Protons, Muons and Electron-Positron Pairs”. In: *Astrophys. J.* 671 (2007), pp. 645–655. DOI: 10.1086/522939 (cited on pages 51, 94).

[190] Katsuaki Asano and Peter Mészáros. “Spectral-Temporal Simulations of Internal Dissipation Models of Gamma-Ray Bursts”. In: *Astrophys. J.* 739.2, 103 (Oct. 2011), p. 103. DOI: 10.1088/0004-637X/739/2/103 (cited on page 51).

[191] Katsuaki Asano, Susumu Inoue, and Peter Meszaros. “Prompt High-Energy Emission from Proton-Dominated Gamma-Ray Bursts”. In: *Astrophys. J.* 699 (2009), pp. 953–957. DOI: 10.1088/0004-637X/699/2/953 (cited on pages 51, 53, 68, 94, 99).

[192] G. Ghisellini et al. “Proton–synchrotron as the radiation mechanism of the prompt emission of gamma-ray bursts?” In: *Astron. Astrophys.* 636 (2020), A82. DOI: 10.1051/0004-6361/201937244 (cited on page 51).

[193] Ioulia Florou, Maria Petropoulou, and Apostolos Mastichiadis. “A marginally fast-cooling proton–synchrotron model for prompt GRBs”. In: *Mon. Not. Roy. Astron. Soc.* 505.1 (2021), pp. 1367–1381. DOI: 10.1093/mnras/stab1285 (cited on page 51).

[194] Ioulia Florou, Apostolos Mastichiadis, and Maria Petropoulou. “An expanding hadronic supercritical model for γ-ray burst emission”. In: *PoS* ICRC2021 (2021), p. 1022. DOI: 10.22323/1.395.1022 (cited on page 51).

[195] Asaf Pe’er and Felix Ryde. “Photospheric Emission in Gamma-Ray Bursts”. In: *Int. J. Mod. Phys. D* 26.10 (2017), p. 1730018. DOI: 10.1142/S021827181730018X (cited on page 51).

[196] Kohta Murase et al. "The Role of Stochastic Acceleration in the Prompt Emission of Gamma-Ray Bursts: Application to Hadronic Injection". In: *Astrophys. J.* 746 (2012), p. 164. DOI: 10.1088/0004-637X/746/2/164 (cited on page 51).

[197] G. Drenkhahn and H. C. Spruit. "Efficient acceleration and radiation in Poynting flux powered GRB outflows". In: *Astron. Astrophys.* 391 (2002), p. 1141. DOI: 10.1051/0004-6361:20020839 (cited on page 51).

[198] Dimitrios Giannios and Henk C. Spruit. "Spectral and timing properties of a dissipative GRB photosphere". In: *Astron. Astrophys.* 469 (2007), pp. 1–9. DOI: 10.1051/0004-6361:20066739 (cited on page 51).

[199] Andrei M. Beloborodov. "Collisional mechanism for GRB emission". In: *Mon. Not. Roy. Astron. Soc.* 407 (2010), p. 1033. DOI: 10.1111/j.1365-2966.2010.16770.x (cited on page 51).

[200] Indrek Vurm, Andrei M. Beloborodov, and Juri Poutanen. "Gamma-ray bursts from magnetized collisionally-heated jets". In: *Astrophys. J.* 738 (2011), p. 77. DOI: 10.1088/0004-637X/738/1/77 (cited on page 51).

[201] Davide Lazzati, Brian J. Morsony, and Mitch Begelman. "Very high efficiency photospheric emission in long duration gamma-ray bursts". In: *Astrophys. J. Lett.* 700 (2009), pp. L47–L50. DOI: 10.1088/0004-637X/700/1/L47 (cited on page 51).

[202] D. Lazzati et al. "Photospheric emission as the dominant radiation mechanism in long-duration gamma-ray bursts". In: *Astrophys. J.* 765 (2013), p. 103. DOI: 10.1088/0004-637X/765/2/103 (cited on page 51).

[203] Asaf Pe'er. "Temporal Evolution Of Thermal Emission From Relativistically Expanding Plasma". In: *Astrophys. J.* 682 (2008), p. 463. DOI: 10.1086/588136 (cited on page 52).

[204] Christoffer Lundman, Asaf Pe'er, and Felix Ryde. "A theory of photospheric emission from collimated outflows". In: *Mon. Not. Roy. Astron. Soc.* 428 (2013), p. 2430. DOI: 10.1093/mnras/sts219 (cited on page 52).

[205] Filip Samuelsson, Christoffer Lundman, and Felix Ryde. "An efficient method for fitting radiation-mediated shocks to gamma-ray burst data: The Kompaneets RMS approximation". In: *arXiv e-prints* (Nov. 2021) (cited on page 52).

[206] Felix Ryde. "Is thermal emission in gamma-ray bursts ubiquitous?" In: *Astrophys. J. Lett.* 625 (2005), pp. L95–L98. DOI: 10.1086/431239 (cited on page 52).

[207] M. Toffano et al. "The slope of the low energy spectrum of Gamma-Ray Burst prompt emission". In: *Astron. Astrophys.* 652 (2021), A123. DOI: 10.1051/0004-6361/202141032 (cited on page 52).

[208] Zeynep Acuner and Felix Ryde. "Clustering of gamma-ray burst types in the Fermi-GBM catalogue: indications of photosphere and synchrotron emissions during the prompt phase". In: *Mon. Not. Roy. Astron. Soc.* 475.2 (2018), pp. 1708–1724. DOI: 10.1093/mnras/stx3106 (cited on pages 52, 115).

[209] Xiang-Yu Wang, Soebur Razzaque, and Peter Meszaros. "On the Origin and Survival of UHE Cosmic-Ray Nuclei in GRBs and Hypernovae". In: *Astrophys. J.* 677 (2008), pp. 432–440. DOI: 10.1086/529018 (cited on page 52).

[210] Kohta Murase et al. "High-energy cosmic-ray nuclei from high- and low-luminosity gamma-ray bursts and implications for multi-messenger astronomy". In: *Phys. Rev. D* 78 (2008), p. 023005. DOI: 10.1103/PhysRevD.78.023005 (cited on pages 52, 81).

[211] Brian D. Metzger, Dimitrios Giannios, and Shunsaku Horiuchi. "Heavy Nuclei Synthesized in Gamma-Ray Burst Outflows as the Source of UHECRs". In: *Mon. Not. Roy. Astron. Soc.* 415 (2011), p. 2495. DOI: 10.1111/j.1365-2966.2011.18873.x (cited on page 52).

[212] Noemie Globus et al. "UHECR acceleration at GRB internal shocks". In: *Mon. Not. Roy. Astron. Soc.* 451.1 (2015), pp. 751–790. DOI: 10.1093/mnras/stv893 (cited on pages 52, 64, 94, 111).

[213] Maria Petropoulou. "The role of hadronic cascades in GRB models of efficient neutrino production". In: *Mon. Not. Roy. Astron. Soc.* 442.4 (2014), pp. 3026–3036. DOI: 10.1093/mnras/stu1079 (cited on pages 53, 94, 95, 99, 100, 113).

[214] Annika Rudolph et al. "Impact of the Collision Model on the Multi-messenger Emission from Gamma-Ray Burst Internal Shocks". In: *Astrophys. J.* 893 (2020), p. 72. DOI: 10.3847/1538-4357/ab7ea7 (cited on pages 55, 61–63, 149, 151–153).

[215] Jonas Heinze et al. "Systematic parameter space study for the UHECR origin from GRBs in models with multiple internal shocks". In: *Mon. Not. Roy. Astron. Soc.* 498.4 (2020), pp. 5990–6004. DOI: 10.1093/mnras/staa2751 (cited on pages 55, 64, 66, 67, 93).

[216] F. Daigne and R. Mochkovitch. "Gamma-ray bursts from internal shocks in a relativistic wind: an hydrodynamical study". In: *Astron. Astrophys.* 358 (2000), p. 1157 (cited on page 57).

[217] Shiho Kobayashi and Re'em Sari. "Ultra efficient internal shocks". In: *Astrophys. J.* 551 (2001), p. 934. DOI: 10.1086/320249 (cited on pages 61, 150).

[218] Motoki Kino, Akira Mizuta, and Shoichi Yamada. "Hydrodynamical effects in internal shock of relativistic outflows". In: *Astrophys. J.* 611 (2004), pp. 1021–1032. DOI: 10.1086/422305 (cited on pages 62, 152).

[219] A. Mignone et al. “PLUTO: A Numerical Code for Computational Astrophysics”. In: *Astrophys. J. Suppl.* 170 (2007), p. 228. DOI: 10.1086/513316 (cited on pages 62, 151).

[220] M. G. Aartsen et al. “Extending the search for muon neutrinos coincident with gamma-ray bursts in IceCube data”. In: *Astrophys. J.* 843.2 (2017), p. 112. DOI: 10.3847/1538-4357/aa7569 (cited on pages 63, 64, 67, 68).

[221] Philipp Baerwald, Mauricio Bustamante, and Walter Winter. “UHECR escape mechanisms for protons and neutrons from GRBs, and the cosmic ray-neutrino connection”. In: *Astrophys. J.* 768 (2013), p. 186. DOI: 10.1088/0004-637X/768/2/186 (cited on page 63).

[222] Jonas Heinze et al. “A new view on Auger data and cosmogenic neutrinos in light of different nuclear disintegration and air-shower models”. In: *Astrophys. J.* 873.1 (2019), p. 88. DOI: 10.3847/1538-4357/ab05ce (cited on page 66).

[223] David Wanderman and Tsvi Piran. “The luminosity function and the rate of Swift’s Gamma Ray Bursts”. In: *Mon. Not. Roy. Astron. Soc.* 406 (2010), pp. 1944–1958. DOI: 10.1111/j.1365-2966.2010.16787.x (cited on page 66).

[224] F. James and M. Roos. “Minuit: A System for Function Minimization and Analysis of the Parameter Errors and Correlations”. In: *Comput. Phys. Commun.* 10 (1975), pp. 343–367. DOI: 10.1016/0010-4655(75)90039-9 (cited on page 66).

[225] M.G. Aartsen et al. “IceCube-Gen2: The Window to the Extreme Universe”. In: *arXiv:2008.04323* (Aug. 2020) (cited on pages 67, 68).

[226] G. A. MacLachlan et al. “Minimum Variability Time Scales of Long and Short GRBs”. In: *Mon. Not. Roy. Astron. Soc.* 432 (2013), p. 857. DOI: 10.1093/mnras/stt241 (cited on page 68).

[227] P. N. Bhat. “Variability Time Scales of Long and Short GRBs”. In: July 2013 (cited on page 68).

[228] Vahid Zach Golkhou and Nathaniel R. Butler. “Uncovering the Intrinsic Variability of Gamma-ray Bursts”. In: *Astrophys. J.* 787 (2014), p. 90. DOI: 10.1088/0004-637X/787/1/90 (cited on pages 68, 112).

[229] Philipp Baerwald, Mauricio Bustamante, and Walter Winter. “Are gamma-ray bursts the sources of ultra-high energy cosmic rays?” In: *Astropart. Phys.* 62 (2015), pp. 66–91. DOI: 10.1016/j.astropartphys.2014.07.007 (cited on page 68).

[230] Yiz-Hong Fan and Tsvi Piran. “Grb efficiency and possible physical processes shaping the early afterglow”. In: *Mon. Not. Roy. Astron. Soc.* 369 (2006), pp. 197–206. DOI: 10.1111/j.1365-2966.2006.10280.x (cited on page 68).

[231] Paz Beniamini et al. “Energies of GRB blast waves and prompt efficiencies as implied by modelling of X-ray and GeV afterglows”. In: *Mon. Not. Roy. Astron. Soc.* 454.1 (2015), pp. 1073–1085. DOI: 10.1093/mnras/stv2033 (cited on page 68).

[232] V. A. Acciari et al. “Observation of inverse Compton emission from a long γ-ray burst”. In: *Nature* 575.7783 (2019), pp. 459–463. DOI: 10.1038/s41586-019-1754-6 (cited on page 68).

[233] Annika Rudolph et al. “Multiwavelength radiation models for low-luminosity GRBs and the implications for UHECRs”. In: *Mon. Not. Roy. Astron. Soc.* 511.4 (2022), pp. 5823–5842. DOI: 10.1093/mnras/stac433 (cited on pages 69, 70, 94, 149, 153).

[234] Z. Bosnjak, F. Daigne, and G. Dubus. “Prompt high-energy emission from gamma-ray bursts in the internal shock model”. In: *Astron. Astrophys.* 498 (2009), p. 677. DOI: 10.1051/0004-6361/200811375 (cited on pages 69, 73, 74, 88, 91).

[235] Željka Bošnjak and Frédéric Daigne. “Spectral evolution in gamma-ray bursts: predictions of the internal shock model and comparison to observations”. In: *Astron. Astrophys.* 568 (2014), A45. DOI: 10.1051/0004-6361/201322341 (cited on pages 69, 73, 88).

[236] G. Ghirlanda et al. “Bulk Lorentz factors of Gamma-Ray Bursts”. In: *Astron. Astrophys.* 609 (2018), A112. DOI: 10.1051/0004-6361/201731598 (cited on pages 70, 106).

[237] Zach Cano et al. “The Observer’s Guide to the Gamma-Ray Burst Supernova Connection”. In: *Adv. Astron.* 2017 (2017), p. 8929054. DOI: 10.1155/2017/8929054 (cited on page 70).

[238] L. Amati et al. “Intrinsic spectra and energetics of BeppoSAX gamma-ray bursts with known redshifts”. In: *Astron. Astrophys.* 390 (2002), p. 81. DOI: 10.1051/0004-6361:20020722 (cited on page 70).

[239] Enwei Liang, Bing Zhang, and Z. G. Dai. “Low Luminosity Gamma-Ray Bursts as a Unique Population: Luminosity Function, Local Rate, and Beaming Factor”. In: *Astrophys. J.* 662 (2007), pp. 1111–1118. DOI: 10.1086/517959 (cited on pages 70, 81).

[240] Francisco Virgili, Enwei Liang, and Bing Zhang. “Low-Luminosity Gamma-Ray Bursts as a Distinct GRB Population:A Monte Carlo Analysis”. In: *Mon. Not. Roy. Astron. Soc.* 392 (2009), p. 91. DOI: 10.1111/j.1365-2966.2008.14063.x (cited on page 70).

[241] Hui Sun, Bing Zhang, and Zhuo Li. “Extragalactic High-energy Transients: Event Rate Densities and Luminosity Functions”. In: *Astrophys. J.* 812.1 (2015), p. 33. DOI: 10.1088/0004-637X/812/1/33 (cited on page 70).

[242] Gabriele Ghisellini et al. "Are GRB 980425 and GRB 031203 real outliers or twins of GRB 060218?" In: *Mon. Not. Roy. Astron. Soc.* 372 (2006), pp. 1699–1709. DOI: 10.1111/j.1365-2966.2006.10972.x (cited on page 70).

[243] Yuki Kaneko et al. "Prompt and Afterglow Emission Properties of Gamma-Ray Bursts with Spectroscopically Identified Supernovae". In: *Astrophys. J.* 654 (2006), pp. 385–402. DOI: 10.1086/508324 (cited on pages 70, 71).

[244] S. Campana et al. "The shock break-out of grb 060218/sn 2006aj". In: *Nature* 442 (2006), pp. 1008–1010. DOI: 10.1038/nature04892 (cited on page 70).

[245] R. L. C. Starling et al. "Discovery of the nearby long, soft GRB 100316D with an associated supernova". In: *Mon. Not. Roy. Astron. Soc.* 411 (2011), pp. 2792–2803. DOI: 10.1111/j.1365-2966.2010.17879.x (cited on pages 70, 71).

[246] M. Kovacevic et al. "A search for *Fermi* bursts associated to supernovae and their frequency of occurrence". In: *Astron. Astrophys.* 569 (2014), A108. DOI: 10.1051/0004-6361/201424700 (cited on page 70).

[247] S. Schulze et al. "GRB 120422A/SN 2012bz: Bridging the gap between low- and high-luminosity gamma-ray bursts". In: *Astron. Astrophys.* 566 (2014), A102. DOI: 10.1051/0004-6361/201423387 (cited on page 70).

[248] S. Klose et al. "Four GRB supernovae at redshifts between 0.4 and 0.8 - The bursts GRB 071112C, 111228A, 120714B, and 130831A". In: *Astron. Astrophys.* 622 (2019), A138. DOI: 10.1051/0004-6361/201832728 (cited on page 70).

[249] A. A. Volnova et al. "Multicolour modelling of SN 2013dx associated with GRB 130702A". In: *Mon. Not. Roy. Astron. Soc.* 467.3 (2017), pp. 3500–3512. DOI: 10.1093/mnras/stw3297 (cited on page 70).

[250] Leo P. Singer et al. "Discovery and Redshift of an Optical Afterglow in 71 deg^2: iPTF13bxl and GRB 130702A". In: *Astrophys. J.* 776 (2013), p. L34. DOI: 10.1088/2041-8205/776/2/L34 (cited on page 70).

[251] Z. Cano et al. "GRB 161219B/SN 2016jca: A low-redshift gamma-ray burst supernova powered by radioactive heating". In: *Astron. Astrophys.* 605 (2017), A107. DOI: 10.1051/0004-6361/201731005 (cited on page 70).

[252] V. D'Elia et al. "GRB 171205A/SN 2017iuk: A local low-luminosity gamma-ray burst". In: *Astron. Astrophys.* 619 (2018), A66. DOI: 10.1051/0004-6361/201833847 (cited on page 70).

[253] Vikas Chand et al. “Shock-breakout and central engine activities in H.E.S.S. detected GRB 190829A”. In: *ArXiv eprints* (2020) (cited on pages 70, 72).

[254] F. Frontera et al. “Prompt and delayed emission properties of gamma-ray bursts observed with BeppoSAX”. In: *Astrophys. J. Suppl.* 127 (2000), pp. 59–78. DOI: 10.1086/313316 (cited on page 70).

[255] F. Daigne and R. Mochkovitch. “The low-luminosity tail of the GRB distribution: The case of GRB 980425”. In: *Astron. Astrophys.* 465 (2007), pp. 1–8. DOI: 10.1051/0004-6361:20066080 (cited on pages 70, 71, 73).

[256] Yi-Zhong Fan et al. “XRF 100316D/SN 2010bh: clue to the diverse origin of nearby supernova-associated GRBs”. In: *Astrophys. J.* 726 (2011), p. 32. DOI: 10.1088/0004-637X/726/1/32 (cited on page 71).

[257] Bin-Bin Zhang et al. “GRB 120422A: A Low-luminosity Gamma-ray Burst Driven by Central Engine”. In: *Astrophys. J.* 756 (2012), p. 190. DOI: 10.1088/0004-637X/756/2/190 (cited on page 71).

[258] J. R. Cummings et al. “GCN Circ. 13481”. In: *GCN Circ. 13481* (2012) (cited on page 71).

[259] A. Pescalli et al. “Luminosity function and jet structure of Gamma-Ray Burst”. In: *Mon. Not. Roy. Astron. Soc.* 447.2 (2015), pp. 1911–1921. DOI: 10.1093/mnras/stu2482 (cited on page 71).

[260] Miguel-Angel Aloy, Carlos F. Cuesta-Martínez, and M. Obergaulinger. “On the existence of a luminosity threshold of GRB jets in massive stars”. In: *Mon. Not. Roy. Astron. Soc.* 478.3 (2018), pp. 3576–3589. DOI: 10.1093/mnras/sty1212 (cited on page 71).

[261] G. Ghisellini, G. Ghirlanda, and F. Tavecchio. “Did we observe the supernova shock breakout in GRB 060218?” In: *Mon. Not. Roy. Astron. Soc.* 382 (2007), p. 77. DOI: 10.1111/j.1745-3933.2007.00396.x (cited on page 71).

[262] C. M. Irwin and R. A. Chevalier. “Jet or Shock Breakout? The Low-Luminosity GRB 060218”. In: *Mon. Not. Roy. Astron. Soc.* 460.2 (2016), pp. 1680–1704. DOI: 10.1093/mnras/stw1058 (cited on page 71).

[263] Eli Waxman, P. Meszaros, and S. Campana. “GRB060218: A Relativistic Supernova Shock Breakout”. In: *Astrophys. J.* 667 (2007), pp. 351–357. DOI: 10.1086/520715 (cited on page 71).

[264] Omer Bromberg, Ehud Nakar, and Tsvi Piran. “Are Low-luminosity Gamma-Ray Bursts Generated by Relativistic Jets?” In: *Astrophysical Journal - ASTROPHYS J* 739 (Oct. 2011). DOI: 10.1088/2041-8205/739/2/L55 (cited on page 71).

[265] Ehud Nakar and Re'em Sari. "Relativistic shock breakouts - a variety of gamma-ray flares: from low luminosity gamma-ray bursts to type Ia supernovae". In: *Astrophys. J.* 747 (2012), p. 88. DOI: 10.1088/0004-637X/747/2/88 (cited on pages 71, 72).

[266] Ehud Nakar. "A unified picture for low-luminosity and long gamma-ray bursts based on the extended progenitor of llgrb 060218/SN 2006aj". In: *Astrophys. J.* 807.2 (2015), p. 172. DOI: 10.1088/0004-637X/807/2/172 (cited on pages 71, 72).

[267] Anatoly Spitkovsky. "Particle acceleration in relativistic collisionless shocks: Fermi process at last?" In: *Astrophys. J. Lett.* 682 (2008), p. L5. DOI: 10.1086/590248 (cited on page 73).

[268] Jonathan Granot, Tsvi Piran, and Re'em Sari. "Images and spectra from the interior of a relativistic fireball". In: *Astrophys. J.* 513 (1999), pp. 679–689. DOI: 10.1086/306884 (cited on page 75).

[269] Christoph Deil et al. "Gammapy - A prototype for the CTA science tools". In: *PoS* ICRC2017 (2018), p. 766. DOI: 10.22323/1.301.0766 (cited on page 76).

[270] C. Nigro et al. "Towards open and reproducible multi-instrument analysis in gamma-ray astronomy". In: *Astron. Astrophys.* 625 (2019), A10. DOI: 10.1051/0004-6361/201834938 (cited on page 76).

[271] A. Dominguez et al. "Extragalactic Background Light Inferred from AEGIS Galaxy SED-type Fractions". In: *Mon. Not. Roy. Astron. Soc.* 410 (2011), p. 2556. DOI: 10.1111/j.1365-2966.2010.17631.x (cited on page 76).

[272] Filip Samuelsson et al. "Constraining Low-luminosity Gamma-Ray Bursts as Ultra-high-energy Cosmic Ray Sources Using GRB 060218 as a Proxy". In: *arXiv e-prints*, arXiv:2005.02417 (May 2020), arXiv:2005.02417 (cited on pages 79, 81–83).

[273] R. Hascoet et al. "Do Fermi-LAT observations imply very large Lorentz factors in GRB outflows ?" In: *Mon. Not. Roy. Astron. Soc.* 421 (2012), p. 525. DOI: 10.1111/j.1365-2966.2011.20332.x (cited on pages 79, 106, 107).

[274] J. Knödlseder et al. "GammaLib and ctools: A software framework for the analysis of astronomical gamma-ray data". In: *Astron. Astrophys.* 593 (2016), A1. DOI: 10.1051/0004-6361/201628822 (cited on page 80).

[275] Kohta Murase et al. "High Energy Neutrinos and Cosmic-Rays from Low-Luminosity Gamma-Ray Bursts?" In: *Astrophys. J.* 651 (2006), pp. L5–L8. DOI: 10.1086/509323 (cited on page 81).

[276] Ruo-Yu Liu, Xiang-Yu Wang, and Zi-Gao Dai. "Nearby low-luminosity GRBs as the sources of ultra-high energy cosmic rays revisited". In: *Mon. Not. Roy. Astron. Soc.* 418 (2011), p. 1382. DOI: 10.1111/j.1365-2966.2011.19590.x (cited on page 81).

[277] Nicholas Senno, Kohta Murase, and Peter Meszaros. "Choked Jets and Low-Luminosity Gamma-Ray Bursts as Hidden Neutrino Sources". In: *Phys. Rev. D* D93.8 (2016), p. 083003. DOI: 10.1103/PhysRevD.93.083003 (cited on page 81).

[278] B. Theodore Zhang et al. "Low-luminosity gamma-ray bursts as the sources of ultrahigh-energy cosmic ray nuclei". In: *Phys. Rev. D* D97.8 (2018), p. 083010. DOI: 10.1103/PhysRevD.97.083010 (cited on pages 81, 82, 84).

[279] Denise Boncioli, Daniel Biehl, and Walter Winter. "On the common origin of cosmic rays across the ankle and diffuse neutrinos at the highest energies from low-luminosity Gamma-Ray Bursts". In: *Astrophys. J.* 872.1 (2019), p. 110. DOI: 10.3847/1538-4357/aafda7 (cited on pages 81, 82, 84).

[280] Filip Samuelsson et al. "The Limited Contribution of Low- and High-Luminosity Gamma-Ray Bursts to Ultra-High Energy Cosmic Rays". In: *Astrophys. J.* 876.2 (2019), p. 93. DOI: 10.3847/1538-4357/ab153c (cited on pages 81–83).

[281] J. J. Brainerd. "Quantum Synchrotron Spectra from Semirelativistic Electrons in Teragauss Magnetic Fields". In: *Astrophys. J.* 320 (1987), p. 714. DOI: 10.1086/165589 (cited on pages 87, 147).

[282] Katsuaki Asano and Peter Meszaros. "Delayed Onset of High-Energy Emissions in Leptonic and Hadronic Models of Gamma-Ray Bursts". In: *Astrophys. J.* 757 (2012), p. 115. DOI: 10.1088/0004-637X/757/2/115 (cited on page 94).

[283] Katsuaki Asano and Peter Mészáros. "Neutrino and Cosmic-Ray Release from Gamma-Ray Bursts: Time-Dependent Simulations". In: *Astrophys. J.* 785 (2014), p. 54. DOI: 10.1088/0004-637X/785/1/54 (cited on pages 94, 95, 99).

[284] Kai Wang et al. "Hadronic origin of prompt high-energy emission of gamma-ray bursts revisited: in the case of a limited maximum proton energy". In: *Astrophys. J.* 857.1 (2018), p. 24. DOI: 10.3847/1538-4357/aab667 (cited on pages 94–96, 110, 113).

[285] Philipp Baerwald, Svenja Hummer, and Walter Winter. "Systematics in the Interpretation of Aggregated Neutrino Flux Limits and Flavor Ratios from Gamma-Ray Bursts". In: *Astropart. Phys.* 35 (2012), pp. 508–529. DOI: 10.1016/j.astropartphys.2011.11.005 (cited on pages 97, 101).

[286] Giacomo Vianello et al. "The Multi-Mission Maximum Likelihood framework (3ML)". In: July 2015 (cited on page 105).

[287] M. Ajello et al. "A Decade of Gamma-Ray Bursts Observed by Fermi-LAT: The Second GRB Catalog". In: *Astrophys. J.* 878.1 (2019), p. 52. DOI: 10.3847/1538-4357/ab1d4e (cited on page 104).

[288] Joshua S. Bloom, Dale A. Frail, and Re'em Sari. "The prompt energy release of gamma-ray bursts using a cosmological k-correction". In: *Astron. J.* 121 (2001), pp. 2879–2888. DOI: 10.1086/321093 (cited on page 105).

[289] Andras Kovacs et al. "Cosmology with Gamma-Ray Bursts Using k-correction". In: *arXiv e-prints*, arXiv:1204.1222 (Apr. 2012), arXiv:1204.1222 (cited on page 105).

[290] M. Ajello et al. "Bright γ-Ray Flares Observed in GRB 131108A". In: *Astrophys. J. Lett.* 886.2 (2019), p. L33. DOI: 10.3847/2041-8213/ab564f (cited on page 105).

[291] A. Giuliani et al. "A prompt extra component in the high energy spectrum of GRB 131108A". In: *arXiv e-prints* (July 2014) (cited on pages 105, 107).

[292] Qing-Wen Tang, Xiang-Yu Wang, and Ruo-Yu Liu. "Evidence of an Internal Dissipation Origin for the High-energy Prompt Emission of GRB 170214A". In: *Astrophys. J.* 844.1 (2017), p. 56. DOI: 10.3847/1538-4357/aa7a58 (cited on pages 106, 110).

[293] R. Hascoet, F. Daigne, and R. Mochkovitch. "Prompt thermal emission in gamma-ray bursts". In: *Astron. Astrophys.* 551 (2013), A124. DOI: 10.1051/0004-6361/201220023 (cited on pages 106, 107).

[294] Re'em Sari and Tsvi Piran. "Predictions for the very early afterglow and the optical flash". In: *Astrophys. J.* 520 (1999), pp. 641–649. DOI: 10.1086/307508 (cited on pages 106, 107).

[295] E. Molinari et al. "A direct measurement of the relativistic expansion velocity of gamma-ray burst fireballs". In: *Astron. Astrophys.* 469 (2007), pp. L13–L16. DOI: 10.1051/0004-6361:20077388 (cited on pages 106, 107).

[296] G. Ghisellini et al. "A unifying view of Gamma Ray Burst Afterglows". In: *Mon. Not. Roy. Astron. Soc.* 393 (2009), p. 253. DOI: 10.1111/j.1365-2966.2008.14214.x (cited on pages 106, 107).

[297] G. Ghirlanda et al. "Gamma Ray Bursts in the comoving frame". In: *Mon. Not. Roy. Astron. Soc.* 420 (2012), p. 483. DOI: 10.1111/j.1365-2966.2011.20053.x (cited on pages 106, 107).

[298] L. Nava et al. "Afterglow emission in Gamma-Ray Bursts: I. Pair-enriched ambient medium and radiative blast waves". In: *Mon. Not. Roy. Astron. Soc.* 433 (2013), p. 2107. DOI: 10.1093/mnras/stt872 (cited on pages 106, 107).

[299] L. Nava et al. "Clustering of LAT light curves: a clue to the origin of high-energy emission in Gamma-Ray Bursts". In: *Mon. Not. Roy. Astron. Soc.* 443.4 (2014), pp. 3578–3585. DOI: 10.1093/mnras/stu1451 (cited on pages 106, 107).

[300] Frederic Daigne and Robert Mochkovitch. "The Expected thermal precursors of gamma-ray bursts in the internal shock model". In: *Mon. Not. Roy. Astron. Soc.* 336 (2002), pp. 1271–1280. DOI: 10.1046/j.1365-8711.2002.05875.x (cited on pages 106, 107).

[301] Saikat Das, Soebur Razzaque, and Nayantara Gupta. "Modeling the spectrum and composition of ultrahigh-energy cosmic rays with two populations of extragalactic sources". In: *Eur. Phys. J. C* 81.1 (2021), p. 59. DOI: 10.1140/epjc/s10052-021-08885-4 (cited on page 114).

[302] Marco Stein Muzio, Michael Unger, and Glennys R. Farrar. "Progress towards characterizing ultrahigh energy cosmic ray sources". In: *Phys. Rev. D* 100.10 (2019), p. 103008. DOI: 10.1103/PhysRevD.100.103008 (cited on page 114).

[303] Xavier Rodrigues et al. "Active Galactic Nuclei Jets as the Origin of Ultrahigh-Energy Cosmic Rays and Perspectives for the Detection of Astrophysical Source Neutrinos at EeV Energies". In: *Phys. Rev. Lett.* 126.19 (2021), p. 191101. DOI: 10.1103/PhysRevLett.126.191101 (cited on page 114).

[304] N. Fraija et al. "Theoretical Description Of GRB 160625B with Wind-to-ISM Transition and Implications for a Magnetized Outflow". In: *Astrophys. J.* 848.1 (2017), p. 15. DOI: 10.3847/1538-4357/aa8a72 (cited on page 114).

[305] Shan Gao, Kazumi Kashiyama, and Peter Mészáros. "On the neutrino non-detection of GRB 130427A". In: *Astrophys. J. Lett.* 772 (2013), p. L4. DOI: 10.1088/2041-8205/772/1/L4 (cited on page 114).

[306] Tetyana Pitik, Irene Tamborra, and Maria Petropoulou. "Neutrino signal dependence on gamma-ray burst emission mechanism". In: *JCAP* 05 (2021), p. 034. DOI: 10.1088/1475-7516/2021/05/034 (cited on page 114).

[307] Ore Gottlieb and Noemie Globus. "The Role of Jet–Cocoon Mixing, Magnetization, and Shock Breakout in Neutrino and Cosmic-Ray Emission from Short Gamma-Ray Bursts". In: *Astrophys. J. Lett.* 915.1 (2021), p. L4. DOI: 10.3847/2041-8213/ac05c5 (cited on page 114).

[308] Hans Dembinski et al. "The Muon Puzzle in air showers and its connection to the LHC". In: *PoS* ICRC2021 (2021), p. 037. DOI: 10.22323/1.395.0037 (cited on page 115).

[309] Z. Citron et al. "Report from Working Group 5: Future physics opportunities for high-density QCD at the LHC with heavy-ion and proton beams". In: *CERN Yellow Rep. Monogr.* 7 (2019). Ed. by Andrea Dainese et al., pp. 1159–1410. DOI: 10.23731/CYRM-2019-007.1159 (cited on page 115).

[310] Indrek Vurm and Juri Poutanen. "Time-dependent modelling of radiative processes in hot magnetized plasmas". In: *Astrophys. J.* 698 (2009), pp. 293–316. DOI: 10.1088/0004-637X/698/1/293 (cited on page 146).

[311] R. Courant, K. Friedrichs, and H. Lewy. "Über die partiellen Differenzengleichungen der mathematischen Physik". In: *Mathematische Annalen* 100 (1928), pp. 32–74. DOI: 10.1007/BF01448839 (cited on page 147).

[312] Petar Mimica, Miguel-Angel Aloy, and Ewald Mueller. "Internal shocks in relativistic outflows: collisions of magnetized shells". In: *Astron. Astrophys.* 466 (2007), p. 93. DOI: 10.1051/0004-6361:20066811 (cited on page 151).

[313] P. Mimica and M. A. Aloy. "On the dynamic efficiency of internal shocks in magnetized relativistic outflows". In: *Mon. Not. Roy. Astron. Soc.* 401 (2010), p. 525. DOI: 10.1111/j.1365-2966.2009.15669.x (cited on page 151).

Details on AM3 A

A.1 Changes to the original code 147

Below we describe the main characteristics of the AM3 code. All calculations are performed in the plasma comoving frame (that we will for the following chapter refer to, although not using primed symbols).
Originally, the code was designed for efficient computation of lepto-hadronic SEDs of AGN. For this purpose, AM3 solves the (coupled) kinematic equations of electrons, positrons, photons, protons, neutrinos, neutrinos, muons and pions for a constant, comoving volume. Secondaries are added to the particle distributions and undergo the same interactions as the primaries. We rewrite the differential equation Eq. 3.1 for each particle species i as

$$\partial_t n_i(\gamma, t) = -\partial_\gamma[\dot{\gamma}_i(\gamma, t) n_i(\gamma, t) - \partial_\gamma(D_i(\gamma) n_i(\gamma, t))/2] \\ -\alpha_i(\gamma, t) n_i(\gamma, t) + Q_i(\gamma, t)\,. \tag{A.1}$$

Here, we define α_i, Q_i $\dot{\gamma}_i$ and D_i as the sum over all processes j for species i ($\alpha_i = \sum_j \alpha_i^j$ etc.). We identify α as escape/sink term, Q as source/injection and $\dot{\gamma}$ as cooling/advection term. For electrons, positrons and photons we calculate the dimensionless energy as $\gamma = E/(m_e c^2)$. In contrast, the arrays of protons, neutrons, pions and muons are defined on an energy grid of dimensionless $\gamma = E/(m_p[\mathrm{GeV}])$.
The difficulties in the numerical modelling arise from processes that couple the PDEs of single particle species to each other, like a reaction of type $a + b \rightarrow c + d$. At such a process we illustrate the necessary steps to retrieve the injection rate of particles of species c $Q_{c,\mathrm{inj}}$ with Lorentz factor γ_c (following the description in [124]). In principle $Q_{c,\mathrm{inj}}$ is obtained by integrating over distribution of particle species b:

$$Q_{c,\mathrm{inj}} = \int R(b \rightarrow c) n_b(\gamma_b) \mathrm{d}\gamma_b\,, \tag{A.2}$$

where $R(b \rightarrow c)$ is again an integral over the distribution of particles of type a:

$$R(b \rightarrow c) = \int R(a, b \rightarrow c) n_a(\gamma_a) \mathrm{d}\gamma_a\,. \tag{A.3}$$

For this last step, the differential cross section $R(a, b \rightarrow c)$ can be obtained by solving

$$R(a, b \rightarrow c) = \frac{c}{2} \int (1 - \mu) \frac{\mathrm{d}\sigma}{\mathrm{d}\gamma_c \mathrm{d}\mu}(\gamma_c, \gamma_b, \gamma_a, \mu) \mathrm{d}\mu\,. \tag{A.4}$$

Here, $\mu = \cos\Theta$ can be obtained from the reaction angle Θ between b and c.

The computation of the injection rates for each energy thus involves several integrals and is typically computationally expensive. Approaches that allow for efficient computation have been presented for example in [138] for photo-pion production on power-law target photon fields.

[138]: Hummer et al. (2010), "Simplified models for photohadronic interactions in cosmic accelerators"

For the computation Eq. A.1 is re-expressed on a logarithmic energy grid of $x = \ln \gamma$:

$$\partial_t n(x,t) = -\partial_x[A(x,t)n(x,t) - B(x,t)\partial_x n(x,t)] - \alpha(x,t)n(x,t) + \epsilon(x,t)\,,$$

with the (differential) number density $n(x) = \gamma n(\gamma)$. The x-grid is equally spaced in linear space (thus ln-space for γ). The densities are normalised to $\sigma_t^{3/2}$ (electrons, positrons and photons) and cm^3 (protons, neutrons, pions, muons, neutrinos). The system is evolved in linear t, with timesteps defined as fractions of a pre-set dynamical time of the system, $t_{\rm dyn}$.
The A, B, α, and ϵ terms can be calculated from the initial, physical quantities in Eq. A.1 as

$$A(x) = \frac{\dot{\gamma}}{\gamma} - \partial_\gamma \left[\frac{D(\gamma)}{2\gamma}\right], B(x) = \frac{D(\gamma)}{2\gamma}, \epsilon(x) = \gamma Q(\gamma)\,, \alpha(x) = \alpha(\gamma)\,.$$

The following physical processes are implemented as functions of α, ϵ and A (omitting B terms which contribute only marginally):

1. injection (inj,$\epsilon^{\rm inj}$, arbitrary distribution) and escape (esc, $\alpha^{\rm esc}$) for all particles
2. adiabatic cooling (ad, $\alpha^{\rm ad}$, $A^{\rm ad}$ for all charged particles)
3. synchrotron
   * synchrotron radiation from all charged particles (syn, $A^{\rm syn}_{\rm e^\pm}$, $A^{\rm syn}_{\rm p}$, $A^{\rm syn}_{\pi^\pm}$, $A^{\rm syn}_{\mu^\pm}$, $\epsilon^{\rm syn}_\gamma$ from $e^\pm$, $\pi^\pm$, $\mu^\pm$ and p)
   * synchrotron-self absorption(ssa, $\alpha^{\rm ssa}_\gamma$)
4. inverse Compton radiation from $e^\pm$ and p (ic, $A^{\rm ic}_{\rm e^\pm}$,s $\alpha^{\rm ic}_\gamma$, $\epsilon^{\rm ic}_\gamma$)
5. photon-photon annihilation (pp, $\alpha^{\rm pp}_\gamma$, $\epsilon^{\rm pp}_{\rm e^\pm}$)
6. photo-pion production
   * proton-photon pion production ($p\gamma\pi$, $\alpha^{\rm p\gamma\pi}_\gamma$,$\epsilon^{\rm p\gamma\pi}_\gamma$, $\alpha^{\rm p\gamma\pi}_{\rm p}$,$\epsilon^{\rm p\gamma\pi}_{\rm p}$, $\epsilon^{\rm p\gamma\pi}_\pi$)
   * neutron-photon pion production ($n\gamma\pi$, $\alpha^{\rm n\gamma\pi}_\gamma$,$\epsilon^{\rm n\gamma\pi}_\gamma$, $\alpha^{\rm n\gamma\pi}_{\rm n}$,$\epsilon^{\rm n\gamma\pi}_{\rm n}$, $\epsilon^{\rm n\gamma\pi}_\pi$)
7. proton-photon (Bethe-Heitler) pair production (BH, $\alpha^{\rm BH}_\gamma$, $A^{\rm BH}_{\rm p}$, $\epsilon^{\rm BH}_{\rm e^\pm}$)
8. pion and muon decay kinematics and neutrino production (dec, $\alpha^{\rm dec}_{\mu^\pm}$, $\alpha^{\rm dec}_{\pi^\pm}$, $\epsilon^{\rm dec}_{e^\pm}$, $\epsilon^{\rm dec}_{\mu^\pm}$, $\epsilon^{\rm dec}_\nu$)

[310]: Vurm et al. (2009), "Time-dependent modelling of radiative processes in hot magnetized plasmas"

The exact treatment of processes 1. - 5. for leptons, positrons and protons is described in [310], [124]. Since then, the synchrotron kernels have been updated and now also include quantum synchrotron radiation of

electrons (following [281]) which may be relevant for strong magnetic fields. In contrast to the description in [124], Bethe-Heitler pair production is calculated following [134].

The kinematic equations (Eq. A.5) are solved with a Crank-Nicolson differential scheme in time t and a Chang & Cooper scheme on energy x. To increase efficiency, a semi-analytical approach is chosen for the highest energies. With full optimizations the code simulates a leptonic SED and light curve in a few CPU seconds and a few tens of seconds for a hadronic case.

[281]: Brainerd (1987), "Quantum Synchrotron Spectra from Semirelativistic Electrons in Teragauss Magnetic Fields"

[134]: Kelner et al. (2008), "Energy spectra of gamma-rays, electrons and neutrinos produced at interactions of relativistic protons with low energy radiation"

A.1 Changes to the original code

Below, we briefly summarise the main additions to the code since [124] relevant for this thesis.

Cooling of muons and pions
As mentioned above, pions and muons are treated as separate species which participate in synchrotron emission/cooling and cool adiabatically (if they have a non-zero charge). Inverse Compton scatterings are neglected. The escape time is equal to that of all other particles species. Finally, their decay time (in the particle restframe) is $\tau_{0,\mu} = 2.2 \cdot 10^{-6}$ s and $\tau_{0,\pi} = 2.8 \cdot 10^{-8}$ s.

Adiabatic Cooling
The adiabatically expanding outflow causes charged particles to cool with $\dot{\gamma} = -\frac{\gamma}{t_{\rm ad}}$. In Eq. A.5, this corresponds to constant cooling term of $A = t_{\rm ad}$.

Adaptive time-stepping
For a decaying particle distribution it is convenient to not keep the timestep δt constant, but instead define δt such that the cooling of the highest-energy particles (located at gridpoint $i_{\rm max}$) can be resolved at each computational time:

$$\delta t = -\frac{\Delta X}{A_{\rm max}(i_{\rm max})} \,. \tag{A.5}$$

Here ΔX is the spacing of the energy grid and $A_{\rm max}(i_{\rm max})$ the largest cooling term A (taking into account synchrotron, inverse Compton and adiabatic cooling) of particles at $i_{\rm max}$. This requirement is also known as the Courant-Friedrichs-Lewy (CFL) condition [311] with a Courant number $C = 1$.
In our calculations an exponential cut-off was assumed for the particle distributions. Thus, in lack of a sharp cut-off, we locate the gridpoint $i_{\rm max}$ that corresponds to the highest-energy particles as follows: After identifying the maximum energy density of the distribution $\max(u_E)$, we iterate from the high-energy end of the grid backwards until $i_{\rm max}$ where

[311]: Courant et al. (1928), "Über die partiellen Differenzengleichungen der mathematischen Physik"

$u_E(i_{\max}) = 10^{-10}\max(u_E)$. The timestep is then calculated from Eq. A.5. The code further re-evaluates the boundary between the matrix and the analytic solver automatically at each timestep.

Additional material on multi-collision internal shock models

B

We extend the results of Chapter 5 by four aspects: First, we test the impact of the discretisation $d\tau = t_{eng}/N_{shells}^{initial}$ for the Daigne and Mochkovitch internal shock scenario. Second, we examine the probability of a two-shell post-collision configuration (as predicted by the ultra-efficient shock scenario) through Pluto simulations. Third, we review the parameter space for the inverse Compton Klein-Nishina and fast-cooling regime for LL-GRBs. Finally, we provide additional model parameters for our GRB-radiation modelling such as the used f_B-$\zeta_{e,0}$ sets.

The results were partially presented in [214, 233].

B.1 The discretisation time in the Daigne and Mochkovitch model 149

B.2 Probability of two-shell post-collision states 150

B.3 Radiation regimes in LL-GRBs 153

B.4 Additional parameter tables for the radiation modelling 154

B.1 The discretisation time in the Daigne and Mochkovitch model

To ensure that our results obtained within the Daigne and Mochkovitch model for GRB internal shocks [168] are independent of the discretisation time $d\tau$, we examine the impact of different $d\tau$ (labelled as 'high', 'medium' and 'low' resolution) on the fireball evolution and collision parameters; for the exact parameters see Table B.1.

[168]: Daigne et al. (1998), "Gamma-ray bursts from internal shocks in a relativistic wind: temporal and spectral properties"

We choose a non-trivial initial Lorentz factor (shown in Figure B.1, upper left plot) and calculate the fireball evolution for three different discretisation times, imposing equal wind luminosity $L_{wind} = 1.86 \cdot 10^{55}$ erg/s. From the initial number of shells the initial shell distribution was calculated by an automated routine; we point out that for the largest discretisation time, the total wind duration is slightly smaller.

In the upper panel we display the comoving dissipated energy E'_{diss} and rest mass density ρ'. E'_{diss} decreases with higher resolution (that corresponds to a low $d\tau$). This can easily be explained by the lower contrasts of Lorentz factor of the colliding shells which reduce the single-collision dissipation efficiency for low $d\tau$/ high resolution. We verified that for all three scenarios the total dissipated energy of the fireball (in the source frame) remains unaffected by the resolution/discretisation. On the other hand, the comoving mass densities ρ' are higher for high resolution (low $d\tau$). This is in accordance with expectations, as for equal wind luminosity, $\rho' \propto d\tau$.

In the lower left plot of Figure B.1, we show the mass of the merged post-collision shell. Independent of resolution, the same behaviour is reproduced. We further verified that the merged shell Lorentz factors also reproduce the same behaviour. These two aspects imply that the overall dynamical evolution of the fireball is independent of $d\tau$.

Table B.1: Parameters for the different resolutions/discretisation times of the Daigne and Mochkovitch model.

	resolution		
	high	medium	low
$d\tau$ [c]	0.02	0.04	0.184
$N_{shells}^{initial}$	1994	996	216
N_{coll}	1171	582	121

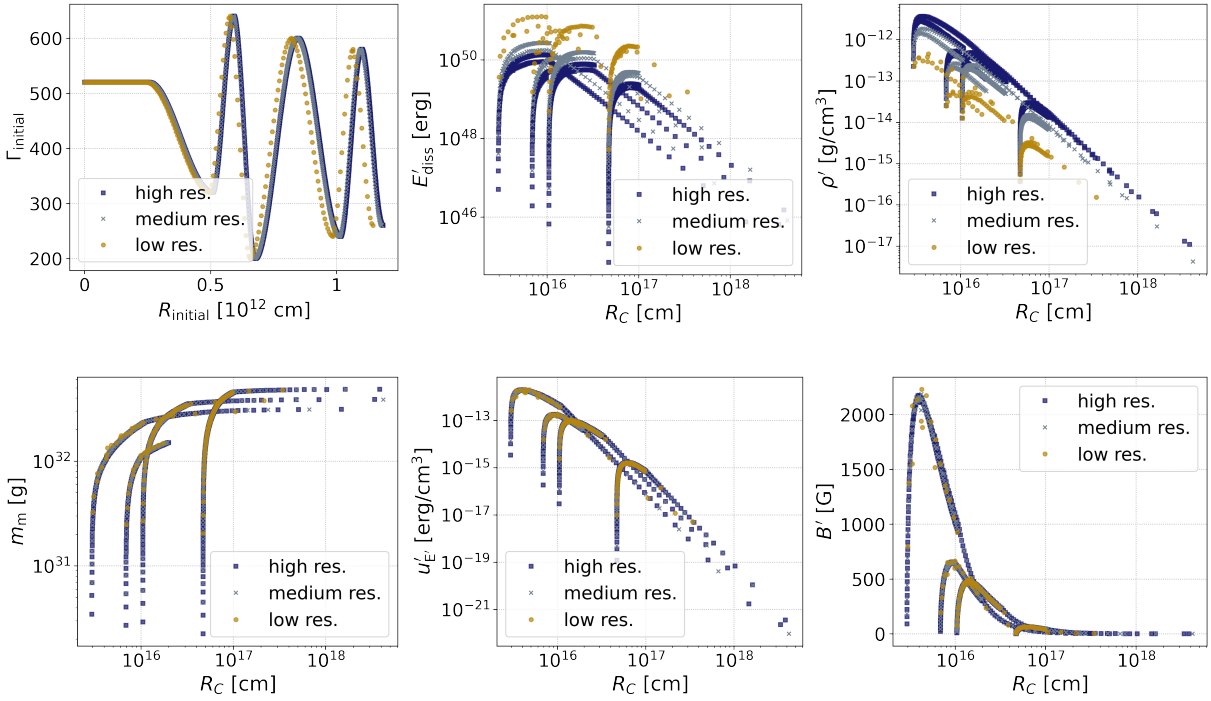

Figure B.1: Testing the intial resolution/discretisation width $\mathrm{d}\tau$ for the Daigne and Mochkovitch model. For parameters of the three resolution schemes see Table B.1, the assumed wind luminosity was $L_{\rm wind} = 1.86 \cdot 10^{55}$ erg/s.
Upper panel: *(Left)* Initial Lorentz factor distribution, *(middle)* comoving dissipated energy $E'_{\rm diss}$ and *(right)* rest mass density ρ' as a function of collision radius $R_{\rm C}$.
Lower panel: *(Left)* merged post-collision shell mass $m_{\rm m}$, *(middle)* comoving energy density $u'_{E'}$, and *(right)* the comoving magnetic field strength B' (for $\epsilon_B = 0.1$) . All as a function of collision radius $R_{\rm C}$.

The left and right plot of the lower panel show parameters that are important for the radiation modelling: The comoving energy density $u'_{E'}$, and magnetic field strength B'. For the calculation of the comoving energy density ($u'_{E'} = \frac{E'_{\rm diss}\rho'}{m_m}$) the differences in the comoving mass density and dissipated energy cancel out and the same evolution is reproduced independent of discretisation. As the magnetic field depends solely on $u'_{E'}$ and ϵ_B it also remains unaffected by the discretisation time/resolution. These results indicate that the radiation modelling is independent of the discretisation scheme.

We conclude that the choice of discretisation time does not affect the fireball evolution nor the radiation modelling and its results, as long as the fireball evolution can be computed with high enough accuracy. In our examination this was not the case for the low resolution scenario, where the low collision sampling especially around the first peak may lead to different results.

B.2 Probability of two-shell post-collision states

[217]: Kobayashi et al. (2001), "Ultra efficient internal shocks"

In [217], a 1D RHD simulation of a two-shell encounter is presented that supports a two-shell final state as proposed by the ultra-efficient shock

model. However, the simulation was just performed for a single set of collision parameters. In light of the questionable representativeness of this simulation, we perform a shock-tube simulations in a parameter-scan over Γ_f/Γ_s and m_f/m_s of the colliding shells (as presented in [214]). Different choices of Γ_s were examined but showed little impact. The simulations are performed with the modular RMHD code Pluto v4.2 [219]. Given the context of the internal shock model we neglect magnetic fields, for studies that invoke magnetisation see *e.g.* [312, 313].
We apply the Relativistic-Hydro-Dynamics (RHD) physics module of Pluto. Further settings are an ideal equation of state, Cartesian geometry, a linear reconstruction, Hancock time-stepping and the CD-restoring HLLC approximate Riemann solver. For better resolution of the shock, we perform the simulations in the rest frame of the Contact Discontinuity (CD, also noted as primed frame in this section). The gas adiabatic index is set to $\hat{\gamma} = 4/3$ (relativistic) if the Lorentz factor of the fast shell in the CD frame is larger than two ($\Gamma'_r > 2$) and $\hat{\gamma} = 5/3$ (non-relativistic) else.

[214]: Rudolph et al. (2020), "Impact of the Collision Model on the Multi-messenger Emission from Gamma-Ray Burst Internal Shocks"
[219]: Mignone et al. (2007), "PLUTO: A Numerical Code for Computational Astrophysics"
[312]: Mimica et al. (2007), "Internal shocks in relativistic outflows: collisions of magnetized shells"
[313]: Mimica et al. (2010), "On the dynamic efficiency of internal shocks in magnetized relativistic outflows"

In difference to earlier studies, we further invoke a simple energy dissipation scheme given by

$$\frac{\partial \rho\, e}{\partial t} = \begin{cases} -\chi \cdot \rho\, e & , E_{\mathrm{diss,total}} \leq \eta^*_{\mathrm{diss}} E_{\mathrm{int,th}} \\ 0 & , \mathrm{else} \end{cases} , \tag{B.1}$$

where ρ is the rest mass density, e the internal energy per unit mass (thus ρe is the internal energy density) and χ a freely chosen parameter. Further, η^*_{diss} controls the total dissipated energy by relating it to $E_{\mathrm{int,th}}$, the dissipated energy as predicted by the internal shock model (Eq. 5.3). In all simulations we set $\chi = 10\, \eta^*/t'_{\mathrm{shock}}$ and $\eta^*_{\mathrm{diss}} = \eta_{\mathrm{diss}}$ (which is the dissipation efficiency of single collisions introduced in the multi-collision modelling).
Simply spoken, this implementation means that energy is dissipated proportionally to the available internal energy until a given threshold is reached.

To evaluate the probability of a two-shell final state, we scan over the parameter space of mass and Lorentz factor ratios of the colliding shells (m_f/m_s and Γ_f/Γ_s). The results are shown in Figure B.2. The upper left and two lower plots correspond to equal shell widths in the source frame ($\Delta_f = \Delta_s$), in the upper right plot we set $\Delta_f = 0.1\Delta_s$. In the upper panel no energy dissipation is included in Pluto, in the lower panel we set $\eta_{\mathrm{diss}} = 0.2$ (left) and $\eta_{\mathrm{diss}} = 0.5$ (right). The lines further indicate where $m_f = m_s$ and $E_f = E_s$ are true (in the source frame).
The contours measure the depth of the dip created between the two shells

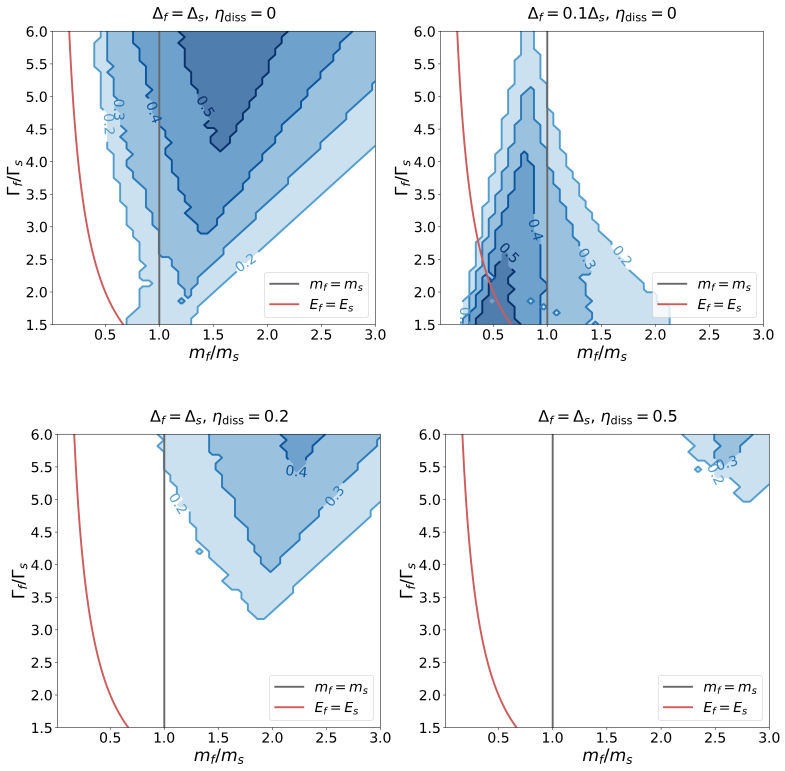

Figure B.2: Depth of the dip $d_{\rm dip}$ (see Eq. B.2) between the post-collision shells, scanning over different mass ratios and Lorentz factor ratios of the colliding shells (m_f/m_s and Γ_f/Γ_s). On the red (black) line, the colliding shells have equal mass (energy).
In the upper left and two lower plots, the colliding shells share the same width in the source frame ($\Delta_f = \Delta_s$), in the upper right plot we set $\Delta_f = 0.1\Delta_s$. While in the upper panel, energy dissipation is not included in PLUTO, we examine $\eta_{\rm diss} = 0.2$ and $\eta_{\rm diss} = 0.5$ in the lower panel.
In white regions, we could not identify two separate post-collision shells.
Figures adapted from [214]

$d_{\rm dip}$, defined as

$$d_{\rm dip} = \frac{\rho_{\rm max} - \rho_{\rm min}}{\rho_{\rm max}}\,, \tag{B.2}$$

where $\rho_{\rm max}$ is the maximum density of the less dense post-collision shell and $\rho_{\rm min}$ the density at the dip between the two peaks. Overall, $d_{\rm dip}$ thus measures how deep the decrease in density is that separates the two final shells and large values of $d_{\rm dip}$ correspond to well-separated post-collision shells. In the white areas of the plots, we could not identify two separate post-collision shells.

[218]: Kino et al. (2004), "Hydrodynamical effects in internal shock of relativistic outflows"

[218] studied post-collision shell configurations by means of analytical estimates for the hydrodynamical timescales governing the system. They find that depending on the ratio of shock-crossing and rarefaction-wave crossing times for the fast and slow shell, single to triple peaked profiles can theoretically be realised. However, in reality the triple-peaked configuration will mostly appear as double-peaked.
Overall, they favour an equal-mass scenario with large Γ_f/Γ_s (for $\Delta_f = \Delta_s$) for a two-shell post-collision state. This is in agreement with our findings in Figure B.2; the center of the triangle-shaped distribution of dip depth lies however at slightly larger mass ratios of $m_f/m_s \simeq 1.5$. For $\Delta_f = 0.1\Delta_s$, the distribution is flipped horizontally, with a much narrower distribution and centered around $m_f/m_s \simeq 0.6$. This behaviour may be explained by the change of shock crossing times for different shell widths.
For our simulations that include energy dissipation (shown in the lower panel of Figure B.2), the parameter-space region for a two-shell post-

collision state moves up to the right corner of the plot, hence to larger Γ_f/Γ_s and m_f/m_s. Especially for $\eta_{\rm diss} = 0.5$, in the largest part of the parameter space only one post-collision shell can be expected.
We conclude that a two-shell post-collision setup is only realised in a specific part of the parameter space and cannot be generally assumed. The parameter-space region may be reduced by effects of energy dissipation on the shock evolution.

For the full fireball simulations were we couple PLUTO shock-tube simulations to our radiation models, *i.e.* we evolve each two-shell encounter with PLUTO). For this we set $d_{\rm dip} = 0.3$ as a threshold for a two shell-final state and impose $\eta_{\rm diss} = 0.5$. The post-collision shell(s) are calculated from the post-collision PLUTO configuration such that the energies and masses are conserved, for more details see [214].

B.3 Radiation regimes in LL-GRBs

As an addition to the LL-GRB results presented in the main text, we investigate different radiation regimes realised during the jet dynamical evolution that may impact the photon spectra, as presented in [233]. In analogy to the results of Chapter 6 we examine a parameter space of $f_{\rm B}$ (x-axis of Figure B.3). The fireball evolution is represented as different collisions between single layers in the GRB evolution, assuming the same fireball evolution that is set by $L_{\rm wind}$ and the Lorentz factor distribution for each GRB. For each f_B, we adjust $\zeta_{e,0}$ such that the observed synchrotron peak remains constant. We then evaluate for each single collision (numbered chronologically by the time they occur in the source frame on the y-axis of Figure B.3) and f_B the following two conditions:

[233]: Rudolph et al. (2022), "Multi-wavelength radiation models for low-luminosity GRBs and the implications for UHECRs"

1. *Fast-cooling regime*
   Following Section 4.4, this regime is realised if the critical Lorentz

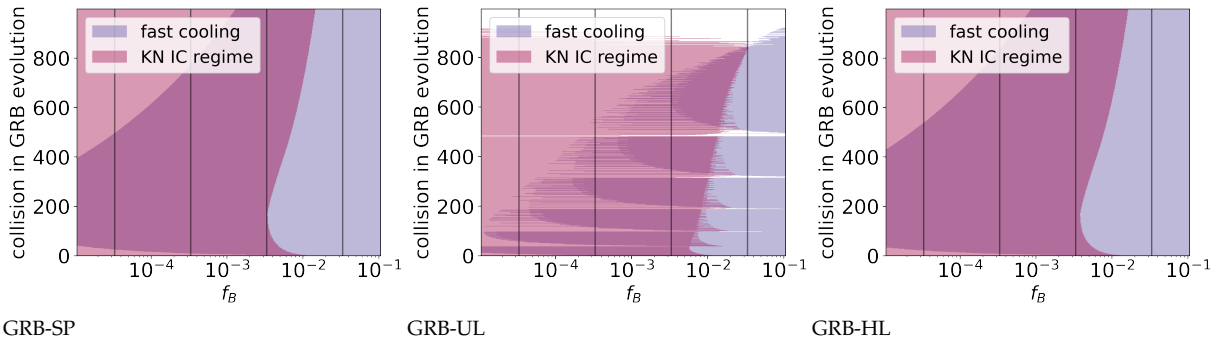

Figure B.3: Parameter space (see text) for the fast-cooling (blue) and Klein-Nishina inverse Compton (purple) regime as a function of $f_{\rm B}$ for GRB-SP, GRBl-long and GRB-HL for a fixed fireball evolution (Lorentz factor distribution and wind luminosity). The dark purple region marks the overlap of both regimes. Vertical lines correspond to the choices for $f_{\rm B}$ considered for the SED modelling.

factor is smaller than $\gamma_{e,\mathrm{min}}$: $\gamma_{e,\mathrm{c}} < \gamma_{e,\mathrm{min}}$. In the fast-cooling regime the complete distribution of primary electrons cools on the dynamical timescale. This implies that primary electrons efficiently convert their energy into non-thermal radiation.
The region in the parameter space fulfilling this criterion is marked **blue** in Figure B.3.

2. *Inverse Compton scatterings occurring in the Klein-Nishina regime*
This regime (identified in [184, 187]) is realised if $\eta_{\mathrm{m}}^{1/3} \leq Y_{\mathrm{Th}} \leq \eta_{\mathrm{m}}^{3}$ holds. The Compton-Y-parameter can be calculated directly as $Y_{\mathrm{Th}} \simeq [(p_e-2)/(p_e-1)]f_B^{-1}$, where $\eta_{\mathrm{m}} \simeq 100\,(\gamma_{e,\mathrm{min}}/100)^3(B'/3000\mathrm{G})$.
The region in the parameter space fulfilling this criterion is marked **purple** in Figure B.3.

[184]: Daigne et al. (2011), "Reconciling observed GRB prompt spectra with synchrotron radiation ?"
[187]: Nakar et al. (2009), "Klein-Nishina effects on Synchrotron and Synchrotron self-Compton spectrum"

The region where **both** criteria are met is depicted as **dark purple**.
We first review the parameter space for the fast-cooling regime: Due to the low luminosity of the events, large magnetic fields (corresponding to large f_B) are required for collisions to be in the fast cooling regime. This is especially true for GRB-UL, where even for $f_B = 3 \cdot 10^{-1}$ this condition is not satisfied in all collisions. We find that for all three prototypes the majority of the collisions are in the slow-cooling regime for $f_B = 3 \cdot 10^{-4}$ which we consequently suggest to be disfavoured energetically. We conclude that $f_B \gtrsim 10^{-3}$ should be chosen and $f_B = 3 \cdot 10^{-4}$ is not a realistic parameter assumption.
The Klein-Nishina inverse Compton regime is generally realised for lower values of f_B.

B.4 Additional parameter tables for the radiation modelling

For completeness we list the f_B-$\zeta_{e,0}$ pairs used in our GRB radiation models in Table B.2. The Table further includes the corresponding minimum Lorentz factor of electrons $\gamma_{e,\mathrm{min}}$ as well as the number fraction of accelerated electrons ζ and the magnetic field strength B' at the peak of the simulated burst (for the models where $\zeta \propto \epsilon'_{\mathrm{diss}}$ was assumed). In the case where we explored ζ = cst. we instead list $\gamma_{e,\mathrm{min}}$ and B' at the peak.

Table B.2: Parameters for the GRB radiation modelling: Parameter sets of f_B and $\zeta_{e,0}$ used for the radiation modelling as well as the minimum electron Lorentz factor $\gamma_{e,\mathrm{min}}$ (that remained constant for $\zeta_e \propto \epsilon'_{\mathrm{diss}}$. We further list the following parameters at the maximum of the pulse (the 'peak', which is defined as the collision where $\epsilon'_{\mathrm{diss}}$ and E_{diss} are maximal): the fraction of accelerated electrons $\zeta_{e,\mathrm{peak}}$ and the magnetic field B'. We define $\zeta_e = \min\left\{\zeta_{e,0} \cdot \frac{\epsilon'_{\mathrm{diss}}}{100\mathrm{MeV/proton}}, 1\right\}$.

The top two tables tables contain the parameters for the LL-GRBs, for the educative example and the *Fermi*-LAT inspired prototypes, all with the fiducial setup of $\zeta_e \propto \epsilon'_{\mathrm{diss}}$. The bottom table lists the parameters for the additional models of the educative example where we explored the impact of modelling assumptions. For the constant-ζ_e model, we list the minimum electron Lorentz factor at the maximum of the pulse.

	GRB-SP				GR-UL				GRB-HL			
f_B	$\frac{\zeta_{e,0}}{10^{-4}}$	$\frac{\gamma_{e,\mathrm{min}}}{10^4}$	$\frac{\zeta_{e,\mathrm{peak}}}{10^{-4}}$	B'_{peak} [G]	$\frac{\zeta_{e,0}}{10^{-4}}$	$\frac{\gamma_{e,\mathrm{min}}}{10^4}$	$\frac{\zeta_{e,\mathrm{peak}}}{10^{-4}}$	B'_{peak} [G]	$\frac{\zeta_{e,0}}{10^{-4}}$	$\frac{\gamma_{e,\mathrm{min}}}{10^4}$	$\frac{\zeta_{e,\mathrm{peak}}}{10^{-4}}$	B'_{peak} [G]
$3 \cdot 10^{-1}$	7.3	3.0	5.8	300	9.2	2.8	7.6	91	5.7	3.6	6.0	126
$3 \cdot 10^{-2}$	4.1	5.3	3.2	94	5.2	5.0	4.3	29	3.2	6.4	3.4	40
$3 \cdot 10^{-3}$	2.3	9.4	1.8	30	2.9	8.9	2.4	9	1.8	11.3	1.9	13
$3 \cdot 10^{-4}$	1.3	16.8	1.0	9	1.6	15.9	1.4	3	1.0	20.1	1.0	4

	educative example				GRB 131108A-like				GRB 170214B-like			
f_B	$\frac{\zeta_{e,0}}{10^{-3}}$	$\frac{\gamma_{e,\mathrm{min}}}{10^4}$	$\frac{\zeta_{e,\mathrm{peak}}}{10^{-6}}$	B'_{peak} [G]	$\frac{\zeta_{e,0}}{10^{-3}}$	$\frac{\gamma_{e,\mathrm{min}}}{10^3}$	$\frac{\zeta_{e,\mathrm{peak}}}{10^{-4}}$	B'_{peak} [G]	$\frac{\zeta_{e,0}}{10^{-3}}$	$\frac{\gamma_{e,\mathrm{min}}}{10^4}$	$\frac{\zeta_{e,\mathrm{peak}}}{10^{-4}}$	B'_{peak} [G]
1	1.8	1.2	5.1	1657	2.3	9.3	3.7	2713	2.1	1.5	2.3	3768
10^{-1}	1.0	2.1	1.9	524	–	–	–	–	–	–	–	–
10^{-2}	0.8	3.6	1.6	165	–	–	–	–	–	–	–	–
10^{-3}	0.4	6.5	0.9	52	0.4	52.5	0.65	85	0.4	8.6	0.4	119

	educative example											
	constant ζ_e			$(\Gamma^{\mathrm{inital}}_{\mathrm{min}}, \Gamma^{\mathrm{inital}}_{\mathrm{max}}) = (100, 500)$				$(\Gamma^{\mathrm{inital}}_{\mathrm{min}}, \Gamma^{\mathrm{inital}}_{\mathrm{max}}) = (400, 900)$				
f_B	$\frac{\zeta_e}{10^{-6}}$	$\frac{\gamma_{e,\mathrm{min,peak}}}{10^4}$	B'_{peak} [G]	$\frac{\zeta_{e,0}}{10^{-3}}$	$\frac{\gamma_{e,\mathrm{min}}}{10^3}$	$\frac{\zeta_{e,\mathrm{peak}}}{10^{-5}}$	B'_{peak} [G]	$\frac{\zeta_{e,0}}{10^{-4}}$	$\frac{\gamma_{e,\mathrm{min}}}{10^4}$	$\frac{\zeta_{e,\mathrm{peak}}}{10^{-6}}$	B'_{peak} [G]
1	4.9	1.2	1657	3.6	6.1	1.3	8702	9.6	2.3	1.5	319
10^{-1}	2.8	2.1	524	–	–	–	–	–	–	–	–
10^{-2}	1.6	3.8	165	–	–	–	–	–	–	–	–
10^{-3}	0.9	6.7	52	0.6	34.3	0.2	275	1.7	12.7	0.3	10